Environmental Effects on Composites Durability with regard to Fibers, Matrix, and Interphase

Vom Promotionsausschuss der
Technischen Universität Hamburg

zur Erlangung des akademischen Grades

Doktor-Ingenieur (Dr.-Ing.)

genehmigte Dissertation

von
Dennis Gibhardt
aus Lüneburg

2024

Vorsitzender des Prüfungsausschusses:	Prof. Dr.-Ing. habil. Stefan Heinrich (Technische Universität Hamburg)
Gutachter:	Prof. Dr.-Ing. habil. Bodo Fiedler (Technische Universität Hamburg) Prof. Dr. Andreas Echtermeyer (Norwegian University of Science and Technology)
Tag der mündlichen Prüfung:	05.04.2024

Technisch-Wissenschaftliche Schriftenreihe

Herausgeber:
Prof. Dr.-Ing. habil. Bodo Fiedler

Anschrift:
Technische Universität Hamburg
Institut für Kunststoffe und Verbundwerkstoffe
Denickestraße 15
21073 Hamburg

Band 46:
Environmental Effects on Composites Durability with regard to Fibers, Matrix, and Interphase
DOI: https://doi.org/10.15480/882.9468

Dennis Gibhardt
https://orcid.org/0000-0002-4684-3068

1. Auflage
Hamburg 2024

ISSN 2625-6029

Bibliographische Information der Deutschen Nationalbibliothek: Die deutsche Nationalbibliothek verzeichnet diese Publikation in der Deutschen Nationalbibliothek; detaillierte Informationen sind im Internet über dnb.de abrufbar.

To Mareike, Lasse, and Finja.

Abstract

High-performance fiber-reinforced polymers (FRPs) are used as structural materials in various applications such as wind energy, aviation, mobility, construction, and piping because of their comparably low densities, high strengths and stiffnesses, corrosion resistance, and their particularly good fatigue properties. The long-term properties become more important, especially when the aspired service lifetime of the products and parts exceeds decades. Depending on the operational area, this often implies severe impacts of the surrounding environments, such as temperature variations, water or moisture contact and absorption, as well as radiation. Due to the great variety of specific composite compositions available and the diverse operating conditions, unified testing standards are still missing today. Therefore, many accelerated aging processes, e.g., using increased aging temperatures, have evolved, each more or less suitable for making lifetime predictions. However, the main challenges remain, on the one hand, to relate the global impact on the composite to the local effects of the constituents and, on the other hand, to understand the mechanisms introduced by relying on accelerated aging procedures. The overarching research hypothesis of this is therefore:

Improving the long-term durability of GFRP structures under severe operating conditions requires an in-depth understanding of the effects of the various environmental conditions on the composite's constituents.

Consequently, the proposed work is based on various aging experiments on composites and their single constituents (fibers, matrix resins, fiber sizings, and interphases). The effects of the aging temperature and the specific materials used were investigated in long-term studies, from which prediction models for strength and lifetime were derived. Due to the outstanding importance of the polymeric matrix, the first chapter focuses on the change of the thermomechanical material properties of epoxy resins used as matrix materials. In

this context, it could be demonstrated that two major processes, plasticization and physical aging (relaxation) co-occur and oppositional affect the major properties such as epoxy strength and ductility. Furthermore, it was proved that the temperature-depending acceleration of the underlying processes is diverging. Hence, the aging temperature has a decisive impact on the development of the properties over time. As a result of these findings, a property prediction model based on the well-known Arrhenius and Kohlrausch-Williams-Watts correlations was developed and expanded to consider the thickness-dependent proportions of diffusion-based plasticization and temperature-based relaxation.

The work's second part focuses on the aging effects on glass fiber-based composites and the specific importance of the fiber and sizing constitution for the lifetime under severe environmental degradation. Therefore, a novel fiber aging methodology was developed and implemented to manufacture composites with artificially aged fiber/matrix interphases. In this way, it was possible to investigate and analyze not only the global impact of various aging procedures on the composites as a whole but also to distinguish between interphase, fiber, and matrix-related damage and their impact on the total lifetime. Furthermore, the damage progress was analyzed and related to major composite properties, such as the epoxy and composite's fracture toughness in modes I and II, including the effects of water absorption and interphase degradation. The results obtained with micro- and micromechanical tests were used to extend a recently published model for composite lifetime prediction by Sörensen et al. [1], including the effects of interphase aging. Finally, the impact of long-term aging on service-life-related situations was investigated. Therefore, the effects of one-sided diffusion on thick, multidirectional composites and the change of evolving damage related to impacts were tested and analyzed. In summary, the work highlights the importance of the aging history (time, temperature, environment) on the properties and lifetime of GFRP. It provides several models and methodologies to investigate and predict the material behavior of composites and their constituents.

Kurzfassung

Faserverstärkte Kunststoffe (FVK) werden aufgrund ihrer vergleichsweisen geringen Dichten, ihrer hohen Festigkeiten und Steifigkeiten, ihrer Korrosionsbeständigkeiten und ihrer besonders guten Ermüdungseigenschaften als Strukturwerkstoffe in verschiedenen Anwendungen wie Windenergie, Luftfahrt, Mobilität, Bauwesen und Rohrleitungen eingesetzt. Die Langzeiteigenschaften gewinnen vor allem dann an Bedeutung, wenn die angestrebte Lebensdauer der Produkte und Bauteile Jahrzehnte überschreitet. Je nach Einsatzgebiet ist dies oft mit starken Umwelteinflüssen wie Temperaturschwankungen, Wasser- oder Feuchtigkeitseinfluss und -aufnahme sowie UV-Strahlung verbunden. Aufgrund der großen Vielfalt an spezifischen Verbundwerkstoffzusammensetzungen und der unterschiedlichen Betriebsbedingungen fehlen bis heute einheitliche Prüfstandards. Daher haben sich viele beschleunigte Alterungsprozesse, z. B. unter Verwendung erhöhter Alterungstemperaturen, entwickelt, die alle mehr oder weniger geeignet sind, um Vorhersagen über die Lebensdauer zu machen. Die größten Herausforderungen bestehen jedoch nach wie vor darin, einerseits die globalen Auswirkungen auf den Verbundwerkstoff mit den lokalen Effekten der Bestandteile in Beziehung zu setzen und andererseits die Mechanismen zu verstehen, die durch die Anwendung von beschleunigten Alterungsverfahren eingeführt werden. Die übergreifende Forschungshypothese lautet daher:

Die Verbesserung der Langzeitbeständigkeit von GFK-Strukturen unter herausfordernden Betriebsbedingungen erfordert ein tiefgreifendes Verständnis der Auswirkungen der verschiedenen Umweltbedingungen auf die Bestandteile des Verbundwerkstoffs.

Die vorliegende Arbeit stützt sich daher auf verschiedene Alterungsexperimente an Verbundwerkstoffen und ihren einzelnen Bestandteilen (Fasern, Matrixharzen, Faserschlichten und Grenzphasen). Die Auswirkungen der Alterungstemperatur und der verwendeten Materialien wurden in Langzeitstudien untersucht,

aus denen Vorhersagemodelle für Festigkeit und Lebensdauer abgeleitet wurden. Aufgrund der herausragenden Bedeutung der Polymermatrix konzentriert sich das erste Kapitel auf die Veränderung der thermomechanischen Materialeigenschaften von Epoxidharzen, die als Matrixmaterial verwendet werden. In diesem Zusammenhang konnte gezeigt werden, dass zwei wesentliche Prozesse, die Plastifizierung und die physikalische Alterung (Relaxation), gleichzeitig ablaufen und sich gegenläufig auf die wichtigsten Eigenschaften wie die Festigkeit und Duktilität des Epoxidharzes auswirken. Darüber hinaus wurde nachgewiesen, dass die temperaturabhängige Beschleunigung der zugrundeliegenden Prozesse divergierend ist. Somit hat die Alterungstemperatur einen entscheidenden Einfluss auf die zeitliche Entwicklung der Eigenschaften. Als Ergebnis dieser Erkenntnisse wurde ein Eigenschaftsvorhersagemodell auf Basis der bekannten Arrhenius- und Kohlrausch-Williams-Watts-Korrelationen entwickelt und um die dickenabhängigen Anteile der diffusionsbasierten Plastifizierung und der temperaturbasierten Relaxation erweitert.

Der zweite Teil der Arbeit befasst sich mit den Alterungseffekten auf glasfaserbasierte Verbundwerkstoffe und der besonderen Bedeutung der Faser- und Schlichtebeschaffenheit für die Lebensdauer unter herausfordernden Umweltbelastungen. Daher wurde eine neuartige Methode zur Faseralterung entwickelt und implementiert, um Verbundwerkstoffe mit künstlich gealterten Faser/Matrix-Grenzphasen herzustellen. Auf diese Weise war es möglich, nicht nur die globalen Auswirkungen der verschiedenen Alterungsverfahren auf die Verbundwerkstoffe als Ganzes zu untersuchen und zu analysieren, sondern auch zwischen interphasen-, faser- und matrixbezogenen Schäden und deren Auswirkungen auf die Gesamtlebensdauer zu unterscheiden. Darüber hinaus wurde der Schädigungsfortschritt analysiert und mit den wichtigsten Verbundwerkstoffeigenschaften, wie der Bruchzähigkeit des Epoxidharzes und der Verbundwerkstoffe in den Modi I und II, in Beziehung gesetzt, einschließlich der Auswirkungen der Wasseraufnahme und der Degradation der Grenzphase. Die mit mikro- und makromechanischen Tests erzielten Ergebnisse wurden verwendet, um ein kürzlich von Sörensen et al. [1] veröffentlichtes Modell zur Vorhersage der Lebensdauer von Verbundwerkstoffen zu erweitern und die Auswirkungen der Grenzphasenalterung einzubeziehen. Schließlich wurden die Auswirkungen der Langzeitalterung auf lebensdauerbezogene Situationen untersucht. Zu diesem Zweck wurden die Auswirkungen der einseitigen Diffusion auf dicke, multidirektionale Verbundwerkstoffe und die Veränderung der sich entwickelnden Schädigung durch Im-

pactschäden getestet und analysiert. Zusammenfassend unterstreicht die Arbeit die Bedeutung der Alterungsgeschichte (Zeit, Temperatur, Umgebung) auf die Eigenschaften und die Lebensdauer von GFK. Die Arbeit beinhaltet mehrere Modelle und Methoden zur Untersuchung und Vorhersage des Materialverhaltens von Verbundwerkstoffen und ihren Bestandteilen.

Contents

List of Abbreviations

AFM	Atomic force microscopy
CAI	Compression after impact
CC	Compliance calibration
CDM	Continuum damage mechanics
CFRP	Carbon-fiber reinforced polymer
CSR	Constant strain rate
DCB	Double cantilever beam
DGEBA	Bisphenol A diglycidyl ether
DGEBF	Bisphenol F diglycidyl ether
DMTA	Dynamic mechanical thermal analysis
EDX	Energy dispersive X-ray spectroscopy
ENF	End-notched flexure
ERR	Energy release rate
FEA	Finite element analysis
FIM	Failure index matrix
F/M	Fiber/Matrix
FRP	Fiber-reinforced polymer
FTIR	Fourier transform infrared spectroscopy
GFRP	Glass fiber-reinforced polymer
GFEP	Glass fiber-reinforced epoxy
HCF	High-cycle fatigue
ILSS	Interlaminar shear strength
KWW	Kohlrausch-Williams-Watts
LCF	Low-cycle fatigue
LVI	Low-velocity impact
MD	multidirectional
NCF	Non-crimp fabric
NIR	Near infrared regime
PMC	Polymer matrix composite
PTFE	Polytetrafluoroethylene
QI	Quasi-isotropic
Q-UD	Quasi-unidirectional

RH	Relative humidity
RT	Room temperature
RTM	Resin transfer molding
R-W	Reiner-Weissenberg
SCF	Stress concentration factor
SEM	Scanning electron microscope
SENB	Single-end-notch bending
SFF	Single fiber fragmentation
TAF	Temperature acceleration factor
TSF	Temperature shift factor
TTSP	Time-temperature superposition principle
TTWSP	Time-temperature-water superposition principle
TWSP	Time-water superposition principle
UD	Unidirectional
UTS	Ultimate tensile strength
VARTM	Vacuum assisted resin transfer molding
WB	Water bath

1 Introduction

Continuous fiber-reinforced polymers (FRP) are structural high-performance materials used in increasing applications, as they combine low densities, high strengths and stiffnesses, superior fatigue performance, and, in general, good corrosion resistance [2–5]. Particularly, glass fiber-reinforced polymers (GFRP) are the most frequently used composites in energy, mobility, industrial, and civil applications because of their comparably attractive price-performance ratio and longstanding processing experience [6–9]. However, in most relevant applications, the composites are exposed to variable and often harsh environmental conditions. Consequently, the structural design has to consider potential impairments caused by long-term aging processes under the given operating conditions [10–13]. These are mainly the range of operating temperatures, humidity and water, UV radiation, and chemical exposure.

Depending on the operating loads and the design philosophy, their fatigue properties are the most relevant material characteristics for long-term safe and reliable dimensioning of lightweight GFRP structures. These, in turn, depend on the ratio of the static properties to the persistent loads and on the damage tolerance of the laminated structures in the given conditions. In the case of composites, several attempts to define damage tolerance have evolved during the last 50 years [14, 15]. Most of them have the fail-safe approach as a common approach [14]. Therefore, damage tolerance refers to the ability to withstand existing and occurring defects such as pores, cracks, or delaminations until they can be detected and repaired if necessary [14, 16]. In more recent definitions, the dependence of the damage tolerance and, thus, of the fatigue properties is explicitly related to the worst possible operating conditions [14, 17].

Due to their complex structure consisting of the three constituents: the polymer matrix, the fibers, and the fiber/matrix interphase as well as the almost arbitrary orientation possibilities of the individual unidirectional fiber/matrix layers within a laminate structure, any approach other than the damage tolerant design

appears to be inefficient. In laminated GFRP composites, most of the load is carried by the strong and stiff glass fibers oriented in the longitudinal direction. In a simplified description, the matrix is responsible for load transfer between the fibers and protecting them from external impacts. On closer inspection, however, the interphase is primarily responsible for load introduction and protection on a microscopic level. This triad of fiber, matrix, and interphase is now subject to multi-scale damage mechanisms, which influence each other due to the complex structures and are all individually and in combination dependent on the environmental conditions [18, 19]. As a result, it is often not possible to simply assess and predict lifetime properties and damage tolerance. Figure 1.1 illustrates the most common failure modes and indicates their complex dependencies on the constituent's properties for a multi-directional GFRP composite.

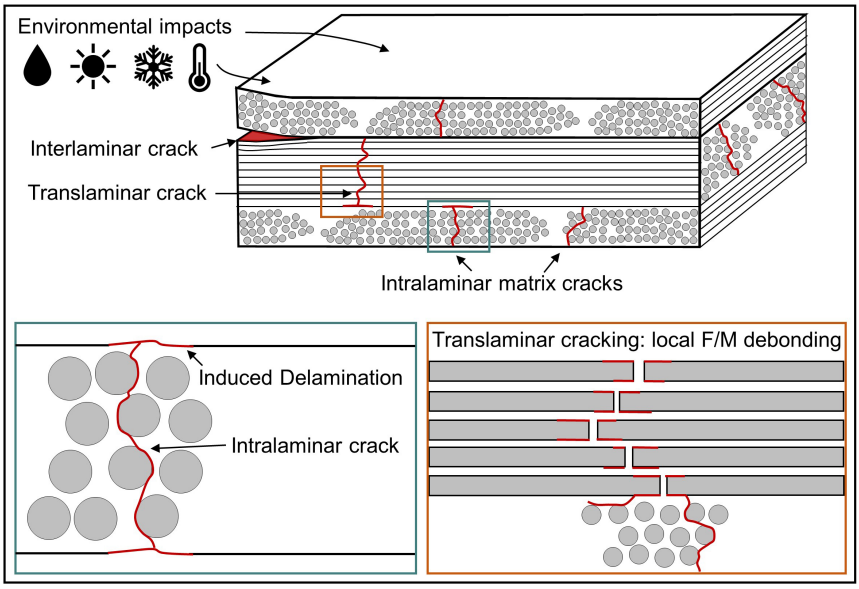

Figure 1.1: Schematic macro and micro representation of typical composite damage in accordance with [20].

Due to the large variety of composites and applications, several attempts were made to define aging procedures standardized. NASA (Langley Research Center, Hampton, Virginia) has already published a comprehensive report on the use of accelerating aging methods for composite characterization [21] back in 2003. This detailed work highlighted, on the one hand, the need for reliable and efficient

accelerating aging methods for composites and, on the other hand, elaborated several limiting factors that must be managed. In this context, it must be taken into account that mechanical degradation, chemical aging, and physical aging are at least the three main processes affecting the three constituents of a composite, most probably to an unequal extent. As a result, the dominating degradation mechanisms might change with specific environmental aging conditions, such as elevated temperatures or media [21]. It becomes even more difficult if the selected aging conditions promote degradation processes that would not occur in a real application. Consequently, some composite aging-related standards have been published over the last years. E.g., a standard to investigate moisture absorption (ASTM D5229/D5229M-20 [22]), a standard to investigate aging of sandwich structures (ASTM C481-99 [23]), and a standard for hot water accelerated aging of GFRP reinforced cement-based composites (ASTM C1560-03 [24]). However, all of these few standards point out that the methods described cannot be used to predict natural aging under operating conditions. Therefore, there is still an essential need for further research in this area to improve understanding and testing capabilities, both with new test methods and new long-term aging data sets.

Today, the number of new aging-related publications is again at a very high level, as the need for reliable long-term use of structural composites is still increasing. Here, the actual demands for sustainable raw material use and reduction of overall emissions from energy production and mobility are key drivers, as long-term use is most often favorable [25, 26]. Based on the known accelerating effects at elevated temperatures, aging of fully immersed composite specimens or laminates at temperatures just below the polymer's glass transition temperature (T_g) is typically used [8, 18, 27–30]. However, as introduced before, these studies must be viewed with caution and a great deal of understanding, as the overlapping processes often cannot be separated. Ideally, accelerated aging testing should be performed at a temperature low enough to not introduce new damage mechanisms, but high enough to significantly reduce the test duration. Otherwise, the attempts will result in unnecessary high safety factors for composite designs.

1.1 Aims and Scope

Due to the complexity of the thematic field outlined in the introduction, it becomes clear that there are still many open questions regarding the environmental

durability and the corresponding testing efforts of composites. Given the wide range of possible variations in the material composition of the composites themselves, it is essential to limit the scope to a specific composite type, which should, however, be as general as possible for many others frequently used in todays and future high-performance applications. Therefore, the present thesis focuses on the durability and differences between natural and accelerated aging of glass fiber-reinforced epoxies, e.g., used in wind turbine rotor blades and marine applications. The overarching research hypothesis of this thesis can be summarized as:

Improving the long-term durability of GFRP structures under severe operating conditions requires an in-depth understanding of the effects of the various environmental conditions on the composite's constituents.

The thesis addresses two key topics following the main hypothesis. The first concerns the environmental effects and the aging behavior of epoxies since they are responsible for the water absorption of composites and are known to be sensitive to temperature. The second focuses on the impacts on static, fatigue, and fracture behavior of primarily unidirectional (UD) GFRP composites and the remaining two constituents, the fibers and the fiber/matrix interphase. Figure 1.2 summarizes the segments and gives an overview of the thesis structure and the correlations between the sections.

The chapter "Long-Term Aging of Epoxy Resins" explores the water absorption phenomena and the related impacts on the thermo-mechanical properties. Since most of the aging-related processes are temperature-dependent, the effect of the temperature is of specific interest. Therefore, all aging and absorption processes are initially carried out at room temperature and, accordingly, are not accelerated. Time-temperature superposition (TTS) and failure envelope models were then developed and applied to create (environmental) temperature- and water-related predictions of the thermo-mechanical epoxy properties. In the second part of this chapter, the effects due to a variation and especially elevation of the aging temperature are investigated. In this course, the opposing processes of plasticization and physical aging are addressed, and a long-term strength prediction model is developed. Finally, it is investigated to which extent physical aging and plasticization affect the thermo-mechanical properties of epoxies.

Consequently, the thesis focuses not only on specific aging conditions of the polymers, such as dried or saturated states, but above all, their aging history.

The chapter "Environmental Impacts on GFRP and its Constituents" contains the transfer of the results obtained in the first chapter to composites. It comprehensively enlarges these by considering the interaction of all constituents. Therefore, various glass fibers and corresponding sizing types were chosen to characterize the respective aging behavior of the manufactured composites. First, typical accelerated aging is applied, and the corresponding static and fatigue properties are explored and compared. Next, again, the effects of the aging temperature were investigated in more detail, as there is evidence that accelerated aging promotes damage mechanisms, which might not be dominant at lower service temperatures. In this context, a new fiber and sizing pre-aging methodology was developed to determine the importance of the fiber/matrix interphase for the long-term durability of GFRP. Thereby, it was possible to highlight that interphase durability is essential for the most relevant static and fatigue properties of GFRP. Finally, the impact of aging, environmental temperature, and interphase properties on damage tolerance and fracture behavior was studied and applied to relevant service damages, such as low-velocity impacts.

1.2 Thesis Outline

Following the introduction, Chapter 2 summarizes all materials, manufacturing, and experimental methods used and applied. If additional specific background information is necessary, the methods and design of experiments are described in more detail at the beginning of the respective results chapters 3 and 4. The corresponding state-of-the-art, materials, results, and conclusions are likewise divided into both main topics. This will enhance the readability and enclose the scope. Furthermore, four single research hypotheses were formulated to answer the overarching hypothesis and guide the thesis. Chapter 5 is dedicated to the summary and outlook. Parts of this thesis have previously been published in journal articles [31–37]. CRediT author statements are provided in the publications describing the contributions of the individual authors.

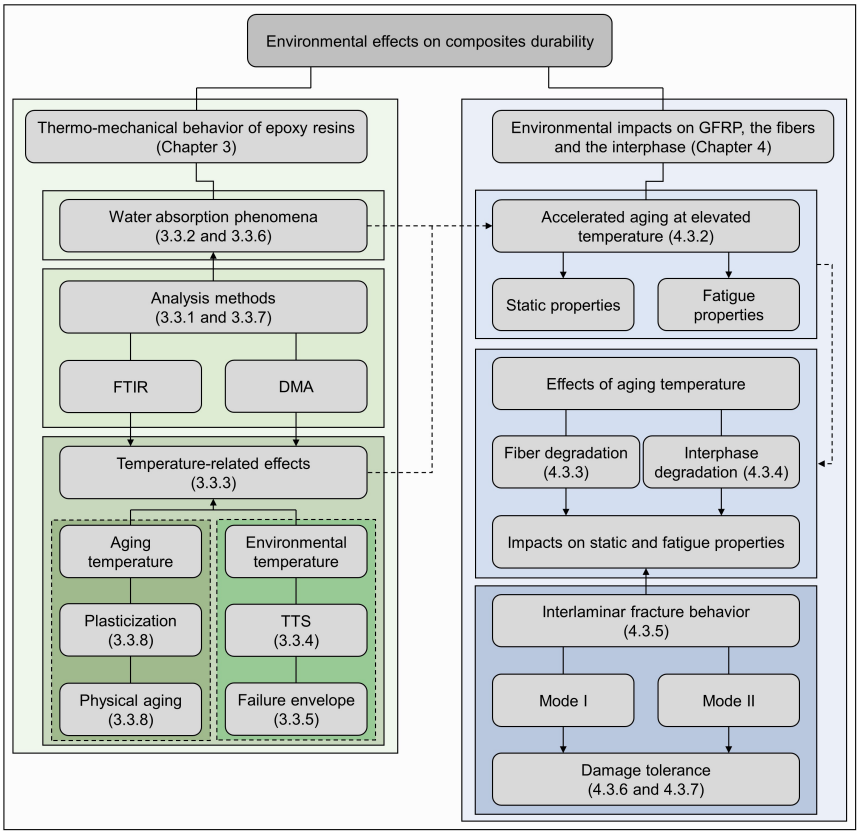

Figure 1.2: Overview of the topics dealt within the present thesis and their contextual relations.

2 Materials, Manufacturing, and Experimental Methods

This chapter describes the investigated materials, the manufacturing processes, and the applied experimental methods. Since several epoxy resins and glass fiber types were studied throughout this thesis, an overview is given. Further details of the specific material compositions are given in the respective chapters.

2.1 Materials

2.1.1 Epoxy Resins

The epoxy resin system primarily investigated and mainly used for GFRP laminate manufacturing is EPIKOTE™ Resin MGS™ RIMR 135 and the amine hardener EPIKURE™ Curing Agent MGS™ RIMH 137 (Hexion Inc., USA), which is a low viscosity and slow hardening system applicable for infusion and resin transfer molding (RTM) processes. The resin component consists of bisphenol A diglycidyl ether (DGEBA) (75 % to 90 %) and 1,6-Hexanediol diglycidyl ether (HDDGE) (10 % to 20 %). Polyoxypropylenediamine (POPA) (50 % to 75 %) and isophorone diamine (IPDA) (25 % to 50 %) are the reactive amines used in the hardener. The mixing ratio was set to 100:30 parts resin and hardener (by weight) according to the data sheet. To investigate the influence of specific epoxy selection on mechanical properties and aging behavior, three additional systems were used in selected experimental series. Table 2.1 gives an overview of trade names, manufacturers, and components. All epoxy systems are low-viscosity systems suitable for infusion processes and commercially widely used in wind energy and maritime applications.

Table 2.1: Information about epoxy resin systems used according to the safety data sheets

Trade Name	Manufacturer	Resin Components	Hardener Components	Mixing Ratio
RIMR135 RIMH137	Hexion, USA	DGEBA (75 %-90 %) HDDGE (10 %-20 %)	POPA (50 %-75 %) IPDA (25 %-50 %)	100:30
RIMR035c RIMH037	Hexion, USA	DGEBA (50 %-75 %) DGEBF (10 %-25 %) DTGE (10 %-20 %)	POPA (50 %-75 %) IPDA (25 %-50 %)	100:28
LY1568 Aradur 3489	Huntsman, USA	DGEBA (60 %-100 %) DTGE (7 %-13 %)	PEG (60 %-100 %) IPDA (13 %-30 %)	100:28
CeTePox AM 3329A/B	CTP Advanced Materials GmbH, Germany	DGEBA (50 %-100 %) DGEBF (10 %-25 %) DTGE (10 %-25 %)	Propylene Glycol (50 %-100 %) HTDA (12 %-35 %) TMG (2 %-10 %)	100:25

2.1.2 Glass Fiber Fabrics and Rovings

Several commercially available and widely used glass fiber types have been investigated throughout this thesis, aiming to identify the differences and commonalities of environmental durability. The main focus was on classical E-glass fibers (Hybon™ 2002), corrosion-resistant E-CR-glass fibers (SE 1500 and SE 2020), and corrosion-resistant and high-strength R-glass fibers (W 2020). The DNV-GL certified Hybon™ 2002 fibers were initially produced by PPG Fiber Glass, USA, and later by Nippon Electric Glass, Japan. They are finished with a silane-based multicompatible sizing suitable for epoxy resins. The Advantex® SE 1500 and SE 2020 E-CR-glass fibers (3B, Belgium) are boron-free and promise higher corrosion resistance than standard E-glass fibers. The SE 2020 fiber is a further development of the SE 1500 fiber with a marine-suitable sizing formulation. The sizings of the SE 2020 and the HiPer-Tex® W 2020 are identical (epoxy compatible). The average fiber diameter is $17 \pm 2\,\mu$m for all fibers. Fiber bundle tests were performed on fiber rovings in the case of the SE 2020 and W 2020 fibers. Concerning the other types, fiber bundles were carefully elaborated from the fiber fabrics. For the manufacturing of GFRP laminates, mainly UD fabrics or UD fabrics with a small share of transverse backing fibers were used. Since aging of the fiber sizings during storage is a known phenomenon, some fabrics with specific fiber types were re-ordered during the investigation period. However, the fiber and sizing compositions should not have differed for a single fiber brand. A detailed overview of all fiber types and fabrics used is given in Table 2.2.

Table 2.2: Overview of the glass fiber fabrics structures and properties. All fabrics are sized with epoxy-compatible sizing.

Supplier	Fabric	Fiber	Manufacturer	Type	Areal weight in $\frac{g}{m^2}$	0°-Share	Denotation
Saertex	UE 1192	W 2020	3B, Belgium	R-Glass	1192	97 %	W 2020
Saertex	UVE 926	SE 1500	3B, Belgium	E-CR-Glass	926	99 %	SE 1500
Saertex	UVE 977	SE 2020	3B, Belgium	E-CR-Glass	977	99 %	SE 2020
Saertex	UE 1182	SE 2020	3B, Belgium	E-CR-Glass	1182	99 %	SE 2020
Saertex	UVE 1166	Hybon 2002	NEG, Japan	E-Glass	1166	99 %	NEG 2002
Hacotech	G300U	Hybon 2002	PPG, USA	E-Glass	373	85 %	PPG 2002
Gurit	UE500	ER469L	CPIC, China	ECR-Glass	500	99 %	ER 469L
R&G	600 UD	-	-	E-Glass	600	90 %	R&G 600
Hacotech	G300BX	Hybon 2002	PPG, USA	E-Glass	325	±45°	PPG 2002
Saertex	X-E-610	E6 396	Jushi, China	ECR-Glass	610	±45°	Jushi E6

2.2 Manufacturing

The following section describes in detail the manufacturing and preparation of all specimens. All neat epoxy plates and GFRP laminates were manufactured using a vacuum-assisted resin transfer molding (VARTM) process.

2.2.1 Resin Transfer Molding

A two-part, polished aluminum mold of about 600 mm in length and 300 mm in width was used for the VARTM. First, the inner surfaces were regularly sealed with a form release agent XTend 1110EP (AXEL, USA). Then, a frame was placed on the lower mold to accommodate the spacing and definition of the laminate thickness (thickness from 0.5 mm to 9.0 mm). Following, the glass fiber fabrics were cut to size and stacked in the mold. After parallel alignment to the sides, a small fleece stripe was placed around the dry fabrics to prevent resin from flowing rapidly along the mold edges. Next, the mold was closed with screws and placed into a heating press at a temperature of 50 °C. The resin was mixed and degassed in parallel. For vacuum testing and infusion, a vacuum of about 4 mbar was put on the trap side of the mold. After checking the consistency of the vacuum for approximately 15 min, the resin reservoir was opened. When the resin reached the trap side, it was clamped and an over-pressure of 2 bar was set on the source side to reduce the epoxy shrinkage during curing. Curing was realized at 50 °C for 15 h in the mold, followed by a post-curing process at 80 °C for 16 h. Post-curing was performed after demolding in an UF450 plus

oven (Memmert, Germany). No fibers or fleece stripes were placed in the mold for the manufacturing of neat epoxy plates.

2.2.2 Specimen Preparation

For specimen preparation, the fleece edges were removed and the laminates were typically cut in two halves using a diamond-coated cutting wheel on a F45 saw (Altendorf, Germany). Cutting of the specimens according to the corresponding standards was either done with a Brillant 265 (large specimens) or a Brillant 220 (small specimens) CNC-saw (QATM, Germany) using aluminum-oxide cutting blades. Non-rectangular specimens were prepared from the laminates using a Euromod 35 mill (Isel Germany AG, Germany) with 1.8 mm diamond-coated bits. The cutting edges of neat epoxy and GFRP fatigue specimens were polished with SiC sand paper up to a grit-size of P2500, to minimize the effects of edge roughness.

2.3 Experimental Methods

In this section, the applied procedures for aging, characterization, testing, and analysis are described. Details in the case of deviating implementation are specified separately in the respective chapter.

2.3.1 Environmental Aging

To study the influence of various humid or wet environmental conditions on the mechanical, thermal, and fatigue properties of neat epoxy, glass fibers, and GFRP composites, short- and long-term aging procedures were defined and applied. Aging was achieved by immersion in deionized water or artificial saltwater baths or by storage in humid air over a temperature range between 8 °C and 70 °C and relative humidities between 20 % and 97 %. For humid air conditioning, an ICH110 or a CTC256 climate chamber (Memmert, Germany) was used. Water bath aging was realized either in insulated plastic containers via controlled heating rods or by storage of water-filled plastic containers inside the climate chambers.

Before aging, all neat epoxy or GFRP specimens were dried using a VO 400 vacuum oven (Memmert, Germany) at 40 °C and ambient pressure of $p \leq 10$ mbar for 72 h to 120 h until no further weight loss was measured. All specimens were

weighed before and after aging, while three of each condition were also weighed regularly during aging. For weight measurements, an AT261 scale (Metler Toledo, Switzerland) with a precision of 0.01 mg was used. All specimens were carefully wiped dry before weight measurements. The relative weight change M_t was calculated in mass-percent using the following definition:

$$M_t = \frac{(m_t - m_0)}{m_0} \cdot 100, \tag{2.1}$$

where m_0 is the dry reference weight after initial drying and m_t is the weight of the aged sample at time t. Care was taken to ensure that all samples for static testing were tested within 30 minutes after removal from conditioning, as drying under ambient conditions can otherwise affect the results. For fatigue tests of wet-aged composites, the specimens and a piece of wet cotton were enclosed by a sealed plastic bag to reduce re-drying during testing. Additionally, the free gauge length was sealed with petrolatum.

2.3.2 Thermal Rejuvenation

In polymers, thermal rejuvenation describes rapid cooling (quenching) of a melt or a rubbery state from temperatures above T_g [38]. This rapid quenching keeps the mainly stress-free molecular state to a large extent unchanged. As a result, the free volume and molecular mobility are significantly increased compared to a slow cooling rate. Thus, it is possible to bring polymers into an almost physical aging-free state [39]. In this work, the method was used to separate the plasticizing and aging effects of water in polymers. The thermal rejuvenation process was performed according to [38]. Epoxy specimens were first manufactured following the standard procedure described in Section 2.2, then sealed in plastic bags, heated up to 90 °C for 5 min in a water bath, and finally quenched in 10 °C cold water. The rejuvenation process for dry specimens was carried out under boiling water conditions to ensure a temperature above the dry T_g.

2.3.3 Analysis and Characterization Methods

In the following section, analysis and characterization methods that are used for quality assurance, damage detection, and determination of the aging effects are introduced.

Quality Assurance

After manufacturing, the epoxy plates and GFRP laminates were regularly examined to ensure a comparable high quality of all specimens. Therefore, all laminates were inspected for pores and dry spots by visual inspection and microscopy. Furthermore, the fiber volume fraction was determined according to DIN EN ISO 1172 [40] by burn-off tests at 600 °C using a muffle-furnace for representative laminate types.

Micro-Specimen Preparation

To analyze the impact of environmental aging on GFRP composites on a microscale, representative samples were elaborated from various specimens after aging or testing. Therefore, smaller areas were cut using a Brilliant 220 circular saw (QATM, Germany) with an aluminum-oxide blade. Additionally, micro-section specimens were embedded in KEM 15 compound (QATM, Germany) and subsequently polished using a Saphir 550 automatic polishing table (QATM, Germany). To achieve expressive insight, polishing was performed in seven steps with final grain sizes as low as 1 µm, which was attained using diamond suspensions.

Light Microscopy

For investigating micro-sections, fracture surfaces, damage distribution and propagation, aging effects, and the GFRP micro-structures, a VHX-6500 microscope (Keyence, Japan) was used.

Scanning Electron Microscopy

Scanning electron microscopy (SEM) images were acquired mainly with a SUPRA 55VP (Zeiss, Germany) using secondary electron (SE) detection with an accelerating voltage of 3 kV. In addition, further recordings were made on a PHENOM XL SEM (Thermo Fisher Scientific Inc., USA) at 5 kV with the SE detector. In the absence of grounding, electrically insulating materials are positively charged by the detachment of the SE, so that no sharp image can be generated. For this reason, all samples were provided with silver conductive paint at the edge of the sample carrier and vaporized with gold for 12 s with a BALTEC SCD

050 SPUTTER (BALTIC Präparation e.K., Germany), creating an electrically conductive layer of a few nanometer thickness on the surface.

Fourier-Transform Infrared Spectroscopy

Fourier transform infrared spectroscopy (FTIR) was used in the near infrared regime (NIR) to analyze the polymer-water interaction. Various spectra were recorded in transmission mode from $1500\,\mathrm{cm}^{-1}$ to $7500\,\mathrm{cm}^{-1}$ using a Bruker Tensor 2 FTIR spectrometer with a resolution of $2\,\mathrm{cm}^{-1}$. Each acquisition spectrum was composed of eight single measurements, and for each conditioning state, at least nine measurements were made on three specimens. For further analysis, the spectra were first checked for irregularities, baseline shifted, and normalized. The peak at a wavenumber of about $5238\,\mathrm{cm}^{-1}$ is considered to evaluate the water content inside the epoxy. Therefore, the area of the peak (peak integral) is determined using Origin 2019 software.

Dynamic Mechanical Analysis

The developments of the epoxies T_gs' concerning aging under various environmental conditions were investigated using a DMA Eplexor 500 (Netsch Gabo, Germany) equipped with a 500 N load cell. Specimens according to Figure 2.1 were subjected to a cyclic load at 1 Hz and constantly increased temperature with a rate of $3\,\frac{\mathrm{K}}{\mathrm{min}}$. In addition to load-displacement curves, storage modulus E', loss modulus E'', and $tan(\delta)$ data were evaluated. DMTA measurements were run from 20 °C to 120 °C. T_g was calculated as $T_{\mathrm{g,onset}}$ of the storage modulus E'. Therefore, the intersection between linear regressions through the low-temperature results and the transition zone is taken for determination as it is typically done in accordance with ASTM D4065/D7028 [41, 42].

2.3.4 Mechanical Testing

The following section describes the mechanical tests performed on neat epoxy and GFRP composites. All tests were carried out on dry specimens under room temperature in the sense of a basic characterization. Aging conditions or elevated temperature testing are mentioned in the respective experimental chapters.

Fracture Toughness

Mode I fracture toughness $K_{\mathrm{I,c}}$ of the neat epoxy was determined using single-edge-notch bending (SENB) specimens according to ASTM D5045 [43] at room temperature. Additionally, tests on dry and wet specimens at low and elevated temperatures were carried out using a temperature chamber. The geometry of the specimens is shown in Figure 2.1. $K_{\mathrm{I,c}}$ for a fracture load F is calculated as follows:

$$K_{\mathrm{I,c}} = \frac{F}{b \cdot \sqrt{w}} f(a/w), \tag{2.2}$$

where b is the width, w is the height of the specimens, and $f(a/w)$ is a correction factor based on the geometry and crack length of the sample. The SENB specimens were milled on a Euromod 35 mill (Isel Germany AG, Germany) using a 1.8 mm diamond bit. The sharp crack was inserted with a razor blade immediately before testing.

The interlaminar fracture toughness and the energy release rate (ERR) of UD GFRP composites were determined using double cantilever beam (DCB) tests in mode I and end-notch flexure (ENF) tests in mode II. Specimens were manufactured according to ASTM D5528 [44] and ASTM D7905 [45]. A 0.01 mm thin polytetrafluoroethylene (PTFE) film FP301100 (Goodfellow, USA) was inserted in the neutral plane prior to resin infusion as intrinsic crack start. The ERR under mode I $G_{\mathrm{I,c}}$ with crack length a is evaluated using the modified compliance calibration method:

$$G_{\mathrm{I,c}} = \frac{3F^2C^{2/3}}{2Abh}, \tag{2.3}$$

with load F, width b, thickness h, compliance C, and slope A of the least squares plot of the normalized delamination length a/h versus $C^{2/3}$.

The ERR under mode II $G_{\mathrm{II,c}}$ with crack length a_0 is evaluated using the compliance calibration (CC) method:

$$G_{\mathrm{II,c}} = \frac{3mF_{\max}^2 a_0^2}{2b}, \tag{2.4}$$

where m is the CC coefficient, $F_{\max}$ is the maximum load, and b is the width of the specimen. All fracture toughness tests were performed on a universal testing machine Z10 (Zwick-Roell, Germany) with a hinged load introduction or three-point bending setup.

Tensile Tests

Tensile tests on rectangular GFRP specimens and fiber bundles were performed using universal testing machines Z2.5, Z10, Z100, and Z400 (Zwick-Roell, Germany) equipped with mechanical, pre-tensioned grips (2.5 kN and 10 kN), mechanical, pre-tensioned wedge grips (100 kN), and hydraulic grips (100 kN). The specifications according to DIN EN ISO 527-4 [46] and 527-5 [47], and DIN EN 1007-5 [48] were fulfilled. For neat epoxy specimens, a dogbone-shaped specimen geometry has been defined and used in reference to the DIN EN ISO 527-2 1BA standard [49]. Tests on neat epoxy were performed using a DMA Eplexor 500 (Netsch Gabo, Germany) equipped with a 500 N load cell. Detailed information about the tensile test setups and specimen dimensions are summarized in Table 2.3.

Table 2.3: Dimensions of the tensile test specimens and related test standards [46–49]

	Neat Epoxy	Longitudinal UD	Transverse UD	Quasi-Isotropic	Fiber Bundle
Standard	DIN EN ISO 527-2	DIN EN ISO 527-5	DIN EN ISO 527-5	DIN EN ISO 527-4	DIN EN 1007-5
Length in mm	34	250	250	250	260
Width in mm	6	15	25	15	-
Thickness in mm	0.5	1-2	2-3	2	-
Gauge Section in mm	10	150	150	150	200
Strain Transducer	DMA Traverse	MultiXtens	MultiXtens	MultiXtens	Video Extensometer or Traverse
Miscellaneous	Dogbone	Rectangular	Rectangular	Rectangular	Sand Paper Tabs

The maximum tensile strength σ_t of the neat epoxy and the composite specimens is calculated as:

$$\sigma_t = \frac{F_{\max}}{w \cdot t}, \tag{2.5}$$

where $F_{\max}$ is the maximum load, w the width, and t the thickness of the specimens. The Young's modulus E is calculated within a region from 0.05 % to 0.25 % of strain according to:

$$E = \frac{\sigma_{0.25} - \sigma_{0.05}}{\epsilon_{0.25} - \epsilon_{0.05}}, \tag{2.6}$$

where σ_i and ϵ_i are the stress and strain at the specific strain i.

The fiber bundles were glued with acrylate glue (Pattex SK mini trio, Henkel, Germany) to sandpaper at their gripping edges. This allowed a uniform load introduction. The fiber failure probability P_j and the tow strength σ_{tow} are calculated according to:

$$P_j = \frac{C_{t,j} - C_t}{C_{t,j} - C_I}, \tag{2.7}$$

and

$$\sigma_{\text{tow}} = \frac{F_{\text{tow}}}{A_0 \cdot (1 - P_{\text{Ftow}})} \tag{2.8}$$

containing the actual total compliance $C_{t,j}$, the compliance at the beginning C_t, the compliance of the test setup C_I, the maximum load on the fiber bundle F_{tow}, the diameter of the fiber bundle A_0, and the probability of fiber failure at maximum load P_{Ftow}.

Shear Tests

Short beam shear specimens according to ASTM D2344 [50] were used to determine the apparent interlaminar shear strength (ILSS) of UD GFRP composites. Rectangular specimens of 24 mm length, 8 mm width, and 4 mm thickness were tested in three-point bending with a support roller distance of 16 mm. The maximum shear strength τ_{12} is calculated as

$$\tau_{12} = 0.75 \cdot \frac{F_{\text{max}}}{w \cdot t}, \tag{2.9}$$

with the maximum load F_{max}, the specimens' width w and thickness t.

Bending Tests

Four-point bending tests were performed according to DIN EN ISO 14125 [51]. Quasi-isotropic (QI) laminates of 9.0 mm thickness were tested using a universal testing machine Z10 (Zwick-Roell, Germany) equipped with an external impedance measurement system to track the specimen deformation at the lowest point. The bending strength was calculated according to [51], using the correction for large deformations:

$$\sigma_b = \frac{3\,F_{max}\,L_0}{2\,w\,t^2}\left[1 + 6\left(\frac{s}{L_0}\right)^2 - 3\left(\frac{s\,t}{L_0^2}\right)\right], \tag{2.10}$$

with the maximum load $F_{\max}$, the specimens' width w and thickness t, the support length L_0, and the deflection s.

Impact Testing

Quasi-isotropic (QI) laminates of 4.0 mm thickness were impacted with low-velocity impacts (LVI) according to ASTM 7136 M [52] using an Instron 9450 weight impact tower and an impact energy of 18 J. The impactor had a semi-spherical tip with a diameter of 16 mm. Furthermore, the specimen chamber is equipped with a thermal conditioning system to cool or heat the surrounding air. Specimens are held at the specific impact testing temperature for at least 10 min before starting the impact. The plates with dimensions of 150 x 100 x 4 mm^3, were clamped with four specific holders, and an anti-rebound device clamped the impactor after the first impact. Subsequently, compression after impact (CAI) tests were performed according to ASTM 7137 M [53] using a Z400 (Zwick-Roell, Germany) universal testing machine equipped with a CAI fixture according to the standard [53].

Fatigue Tests

All fatigue tests were performed with sinusoidal cyclic loading on universal hydraulic testing machines (Instron-Schenk, Germany) equipped with 63 kN or 100 kN load cells. A controlled temperature chamber with integrated grip cooling was used for elevated temperature tests. Individual test series were carried out on only one machine at a time to exclude any influence of the machine. As rectangular specimens, according to the DIN EN ISO 527-5 standard [48], frequently fail inside the gripping region or by longitudinal splitting, dogbone-shaped designs were implemented for the fatigue testing of UD composite specimens. The development of tension-tension and tension-compression specimen geometries are described in Chapter 4.2.1. An overview of the specifications is given in Table 2.4, and the specimens are shown in Figure 2.1.

Table 2.4: Fatigue test specimen dimensions for tension-tension (T-T) and tension-compression (T-C) loading. Short T-C specimens were tested without an anti-buckling device.

Type	Total Length in mm	Gauge Length in mm	Parallel Length in mm	Min-Max Width in mm	Min-Max Thickness in mm	Radius in mm
T-T UD (Long)	250	150	40	15-20	2	2163
T-T QI (Long)	250	150	150	15	2	-
T-C UD (Short)	125	25	10	18-25	2-4	9.8 - 78.6

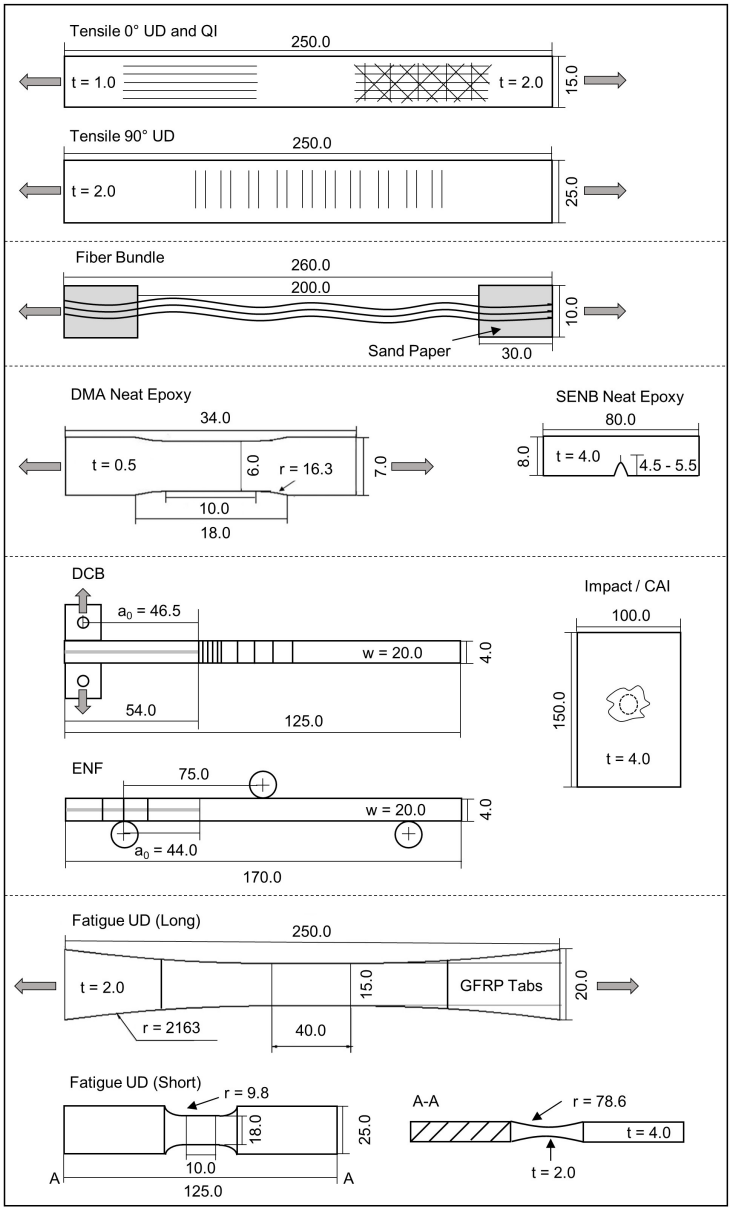

Figure 2.1: Specimen geometry overview with given dimensions in mm.

3 Long-Term Aging of Epoxy Resins

As described in the introduction, this chapter is focused on the impacts of environmental factors, such as temperature and water absorption, on the short- and long-term properties of epoxy resins. The knowledge about the effects of environmental aging on the mechanical and thermal properties of matrix materials is essential for understanding and predicting the hygrothermal behavior of polymer matrix composites (PMCs). Consequently, the working hypothesis for this chapter is:

The hygrothermal aging history has a decisive impact on the thermo-mechanical properties of epoxies. Thus, time, temperature, and moisture conditions during the service life and accelerated testing have to be considered for valid predictions of epoxies' long-term properties.

Following, state of the art regarding temperature dependence and aging phenomena, as well as prediction and accelerated aging methods for epoxies as representative of thermosets in general, are described in detail. Additionally, specific details for the epoxy aging and testing methodologies used in this thesis are given. Finally, the results and discussion are presented, and the main findings are concluded.

3.1 State of the Art

Short motivation due to use in FRP

Today, lightweight structures made of polymer composites are widely used to achieve efficient and sustainable use of raw materials and energy [18, 54, 55]. These are typically made of thermosetting resins or adhesives, whose compositions and properties are continuously refined and renewed because their demand is still increasing [56]. However, their durability potential must be further exploited to make a decisive contribution to the energy and mobility transition of

the future. It is especially mandatory to extend the operating life of structures and components even under harsh environmental conditions while at the same time ensuring safe operation. Therefore, deep knowledge about how composites and their polymer matrices change their properties during application over time and under the influence of water, moisture, and different temperatures is required. Numerous studies have already dealt with the durability in case of water absorption [54, 57–60] or various operating temperatures in the past [61–64]. Due to slow diffusion rates at moderate ambient temperatures, most of them have in common that they rely on accelerated aging processes at elevated temperatures to predict property development [65–69]. Thanks to these studies, it is known that absorbed water can cause significant changes in thermo-mechanical properties because of simultaneously occurring plasticization, relaxation (physical aging), and, in some cases, hydrolysis processes [38, 70].

FRPs are typically designed for lifetimes from 20 to 50 years or even longer in structural applications [71, 72]. During this period, the structures are in contact with water, causing deterioration of the mechanical properties [18, 32, 73]. As a result of the long-spanning service period, predicting the deterioration and degradation of mechanical properties over time is of great interest to the industry for designers and end-users of FRP materials and structures [31, 74–76]. However, the vast differences between the operating lifetime and the product design cycle are challenging, as the time for durability testing is often limited.

Epoxy thermosets are widely used as a matrix material in FRPs [77, 78]. Bisphenol A diglycidyl ether (DGEBA) epoxies (used in this work) constitute more than 80 to 85 % of the epoxy market [79]. These materials possess high specific moduli and strengths, low volatility and shrinkage, and relatively high chemical resistance [77, 78, 80]. Differences within the group of epoxies are mainly attributed to the kinds of curing agent used, e.g., amine- or anhydride-based systems. Furthermore, different resin blends, such as DGEBF epoxies or various types of diluents, accelerators, or (toughening) particles, can be added. Water interaction often results in reversible and irreversible effects in epoxy polymers [13, 81, 82]. While plasticization is usually reversible (upon redrying), irreversible aging typically occurs due to mechanisms such as oxidation, leaching, physical aging, and post-curing facilitated by water, resulting in embrittlement of epoxies. [33, 77, 83, 84]. Epoxies are particularly affected by the effect of physical aging (relaxation, annealing) that can be amplified by water ingress and is typically reversible by heating above the T_g and subsequently quenching [33, 38]. However,

the temperature-based reversibility usually has no advantage in composites, as the interphase does not recover likewise [29].

Effect of environmental temperature (without moisture)

Thermosets' thermo-mechanical properties primarily depend on their molecular composition, structure, conversion, and cross-linking degree [85–87]. Additionally, it is known that external factors, like temperature or humidity, significantly impact the mechanical properties of polymers and thermosets in particular [33, 35, 62, 88–90]. In this regard, the T_g of the epoxies is the most important characteristic parameter [35]. All main mechanical properties, such as tensile, compressive, and shear strengths, as well as the corresponding moduli, decrease with increasing temperature. For most of them, a linear dependency on the temperature was shown at least as long as the environmental temperature was about 20 °C below the T_g [35, 91, 92]. Furthermore, damage-relevant characteristics, e.g., fracture toughness, are temperature-dependent [93–95]. However, the behavior is usually non-linear, and the results presented are to some extent contradictory. From an engineering point of view, this temperature-dependent material behavior must be considered in the design and construction of composites and bonded structures [96].

Water absorption and aging phenomena in thermosets

Most studies in the field focus on the effects of humidity- or water-related aging on polymeric matrix resins. The impacts of water absorption on residual strength and stiffness [33, 36, 38, 65, 73, 97, 98], the T_g [33, 38, 98–100], and the water absorption process in general [18, 33, 97, 98, 101, 102] are frequently investigated. Therefore, it is known that the absorbed water interacts in a complex manner with the resin's molecular structure. While the plasticizing effect regularly reduces strength, stiffness, and the T_g, significant physical aging occurs, especially with accelerated aging at elevated temperatures [33, 38, 103, 104].

Since the plasticizing effect of water is understood as a reduction of the intramolecular forces by increasing the chain distances, it is often compared with an increase in ambient temperature. Consequently, models for predicting the mechanical properties of dry polymers in relation to their T_gs and the ambient temperature, like modifications of the Eyring [91, 92] or Kambour [105] correlations, were also applied for wet polymers [65, 106]. Generally, it has been shown

that the tensile strength and the T_g are the most affected properties by water absorption as they can be reduced by a factor of two or even more [73, 99].

The equilibrium amount of water absorbed in polymers depends on the polymer's molecular structure [104, 107, 108]. Historically, a distinction was often made between "volumetrically" and "interactionally" determined explanations. Here, the volumetric approaches mainly consider the absorption into the free volume, which might be varied by the curing degree and temperature, and into the space, which is a consequence of undesirable defects such as micro-pores or cracks [109]. Following this approach, interactions between water and the polar sites of the polymer network are neglected for the most part.

In contrast, it is just these water-polymer network interactions that are nowadays often considered to dominate water uptake [108, 110]. Therefore, it was shown that water molecules are attracted by the polarities of the polymer's chemical structure and that water also binds with these molecule segments by hydrogen bonds [97, 111]. Furthermore, spectroscopy and absorption-desorption experiments showed that at least three conditions in which water interacts with the molecular network can be identified. They are defined as free or unbound water, weakly bound water (type I), which forms one hydrogen bond with the network, and strongly bound water, which forms two hydrogen bonds (type II) [97]. While it was postulated by Zhou et al. [99] that type II water bonding increases the wet epoxy's T_g, effects on other mechanical properties like strength, stiffness, and failure strain were not reported. Another approach to evaluate the effect of the molecular network structure on water absorption can be achieved by considering the actual physical aging condition of the polymer [103, 104]. Elkebir et al.- [103] and Kada et al. [104] demonstrated that the amount of physical aging can change the maximum water absorption amount in epoxies by up to 20 %, although the epoxies consist of the exact same chemical composition. Therefore, it is hypothesized that the accessibility of attractive sites is reduced the further the relaxation process advances [104]. Besides gravimetric measurements, FTIR spectroscopy is used to determine the water content [98, 112] and type of water-network interaction [113, 114] in polymers. Both measurement methodologies are used within this thesis to compare the water absorption in dependence on the aging environment.

More recently, Le Guen-Geffroy et al. [38] published an extensive investigation on the coupling of plasticization and physical aging for an amine-epoxy. In order

to separate the effects of both phenomena, an artificial state mostly free of relaxation achieved by thermal rejuvenation was used as a basis. Aging in air and water allowed them to draw valuable conclusions, showing that physical aging is dramatically accelerated due to the presence of water, which reduces the T_g significantly and thus the distance between aging temperature and T_g. On the contrary, it was shown that physical aging has minimal effect on plasticization. Even though both processes were shown to be reversible during high-temperature treatment, this is not feasible in most applications. To further develop a prediction model based on the findings of Le Guen-Geffroy et al. [38], the temperature range of long-term aging tests was enlarged within the present thesis to cold temperatures below room temperature and warm temperatures above T_g, not to focus only on accelerated aging conditions, as it is regularly done [18, 80].

For the mainly studied amine-cured DGEBA epoxy (RIMR135/H137), it has been reported that it is prone to undergo plasticization [98], hygroscopic swelling [12], and to changes in its viscoelastic properties, when affected by environmental aging [115]. However, it is not being affected by hydrolysis or other chemical degradation [80, 98]. Under moderate temperature aging conditions, changes due to thermal oxidation and leaching did not significantly affect the mechanical properties of the investigated epoxy [80, 98].

Property prediction methods

Substantial cost and testing effort savings can be made through efficient use of modeling and simulation tools [74, 116]. Typically, developing novel FRPs and their validation is time-consuming and expensive. Resources such as time and funding become the bottleneck for new composite developments. A benefit would be providing new testing and modeling solutions to the composite industry for faster and more efficient processes [11]. A significant percentage of a polymer's development cost is dictated by the decisions made early in the design process. Here, testing is the most time-consuming part of novel FRP product development for the composite industry. Thus, durability prediction methods are seen helpful in reducing the involved costs [13, 75, 117].

As introduced before, accelerated testing methodologies (sometimes termed "accelerated degradation tests") are testing programs that are designed to accelerate the property degradation of materials such as polymers and FRPs by subjecting them to conditions outside their normal service range [118, 119]. In such

methodologies, the degradation is controlled, providing a reliability estimation combined with modeling while reducing the experimental testing time [120, 121]. The service lifetime is predicted by modeling the evolution of the critical mechanical characteristics (e.g., strength, stiffness) under controlled accelerated testing conditions, thus establishing safety and reliability criteria [74].

Polymers typically exhibit non-linear and time-dependent behavior that, combined with susceptibility to environmental aging, makes it challenging to model their long-term performance [74]. The mechanical properties of polymers show a time- and temperature-dependent viscoelastic behavior [122]. Time-temperature equivalence has been verified for many polymeric systems, such as epoxies. For thermo-rheologically simple materials [119, 120], it is possible to establish temperature functions that translate individual isothermal segments of the chosen response function, e.g., creep compliance, along the time scale and compose a master curve recorded at a reference temperature, T_{ref}. This approach is called the time–temperature superposition principle (TTSP), and it allows to extend the time scale beyond the time limits of convenient testing, giving an accelerated testing method.

Prediction methods can be categorized into rate-based, such as Arrhenius, Eyring, or Zhurkov approaches, superposition-based, coupling-based, and parametric models [38, 74]. Each has advantages and disadvantages regarding complexity, information content, and transferability. Therefore, a precise analysis of the boundary conditions and prediction limits is required. The design lifetime of structural composites is practically estimated based on short-term data using predictive models [74]. For instance, Nakada et al. [118] have shown that the long-term viscoelastic behavior of dry epoxies at temperatures below the T_g can be predicted accurately by measuring the 3-hour-short-term creep behavior at elevated temperatures based on the TTSP. Thus, there is a similarity between the effect of water and temperature, as described by the time-water (moisture, plasticization) superposition principles (TWSP) [123, 124]. It was also demonstrated that TTSP and TWSP for dry and wet materials can be superimposed, allowing the generation of a single master curve [115]. The T_g can be used as an indicator of polymer chain mobility, as it reduces with increasing water content in epoxies [35, 125, 126].

Aims of the chapter

Following the state of the art, there are still open questions of how epoxie's time, temperature, and moisture aging history affects their mechanical properties and how these environmental impacts interact. Thus, various long-term aging tests were conducted in environments from 8 °C to 70 °C with different epoxies used in rotor blade manufacturing. Furthermore, aiming to enlarge the properties under consideration, tensile, creep, fracture toughness, and DMTA tests as well as FTIR spectroscopy, were performed for various time-temperature-moisture combinations. Consequently, the thermo-mechanical behavior of the amine-epoxies is studied and related to their initial properties after manufacturing. Therefore, the epoxies are first thoroughly characterized before water absorption, and the resulting thermo-mechanical properties are examined in more detail. Here, the effects of the environmental temperature (during the testing) and the aging temperature were separated. For both types of temperature-dependent aging, prediction models were established. Finally, it is shown that with the help of DMTA, fundamental differences between individual conditions can be revealed, although the water content and strength can be identical.

3.2 Materials and Experimental Setup

As in the entire thesis, the main part and in-depth analysis of the following study refer to the RIMR135/H137 epoxy system. Furthermore, most of the tests were also carried out with the three other systems mentioned in Section 2.1. If the results refer to these other epoxies, it is mentioned explicitly. For constant strain rate (CSR) tensile and diffusion tests at room temperature, dogbone-shaped samples of average thickness $a = 1.13\,\text{mm}$, length $l = 150\,\text{mm}$, and width $b = 10\,\text{mm}$ in the parallel part and $b = 20\,\text{mm}$ in the gripping part according to the DIN EN ISO 527-2 1BA standard were used. A shorter and thinner dogbone-shaped specimen geometry in reference to the same standard has been used for investigating the long-term aging of epoxies. The adapted geometry is shown in Figure 2.1. SENB tests were based on 4 mm thick epoxy samples according to the ASTM D 5045 standard. The edges of all specimens were polished with 2500 grit-size sandpaper in a defined process of 20 repetitions per side. Subsequently, all samples were dried in a vacuum oven at 40 °C for at least 72 h.

For hygrothermal aging, water bath and humid air conditioning were executed up to 17 500 h (730 days). Temperatures between 8 °C and 70 °C and relative

humidity between 20 % and 97 % were considered. A detailed overview of all conditions and aging duration is given in Table 3.1. For short-term aging, the tests were performed as soon as saturation was reached. In addition, long-term aging was performed for specific conditions to investigate the effect of aging time. Re-drying and repeated absorption were investigated after aging in 8 °C, 22 °C and 50 °C water. In the case of conditioning in 40 °C water, additional tests with re-dried and rejuvenated specimens were conducted. The re-drying was carried out in a vacuum oven at 40 °C for up to 310 h until no further weight change was measured within 24 h or for 20 h at 90 °C to investigate the effects of drying at a temperature above the wet T_g. Since the weights after re-drying were not lower than the initial dried weight, it can be confirmed that there is no material loss during water aging. Single-sided absorption into a 10 mm thick epoxy plate was realized with an on-the-upper-side glued water bath. The setup was stored in a climate chamber at 50 °C and 70 % RH, aiming to accelerate the absorption process, preventing strong drying over the other surfaces, and simultaneously setting two defined saturation water contents.

Tensile tests were performed for dry reference and aged specimens with a speed of 1 $\frac{\text{mm}}{\text{min}}$ until failure. Dry reference specimens were also tested at various ambient temperatures ranging from −20 °C to 60 °C. For CSR-tests, three testing temperatures 22 °C, 40 °C, and 50 °C, as well as three constant crosshead speeds of 0.1 $\frac{\text{mm}}{\text{min}}$, 1.0 $\frac{\text{mm}}{\text{min}}$, and 10.0 $\frac{\text{mm}}{\text{min}}$ were applied. These correspond to strain rates of $\dot{\epsilon} = 2.8 \cdot 10^{-5}, 2.8 \cdot 10^{-4}$, and $2.8 \cdot 10^{-3} s^{-1}$, respectively. During temperature testing, each sample was held at the specific temperature for 5 minutes before starting the test to ensure a homogeneous sample temperature. The number of tensile samples tested per single condition was regularly $n = 3$ as the standard deviations were small. SENB tests were run at a speed of 10 $\frac{\text{mm}}{\text{min}}$ until fracture with at least five test samples per configuration.

3.3 Results and Discussion

3.3.1 Epoxy Characterization in Initial Dry Condition

A characterization of the initial conditions is presented first because the properties of epoxies depend on their chemical composition, the particular manufacturing process, the degree of cure, and the time-temperature history. In detail, the tensile stress-strain behavior (Figure 3.1), DMTA response in terms of the E' and $tan(\delta)$ versus temperature curves (Figure 3.2), and FTIR spectra (Figure

Table 3.1: Hygrothermal aging conditions of epoxy specimens for mechanical testing. A distinction is made between the water bath (WB) and the climatic chamber aging at relative humidity (RH).

Type	Temperature in °C	Rel. Humidity in %	Aging Duration in h
WB	8	100	24 to 6000
WB	22	100	400 to 6000
WB	30	100	1000
WB	40	100	400 to 6000
WB	50	100	76 to 6000
WB	70	100	400 to 1550
RH	10	90	950
RH	22	20, 43, 50, 75, 80, 90, 97	250 to 1500
RH	30	70	300
RH	36	50	336
RH	40	80	215
RH	50	50, 80	500, 325

3.3) are analyzed. As hygrothermal aging involves simultaneous plasticization and physical aging, the condition of the material after the manufacturing process is determined. For this purpose, the initial briefly dried state is compared to standard laboratory conditions (22 °C and 50 % RH) and an artificial state mostly free of any relaxation and physical aging as produced by the rejuvenation process. However, because the epoxy will not remain in this artificial state while being used in applications, the investigation focuses mainly on the development of the properties based on the condition of the material after regular manufacturing. Basically, the epoxy shows typical elastoplastic behavior with a linear elastic part for low strains and a pronounced plastic yield part for higher strains under all conditions. The stress-strain curves in Figure 3.1 highlight differences in tensile behavior depending on the extent of absorbed moisture and physical aging. Although moisture absorption from laboratory conditions does not change the shape of the stress-strain curves, the yield strength decreases significantly, and the strain to failure increases slightly compared to the dried condition. The rejuvenated epoxy shows a change in behavior with a substantially higher failure strain and markedly lower yield strength and stiffness. Between initially dried and rejuvenated specimens, the strength differs by about 12.1 MPa (−18.5 %), Young's modulus by about 0.38 GPa (−15.6 %), and the strain to failure by about 6.7 % (43.9 %). Moisture absorption under standard laboratory conditions decreases the strength about 7.6 MPa (−8.9 %). The stress-strain behavior shown

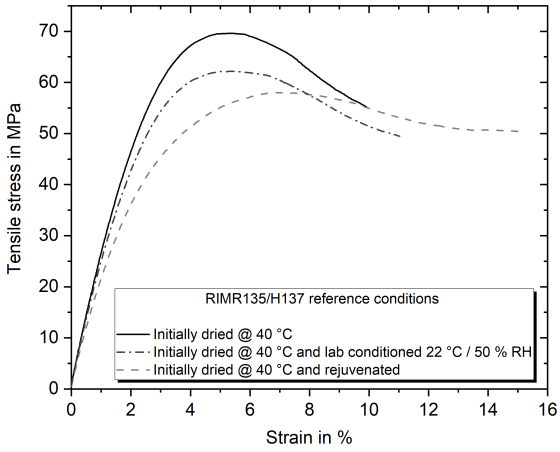

Figure 3.1: Representative stress-strain curves of initially dried, laboratory-conditioned, and dry rejuvenated conditions for the RIMR135/H137 epoxy.

is equally applicable to the other epoxies studied. The ability of amine-cured epoxy to undergo large plastic deformation also under dry conditions was recently shown to be based on load-dependent intramolecular and intermolecular interactions [127]. The mechanical properties of the dried reference condition (strength: 69.9 MPa, modulus: 2.75 GPa and failure strain: 8.8 %) are used as benchmark properties within this thesis. For creep and CSR tests, laboratory-conditioned samples are taken as references. An overview of the basic thermo-mechanical properties of all four epoxies in the initial dried condition is given in Table 3.2, and a detailed summary for the RIMR135/H137 epoxy is given in Table 3.3.

Table 3.2: Basic thermo-mechanical properties of all investigated epoxies in initial dried reference condition.

	Tensile Strength in MPa	Young's Modulus in GPa	Failure Strain in %	Glass Transition Temperature in °C
RIM135	69.9 ± 0.3	2.75 ± 0.02	8.8 ± 0.9	89.3 ± 1.3
RIM035c	73.0 ± 0.9	3.00 ± 0.04	7.5 ± 0.4	82.1 ± 1.0
LY1568	73.0 ± 1.6	2.81 ± 0.12	7.3 ± 0.7	83.6 ± 0.9
CeTePox	73.3 ± 0.3	2.87 ± 0.05	8.3 ± 0.3	85.2 ± 0.3

To reveal to what extent manufacturing and post-curing processes affect the thermo-mechanical properties by physical aging, DMTA results are presented in Figure 3.2. Again, DMTA confirms the difference in stiffness between dried and rejuvenated epoxy. Furthermore, it becomes evident that the T_g of rejuvenated

(86.5 °C) and laboratory-conditioned specimens (85.4 °C) is slightly lower than the T_g of the reference specimens (89.4 °C). In the first case, this can be explained by the higher mobility of the molecular chains and the increased free volume, and in the latter case, by the plasticizing effect of the absorbed water molecules [128]. In addition to the difference in T_g, the $tan(\delta)$ curves reveal that the damping of the material under rejuvenated and laboratory conditions begins at much lower temperatures. The peak has not only shifted, but also becomes wider at the base.

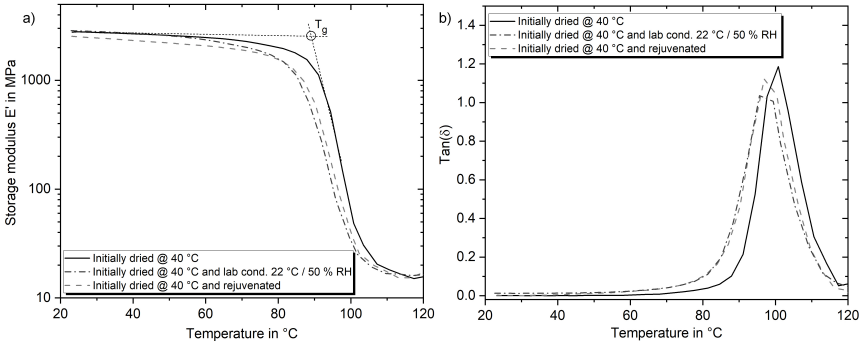

Figure 3.2: Representative DMTA curves of E' and $tan(\delta)$ versus temperature for the initial dry reference condition, lab conditioned, and the dry rejuvenated condition of RIMR135/H137.

Finally, Figure 3.3 shows the FTIR spectra obtained in transmission for the NIR range from 3500 cm^{-1} to 7500 cm^{-1}. Characteristic peaks are highlighted and assigned to the corresponding vibrations. As the dried and rejuvenated curves overlap for almost the entire range, it can be noted that differences in the physical aging condition cannot be easily identified using this specific setup. The only significant difference in the spectra can be seen in the peak around the wavenumber of 5238 cm^{-1}, which is associated with the bending and stretching modes of the OH group of the water molecule [98]. As the peak area increases for the rejuvenated specimens, it can be assumed that they have absorbed a minor amount of water during the process. Taking the peak area and, therefore, the low amount of absorbed water into account, it is expected that this will decrease the strength only to a small extent. The peak area in terms of the integral presented is used to monitor the water content of various dry and wet conditions during this investigation, as proposed by Krauklis et al. [98]. Thus, the average peak integral of the dried reference condition is 1.3, while it is 5.7

for the rejuvenated case. After aging to apparent saturation (400 h) in 40 °C water, the value is largely increased to 34.6. In conclusion, it can be stated that the reference specimens contain only a marginal amount of water, which the initial drying process at 40 °C could not remove. However, even storage under standard laboratory conditions leads to significant moisture absorption, negatively affecting the thermo-mechanical properties (about 0.9 m% moisture uptake).

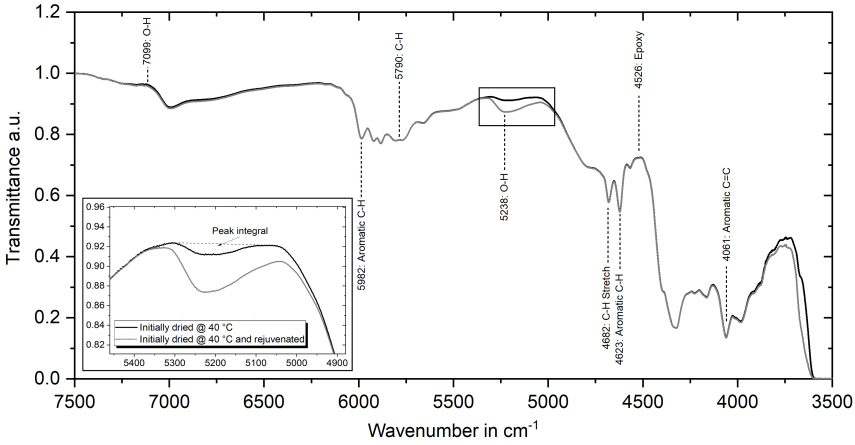

Figure 3.3: Representative normalized transmittance FTIR curves in the NIR range for the initial dry reference condition and the dry rejuvenated condition (RIMR135/H137). Enlarged illustration of the OH-peak at 5238 cm^{-1} as a representation of the water content.

Table 3.3: Summary of RIMR135/H137 thermo-mechanical properties in dry condition (experimental and literature summary).

Curing Degree in %	Tensile Strength in MPa	Young's Modulus in GPa	Failure Strain in %	Compr. Strength in MPa	Compr. Elongation at Break in %
99.5 [129]	69.9	2.75	8.8	104.7 [35]	54.5 [35]
Shear Strength in MPa	**Shear Modulus in MPa**	**Critical Stress Int. in MPa$\sqrt{m}$**	**Energy Release Rate in kJ/m²**	**T_g in °C**	**Poissons Ratio in –**
45.9 [129]	1103 [129]	1.6	0.8	89.3	0.35 - 0.4 [80, 129]

3.3.2 Water and Moisture Absorption at Room Temperature

As the thermal and mechanical properties of epoxy change with the diffusion of water into the molecular structure, the water absorption characteristics are

presented first. Absorption at room temperature and at temperatures between 8 °C and 70 °C are analyzed successively because the environmental temperature during water absorption affects the process itself. The weight gain curves of the epoxy samples initially dried and exposed to different relative humidities at 22 °C are shown in Figure 3.4. The aging of specimens at specific RH and temperature conditions enables one to generate homogeneous water distributions within individual specimens at various equilibrium water contents and with similar temperature histories. The diffusion coefficient D is known to be exceedingly temperature-dependent but independent of the relative humidity. Here, diffusion is considered to be the dominant mechanism of water absorption in epoxies [13, 33, 97]. Although simple Fickian absorption models can describe the absorption process at the early stage of water uptake of up to about 80 % of the maximum weight change quite satisfying, clear deviations can be found in the transition from linear to asymptotic range. It appears as a linear dependence of $M(t)$ versus $\sqrt{t}$ followed by asymptotic approaching the equilibrium. Furthermore, all samples reached apparent saturation at $\sqrt{t} \approx 30\,h^{1/2}$, but afterwards a continuous increase of weight changes, typical for two-stage or non-Fickian sorption behavior, is observed. Such deviations from Fickian sorption in non-hydrolyzable epoxies are more pronounced with higher water activity and are typically related to water-induced relaxation phenomena in epoxy [13, 130–132]. For other types of epoxy or thermosets containing hydrolyzable groups, deviations from the Fickian behavior are often explained by an overlap of diffusion, hydrolysis, and lixiviation processes [133]. Similarly, excessive temperatures or pH values can lead to deviations.

Since the length l and width w are much larger than the thickness h of the samples, the diffusion of water is treated as a one-dimensional process. Calculations by Fick's model for 1D and 3D cases are demonstrated in the Appendix of Gibhardt et al. [36]. Differences between 1D and 3D calculations were negligible for given samples' dimensions, thus leveling out the contribution from the irregular width (irregular dog-bone shape) of samples. This fact approves the applicability of the 1D sorption models within this study.

As a modeling approach, the diffusion-relaxation model of Berens and Hopfenberg was applied to describe the two-stage sorption behavior of the epoxy [130]. According to this model, the diffusion of water in a glassy polymer is contributed by two phenomena: a concentration gradient (Fickian) diffusion and polymer relaxation that contributes to free volume changes, molecular rearrangement, and

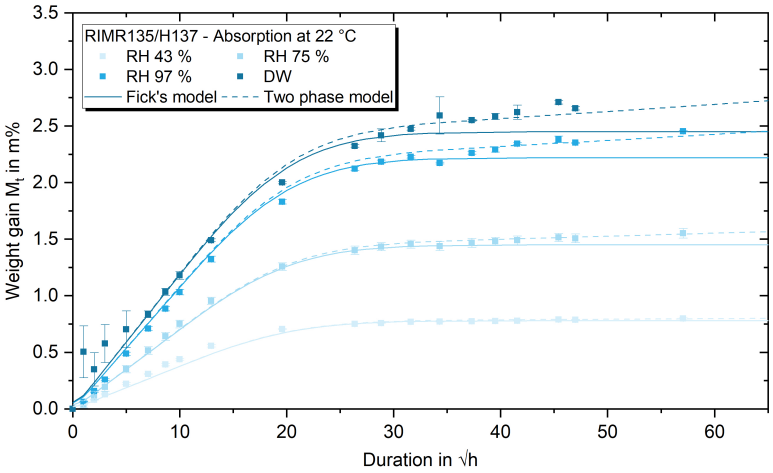

Figure 3.4: Experimental and modeling weight gain curves of 1.13 mm thick epoxy samples at room temperature (22 °C) exposed in different environments.

plasticization. It is assumed that these two processes can exist independently and can be linearly superimposed. However, depending on the environmental temperature, both processes can be accelerated, but not necessarily to the same extent. A sum then gives the total weight gain $M(t)$:

$$M(t) = M_d(t) + M_r(t), \tag{3.1}$$

where the subscripts d and r are related to diffusion and relaxation, respectively. The diffusion component in Equation 3.1 is given by Fick's equation [134]:

$$M_d(t) = M_{d,\infty}\left[1 - \frac{2}{\pi^2}\sum_{m=1}^{\infty}\frac{(1-(-1)^m)^2}{m^2}\exp\left[-\left(\frac{\pi m}{h}\right)^2 Dt\right]\right], \tag{3.2}$$

where D is the diffusion coefficient and $w_{d,\infty}$ is the equilibrium water content.

The relaxation component in Equation 3.1 is expressed by a decaying exponential function related to the polymer relaxation time, as it is typically used in the literature [130, 131]:

$$M_r(t) = M_{r,\infty}\left[1 - \exp\left(\frac{-t}{\tau}\right)\right], \tag{3.3}$$

where $M_{r,\infty}$ is the equilibrium water content specified by the network relaxation and τ is the relaxation time. Obviously, the total equilibrium content is a sum of two corresponding components $M_\infty = M_{d,\infty} + M_{r,\infty}$.

The approximation results of the water absorption curves by Fick's diffusion model and diffusion-relaxation model are shown in Figure 3.4. The fitting procedure was divided into two steps. First, Equation 3.2 was applied to model water diffusion into epoxy up to the apparent saturation $M_{d,\infty}$. The diffusivity was determined from the initial slope of the curve $M(t)$ vs. $\sqrt{t}$, i.e., by using the formula [134]:

$$D = \frac{\pi}{16}\left[\frac{M(t)}{M_{d,\infty}}\frac{1}{\sqrt{t}/h}\right]^2 \tag{3.4}$$

For the RIMR135/H137 epoxy, the diffusivity at room temperature is $D = 6\,(\pm 0.5)\cdot 10^{-4}\ \frac{mm^2}{h}$, and this value is comparable to other types of epoxies [131, 135, 136]. Next, τ and $M_{r,\infty}$ were found by fitting the experimental data and providing a smooth approximation at longer sorption times. The relaxation time at room temperature conditions (22 °C) was fitted as $\tau = 8.5{\cdot}10^3\ h$ independently of the relative humidity of the environment. The higher τ is, the more time is required for the complete structural rearrangement of the polymer network. This depends on the material, curing degree, and test or aging temperature [33, 38, 131, 137]. Relaxation times determined in water absorption tests correlate well with those determined by alternative methods, e.g., creep tests [138, 139] or tensile tests [33, 34, 38], which will be discussed later in this thesis. The water absorption capacity generally increases with water activity (relative humidity of the environment). The room temperature sorption isotherms for both $M_{d,\infty}$ and $M_{r,\infty}$ are shown in Figure 3.5. From the modeling results can be obtained that the maximum water absorption of the epoxy under immersed conditions (sub-T_g) will ultimately gain about 3.1 m%, which is in line with data based on high-temperature accelerated aging presented in Chapter 3.3.6 and elsewhere for the same epoxy [33, 98]. Furthermore, the experimental results and the modeling demonstrate that the maximum water absorption for epoxy resins aged at room temperature or lower temperatures is significantly underestimated when only the Fickian absorption is considered until apparent saturation arises.

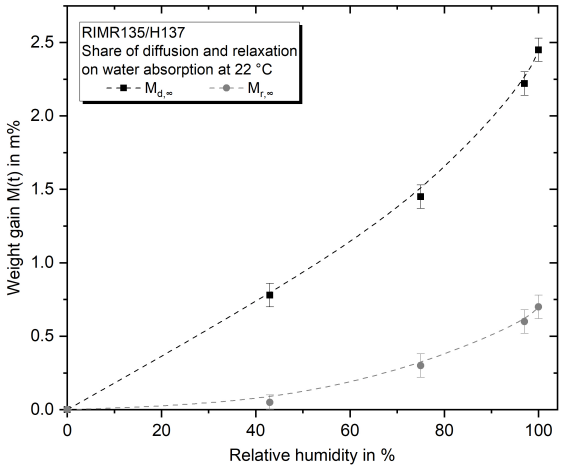

Figure 3.5: Equilibrium water contents related to the diffusion ($M_{d,\infty}$) and relaxation of the epoxy network ($M_{r,\infty}$).

3.3.3 Basic Effects of Environmental Temperature and Water Absorption

In this section, the dependencies of the thermo-mechanical properties of the RIM epoxy on ambient temperature and water absorption content are studied and classified in comparison with other epoxy resins. Care was taken to ensure that the influence of temperature was strictly limited in time for a fundamentally comparable description of the effects of temperature and water absorption. Therefore, water absorption was only considered at room temperature until saturation. Furthermore, it is assumed that tests at elevated temperatures did not change the chemical and physical condition of the samples, as the testing duration was short. For the description of the basic temperature- and water-related effects, the following assumptions are supposed:

- The polymer is in a glassy state ($T < T_g$);
- Temperature-related aging effects are negligible;
- Uniform water distribution (in saturated samples);
- Only plasticization effects are considered (no degradation, no aging);
- Relaxation/physical aging effects are insignificant;

- The same failure mechanism occurs;

The change of the tensile yield strength in relation to the ambient temperature is shown in Figure 3.6a) for the three primary conditions (dried, lab-conditioned, and RT-saturated). The results clearly demonstrate a strength reduction with increasing temperature like it is reported elsewhere for epoxies [35, 140, 141]. Furthermore, a two-part behavior can be identified. A linear relationship is unambiguous for temperatures of at least 20 °C below T_g. Higher temperatures reduce the strength considerably more because of the proximity to the T_g-regime. As a consequence of moisture or water absorption, the yield strength decreases

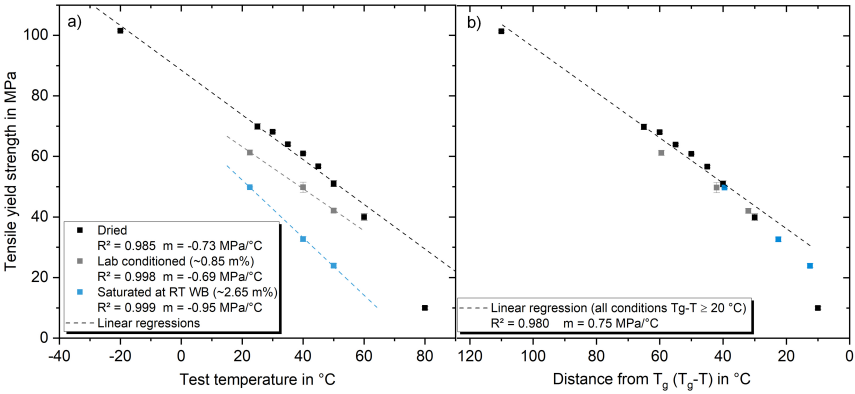

Figure 3.6: a) Correlation between tensile yield strength and test temperature in absolute values and b) under consideration of the distance from test temperature to T_g. The 80 °C result is excluded from the regressions.

likewise, whereas the temperature dependence changes slightly only in the case of full saturation. The strength can be described as a function of temperature for the application range in the following form:

$$\sigma_t(T) = m \cdot T + B, \tag{3.5}$$

with the slope of the linear regression m and the intercept (strength at 0 °C) B. Compared to other epoxies [35], the temperature sensitivity of the RIM epoxy is with about 0.70 to 0.95 $\frac{\text{MPa}}{\text{°C}}$ very pronounced but in a typical range for low-T_g systems. Thus, Drummer and Gibhardt et al. [35] were able to show a correlation between the temperature sensitivity and the T_g of epoxies. The higher the T_g, the lower the temperature sensitivity, even far below the glass transition.

Considering that the T_g decreases with water absorption (see Figure 3.9b), the results in Figure 3.6b) were expressed in terms of the distance of the ambient temperature with respect to the T_g. Following the assumptions given, it can be concluded that the strength depends equally on the plasticization due to temperature and water absorption and that these two parameters are coupled by the T_g. Consequently, the strength can be calculated in relation to the T_g (for $T_g - T \geq 20\,^{\circ}\mathrm{C}$) as:

$$\sigma_t(T, T_g) = m \cdot (T_g - T) + B, \tag{3.6}$$

with $m = 0.75\ \frac{\mathrm{MPa}}{^{\circ}\mathrm{C}}$ and $B = 21.2$ MPa for the RIM epoxy.

Additionally to the strength, the temperature- and water-absorption-dependent stiffnesses and failure strains are analyzed. The development of the storage modulus E' in a linear scale is shown in Figure 3.7a). Again, the expected two-part behavior is identified. While the modulus decreases linearly with increasing temperature in the lower temperature regime, the stiffness drops significantly in proximity to the T_g. For RT-saturated epoxy, the drop is shifted to lower temperatures. In the approximately linear regime, the water saturation reduces the stiffness about 100 MPa, which is equal to 3.5 %.

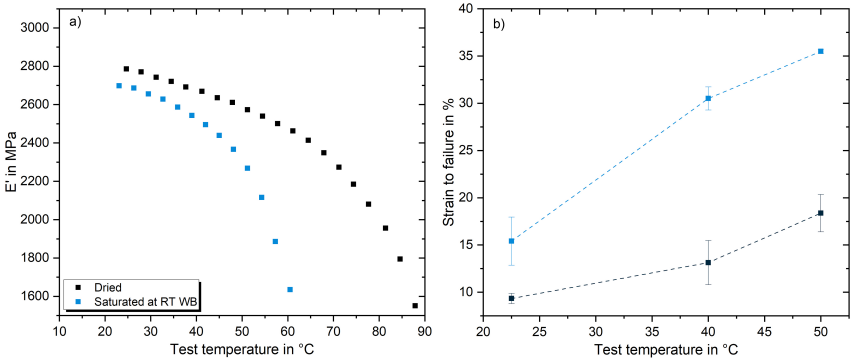

Figure 3.7: a) Correlation between storage modulus E' and test temperature (DMTA measurement) for dry and at RT saturated condition. b) Correlation of global failure strain and test temperature.

In contrast to the moderate effects on the modulus, the failure strain increases significantly both with increasing temperature (up to 15 %) and, especially, due to water absorption (up to 35 %). The results presented in Figure 3.7b) reveal that the plasticizing effect of absorbed water causes the epoxy to become very

ductile and to achieve strains and plastic deformations above what is usually expected. The strain rate-dependent stress-strain behavior is accordingly given for the most relevant conditions in Figure 3.8a). The curves demonstrate both the strength-increasing and failure strain-decreasing influence of the higher loading rate and the strength-reducing and strain-increasing influence of water and temperature. Taking into account all data, it becomes clear that the tests at 50 °C for the water-saturated case already show fundamental changes. Here, e.g., no clear maximum yield stress can be defined in the considered area. Therefore, the stress at the turning point around 8.0 % strain was defined as yield strength for this special condition. The assumptions of including only glassy states and similar failure behaviors are probably no longer completely fulfilled. Consequently, the recommended distance to the (condition-dependent) T_g of at least 20 °C is set as a limitation for modeling and prediction approaches. To confirm this conclusion, Figure 3.8b) shows the combined effects of the strain rate, the environmental temperature, and the water uptake on the strength. While the strain rate-dependent change is of a similar dimension for all temperatures in dry conditions, the effects almost disappear at 50 °C for saturated specimens. Due to the plasticizing effect of water already under room temperature conditions, the strain rate sensitivity seems to be more pronounced in the saturated than in the dry state.

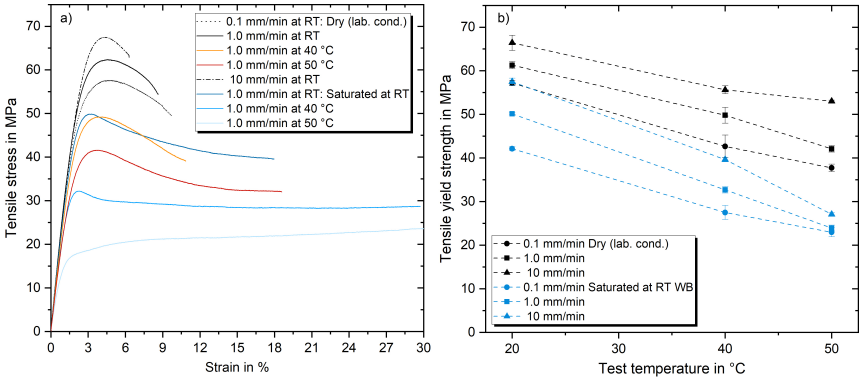

Figure 3.8: a) Representative stress-strain curves for important conditions. b) Yield strength in relation to test temperature for different strain rates.

To determine the impact of the amount of absorbed water on the mechanical properties, specimens were stored under different humidity levels until saturation. In all cases, tensile tests were performed within 650 h (1 month) of aging,

which was shortly after saturation was reached. Therefore, a homogeneous moisture distribution in the samples can be assumed. The results presented in Figure 3.9a) indicate that the strength appears to be linearly dependent on the amount of absorbed water, which is in line with what was found by authors like Ilioni et al. [65]. Hence, a regression describing this correlation for the RIM135/H137 system can be formulated as:

$$\sigma_{22}(\phi) = 69.9\,MPa - 7.8\,MPa/m\% \cdot M_\infty(\phi), \tag{3.7}$$

where $\sigma_{22}(\phi)$ is the tensile yield strength after aging at 22 °C and $M_\infty(\phi)$ is the weight gain at saturation as a function of the relative humidity ϕ.

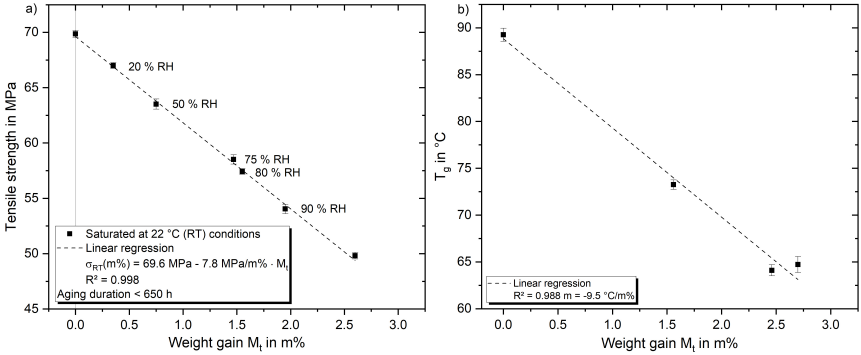

Figure 3.9: Correlation between tensile yield strength a) or T_g b) and weight gain at RT conditions.

The correlation of water absorption content and T_g is displayed in Figure 3.9b) The plotted linear regression, stating a T_g-reduction of about 9.7 °C/m%, fits well to the experimental results typically reported for amine-epoxies [142]. This interrelation is usually described with the polymer-diluent model or the Simha-Boyer equation [38, 143] and is caused by the plasticization due to the water-molecule-interaction. Using a linear regression, the T_g can be calculated as:

$$T_g(M_t) = 89.2\,^\circ\mathrm{C} - 9.5\,^\circ\mathrm{C}/m\% \cdot M_t. \tag{3.8}$$

Assuming that a linear superposition of the temperature and water absorption phenomena is permissible for the described conditions due to their T_g relation,

it is possible to predict the tensile yield strength for an arbitrary temperature and water content state by combing Eq. 3.6 and Eq. 3.8 to:

$$\sigma_t(T, M_t) = 21.2 + \left[0.75\big((89.2 - 9.7 \cdot M_t) - T\big)\right], \tag{3.9}$$

where strength is given in MPa, temperature in °C, and water content in m%. The resulting temperature and water content dependent strength model is shown in Figure 3.10. The spanned plane coincides well with the test results for the experimentally investigated range. As explained above, the model shows close agreement for the temperature range between −20 °C and around 20 °C less than T_g. Extrapolations for untested combinations, such as high water content and low temperatures, can now be precisely approximated using the model.

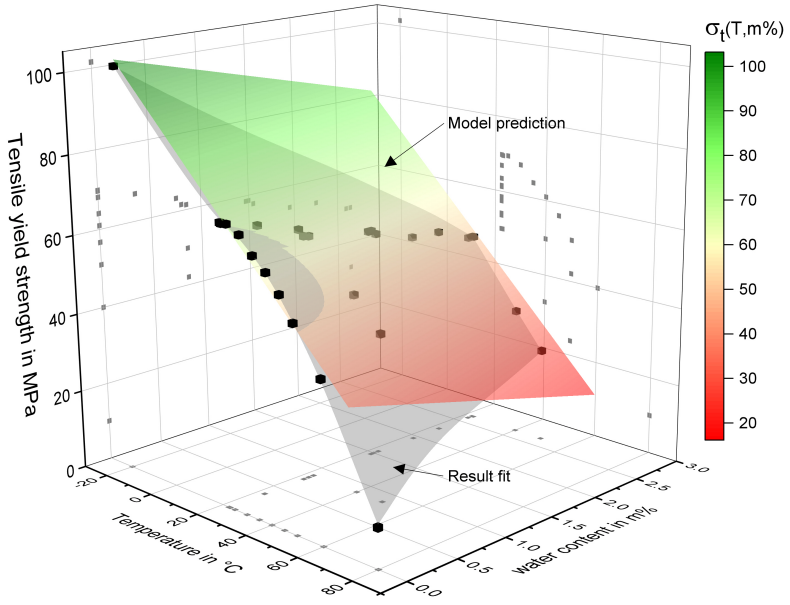

Figure 3.10: Experimental results (black symbols and shaded area) and model prediction based on Eq. 3.9 (colored area) of tensile yield strength in relation to temperature and weight gain at RT. The gray symbols are the projections of the experimental results on the corresponding plane and guide the eyes.

Impact on Fracture Toughness

Thermoset polymers are typically used as matrix material in FRPs, so properties that describe the damage behavior are highly interesting. Here, the fracture toughness and the critical ERR, measured according to the ASTM D 5045 standard, provide a reliable characterization of the damage-related toughness properties. From a chemical and structural point of view, it is expected that the toughness of (brittle) thermosets is due to the plasticizing effects of both temperature and water-aging dependent [144]. Therefore, SENB tests with dry and wet-aged specimens were performed. Dry specimens were tested at RT, low (−30 °C), and high (70 °C) temperatures. Wet-aged specimens were tested after immersion for 69 days at 40 °C water under RT conditions. K_{1C} and G_{1C} values are plotted against the testing temperature in Figure 3.11. The fracture toughness and critical energy release rate (ERR) of the RIMR135/H137 epoxy are with 1.6 MPa$\sqrt{m}$ and 0.8 kJ/m² within the range typically reported in the literature [93, 94, 145]. The results show a clear increase in fracture toughness with increasing temperature and water aging. These results align with what authors like Pitaressi et al. [144] and Han et al. [145] proposed. At temperatures far below the T_g, the temperature-related changes of the fracture toughness and ERR are comparably low. Accordingly, the decrease of K_{1C} and G_{1C} from RT to −30 °C was found to be 9.3 % and 17.6 %, respectively. The increase between RT and 70 °C, which corresponds to the same temperature difference, was significantly higher with 36.7 % and 145.5 %.

Clearly, a non-linear behavior is revealed. The enhanced mobility of the polymer network at temperatures close to the T_g leads to more pronounced yielding and softening of the epoxy. At high temperatures and due to water absorption, the plasticizing effects reduce brittleness and equally increase the damage tolerance of the epoxy. In contrast, the effects are less pronounced for low temperatures. This is because the mobility of the network is not significantly more reduced as far as the distance to the T_g exceeds a certain distance. The differences between K_{1C} and G_{1C} can be explained by the additional temperature- and moisture-dependence of the Youngs modulus.

For comparison, the fracture surfaces of the SENB tests are shown in Figure 3.12. The microscopic images highlight the differences in fracture initiation and progress. A mirror-like fracture surface with brittle initiation at the natural crack tip can be observed at low temperatures. Apart from a few brittle fractures in

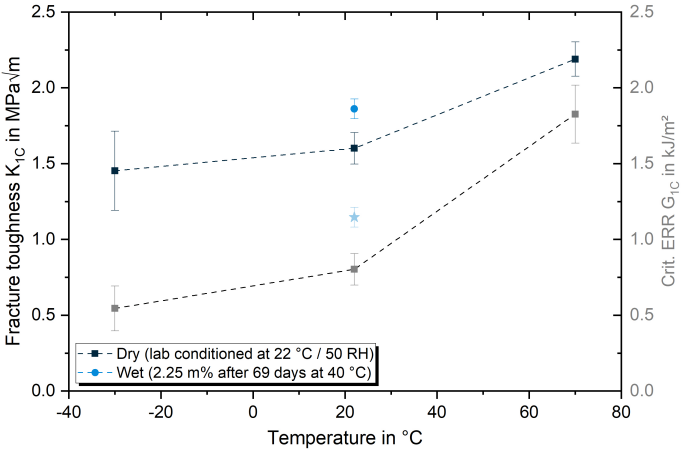

Figure 3.11: Experimental results for fracture toughness K_{1C} (black/blue) and critical energy release rate (ERR) G_{1C} (grey/pale blue) in dependence of the testing temperature and moisture condition.

the initiation area, the fracture surface is completely smooth. Similarly appears the fracture surface at RT. Here, only a slight increase of the brittle fracture at the initiation is observable. Accordingly, the mechanical results also fit well with the quite similar fracture patterns. A dramatic change in the fracture behavior can be found for both the high-temperature and water-aging specimens. Under high temperatures, the fracture surface is characterized by smeared damage, probably all initiated at different times. There is not one crack running through the sample; there are plenty. Therefore, the failure behavior can be characterized as much more ductile.

The wet-aged specimens show a failure behavior containing both elements, a ductile smeared damage in the initiation area and a brittle failure further away. Correspondingly pronounced is the toughening effect of the water. Absorption and plasticization increase the fracture toughness by 16.2 % and the critical ERR by 57.9 %. Compared to the literature for toughening of thermosets by incorporating a second phase (typically nanoparticles), the toughening effect of water is comparably high. As a result of nanoparticle induction, e.g., Körbelin et al. [146] recently reported a toughening enhancement about 3 to 12 %. The comprehensive study, including six different nanocomposites is also in line with what was reported by others before [94, 147]. The plasticization-induced toughening effect of the comparably small water molecules is accordingly very effective and can

have positive effects on the damage behavior of the resin and its composites (see Chapter 4.3.5).

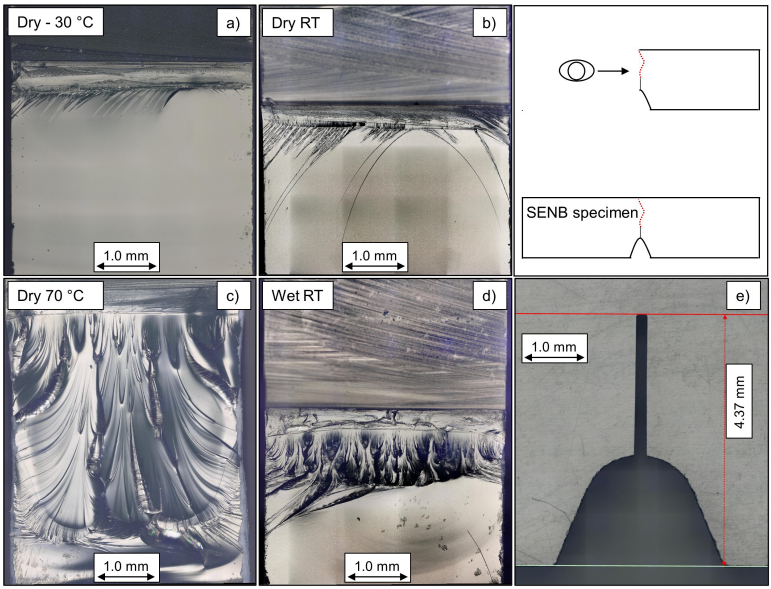

Figure 3.12: Micrographs of SENB fracture surfaces a)-d), and e) micrograph of initial crack before razor blade cutting.

3.3.4 Time-Temperature-Water Superposition for Property Prediction

Based on the previous findings, predicting mechanical properties and creep life under the influence of water absorption and temperature is implemented based on the superposition principle in the following. In this context, the viscoelastic nature of failure in thermosets is important. Thus, methods used to predict viscoelastic properties can also be used to predict the ultimate properties. Miyano et al. [7, 148, 149], by the example of various epoxy and vinyl ester-based CFRP and GFRP, validated using the time-temperature-superposition principle (TTSP) for several static, creep, and fatigue strengths investigations [7, 148–150]. Similar notes on constructing master strength curves by TTSP with the same shift functions derived from creep tests are discussed, e.g., in Guedes et al. [151].

Now, if a material follows the principle of TTSP [74, 120, 148], viscoelastic properties, strength in this case, can reach the same values at different time moments (failure times t_{f0} and t_{f1}) [36]:

$$\sigma(t_{f0}, T_0) = \sigma(t_{f1}, T_1). \tag{3.10}$$

Here, σ can be applied stress in creep tests or rupture stress in CSR tests. Eq. 3.10 is valid when time and temperature are equivalent and interrelated. This fact allows a transition to the effective or reduced time by correlating the intrinsic time scale of a material with the observation time. The temperature shift factors $a_T(T)$ are introduced to quantitatively characterize the acceleration of viscoelastic processes, or in other words, the extension of the observation time scale. According to the effective time concept [36],

$$t_{f0} \times a_T(T_0) = t_{f1} \times a_T(T_1). \tag{3.11}$$

a_T at the reference temperature T_0 is normally taken as unity, $a_T(T_0) = 1$. Then, by taking the equivalence in the logarithmic scale from both sides of Eq. 3.11 results in [36]

$$\log t_{f0} = \log t_{f1} + \log a_T. \tag{3.12}$$

It follows from Eqs. 3.10 and 3.12 that the strength curves at T_0 and T_1, when plotted vs. $\log t_f$, are horizontally shifted to each other for the value $\log a_T$. The master curve is obtained by shifting the strength curves for a wide range of temperatures. For glassy polymers at $T < T_g$, the temperature dependence of the shift factor $\log a_T$ is represented by the Arrhenius equation [74, 115, 148]:

$$\log a_T = -\frac{E_a}{2.303R}\left(\frac{1}{T} - \frac{1}{T_0}\right), \tag{3.13}$$

where E_a is the activation energy, R is the universal gas constant, and the temperature is taken in Kelvin.

Following analogous discussions, the accelerating effect of absorbed water on the viscoelastic properties of polymers is considered by applying the time-water-superposition principle (TWSP). In this case, the time scale is extended by introducing the time-water shift factor a_w (w is the water or moisture content in a polymer). Under coupled influence of temperature and water, Eq. 3.10 transforms to [36]:

$$\sigma(t_{f0}, T_0, w_0) = \sigma(t_{f1}, T_1, w_1). \tag{3.14}$$

Then, assuming additive contributions from both factors, Eq. 3.12 transforms to [36]

$$\log t_{f0} = \log t_{f1} + \log a_T + \log a_w, \tag{3.15}$$

i.e., the lifetime is predicted from the sum of single shift functions. In this thesis, TTSP and TWSP (and coupled TTWSP) were applied to construct the creep strength (creep failure) and static strength master curves. However, the principles of TTSP, TWSP and TTWSP can only be applied to alike material conditions, which ensure that the model prediction is not affected by chemical or physical changes that will never occur in the reference condition. Therefore, the assumptions given in the last chapter are valid for the TTWSP as well.

Creep-rupture master curves

Figure 3.13 shows the results of the creep tests in terms of applied creep stress versus log failure time. The left part of Figure 3.13 displays the acquired results for the different test temperatures of dry and water-saturated specimens. Here, it becomes clear that the absorbed water decreases the allowable stress to gain a similar creep lifetime under room temperature conditions in the same dimension as a temperature increase of about 20 °C for dry specimens. This is equivalent to a reduction of the applied stress by about 20 %. For loading of wet epoxy at elevated temperatures of 40 °C, the stresses have to be even halved in order to achieve the same lifetimes as the dry material. In the right part of the Figure, the resulting TTWSP creep master curve is presented together with the temperature, water, and combined shift factors. The temperature shift factors are described by Eq. 3.13 with $E_a = 196\,kJ/mol$ (R^2=1). For any other test temperature, $\log a_T$ can be easily determined with Eq. 3.13.

As can be taken from the master curve, coupled TTWSP essentially increases the predicted creep lifetime from about three years (dry tests) to 65 years (wet test). At this point, it is essential to mention that all aging procedures were done at room temperature (slow temperature-aging effects). The room-temperature methodology ensures a similar and realistic (in the sense of typical applications) contribution of physical aging effects to all tested specimens. Furthermore, it was validated with hot water conditioning [33, 115] that no chemical degradation or chain scission occurs during long-term wet aging.

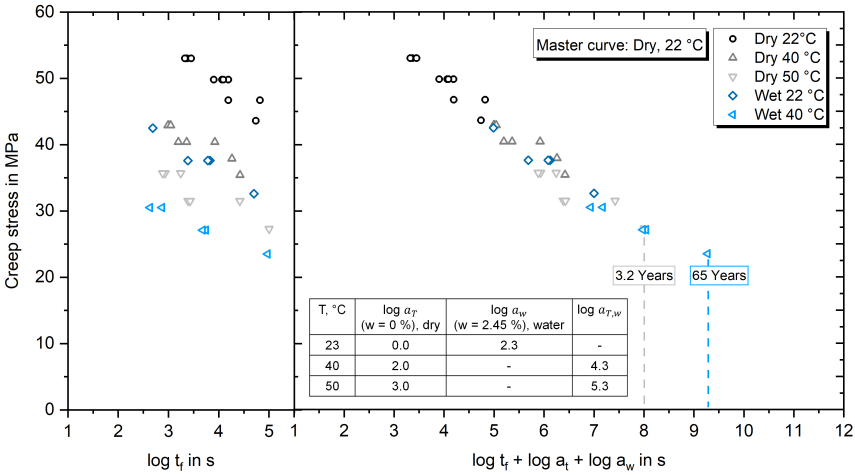

Figure 3.13: Testing temperature and aging dependent applied tensile stress vs. creep failure time (left) and time-temperature-water-superposition (TTWSP) master curve shift (right)

Static strength master curves

The same evaluation and fitting procedure as for creep tests was applied to the CSR tests data (shown in Chapter 3.3.3) and can be seen in Figure 3.14. Here, time to failure was taken from the experimental results in terms of the time to reach the yield strength.

Again, the left part of the Figure shows the original experimental data and the right part displays the master curve, obtained with the same temperature and water shift factors as for the creep tests. This approach shows generally a very good agreement for the CSR data. Nevertheless, the master curve shift also illustrates that the wet 50 °C samples do not fit very well with the remaining. The curve is clearly flattened and the strength underestimated in comparison with dry and wet 40 °C specimens.

CSR tests were also performed with specimens aged and saturated at room temperature at different levels of water activity (different levels of relative humidity) to extend the findings to a TWSP. The results in Figure 3.15 reveal the impact of the environment, and respective water saturation content on the moisture shift factors $\log a_w$. The best fitting solutions suggest an exponential behavior of the shift factors ($\log a_w$) in relation to the relative humidity, as shown in

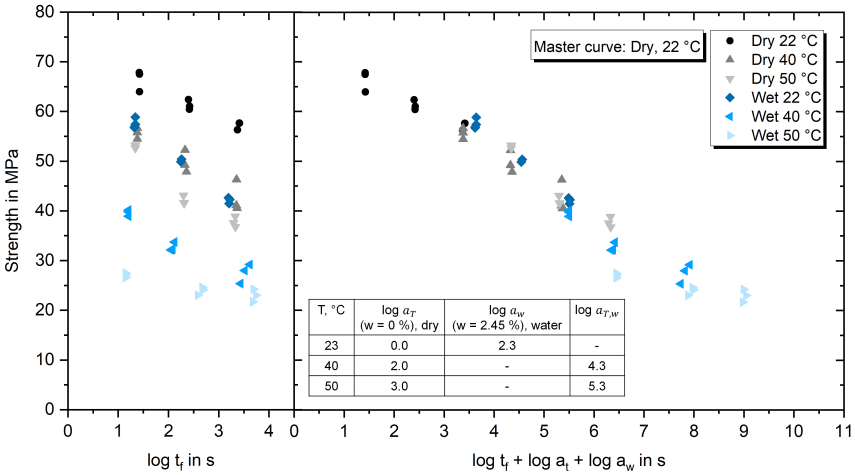

Figure 3.14: Testing temperature and water-dependent constant strain rate (CSR) tensile strength vs. failure time (left). Time-temperature-water-superposition (TTWSP) master curve shift (right)

Figure 3.16. This is in line with the curves for the maximum amount of absorbed water (Figure 3.5) and can be explained by the exponential nature of the polymer-moisture interaction.

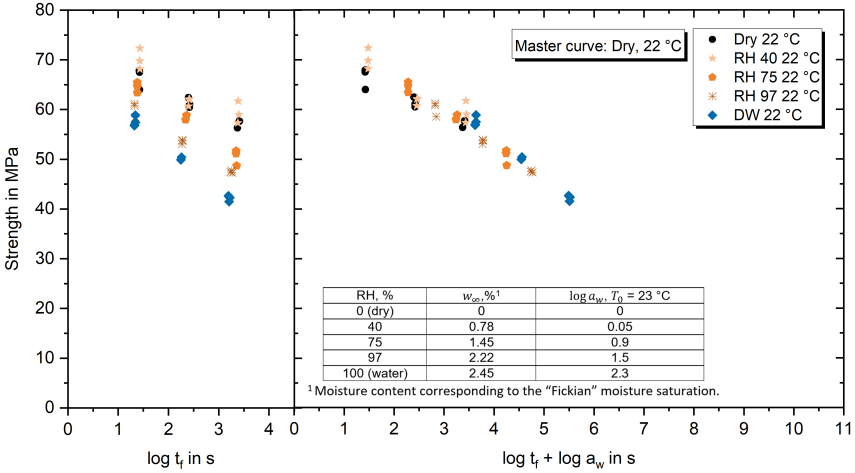

Figure 3.15: Moisture dependent constant strain rate (CSR) tensile strength vs. failure time (left). Time-moisture-superposition (TMSP) master curve shift (right)

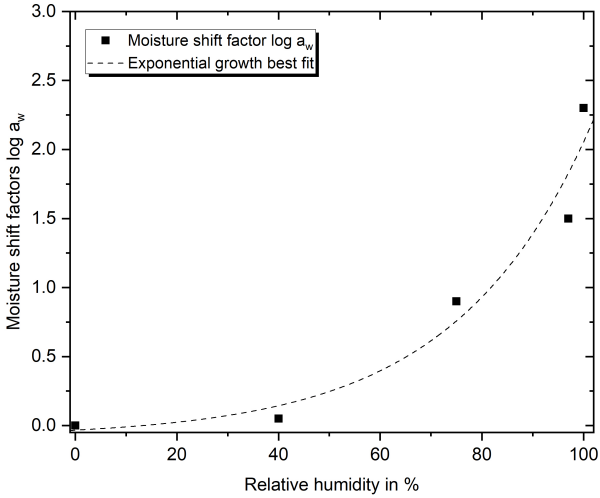

Figure 3.16: Moisture shift factors $\log a_w$ vs. relative humidity in %. Additionally, the best fitting exponential growth function is plotted to guide the eyes.

3.3.5 Correlation of CSR and Creep Data

The creep lifetime of epoxy was also modeled by applying the Reiner-Weissenberg (R-W) criterion [120, 151, 152] to the full data set. According to the R-W approach for time-dependent failure of viscoelastic materials, failure occurs when the stored energy exceeds the limit value that is a material constant. The applicability of TTSP to the R-W energy-based approach is discussed in [153]. The lifetime under constant load for R-W criterion, considering unidirectional creep of linear viscoelastic material, is given as:

$$\left(\frac{t_f}{\tau_0}\right) = \left(\frac{1}{2-2^n}\right)^{\frac{1}{n}} \left(\frac{D_0}{D_1}\right)^{\frac{1}{n}} \left(\frac{1}{\gamma}-1\right)^{\frac{1}{n}}, \text{with}\, \gamma = \frac{\sigma_0^2}{\sigma_R^2}. \tag{3.16}$$

Here, D_0 is the elastic material constant (compliance). D_1, n are viscoelastic material constants, τ_0 is time unity (equal to 1 s in this work, since t_f is measured in seconds). σ_R is the strength under instantaneous conditions and σ_0 is the applied creep stress.

Additionally, another fracture mechanics-based prediction method developed by Christensen [151, 154, 155] was applied to the data set. Here, following a kinetic

crack formulation, the creep rupture lifetime is found from the time needed for an initial crack to grow to a size critical to cause its instantaneous further propagation. The Christensen criteria for the creep lifetime is given as follows:

$$\left(\frac{t_f}{\tau_0}\right) = \frac{\alpha}{\sqrt{\gamma}}\left(\frac{1}{\sqrt{\gamma}^{1/m}} - 1\right), \tag{3.17}$$

where α and m are material parameters. For both criteria, it should be mentioned that most of the model parameters must be obtained from the fit of experimental lifetime data [154].

Equations 3.16 and 3.17 were used to fit the combined experimental creep and CSR strength master curve, and both demonstrated good approximation performance, as can be seen in Figure 3.17. The model parameters used for calculations are $D_0 = 0.34$ GPa^{-1}, $D_1 = 0.08$ GPa^{-1}, $n = 0.19$, $\alpha = 25$ and $m = 0.07$. As the reference strength under instantaneous conditions, data from CSR tests at $1\,\frac{\text{mm}}{\text{min}}$ were taken. In this way, the two criteria could be successfully applied for the first time to a combined creep/CSR master curve spanning a period of at least 65 years (nearly nine decades) generated with the TTWSP.

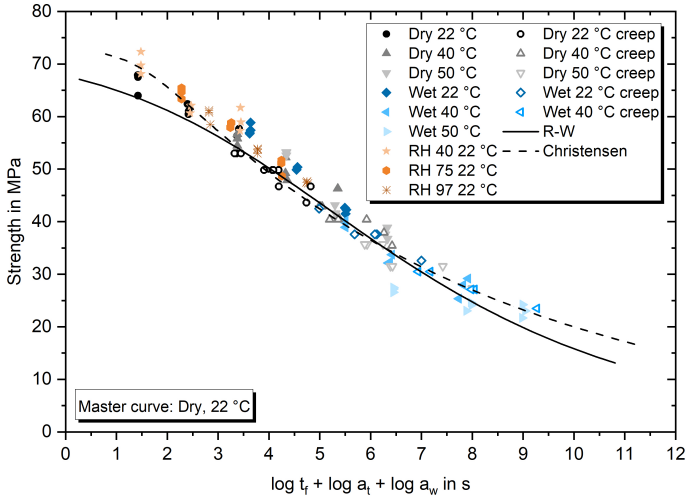

Figure 3.17: Master curve for combined creep and CSR tests (all data). Additionally, R-W and Christensen creep model fittings.

Most importantly, it is evident that the typical creep lifetime in applications with service lives of up to 50 years can be predicted very accurately using time-saving CSR tests only. Deviations between the RW and Christensen model approaches occur mainly for long prediction times of more than four years or high-stress loads resulting in less than one-hour lifetimes. However, based on the created data set, the Christensen approach fits slightly better, especially for long- or short-term predictions. By comparing all results of the combined master curve, it appears that CSR testing not only enlarges the prediction horizon but also replaces time-consuming creep testing. Therefore, the presented TTWSP methodology focusing on CSR testing and including wet-aged polymers to predict their long-term behavior proves to be an efficient and reliable procedure. The predictions made from two different types of tests (CSR and creep) and two factors (temperature and water) are in reasonable agreement, so their validity is to be assumed. Further validation using control tests over several years is complex (costly) to realize and control and, thus, is not an effective engineering solution.

Using the creep strength prediction model combined with the knowledge about the temperature, moisture, and combined shift factors makes it possible to predict creep lifetime not only for a reference master curve but also for any conditions (fulfilling the basic assumptions). As an example, in Figure 3.18, the resulting epoxy failure envelope based on the Christensen model fit is shown in a 3D space defined by the environmental temperature, the absorbed water content, and the time to failure under loading.

The exemplary surfaces shown are representative of three different load levels. It can be seen that the lifetime is affected by the ambient temperature and simultaneously by the amount of absorbed water. The shown surfaces are based on temperature and moisture shift data equivalent to the tested data set and additional interpolations for testing at 30 °C and/or 90 % RH. Each plane in the example is based on 24 data points (15 validated with experimental results). Thus, the entire load-dependent solution space can be spanned. As a short summary, the presented methodologies and derived models allow a detailed characterization of individual or combined temperature and moisture effects on mechanical properties and lifetime in a remarkably short time. The requirement is that these are subject to the model assumptions (e.g., no degradation by water absorption occurs). Therefore, from now on, the questions regarding the influences of

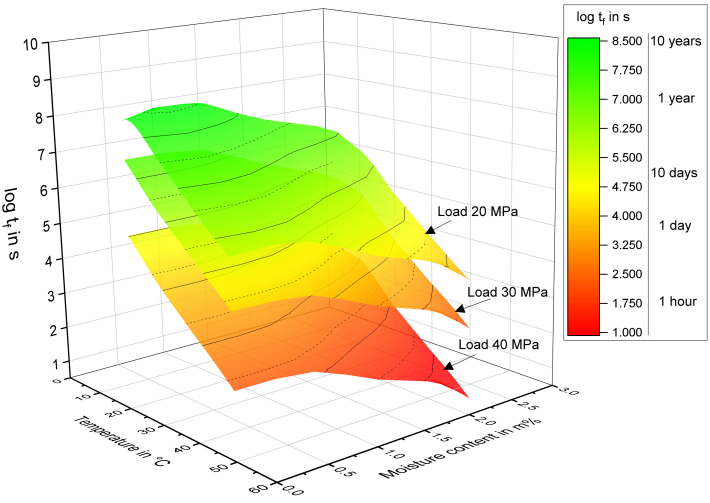

Figure 3.18: Predicted epoxy failure envelope based on the Christensen model fit in a three-dimensional representation.

(temperature) accelerated aging processes on polymer properties and how these affect the predictions will be addressed.

3.3.6 Temperature-Dependent Absorption and Desorption

The short-term equilibrium water uptake of the RIMR135/H137 resin is between 2.5 and 3.0 m% at 8 °C or 50 °C immersed water bath condition, respectively. This is within a typical range reported for similar systems, which cover a range from 1.0 m% to 5.0 m% [57, 102, 108, 133]. The representative water uptake behavior of the epoxy specimens is shown in Figure 3.19. It depends on relative humidity and ambient temperature. The weight change curves in the left part reveal that the apparent (Fickian) maximum water uptake increases with temperature from 8 °C to 50 °C by more than 0.4 m%, which is a significant rise of about 15 %. Aging above the wet-T_g at 70 °C increases the water uptake by another 0.15 m%, attributed to the rise in molecular mobility and free volume. However, similarly to the water absorption behavior at room temperature, the results cannot be accurately described during the whole absorption process by using the Fickian absorption model only. Clear deviations can be found in the transition region from linear to asymptotic uptake. The best fitting of ex-

perimental results and Fick's diffusion can be observed at low temperatures as 8 °C.

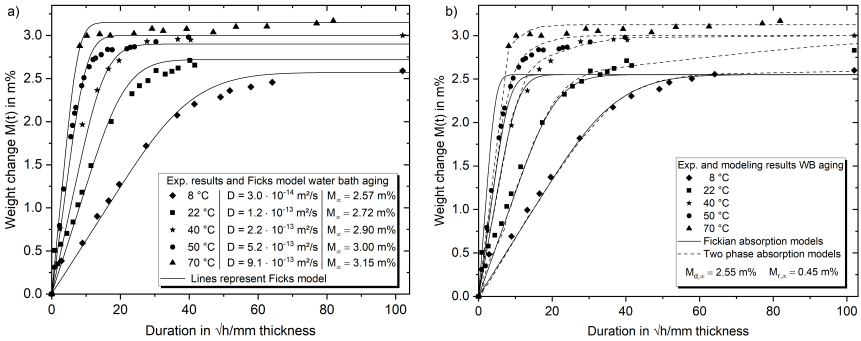

Figure 3.19: Experimental weight gain curves for epoxy aging in water of different temperatures. Lines indicate modeling of Fickian-type diffusion (a) and diffusion according to the two-phase model of Berens and Hopfenberg (b).

The water activity and the mobility of the molecular network are significantly reduced at these low temperatures. Since the epoxy's polarity and chemical structure are independent of the ambient temperature and the free volume below T_g is only weakly temperature-dependent in the range considered, it is unlikely that these are the reasons for the different apparent maximal water absorption. Therefore, the proposed explanation is that there is not enough energy available in the system at low temperatures to allow the water molecules to diffuse into all the theoretically attractive regions of the free volume and in between the molecule chains [103, 156]. For example, due to reduced molecular motion and steric hindrance, not all water molecules could reach the vicinity of particularly polar chain parts such as hydroxyl groups within a reasonable time period. In other words, the speed of physical aging is significantly depressed. As the ambient temperature or the aging duration increases, more and more of the attractive but inaccessible regions can be entered by the diffusing water. For the specific epoxy (RIMR135/H137), long-term saturation was achieved after about 40 days at 50 °C.

Since the rates of the physical aging processes are highly temperature dependent, physical aging is considered as the main driver for the difference in the water absorption behavior. Water absorption and physical aging are developing simultaneously for aging at elevated temperatures. Consequently, the experi-

mental water absorption curves result in the superposition of both processes. The lower the aging temperatures, the more the effects of pure diffusion and physical aging are separated in time. Assuming now that physical aging processes are mainly responsible for the deviations of the water absorption behavior between low and high aging temperatures, the model of Berens and Hopfenberg (3.1) is also applied to describe temperature-dependent water absorption. Since physical aging is largely depressed at low temperatures, it is reasonable to measure and define the diffusion-dependent maximum water absorption, $M_{d,\infty}$, in low-temperature aging specimens. The corresponding experimental and modeling results are shown in the right part of Figure 3.19. Here, $M_{d,\infty}$ is taken as 2.55 m%, while any additional uptake is considered by $M_{r,\infty}$ of 0.45 m%. The parameters $D(T)$ and $\tau(T)$ were fitted to represent the water uptake during the diffusion and relaxation-driven phase. By comparing both modeling approaches, it becomes clear that the two-phase model can describe the absorption behavior much more precisely. By only considering the Fickian model, short-term absorption at relatively low temperatures results in misleading low apparent saturation values. However, for real applications, the time needed to complete the physical aging has to be considered, as the process will take decades to complete at low temperatures.

In Figure 3.20, the Arrhenius plots of $D(T)$ and $\tau(t)$ taken from the two-phase diffusion model fits are presented in a logarithmic scale. Taking into account the temperature-dependent diffusion coefficients presented in Figure 3.19, it is possible to calculate the activation energy of $D(T)$ by the following Arrhenius relationship:

$$D(T) = D_0 \exp^{\frac{-Q_D}{T \cdot R}} . \tag{3.18}$$

Here, D_0 is the temperature-independent diffusion coefficient, R is the molar gas constant, and Q_D is the activation energy of the diffusion coefficient. The activation energy Q_D was found to be 52.4 $\frac{\text{kJ}}{\text{mol}}$, which is well in line with the results presented, e.g., by Zhou and Lucas [97] who calculated the activation energies between 43.5 $\frac{\text{kJ}}{\text{mol}}$ and 51.1 $\frac{\text{kJ}}{\text{mol}}$. Results of about 50.0 $\frac{\text{kJ}}{\text{mol}}$ mean that an increase of the aging temperature by 10 K will double the diffusion coefficient and, therefore, the water uptake rate.

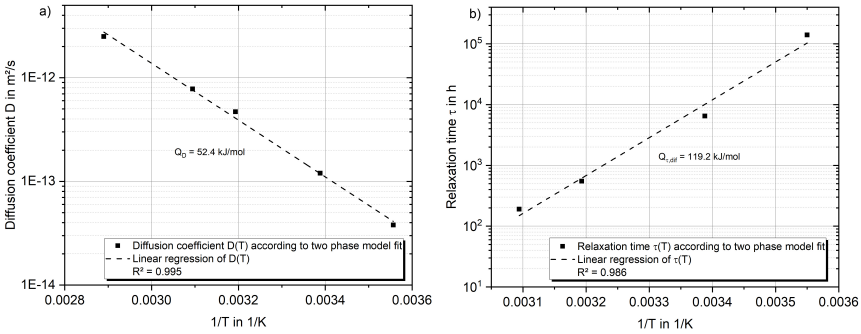

Figure 3.20: Arrhenius plot of the diffusion coefficient D (a) and the relaxation parameter τ according to the two-phase model of Berens and Hopfenberg (b).

Similarly, the Arrhenius plot of the relaxation parameter $\tau(T)$ as a function of temperature T is shown in Figure 3.20. By assuming a pure Arrhenius relationship, τ is calculated as:

$$\tau(T) = \tau_0 \exp^{\frac{-Q_\tau}{T \cdot R}} . \tag{3.19}$$

The linear regression shown also demonstrates a good correlation and, therefore, the dependence of the physical aging process on temperature. The calculated activation energy $Q_{\tau,dif}$ of about 119.2 $\frac{\text{kJ}}{\text{mol}}$ corresponds approximately to a fivefold increase in aging rate with an increase of the ambient temperature by 10 K. In fact, this means that the same aging process that occurs at 10 °C within a year is completed at 50 °C after only about 14 h. Nevertheless, deviations from the linear correlation can be observed, especially at cold temperatures. Similar deviations from an Arrhenius-type behavior have frequently been reported for aging at temperatures far below T_g [157–160]. Hence, the function of the relaxation time τ is considered to depend not only on the temperature but also on the structure or, in more detail, on the distance from the structural equilibrium [161]. The common approaches to model the relaxation time τ are the well-known KAHR model by Kovacs et al. [162] and the TNM model by Tool–Narayanaswamy–Moynihan et al. [163]. However, since the relaxation time τ can be described quite sufficiently with an Arrhenius-type model based on the diffusion tests conducted, this simpler model is taken for now.

The presented temperature-dependent absorption behavior is, furthermore, an extension of the well-known findings by Zhou et al. [97], who stated that equilibrium water uptake of epoxies is independent of the aging temperature. While

Zhou et al. [97] only investigated aging temperatures $\geq 45\,°C$, which already provide much external energy for water absorption and physical aging processes, the cold water absorption presented in this thesis provides far less external energy. Based on the experimental and modeling results, it is revealed that water absorption behavior for low-temperature applications will differ significantly from what might be expected by high-temperature accelerated aging procedures. More recent studies on the water absorption behavior of physically aged and un-aged epoxy coatings by Elkebir et al. [103] also covered a wide temperature range from 30 °C to 60 °C. Similar to the present case, the authors found temperature-dependent differences for the maximum water absorption.

Furthermore, they were able to show that physical aging has a severe impact on the water absorption content [103]. In detail, it was revealed that water absorption could be depressed by more than 1.0 m% when physical aging occurred before water absorption. These results are in line with the findings of Kong et al. [39] and Odegard et al. [161], who stated that the limited accessibility of attractive molecular chain regions, accordingly, leads to a significant reduction in maximum water uptake. Consequently, whether physical aging occurs during water absorption or before makes a difference. To address this topic, repeated ab- and desorption cycles were performed on the RIMR135/H137 epoxy under different ab- and desorption temperatures. The corresponding weight change curves are shown in Figure 3.21. Apart from the dependence of the maximum water absorption on the aging temperature described before, the drying-temperature-dependent remaining water content and the differences in the second water absorption are particularly remarkable.

In detail, for the desorption at 40 °C ($< T_g$), approximately 0.16 m% more water remains in the epoxy structure compared to the desorption at 90 °C ($\geq T_g$). Following the argumentation of Zhou et al. [97, 99], it is expected that mainly type-one bound water (free or with a single water-bridge binding) is removed at the lower drying temperature. As a higher activation energy is needed to remove type-two bound water, this happens mainly at the high desorption temperature.

When looking at the second water absorption curves (after 40 °C and 90 °C re-drying), it becomes clear that the drying temperature (and duration) significantly impact the absorption behavior. The water absorption is substantially smaller after re-drying at a high temperature than after drying at a lower temper-

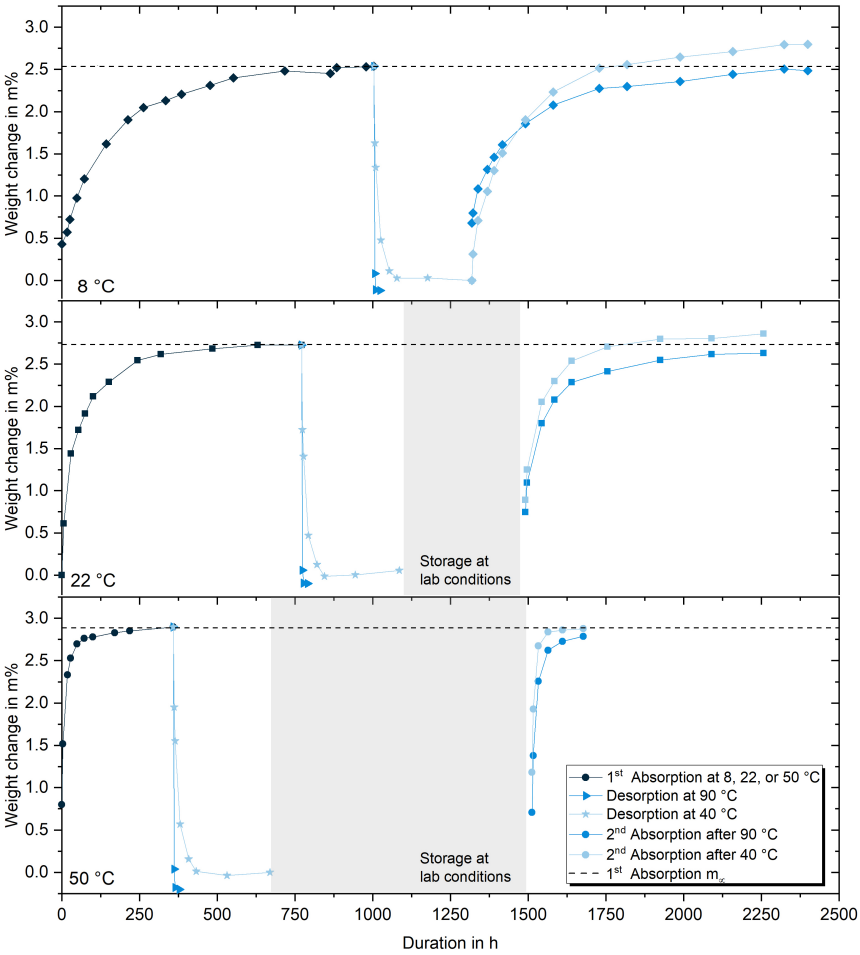

Figure 3.21: Water absorption and desorption cycles for aging in 8 °C (top), 22 °C (middle), and 50 °C (bottom) water. Re-drying was performed at 40 °C and 90 °C.

ature, regardless of the water-aging temperature itself. However, the maximum weight difference was larger the colder the primary and secondary water-aging temperature was. These results appear logical when the process of physical aging during water absorption and re-drying is considered. During water absorption at low temperatures, the physical aging process is strongly depressed. Drying these wet specimens at a moderate temperature of 40 °C abruptly accelerates the

physical aging process under the simultaneous presence of water in the molecular structure. During the re-absorption cycle, the aged molecular structure is easier and more widely reachable for the water molecules. Consequently, the maximum water absorption increases.

In contrast, the drying at 90 °C ages the molecular structure mainly without the presence of water, as the drying process is exceedingly fast at this temperature. The largest part of additional aging is added in dry conditions. Therefore, the aged structure is less attractive and accessible for water absorption, which corresponds to the recent findings of Elkebir [103] and Kada [104] for previously physically aged epoxy adhesives. Considering the physical aging that co-occurs with water absorption at high temperatures like 50 °C, it is clear that the drying process changes the molecular state only slightly. Consequently, the second absorption process resembles the first one more than the other conditions. In summary, the results indicate that the state of physical aging is decisive for water absorption processes and that it is essential if aging occurs under the presence of water in the molecular structure or without. Furthermore, it seems likely that a small amount of about 0.16 m% water is strongly bonded to the network and requires high temperatures for desorption.

Experimental results for the water absorption behavior at temperatures above the wet T_g were obtained at 70 °C and are shown in Figure 3.19 as well. At this temperature, the saturated epoxy is already in a rubber-elastic state, and compared to the sub-T_g aging, the additional water uptake is about 0.15 m%. Therefore, the molecule chain's reorganizations and water's diffusion are considerably increased. But unlike sub-T_g aging, physical aging (structural relaxation) does not occur because there is little restriction on mobility. As a result, it can be assumed that all molecular regions attractive to water are accessible in this condition. Furthermore, the free volume also increases significantly, although it must be assumed that the increase in free volume does not have to lead to a higher water absorption directly. Some authors have already shown by means of molecular dynamics simulations that (saturation) water absorption of up to 7.0 m% in epoxy is far from sufficient to fill the entire free volume [164–166]. For example, Li et al. [164] found only 6 % of the free volume of their model epoxy was occupied by water at a water uptake of 4.0 m%. Similarly, Tam et al. [165] reported a decrease in free volume of approximately 9 % for the same amount of absorbed water. Even the approximately 19 % reduction in free vol-

ume at 7.0 m% water uptake from the calculations of Lee et al. [166] is far from complete filling.

3.3.7 Monitoring Water Absorption by FTIR Analysis

Additionally to gravimetric measurements, FTIR spectroscopy is used to determine the water content within the epoxy. FTIR spectra are exemplary shown in Figure 3.22a) for the water absorption in 8 °C water for a duration of up to 2600 h. As introduced before, it is evident that the peak at about 5238 cm^{-1} rises during water absorption. Figure 3.22b) compares the gravimetrically determined weight gain and the peak integral. The linear regression, displayed with the dashed line, indicates the high accordance of both techniques. Therefore, the maximum water content can also be evaluated using spectroscopy data as follows:

$$M(t) = \frac{A_I - 0.2}{10.8} \tag{3.20}$$

containing the normalized peak integral A_I. Accordingly, it confirms the peak integral evaluation for long-term aging under various temperature differences in maximum water content found by weight measurements. This kind of analysis was likewise performed for all other aging conditions. In accordance with what was gravimetrically determined, the average peak integral of 8 °C aging after 2600 h is 13.3 % smaller than the 50 °C integrals. Considering the regression presented in Figure 3.22b), this corresponds to a weight gain difference of about 0.43 m%, which is exactly the difference measured gravimetrically. Aging at 70 °C results in the highest peak values, indicating additional water uptake of about 0.25 m% compared to aging at 50 °C. The FTIR measurement is, furthermore, applied for the through-thickness determination of the water distribution in thick samples during one-sided water diffusion. The results are presented in Chapter 4.3.7.

3.3.8 Impact of Aging Temperature on Mechanical Properties

In Figure 3.23a), the maximum tensile yield strength is plotted for comparison again in relation to the apparent equilibrium contents of absorbed water at 22 °C for various relative humidity and a water bath immersion. It must noted that the corresponding tensile tests were executed within 650 h (one month) of aging, which is shortly after saturation. So far, the results suggesting a clear correlation between absorbed water content and tensile strength are in line with what has

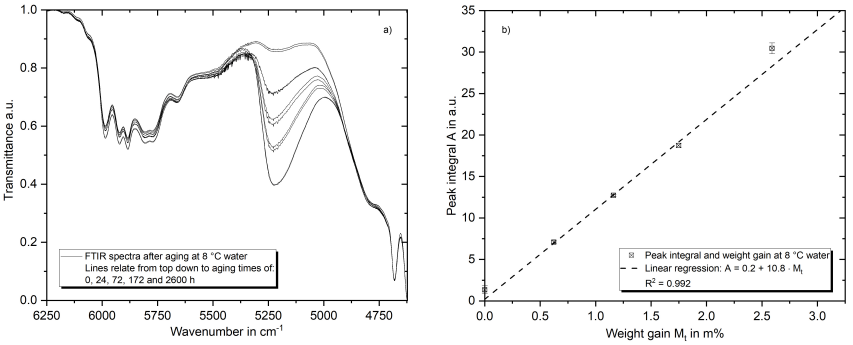

Figure 3.22: FTIR spectra of the RIMR135/H137 epoxy aged in 8 °C water in the region of the water absorbance band (5238 cm^{-1}) for several aging times (a). In b), the correlation between the peak integral and the weight gain (gravimetric measure) is shown. A linear regression indicates a high level of determination.

been shown previously by authors such as Ilioni et al.[65]. In contrast, additional investigations on specimens aged at various other temperatures but still tested under homogeneous saturation conditions within about one week after saturation was reached disclose that the tensile strength of the epoxy is not a simple function of the amount of absorbed water. Instead, it becomes evident that the ambient temperature at which the water was absorbed has a decisive influence on the tensile strength. Knowing the amount of absorbed water exclusively without information about the temperature history is not enough to predict the tensile strength.

Nevertheless, the strength follows a linear relationship with the amount of absorbed water for each aging temperature. Contrary to what might be intuitively expected, the strength increases with increasing aging temperature. Moreover, this implies that the higher water absorption at elevated temperatures, already shown in Section 3.3.6, has no additional negative influence on the tensile strength. Again, all results shown in Figures 3.23 and 3.24 are acquired shortly after reaching saturation.

Representative stress-strain curves for wet saturated specimens after aging in water of different temperatures are presented in Figure 3.24. The stress-strain curve of the dry epoxy in the reference condition is also shown for comparison. In addition to the fact that the strength decreases with decreasing aging temperature, it also appears that the maximum strain at break increases or decreases depending on the conditioning type. While water absorption at 8 °C

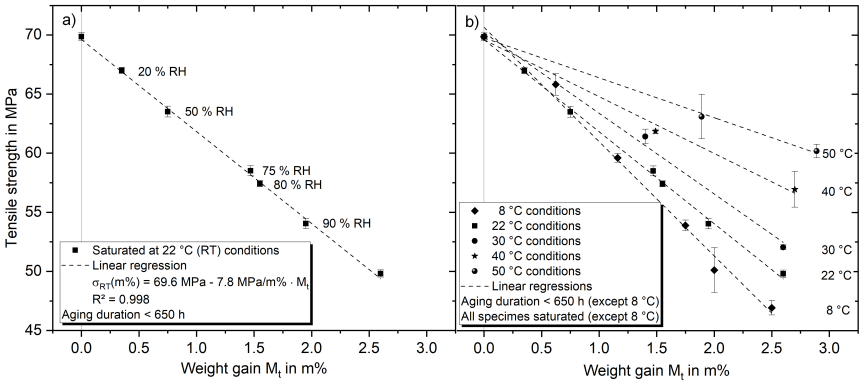

Figure 3.23: Relation between maximum tensile yield strength and amount of absorbed water at 22 °C (a) and absorbed water at various aging temperatures (b). All specimens were aged until homogeneous saturation conditions were achieved.

significantly enlarges the failure strain to more than 20 %, at 50 °C, a decrease is apparent. Furthermore, defined yield points and additional strain-softening with pronounced plastic deformation are apparent for all conditions. The stiffness is slightly lower in all saturated conditions than in the dry condition (from 2.5 GPa for 50 °C to 2.7 GPa for 8 °C aging). This leads to apparent differences at strains of about 3 %, which mark the beginning of the yielding region. The behavior after cold water aging is particularly striking since, in this case, with increased elongation, almost no stress loss occurs. Under these specific conditions, the plasticizing effect of the water absorption comes into full effect. Since the amount of water absorbed is relatively similar for the considered conditions, the stress-strain behavior is significantly influenced by the hygrothermal history defining the water-epoxy molecule interaction. In fact, as the plasticizing effect of the water is expected to affect all saturated samples similarly, the degree of physical aging will mainly contribute to the strength and failure strain variations.

The tensile strengths at apparent saturation after aging in water of various temperatures and different aging times are presented in Figure 3.25. Also, all tensile tests were performed at room temperature in this case. Again, compared to the dry strength, it is evident that the wet strength decreases the more, the colder the aging temperature is. This applies over a range from 8 °C to 50 °C. Furthermore, testing after long-term aging of at least 2600 h, which implies a minimum

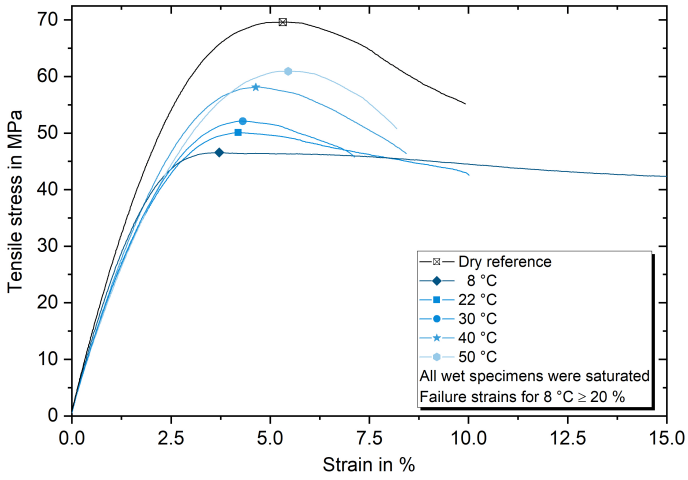

Figure 3.24: Representative stress-strain diagrams of specimens aged at various temperatures. Tests were performed as soon as saturation was reached.

of two months after saturation was reached, reveals that the tensile strength increases significantly with an extension of the aging duration.

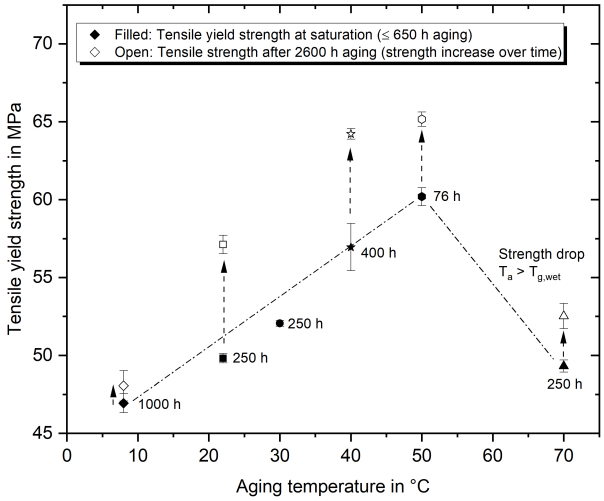

Figure 3.25: Correlation between water bath aging temperature and maximum tensile yield strength shortly after reaching saturation (filled symbols) and after 2600 h of aging (open symbols).

In contrast, aging at 70 °C also largely decreases the strength to about 49.3 MPa, which is a drop of 29.3 % compared to the dry strength. This result corresponds well with the strength reported by Krauklis et al. [80] for the same epoxy system aged at 60 °C in water. The significant difference between aging in environments of up to 50 °C and at higher temperatures can be explained by the fact that the T_g is drastically depressed due to water absorption. In this specific case, the in water-saturated epoxy has an aging condition-dependent T_g of about 61.5 °C to 66.5 °C (shown in Figure 3.31). The resulting T_gs are close but even lower than the hottest aging condition at 70 °C. As the epoxy is not in a glassy state during the 70 °C aging condition, it can be assumed that the water-epoxy interaction is also different. Following the reasoning proposed by Zhou and Lucas [97], or more recently Le Guen-Geffroy et al. [38], mainly two effects will come into play. The first is considering the type of bond state the water can form with the epoxy network. In this context, Zhou and Lucas [97] showed that the fraction of type II bound water increases with increasing aging temperature and duration, at least for sub-T_g aging. The second effect is the assumption that physical aging will be eliminated entirely or depressed at temperatures above T_g, as the molecular network is more mobile and the free volume significantly enlarged [38]. Therefore, a comparison of the cold water (8 °C) and above T_g aged samples allows drawing some conclusions on the proportions of these two mechanisms to the development of the tensile strength. As the degree of additional physical aging in a short-time, low-temperature aged epoxy is exceedingly small in above T_g aged samples, differences of the strength might be related to the bond type of water and epoxy. In this regard, it is reasonable to assume that the proportion of type II bound water due to 8 °C aging is very small, while it could be considerably higher for 70 °C. The tensile strength difference of about 2.5 MPa (5.3 %) after the short-term and 4.5 MPa (9.0 %) after the long-term aging at 70 °C is accordingly attributed to the higher proportion of water incorporated into the molecular structure (type II). Equally, this also means that most of the strength recovered over time during sub-T_g aging results from physical aging.

Generally, it was found that the rate of strength increase is higher, the higher the surrounding temperatures are. An approach to modeling this time-temperature-related behavior is to use so-called relaxation functions, which can describe quantities such as mechanical or thermal properties as a function of time. Here, the semi-empirical Kohlrausch-Williams-Watts (KWW) correlation, taking the temperature-dependent relaxation time τ into account, is a favorable approach,

as its parameters have a physical meaning and its applicability for polymers was shown in the past [38, 70, 159, 161]. The monotonic property change over time $\Phi_\Delta(t,\tau)$ is a result of the relaxation (physical aging) process. It can accordingly be described as [161]:

$$\Phi_\Delta(t,\tau) = \exp^{-(\frac{t}{\tau})^\beta}, \tag{3.21}$$

where β is a stretching parameter ($0 \leq \beta \leq 1$) describing the distribution of relaxation times. To model the polymer strength with regard to the state of relaxation, the formulation must be extended by distinguishing between the time-varying strength σ_Δ and the initial strength σ_0 in the unrelaxed state. The KWW model for time- and temperature-dependent yield strength $\sigma_y(t,\tau)$ prediction of physically aged polymers can be accordingly formulated as:

$$\sigma_y(t,\tau) = \sigma_0 + \sigma_\Delta(1 - \exp^{-(\frac{t}{\tau})^\beta}). \tag{3.22}$$

where σ_0 is the strength without additional physical aging, σ_Δ is the maximum strength increase due to physical aging, and t is the aging duration. For the case of a hygrothermal aging process, the plasticizing effect of absorbed water has to be considered likewise, as it affects the strength in the opposite way. To account for this, the initial strength for the hygrothermal case $\sigma_{0,wa}$ is determined by the difference between the initial dry strength σ_0 and the loss of strength due to plasticization σ_ϕ. It follows:

$$\sigma_{0,wa} = \sigma_0 - \sigma_\phi, \tag{3.23}$$

with $\sigma_0 = 69.9\,\text{MPa}$ (initial dry strength) and $\sigma_\phi = 23.4\,\text{MPa}$ (maximum strength loss at saturation without additional physical aging by water absorption at 8 °C) from experimental results. Furthermore, it is demonstrated by high-temperature aging that the strengths apparently converge to a maximum value of about 65.5 MPa at very long aging times. While this is almost reached after about 2600 h at 40 °C and 50 °C, the underlying processes are much slower at colder temperatures. Figure 3.26 shows all determined yield strength data for aging in water at four different temperatures and durations up to 6200 h. The KWW models are generated with the fixed initial and long-term strengths values as well as with a fixed β of 0.55. The relaxation time parameters $\tau(T)$ are taken from the diffusion experiments (Figure 3.20) and shown in solid lines. Additionally, $\tau(T)$ was fitted to the experimental results of the tensile tests, shown with dashed lines. In general, the experimental tensile strengths and the diffusion-based modeling curves show a high level of agreement. By implication, it is possible

to predict the strength development of polymers over time based on diffusion experiments.

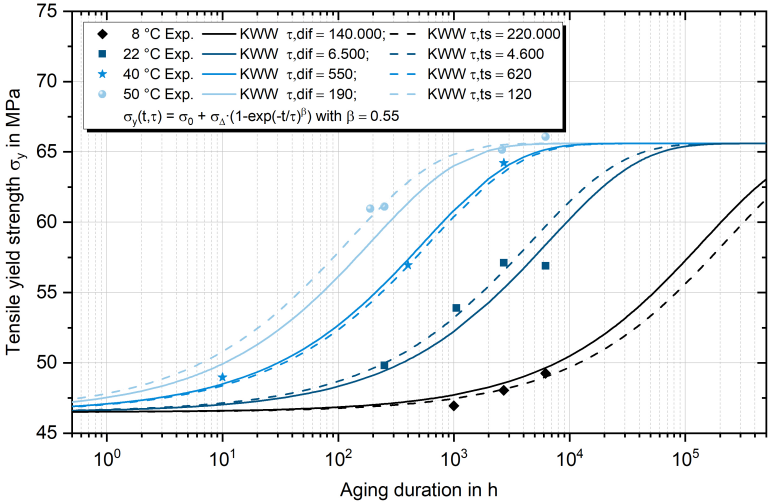

Figure 3.26: Experimentally determined yield strength (symbols) in relation to the aging temperature and duration. The solid lines show the analytical KWW model predictions for the diffusion-based values of τ. The dashed lines represent the best-fitting solutions of τ based on the tensile strengths.

However, the model shown in Figure 3.26 implies some simplifications that will be addressed further. As demonstrated by the sigmoidal appearance, the current approach implies saturation already at the beginning of the aging process. But this is only true, to a first approximation, for very thin specimens and elevated aging temperatures. The parallel progress of water absorption and physical aging is not considered yet. Therefore, strong deviations from the predicted and actual strengths must be expected, especially for a natural aging and absorption process in thicker structures and colder temperatures. The accurate water content as a function of aging time must first be considered to improve the prediction accuracy for any sample. Therefore, $\sigma_{0,wa}$ from Equation 3.23 is extended by a plasticization term that contains the actual amount of absorbed water $M(t)$ and the strength depression that is associated with the pure plasticizing effect of the water m_M. If the water absorption is moreover included as the two-phase

process described in Section 3.3.6, a new formulation for $\sigma_{0,wa}$ can be defined as:

$$\sigma_{0,wa} = \sigma_0 - \sigma_\phi = \sigma_0 - m_M \cdot M(t) = \sigma_0 - m_M \cdot (M_d(t) + \cdot M_r(t,\tau)), \quad (3.24)$$

with the total amount of absorbed water $M(t)$ being the sum of $M_d(t)$ (Equation 3.2) and $M_r(t,\tau)$ (Equation 3.3).Here, m_M can be designated based on the strength evolution during water absorption at cold temperatures. This approach considers the unknown physical aging state after manufacturing and the negligible increase of physical aging at cold temperatures for a short duration. For RIMR135/H137, the evaluation of the cold water aging effects (Figure 3.23) results in:

$$\sigma_{0,wa} = \sigma_0 - 9.57(\pm 0.36)\frac{MPa}{\mathrm{m\%}} \cdot M(t), \quad (3.25)$$

with $\sigma_0 = 69.9\,\mathrm{MPa}$. In addition, a temperature dependence of β should be introduced because of the gradient in strength development obtained for varying temperatures. The yield strength evolution, including the diffusion process itself, can be described with an extended KWW model as:

$$\sigma_y(t,\tau) = \sigma_0 - m_M \cdot (M_d(t) + \cdot M_r(t,\tau)) + \sigma_\Delta(1 - \exp^{-(\frac{t}{\tau})^{\beta(T)}}). \quad (3.26)$$

In Figure 3.27, the extended KWW model and the experimental results of the tensile strength evolution are shown. In addition to Figure 3.26, experimental results of non-saturated cold water aging specimens are displayed. Water absorption and physical aging occur in different orders of magnitude for cold water aging. The plasticizing effect of the water can be clearly seen first, followed by the strengthening effect of structural relaxation. At higher aging temperatures, both processes superimpose so that the strength of specimens aged at temperatures close to the wet T_g will never be as low as that of specimens far below the T_g. The high agreement between tests and the extended KWW model shows that it is possible to predict the strength development over the entire aging process using the 0.5 mm thin specimens.

With the extension of the KWW model by including the effects of water absorption introduced in Equation 3.26, the relaxation time τ must now be more differentiated. This is because the speed of physical aging is dramatically accelerated by absorbed water. Le Guen-Geffroy et al. [38] demonstrated that the aging process is about five to ten times faster in the presence of water than in air of the same temperature. For thicker specimens, the diffusion of water into

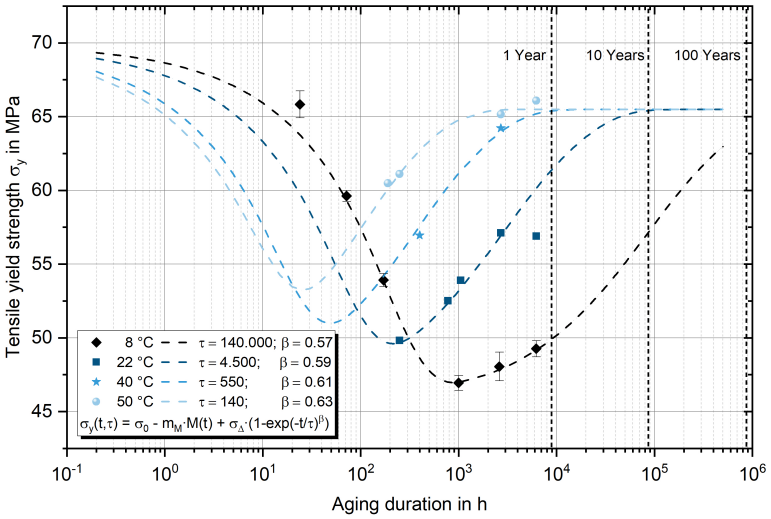

Figure 3.27: Experimentally determined yield strength of 0.5 mm thin specimens (symbols) in relation to the aging temperature and duration. The dashed lines represent the best-fitting solutions of the extended KWW model with respective $\tau(T)$ and $\beta(T)$ based on the tensile strength evolution.

the epoxy takes a longer time. Therefore, it would certainly be wrong to assume a high aging rate in the entire sample during absorption, which is determined in the saturation state.

Furthermore, the temperature dependence of the diffusion rate D is also several times smaller than that of the physical aging process (cf. Figure 3.20). The deviations between the model and reality would thus become increasingly larger the more extreme the temperatures (cold or warm) and the thickness of the sample became. Potential model assumptions and the related limiting cases to account for the dependence of the aging process on thickness and water absorption are shown schematically in Figure 3.28. While cases a) and b) represent the maximum (constant τ_{wet}) and minimum (constant τ_{dry}) aging rate assumptions, cases c) and d) consider a transition from dry to wet state. As a first approach, the water absorption and the two constant factors τ_{wet} and τ_{dry} are taken into account by a volumetric consideration of the proportion of the maximum water absorption in c). Finally, the volumetric consideration could be extended by the detailed description of the diffusion process, which is dependent on the actual aging condition and diffusion parameters.

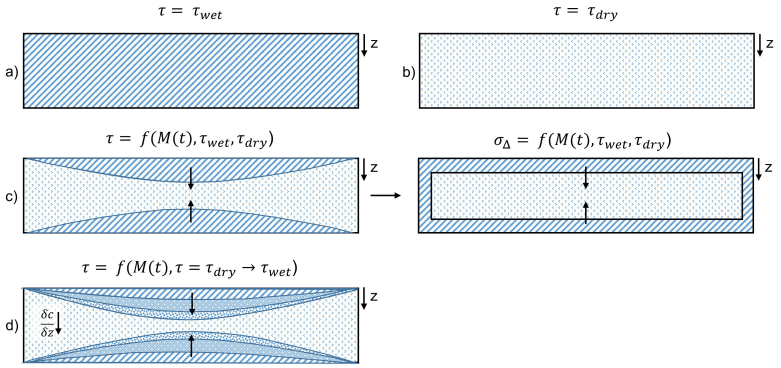

Figure 3.28: Potential model assumptions for the time-, thickness- and diffusion-dependent variation of the relaxation parameter $\tau(T)$.

The increase in strength due to physical aging is divided into two areas. For simplicity, it is assumed that the area that has already absorbed water can be approximated with the relaxation rate τ_{wet} and the still-dry area with the rate τ_{dry}. In order to reasonably match the distribution of the two regions, the proportion is determined in each case as a function of the maximum amount of water to be absorbed based on the diffusion equations (Equations 3.2 and 3.3). In this way, the aging rate directly correlates with the diffusion process.

Figure 3.29 shows the model curves of the tensile strength according to Equation 3.26 for 5 mm thick epoxy specimens. The model's limits become clear when either only the physical aging rate in the saturated state (τ_{wet}) or the up to ten times slower rate in the dry state (τ_{dry}) is selected for τ.

Since, in the first case, the entire physical aging would be completed well before complete water absorption, there is initially a strong increase in tensile strength, which subsequently decreases again due to the plasticizing effect of the water. Even though it is principally possible that physical aging progresses faster than water absorption, the rate here is undoubtedly too high. By only taking τ_{dry} into account, the curve is considerably shifted to the right, and the aging process is correspondingly as slow as it would be in the air without water absorption. The strength will now be within this spanned space, as τ will gradually change with water absorption. To account for this behavior, the KWW model has to be

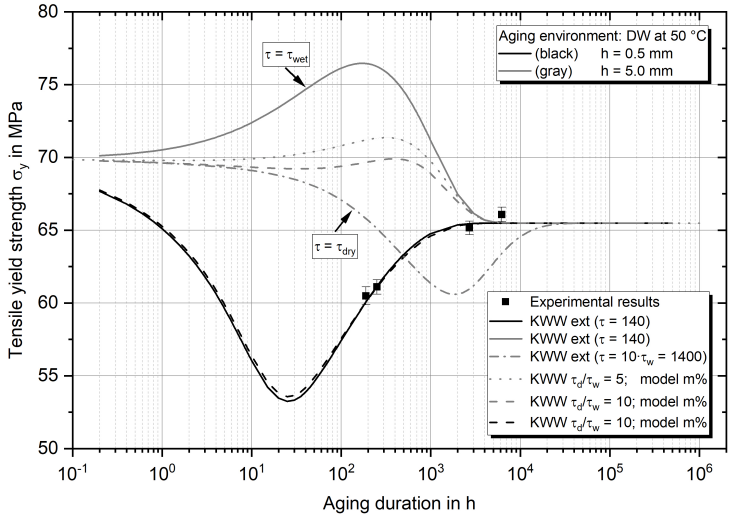

Figure 3.29: Experimentally determined yield strength of 0.5 mm thin specimens (symbols) aged at 50 °C. The grey lines represent different KWW model extensions for 5 mm thick specimens, taking the thickness dependence of $\tau(T, h)$ into account.

extended by a term, which gradually changes τ from τ_{dry} to τ_{wet}. Consequently, equation 3.26 is further modified for this purpose as follows:

$$\sigma_y(t,\tau) = \sigma_0 - m_M \cdot M(t) + \left(\frac{M(t)}{M_\infty}\right)\sigma_\Delta K1 + \left(1 - \frac{M(t)}{M_\infty}\right)\sigma_\Delta K2, \qquad (3.27)$$

with

$$K1(t,\tau) = (1 - \exp^{-(\frac{t}{\tau})^{\beta(T)}}), \qquad (3.28)$$

and

$$K2(t,\tau) = (1 - \exp^{-(\frac{t}{\theta\tau})^{\beta(T)}}). \qquad (3.29)$$

Here, the difference between the physical aging rate at dry and wet conditions is considered in terms of the factor θ:

$$\theta = \frac{\tau_{dry}}{\tau_{wet}}. \qquad (3.30)$$

Resulting strength predictions for thick and thin specimens with θ values of five and ten are shown in Figure 3.29 for comparison. Clearly, the developed model

can still accurately reproduce the experimental results on thin samples while, at the same time, the prediction for thick structures is within the expected range. Furthermore, a maximum strength deviation of about 2 MPa (3 %) is predicted, although the dry τ values are five to ten times higher than the wet ones. Considering the long prediction periods, the expected deviations appear acceptable. Figure 3.30 presents the predicted strength evolution in dependence of the thickness for aging under 8 °C and 50 °C, assuming a factor of ten for θ. This indicates that the strength-increasing physical aging process is slowed down so much at cold temperatures that diffusion usually dominates initially, and a reduction in strength is expected during typical application duration.

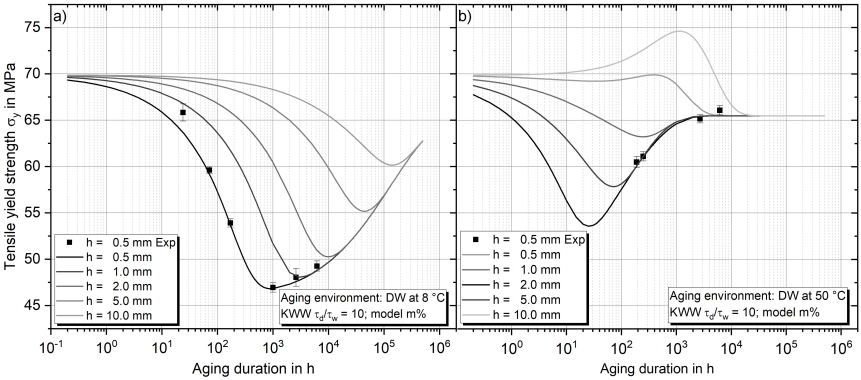

Figure 3.30: Experimentally determined yield strength of 0.5 mm thin specimens (symbols) aged at 8 °C a) or 50 °C b). The lines represent the strength evolution for specimens of different thicknesses according to the water uptake and thickness-dependent KWW model (Eq. 3.27) and a chosen ratio of ten for θ (see Figure 3.29).

In contrast, either plasticizing diffusion or physical aging dominates at high aging temperatures. Depending on the structure's thickness, there will be an initial decrease or increase in strength during usage. Limitations of the developed model are not considering swelling strains and stresses so far. For thick structures with high concentration gradients, swelling stresses could reduce the strength of an epoxy. As a note of caution, it should be kept in mind that the swelling stresses tend to be normal to the externally applied loads when considering a planar, more plate-like structure. Even though the stresses can theoretically be as high as 20 MPa, their influence on the tensile strength should not be overestimated, as the deformation of the neat epoxy is not constrained. In this context, it is referred

to a study by Krauklis et al. [83]: Here, the authors showed that swelling strains of up to 1.0 % can result from water absorption of 3.0 m%. Furthermore, the swelling strain scales linearly with the amount of absorbed water, which results in a hygroscopic expansion coefficient of $\beta_m = 0.332$. However, validation tests for thick specimens are not available yet. Therefore, the modified KWW model approach has not yet implemented the swelling-related strength evolution. Since the swelling stresses only occur during absorption, they might further reduce the strength during this time and lower the minimum passed through during water absorption. Compared with neat epoxy, the swelling stresses could have a critical influence on the composite, where the fibers strongly constrain the deformation.

3.3.9 Evolution of Thermo-Mechanical Properties During Hygrothermal Aging

The correlation of water absorption content and T_g is displayed in Figure 3.31 for both aging in humid air and water until saturation. The plotted linear regression (considering temperatures up to 40 °C), stating a T_g decrease of about 9.7 $\frac{^\circ\mathrm{C}}{\mathrm{m\%}}$, fits well with the experimental results typically reported for amine-cured epoxies [142]. This interrelation is usually described with the polymer-diluent model or the Simha-Boyer equation [38, 143]. However, significant deviations from this expected behavior are found, particularly for aging at high temperatures and with longer aging times. Therefore, the development of the T_g over aging time is presented in Figure 3.31 with open symbols as well. The results of warm water aging at 40 °C and 50 °C show a T_g increase of 1.6 °C and 2.1 °C respectively after 2600 h compared to the short-term results reached directly after saturation. During aging under room temperature or cold water, the T_g does not increase in the same period. Thus, it is evident that the T_g decreases significantly more due to the plasticizing effect of the water absorbed than it increases due to physical aging or an increase in the amount of type II bound water. Compared with the strength results presented in Figure 3.25, it becomes clear that the strength increase over time is mainly independent of the T_g development. Assuming that T_g is a measure of the mobility of the molecular structure, it follows that the reduction of free volume and the rearrangement of chain segments (physical aging) under the presence of water hardly leads to an impediment of mobility at room or colder temperatures. At higher temperatures, the change in T_g indicates a water-molecule interaction that reduces the mobility of chain segments.

In summary, this is a strong indication of an increased formation of type II bound water with higher immersion temperatures and longer duration, similar to those proposed by Zhou and Lucas [99]. Another important finding derived from the presented results is that there seems to be a temperature threshold at which the polymer-water interaction changes more fundamentally. In detail, it can be identified that the wet T_g of the epoxy aged at temperatures $\geq 40\,°C$ is considerably higher than at lower temperatures, even after long-term aging.

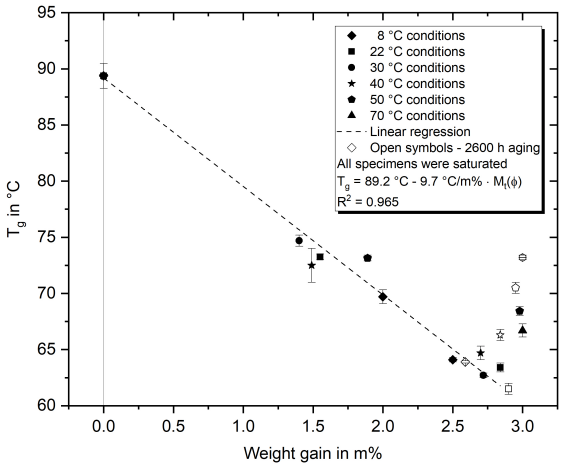

Figure 3.31: Relation between water absorption content and T_g. A distinction is made between aging times: Shortly after reaching saturation (filled symbols) and after 2600 h of aging (open symbols).

As the tensile strength of polymers is a consequence of their physical and chemical condition, this information can be used for property predictions. In the past, it was shown that the strength is especially affected by the mobility of molecular chains and segments, which the T_g of the polymer usually reflects [35, 141, 167]. In detail, many authors found semi-empirical relations between the strength of a polymer and the difference between the T_g and the ambient testing temperature [61, 141]. For most polymers, including epoxies (shown in Chapter 3.3.3), the tensile strength decreases linearly with increasing testing temperatures. The underlying relationship is represented by the Eyring equation, which is frequently used in the following form [65]:

$$\sigma_y = A \cdot (T_g - T) + B, \tag{3.31}$$

where σ_y is the tensile yield strength, T is the testing temperature and A and B are individual constants. For the RIM epoxy, tensile tests at various temperatures were run with the initial dry material. The results and the resulting linear relationship are shown in Figure 3.32 with open-crossed squares and the solid line. As expected, the Eyring correlation is valid for the dry epoxy. In addition, the relation between $T_g - T$ and tensile strength is also presented for the wet-aged epoxy. As before, a distinction is made between the aging temperature, environment, and duration. Compared with the prediction based on the dry specimens, it becomes clear that strong deviations are apparent for many wet-aged conditions. In detail, conditions that lead to a significant underestimation and a significant overestimation of strength can be identified. On closer analysis, it becomes clear that the respective ranges can be assigned to specific physical conditions and form a lower and an upper limit equally. The lower limit is formed by the low temperature and above-T_g aged specimen, which both have in common that their extent of additional physical aging is relatively low.

On the other hand, the upper limit is formed by the long-term and warm condition aged specimens (40 °C and 50 °C), which should contain the highest proportion of physical aging and the strongest water-polymer interaction. All other temperature-duration combinations, however, fit within the complete range described by the two limits. Although some of these coincide well with the Eyring prediction, these matches are only valid for a given point in time. In any case, making a generally valid prediction of the strength based on the Tg is impossible since the two properties develop dissimilarly as a function of temperature and duration.

Analysis of Water-Epoxy Interaction Using DMTA

As already introduced in Chapter 3.3.1, DMTA can be used to analyze the thermo-mechanical response of polymers. For the case of hygrothermal aged polymers, the method is usually used to measure the T_g or its respective change during water absorption, as it is done within this study. Based on the broad hygrothermal aging conditions considered in this study, substantial differences in the expression of the $tan(\delta)$ behavior were additionally found. In Figure 3.33, it is shown that the $tan(\delta)$ peak is split into two peaks. This is regularly observed and explained by the water diffusion (drying) during the test [168, 169]. However, more surprising is the finding that the peak shape and, in detail, especially the width of the left base of the peak, show fundamental differences as

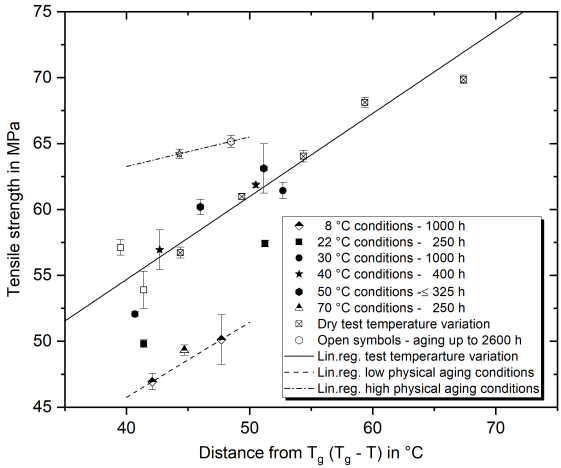

Figure 3.32: Tensile strength in correlation to the distance between T_g and testing temperature T ($T_g - T$) for several water-aged conditions and dry specimens at various temperatures.

a function of the aging temperature. While an inclination of the curve can be found even at temperatures as low as 35 °C for aging at 8 °C the same inclination starts at above 60 °C after aging in 50 °C water. Assuming that there is always water saturation with only little deviations of water content in the samples at the beginning of the test, this result can be interpreted as a consequence of basically different water-molecule-network interactions. Since $tan(\delta)$ is a measure of the energy that is reversibly stored or dissipated, the earlier increase describes an earlier energy dissipation in the cold-aged epoxy. In terms of the water-filled molecular network, this difference can result from water being mainly free or loosely bound (cold aging) or strongly bound (warm aging) to the network. In addition, it must be considered that accelerated physical aging may also be involved in these results. Considering the long-term aging results, it becomes clear that the typical curve shape of each aging type does not change substantially. With increased aging time, the curves of all conditions at $\geq$ 22 °C slightly shift to higher temperatures. In summary, the $tan(\delta)$ curve's shape was found to be an indicator of the water-polymer network interaction, as it demonstrates significant differences. At the same time, the weight gain and T_g measurements and the FTIR peak evaluation don't show distinct deviations.

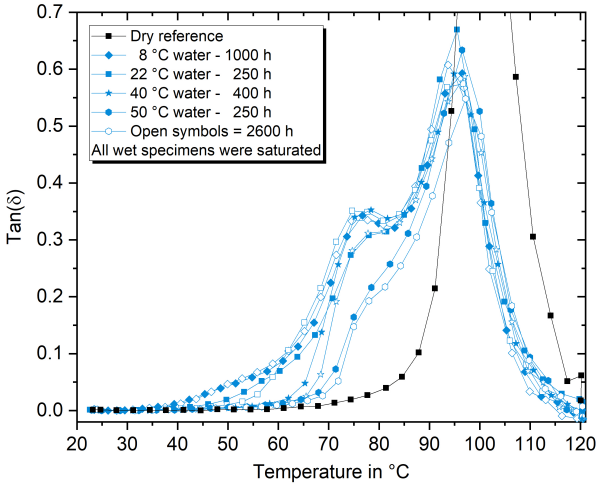

Figure 3.33: $Tan(\delta)$ versus temperature curves after aging in water baths between 8 °C and 50 °C for short-term saturated conditions (filled symbols) and long-term aging (2600 h) (open symbols).

The properties of specimens aged under particular conditions and tested subsequently at room temperature will be compared, as their mechanical properties or time-temperature aging history will allow us to draw more detailed conclusions on the molecular interactions and processes acting during aging. The first pair of interest is the epoxy aged at 40 °C for 400 h or at 22 °C for 2600 h. After both aging procedures, the resulting strength is 57.0 MPa, the strain to failure is about 9.0 %, and the water absorption amount is about 2.8 m%. Representative stress-strain curves are shown in Figure 3.34 as black lines. As both conditions should theoretically be influenced by the same plasticizing effect of the absorbed water, equal yield strength and strain to failure could result from the same state of physical aging. However, in contrast, a first deviation can be found in Young's moduli evaluated from the tensile tests, which is about 0.20 GPa higher in the case of long-term room temperature aging. In addition, a comparison of the DMTA results of the same conditions also reveals significant differences. Especially the stiffness, in terms of the storage modulus E', the T_g, and the development of the loss factor $tan(\delta)$ differ clearly. While for the 40 °C condition the storage modulus at 23 °C is 2.55 GPa, which is considerably lower than 2.90 GPa for the 22 °C condition, the T_g is with 64.7 °C higher than 61.5 °C. Furthermore, as shown with representative curves in Figure 3.35, the $tan(\delta)$ curves show ap-

parent differences in the peak width. In detail, the $tan(\delta)$ increases at notably lower temperatures in the case of the 22 °C aging. Overall, it is evident from this comparison that even if the same amount of water is absorbed in the epoxy and the resulting strength and elongation at break are identical, the water-molecule interaction can differ significantly depending on the hygrothermal history.

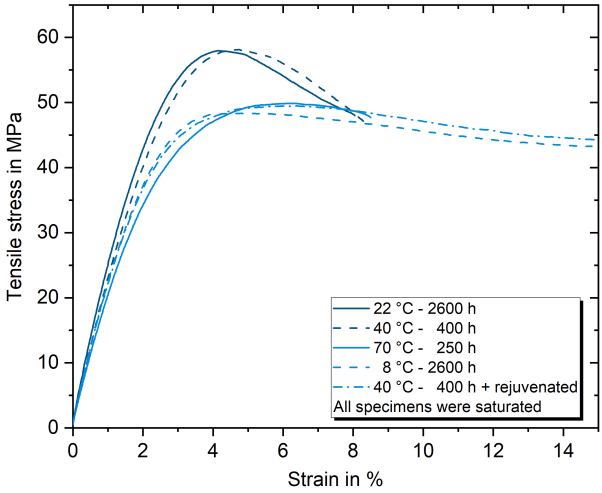

Figure 3.34: Representative stress-strain curves of aging conditions resulting in a strength of about 57 MPa (dark) or 49 MPa (bright).

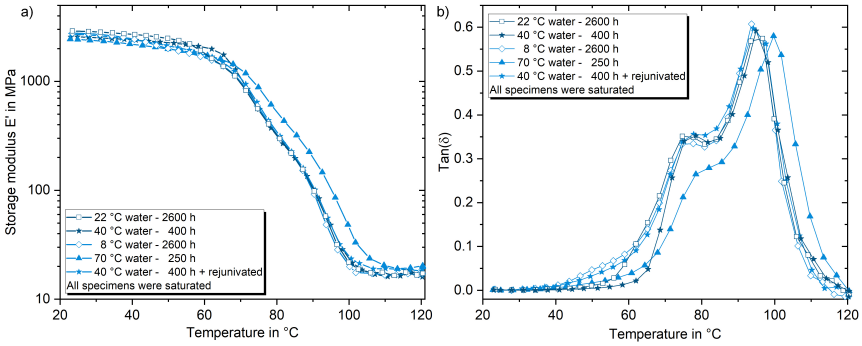

Figure 3.35: Representative E' and $tan(\delta)$ versus temperature curves of aging conditions resulting in a strength of about 57 MPa (dark) or 49 MPa (bright).

The second set of remarkable conditions refers to the stages of low strength. The strength of long-term cold water (8 °C) and short-term hot water (70 °C)

saturated specimens, as well as specimens saturated at 40 °C and subsequently rejuvenated, is all about 49 MPa. Nevertheless, distinct differences can be found in these cases as well. Noteworthy are the low stiffness of only 2.15 GPa but high T_g of 66.7 °C after aging in 70 °C water. As discussed in Chapter 3.3.6, the aging above wet T_g represents a unique case in which the physical aging should be suppressed to the greatest extent. As the water content and the external activation energy by the environment are simultaneously the highest, it can be hypothesized that the amount of strongly bound water is likewise very high.

Furthermore, the drop in stiffness and increase in T_g show analogies to the development of these properties as a function of the curing degree identified by Antoniou et al. [87] for a similar epoxy system. In this regard, the type II bound water could act like a secondary cross-linking, depressing the stiffness but increasing the T_g compared with sub-T_g aged conditions. But the comparison of Young's moduli of long-term aged epoxy at 8 °C (2.50 GPa) and 50 °C (2.55 GPa) reveals that the increased proportion of type II bound water slightly increases the stiffness, even though the absolute amount of absorbed water is higher after aging at 50 °C. Therefore, the significant drop in stiffness after aging at 70 °C is expected to result from the alongside-running rejuvenation process due to aging above T_g and the high amount of absorbed water. Nevertheless, a shift of the $tan(\delta)$ peak base towards higher temperatures, thus, can be interpreted as a measure of type II bound water as it is shifted significantly for aging at high temperatures and long duration. It also fits that the strain to failure is significantly lower since type II bound water should not contribute to plasticization. Following this argumentation, it also matches that both other configurations behave very similarly in all measured properties, as presented in Figures 3.34 and 3.35. While the increase in physical aging should be minimal at 8 °C, the rejuvenation process also resets the physical aging after saturation at 40 °C. Again, the slight differences in stiffness (0.2 GPa) and $tan(\delta)$ behavior follow the proposed argumentation and might be mainly explained by the increased free volume and higher amount of absorbed water in the case of the 40 °C rejuvenated specimens. For the rejuvenated case, it is suspected that the process temperature is not high enough to dissolve the type II bindings, formed during aging. This is in line with Zhou and Lucas's [97] findings proposing the need for very high temperatures to remove type II bound water.

Reversibility and Effects of Re-drying

In addition to what was found by Krauklis et al. [98] or Rocha et al. [18] for re-dried RIMR135/H137 specimens after aging in 60 °C water, aging in water at different temperatures and re-drying at sub-T_g or T_g-conditions (cf. Figure 3.21) were used to investigate the reversibility and impact of physical aging on the thermo-mechanical properties. The evolution of the tensile yield strength in relation to the aging and re-drying temperature is shown in Figure 3.36. Mechanical tests were performed as soon as the specimens reached apparent saturation (200 h to 1000 h), depending on the diffusion rate, to reduce the impact of additional physical aging within this testing series. The results after the initial water uptake are consistent with those previously shown. However, re-drying after water absorption at different temperatures and with varying drying temperatures reveals an impact on the reversibility of the strength. Generally, re-drying at lower temperatures (40 °C) makes it impossible to fully regain the initial strength (after initial drying at the same temperature). The remaining water (likely bound) and structural molecular changes are depressing the recovered strength by 1.0 % to 4.0 %. Nevertheless, short-term water absorption and low-temperature re-drying lead to almost reversible tensile strength and stiffness (2.70 GPa) properties for sub-T_g aging. The results after aging at 70 °C are somehow different. Here, the strength and stiffness (2.45 GPa) are significantly lower after aging and re-drying compared to the reference material.

As a result of the additional water desorption at 90 °C, the strength is higher than for the reference. Following the analytical calculation of the strength depression by the plasticizing effect of water, the additional removal of about 0.16 m% should increase the strength by about 1.5 MPa compared to the reference. This range is slightly exceeded. Therefore, it is concluded that high-temperature drying dramatically increases the physical aging process (even though drying was finished after 20 h) and/or additionally causes oxidation. Again, the aging at 70 °C reveals significant deviations. In this case, the strength is about 11.0 % higher compared to the reference. The Youngs moduli showed a significant difference after re-drying. In each case, the stiffness was about 0.15 GPa (5.5 %) lower when re-drying occurred at 90 °C.

The strength development after the second absorption cycle shows the impact of the additional physical aging during immersion, which increases temperature-related strength. But remarkably, no differences could be found concerning

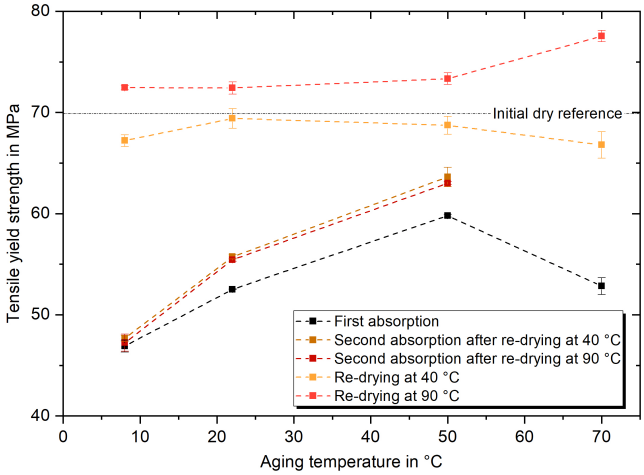

Figure 3.36: Tensile yield strength in relation to the aging and re-drying temperature for two absorption cycles.

the drying temperature. This is surprising, as the water absorption amount is significantly different (cf. Figure 3.21). Consequently, additional methods to reveal the epoxy condition should be applied to explain this phenomenon in more detail in the future. In general, the study showed that it is too superficial to assume that the epoxy properties are completely reversible by re-drying. Again, the time-temperature history of aging and re-drying has a decisive impact on the mechanical properties. Any (accelerated) aging process used for long-term property prediction has to consider these effects.

3.3.10 Transfer to Other Epoxies

To verify that the environmental impacts described and analyzed before for the RIM135/H137 epoxy are valid for other amine-cured epoxies, important properties were evaluated with a test campaign on the other three systems introduced in Chapter 2.1.1 in the following chapter. Consequently, the water absorption behavior (Figure 3.37a), the absorption-related tensile strength development (Figure 3.37b), and the T_g evolution (Figure 3.38) are analyzed.

First, it can be stated that no chemical degradation could be detected during wet-aging for any of the epoxies in the range between 8 °C and 40 °C. All systems

showed apparent Fickian absorption behavior without abnormal mass loss or increase after long-term aging, similar to the RIMR135/H137 epoxy. However, the maximum water absorption content differs significantly. The largest difference with ΔM_∞ of about 1.0 m% (40 %) was found between the RIMR135/H137 and the LY1568 epoxies. Considering also the particularly equal water absorption behavior of the RIMR035c/H037 and the CeTePox 3329A/B system and the chemical compositions of all investigated epoxies (cf. Table 2.1), there are indications that the water absorption depends mainly on the resin formulation. While the resin component is based on DGEBA, DGEBF, and DTGE, the curing agent formulations differ clearly for the latter epoxies, even though their water absorption behavior is almost the same. Based on the given formulations, the higher water absorption of the RIMR135/H137 epoxy is expected to result from the reactive diluent (HDDGE) proportion. All other investigated epoxies are based on DTGE as the reactive diluent and hence show a lower water absorption.

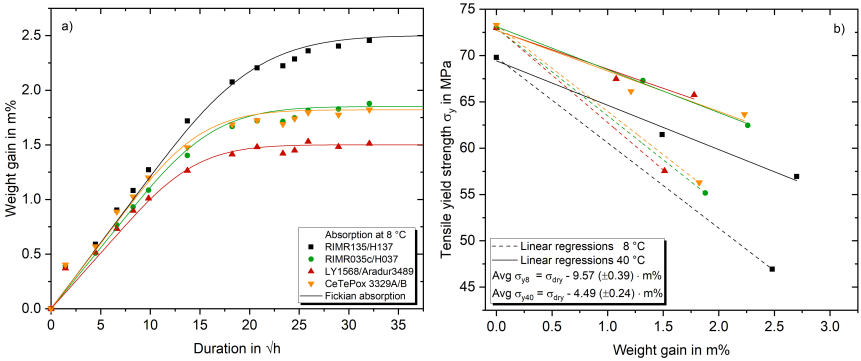

Figure 3.37: a) Weight gain curves of all neat epoxies for aging in 8 °C water. b) Correlation between tensile yield strength and amount of absorbed water at 8 °C and 40 °C. Tensile tests were performed as soon as saturation was reached.

The effect of the absorption in cold (8 °C) and warm (40 °C) water on the tensile yield strength is shown with isothermal regressions in Figure 3.37b) for absorption until saturation was reached. Similarly to what was found and discussed before for the RIMR135/H137 epoxy, the strength decreases linearly with the water absorption amount. The strength reduction is of the same dimension per water amount and aging temperature. Accordingly, the strength of the epoxies that absorb less water even in the saturated state remains significantly higher

than that of the other epoxies. Considering the similar impact of the water absorption on the T_g of all epoxies (shown in Figure 3.38), it can be concluded that the thermo-mechanical behavior of one system can accurately be used to infer that of the others. The temperature- and environmental-dependent aging behavior of the RIMR135/H137 epoxy, extensively analyzed in this thesis, can also be transferred to different epoxy systems. So, the extent of investigation can be dramatically reduced for analyzing similar epoxies in the future. Of course, it must always be ensured that the thermosets under study are not subject to chemical degradation and that the temperature range for predictions does not exceed the limits determined by the T_g of the material.

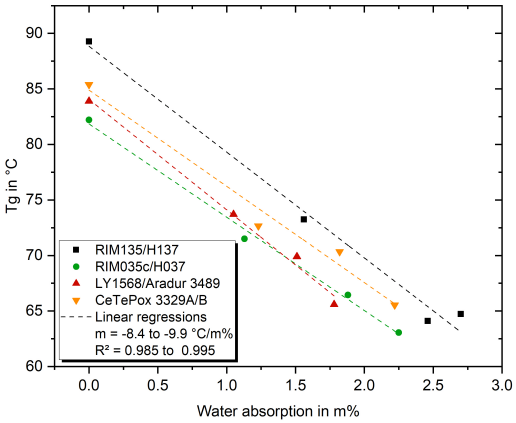

Figure 3.38: Relation between T_g and water absorption for all epoxies after aging in water between 8 °C and 40 °C.

3.4 Conclusions

In summary, the presented results demonstrate a strong dependence of the epoxies' thermo-mechanical properties on the time-temperature history under hygrothermal aging. Therefore, the research hypothesis:

The hygrothermal aging history has a decisive impact on the thermo-mechanical properties of epoxies. Thus, time, temperature, and moisture conditions during the service life and accelerated testing have to be considered for valid predictions of epoxies' long-term properties.

can be entirely confirmed. Considering water absorption and thermo-mechanical analyses, it is likely that not all properties will converge to the same values for different operating temperatures, even after extremely long periods. The main reasons for this are the different amounts of free water acting as a plasticizer and strongly bound water acting as additional cross-linking. In detail, the plasticizing effect of about 3.0 m% of water absorption in the RIMR135/H137 epoxy leads to a strength reduction of up to 24 MPa or 34 %, increasing the failure strain by more than 200 %. Long-term aging of up to 2600 h at elevated temperatures demonstrated that the epoxy can regain up to 93 % of its dry strength, even though the polymer is saturated with about 3.0 % water. However, the high strength is then accompanied by a slightly reduced fracture strain compared to the initial dry value.

Plasticization and physical aging are the main processes determining the thermo-mechanical properties of epoxies in view of hygrothermal aging. The results obtained clearly highlight that both processes are not independent of each other. While, in general, the presence of water dramatically accelerates the physical aging process, on the contrary, it is crucial if the physical aging takes place during water absorption or before. In the first case, the molecular rearrangement increases the water absorption capability, while it is decreased in the other case. Furthermore, it was demonstrated that plasticization and physical aging are affected to different degrees by the aging temperature. As a result, the latter is significantly more slowed down at low and correspondingly accelerated more at high aging temperatures. Consequently, the plasticizing effect is predominant for long-term use under cold conditions, e.g., if the epoxies are used below 10 °C. Even if it is assumed that the relaxation likewise will take place at low temperatures to the same extent, it would need far more than 50 years to reach the state, which results after about four months at elevated temperatures of 50 °C.

Concerning modeling and long-term predictions, a clear recommendation for appropriate actions can thus be derived: For cold operating environments, the artificial aging for durability predictions must necessarily be performed at sufficiently low temperatures to suppress extensive physical aging. Subsequently, time-temperature-moisture superposition methods can be applied as long as the test duration at elevated temperatures, e.g., with creep or constant strain rate tests, is so low that both re-drying and relaxation during the test can be avoided. If, to the contrary, the operating conditions are subject to significantly higher temperatures, e.g., regularly $\geq$40 °C, then aging should also be carried out at

a higher temperature. In this case, the aging temperature might also be significantly higher than the operating temperature since the polymer relaxation can be expected to reach the limit state during the service lifetime. Again, superposition methods can be applied subsequently. For service conditions in between, e.g., about room temperature, a more detailed consideration of the physical aging rate is necessary. Here, an extension of the time-temperature-moisture superposition methods by corresponding relaxation shift parameters appears reasonable.

From a testing and engineering point of view, it was proven for the first time that TTMSP methods could be applied to time-efficient and simple constant strain rate tests and, therefore, successfully replace time-consuming creep tests to predict the long-term failure of epoxies under diverse operating conditions. Furthermore, in this way, it was possible to construct not only single master curves but also a complete load-level, temperature- and water-absorption-dependent failure envelope of the studied epoxy.

Contrary to what is regularly reported, it was demonstrated that the correlation between the mechanical properties and the glass transition temperature of thermosets is more complex than often assumed. While tests at different ambient temperatures suggest a linear relationship between the strength and the distance to the T_g, this no longer applies without restriction as soon as aging plays a role. Thus, it was shown that aging, whether accelerated by water or not, affects the epoxy strengths far more than the Tg. As a result, it is neither sufficient to know the distance of the operating temperature to the initial T_g nor to know only the amount of absorbed water to predict the actual or long-term strength. If more than a single point in service life is considered, T_g-based strength predictions, as typically used with the Eyring correlations, are not sufficient anymore. For example, an upper and lower limit with strength differences of up to 16 MPa or 30 %, respectively, could be described for the same distance between T_g and testing temperature. Again, the aging history must be considered.

With the help of thermo-mechanical investigations and thermally rejuvenated specimens, differences in the degree of physical aging and the amount of strongly bound water could be identified. For identical T_g, weight gain, and strength, the peak shape of $tan(\delta)$ allows the reveal of significant differences between aging conditions. As disclosed by aging in various ambient temperatures below and above the epoxy's wet-T_g, the amount of strongly bound water (type II) is

expected to increase significantly with higher temperatures. When considering T_g development over time, it can also be assumed that almost no type II bonds are formed at temperatures of less than 40 °C. For lower temperatures, the T_g, therefore, also shows a time-independent linear behavior with the water content, which can be modeled using the well-known Simha-Boyer equation or other polymer-diluent models. For higher temperatures, the T_g increases over time. In the future, the DMA and FTIR data can be used to determine a probable time-temperature-water aging history of epoxies. Therefore, both the tanδ peak and the FTIR spectra will be analyzed using neural networks as demonstrated by Doblies et al. [127]. Apparently, these data could contain all necessary molecular information.

4 Environmental Impacts on GFRP and its Constituents

As shown in the previous chapter, the thermo-mechanical properties of composite epoxy matrices are remarkably affected by moisture or water contact as well as by environmental and aging temperatures [33, 34, 38, 106]. It was shown that the long-term thermo-mechanical properties under various conditions are both predictable and largely reversible. The dominating mechanisms have been identified on the molecular level as water absorption-induced plasticization and temperature-driven relaxation (physical-aging) processes. The matrix polymer still determines the water absorption in the composite [18, 31, 74]. Therefore, both mechanisms will play a major role. But in contrast to the studies performed on neat polymers, GFRP consists of two additional parts: (i) glass fibers and (ii) the fiber/matrix interphases (F/M interphase), which both are likely to respond differently to external influences [76, 115, 170, 171] and could affect each other [172]. The overlapping effects and the additional variability due to the composite layup structure and the anisotropic properties on micro and macro scales complicate the entire situation. Consequently, in the following, the aim is to clarify whether the knowledge gained for the resins can also substantially explain the aging behavior of GFRP composites and where other mechanisms predominate. Therefore, the first working hypothesis for this chapter is:

In contrast to the long-term behavior of the epoxy resin matrices, the corresponding performance of composites cannot be simply described by (aging-) temperature-dependent acceleration factors. This is because fiber and interphase degradation are neither independent of each other nor follow the same continuously accelerated mechanisms.

As the use of GFRP in structural applications has a long history, numerous specific types of composites and constituents have been developed. The numerous types of glass fibers, matrix polymers, and sizings lead to an unmanageable

variety of possible combinations. While it is easy to simplify the investigation process by referring to a defined polymer system, such as epoxies, in this case, the fiber and interphase effects introduced are much more obscure. Although no specific corrosion resistance is often known [173, 174], quite precise compositions and defined classes are available for fibers [173, 175]. This enables a certain degree of comparability. The situation is entirely different with sizings. Their exact ingredients are one of the best-kept secrets of fiber manufacturers [176–178]. Usually, nothing more is known than the basic compatibility. For example, the use of film-forming agents based on epoxy resins and silanes, characterized by the corresponding reactive groups, is indicated [179]. How these are structured in detail remains unknown [176]. This circumstance is particularly critical, as the interphase is essential for the load transfer between fiber and matrix and can also be particularly strongly influenced by water absorption [170, 180] Consequently, the second working hypothesis for this chapter reads as follows:

The resilience of the F/M interphase during aging is of utmost importance for the durability of GFRP composites. Both static and fatigue properties will break down when the integrity is disturbed.

As outlined in the introduction, the damage tolerance of composites is of outstanding importance for both the static load capacity after a single damage event of whatever nature and the continuous damage increase during fatigue loading in operation. In most cases, the damage tolerance of composites is associated with the three main types of damage, namely: (i) inter- and intralaminar matrix cracking, (ii) interlaminar delamination of plies, and (iii) translaminar fiber failure (breaks) [181–183]. Referring to the results achieved in Chapter 3, at least the first two are matrix-related and, therefore, likely to be affected by environmental aging and the environmental temperature. However, as the interphase is similarly of polymeric nature and known to be potentially susceptible to hydrolysis, its impact on damage tolerance and fatigue performance should not be neglected. In order to investigate the aging-condition-dependent predominant mechanisms, finally, the third working hypothesis of this chapter is:

The damage tolerance of GFRP composites is significantly affected by the operating conditions and environmental aging, whereas the damage processes are likewise controlled by resin and interphase properties.

Following, state-of-the-art aging phenomena and temperature dependences, as well as prediction and accelerated aging methods for composites, are summarized with a focus on GFRP. Additionally, specific details for the aging and testing methodologies are given. Particular attention is paid to developing and introducing a new interphase aging method. Its application enables the isolated observation of interphase-dependent damage and clarifies many correlations for the first time. Finally, the experimental and modeling results and discussion are presented, and the main findings are concluded.

4.1 State of the Art

Since it is impossible to investigate the durability of composites' variants mentioned above with regard to their resistance to various environmental factors within the scope of a single study, this chapter is mainly limited to glass fiber-reinforced epoxies (GF/EP). Furthermore, the focus is on materials used for infusion processes. These are primarily uni- or multi-directional laminates based on fiber fabrics with typical grammages of between 300g/m² and 1200g/m², used in rotor blade, ship and marine, automotive and transportation, as well as construction applications. In contrast to significantly more homogeneous composites, such as prepreg-based laminates, these show a high local variation of the fiber volume fraction [184, 185] and additional ply-discontinuities like transverse backing fibers or connecting stitching yarns [186]. A schematic overview of the macro- and micro-structure of such a typical (quasi) UD composite is given in Figure 4.1.

Damage and Failure of Composites

Due to their inhomogeneous and anisotropic structure, damage and fracture are manifold in layered FRP composites. Typical, first evolve non-critical matrix cracks or fiber/matrix debonding in transverse or rotated layers as a consequence of high matrix stresses in densely fiber-packed areas [187]. In fabric-based composites, the first damage likely starts at transverse backing fiber bundles or stitching yarns [184, 185]. With increasing or repeated loading, these damages can grow and connect to large cracks spanning through a whole layer [187]. When the crack tips reach the layer interface, they might introduce the growth of delaminations between the plies and lead to local fiber failure of the load-carrying 0°-fibers. This kind of transverse-translaminar damage is often the most critical,

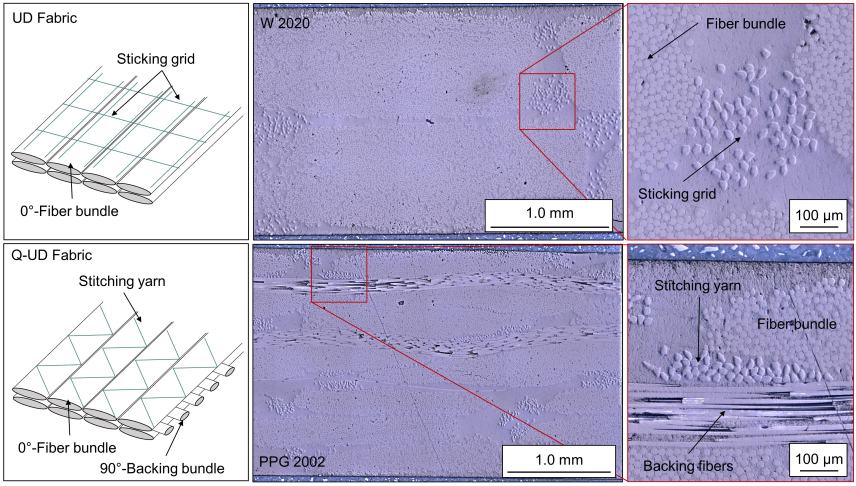

Figure 4.1: Schematic presentation of macro- and micro-structure of UD (top) and Q-UD (bottom) GFRP fabrics and composites. The micro-graphs show 2 mm thick examples of W 2020 (top) and PPG 2002 composites.

as it directly reduces the load-carrying capacity of the composite and introduces higher stresses on the surrounding fibers. The damage accumulation follows a typical pattern within the longitudinal fiber layers or in unidirectional composites. A progressive fiber/matrix debonding drives a stress peak in front of itself, starting from a fiber break. This stress field affects the nearest surrounding fibers and leads to further fiber breaks when overloading a weak point. The procedure is then repeated until a major cluster failure finally occurs [1, 188, 189]. This brief introduction already shows that it is now very plausible that environmental factors can have a strong but also diverse influence on the development and propagation of damage. While the ambient and aging temperature primarily affects matrix and interphase properties, water absorption-related aging can additionally affect fiber strength [190]. Therefore, temperature and water absorption change the tolerable loadings [30], the actual global and local stress states [13], and the constituent's thermo-mechanical properties [38, 106] simultaneously. Schematic representations of the damage types and their correlations to environmental factors are given in Figures 1.1 and 4.10.

Environmental Effects on Static Properties

Even though more than 60 years of academic and industrial research have focused on the environmental durability of composites [191, 192], this research topic is still active today. Due to ever-new materials and rising research opportunities, many questions remain unanswered or appear to be newly interpreted, although a large number of studies have already been carried out. Most authors have stated that moisture absorption negatively influences the mechanical properties of various FRPs. But there are also counterexamples [31, 131, 193].

Physical and chemical aging, such as matrix plasticization, hydrolysis effects, additional stresses due to swelling, interphase debonding, crack formation, and stress corrosion phenomena, can result from moisture diffusion into the composite [194, 195]. Their complexity and mutual interaction are often difficult to separate in detail, and overarching or phenomenological results are presented. However, realizing aging studies under severe environmental conditions is often difficult and usually not directly comparable. Tests are typically very time-consuming and thus expensive. In addition, no comprehensive standardization to address aging and environmental impacts is available or extensively used. As a result, numerous different test procedures have been released. Still, all of them are non-generic or unspecific as the variety of composites, and especially their temperature response, is too large [196]. The scope of the investigations ranges from studies lasting up to 10 years under outdoor conditions [193, 197, 198] to short-term experiments at almost boiling water conditions [199, 200]. Nevertheless, accelerated aging tests are most commonly used at temperatures below the polymers T_g and range from 30 °C to 70 °C [12, 18, 31, 54, 201, 202].

The interaction of water diffusion and the mechanical properties of composites is of particular interest. Although diffusion in composites is more complex than in homogeneous materials, numerous authors report that water uptake characteristics are often well described by the principle of Fickian diffusion [180, 203]. Others, in contrast, have reported strong deviations from Fick's laws, especially in long-term experiments and at elevated temperatures [133]. So far, a few studies have investigated the diffusion properties at different temperatures [133, 202] or carried out mechanical tests after variable conditioning periods [204]. Unfortunately, there is often no link between the two types of tests, or the test database is very small. A complete picture of dependencies is still missing.

For UD GFRP composites, it is evident that tensile strength is one of the main affected characteristics, with a large variance in presented results. Whereas some authors refer to a decrease in strength of about 5 % to 15 % [205–207], others found drastic reductions of up to 50 % [30, 204, 207]. However, a direct comparison of previous studies is challenging. For the studies mentioned above, for example, important differences have to be considered. In addition to the exact fiber–matrix combination, different specimen geometries and water aging temperatures have been used. As long as the extent of the influence of elevated conditioning temperatures on the results of a specific GFRP composite is not known, it is difficult to describe generally valid relationships across studies.

Besides the tensile strength, most other material properties are known to suffer at least due to wet aging at elevated temperatures. Only some studies are available investigating the effects on transverse [61] or compressive [208, 209], and more on interlaminar shear strength [18, 54]. Here, the latter is also frequently used to describe the impact of aging on the F/M interphase, as the failure often progresses extensively through the interphase area under various shear stress-driven methods, such as the short beam shear test according to ASTM D2344 [50]. Again, the aging temperature, medium, and duration seem to affect the measured impacts.

The effects of pure temperature changes during the test on the properties described above are susceptible to the load case. Under tensile loading, when the glass fibers bear the most load, strength reductions are as low as 0 % [210] to 6 % [211, 212] at temperatures of up to 95 % of the matrix T_g [212]. Even at temperatures of up to 200 °C, which clearly exceeds the T_g of most thermosets, the residual tensile strength can be up to 65 % compared to room temperature. In contrast, the compressive strength is highly dependent on the supporting function of the matrix against fiber buckling. Here e.g., Drummer et al. [213] reported that the residual compressive strength of a woven cross-ply GFRP decreased first moderately ($\leq$ 10 %) up to 50 °C and then more rapidly. The residual compressive strength at 90 °C, which is about 20 °C below the T_g, was only 19 % of the pristine strength. Similarly, the composite's shear properties decrease with rising temperatures. Here, the strength reductions typically follow a linear trend [214] in accordance with the resin's properties. However, as the resin shear strength is usually lower than the tensile or compressive strength, total strength loss occurs before the T_g is reached. Furthermore, damage modes changed from interlaminar matrix failure at room temperature toward intralam-

inar interphase failure was reported [54]. These observations indicate that the F/M interphase is even more susceptible to increasing temperatures than the matrix polymers. In turn, it appears likely that the interphase T_g^i is significantly lower than the matrix or composite T_g.

The last group of important composite properties, which are affected by aging and temperature changes, are the damage and fracture-related parameters, such as fracture toughness and corresponding energy release rates (ERRs). However, fewer studies have been published regarding the effects of temperature-, water- or chemical-based aging on these properties. In addition, the investigations carried out show contradictory results and findings. There are examples for almost every dependency, whether increasing or decreasing fracture toughness in mode I or II with temperature elevation or water absorption [215–220]. The reasons for this can be both the dependence on several possibly opposing factors, such as the strength and ductility of the matrix [221–223], and the additional influence of the composite layup, layer thickness, fiber volume fractions, or fiber distributions [224]. Therefore, today there is still a discussion if fracture toughness is a "real" material parameter. Nevertheless, it is unquestioned that the principle of damage analysis regarding energy release rates and fracture progress is meaningful. Consequently, there is a demand to improve further and deepen the understanding of the affecting factors.

Environmental Effects on Fatigue Properties

Besides their quasi-static resilience, knowledge of the long-term performance of FRPs is indispensable, as efficient and sustainable use requires a trouble-free service life over decades. Particularly in the maritime, offshore, and construction sectors, durability under severe humid or wet environmental conditions is very important, as GFRPs suffer under harsh conditions [28, 31, 54, 225–227]. In this context, the fatigue tests themselves and the additional effort dedicated to aging require considerable time.

As a result, several past studies have been conducted on fatigue behavior under wet environmental conditions [31, 54, 208, 228, 229]. However, compared to other fields, the available database for environmental fatigue is still not particularly large. Furthermore, some of the published results on environmental fatigue show contradictory results. While some authors found substantial lifetime decreases [54, 225, 228], others could hardly find any influence [193], and still others saw

more load-level and aging-condition-dependent behavior [31, 208]. Of course, in addition to the material-specific differences, there are also layup-related variations. Hence, it is difficult to clearly assign the reasons for the potential lifetime reduction since the classical aging of composites in a water bath affects all constituents simultaneously.

Glass Fiber, Sizing, and Interphase Degradation

Glass fibers are susceptible to hydrolytic attacks, leading to slow degradation by the leaching of surface ions [230, 231]. As intrinsic flaws are exposed and enlarged, the resulting fiber strength decreases with time [115, 232]. However, the extent to which the fibers are protected from the water by the matrix and the interphase region within a composite is frequently discussed. The consensus in this context is that the integrity of the fiber/matrix interphase will mainly contribute to sufficient protection. Due to its microscale size, investigating aging effects on the fiber/matrix interphase is challenging. With atomic force microscopy investigations, it was revealed that the interphase properties are severely reduced by water absorption, with the weakened region significantly increasing in size [170, 233].

Most commercial glass fiber sizings consist mainly of reactive organofunctional silanes as coupling agents and matrix resin-compatible film formers [178, 230]. Additionally, sizing often contains antistatic agents, lubricating agents, and surfactants, which makes them a highly complex and difficult component to explore [178]. Since most of these ingredients are reactive, they are subject to natural aging, resulting in declining sizing functionality over time [234]. However, as the exact composition of the sizings is usually not known, there exists little knowledge about the aging behavior of sizing. Most laboratory studies have tried to reduce the number of sizing ingredients to mainly silanes and film formers to reduce the complexity [235–237].

For the composite industry and academia, the degradation stability of fiber sizings is particularly important, as it has to be known within which time frame fibers can be further processed into composites without drastic performance reductions. From a chemical point of view, several mechanisms are involved in the aging of sizing and composite interphases. First, the hydrolysis reactions of the organofunctional silanes in the fiber/sizing interphase under the impact of moisture and heat are expected to reduce the interfacial adhesion

since the condensation reaction of the Si-O-Si bonds is reversible [179]. Here, water molecules adsorb to the surface, diffuse into the sizing, and incrementally resolve the fiber/sizing bonding [177, 234]. Of course, this is especially true for non-processed fibers, where moisture can more easily reach the fiber/sizing interface. Nevertheless, these chemical bondings are theoretically still susceptible to degradation even in the fiber/matrix interphase formed. They could represent a link between classical aging in the composite and sizing aging. Furthermore, hydrolysis of chemical functions, either in silanes or polymeric film formers, occurs in the presence of moisture and is accelerated with heat [179, 237]. Although it is not clear to what extent the film formers will be integrated by chemical bonding into the matrix [178], it was found by FTIR investigations that the reactivity of, e.g., epoxy functions decreases during storage and aging [179, 238]. The reduced reactivity of the sizing also causes a significant reduction in fiber/matrix adhesion in the subsequently manufactured composites. However, besides these frequently referred processes, a number of unknown ingredients, such as lubricants, are part of commercial sizings. The complex interplay between the components responsible for adhesion and those required for process technology certainly also affects the resistance and long-term durability of the sizings, e.g., by changing the morphology, accessibility, or pH value of the interphase. Therefore, a standardized methodology for durability comparison is needed.

The fundamental studies and findings about the aging of fiber sizings by Plonka et al. [237] and especially Peters [179] or for fibers by Brown et al. [230] were used as a starting point for developing and extending a tailored fiber sizing aging methodology. Although the idea of aging fibers and sizings is not entirely new, the implementation and analysis of the effects on the static and fatigue properties of the resulting composites are not yet reported. A novel fiber pre-aging procedure [32, 36] has been developed and investigated to compare the sizing and interphase durability of GFRPs and to complement and improve the testing and prediction opportunities. The main advantage of this novel fiber-aging-based methodology is the possibility of directly aging individual composite constituents. For this purpose, the fibers are stored for several weeks under high humidity and temperature and subsequently infused with resin. Therefore, aging becomes independent of diffusion processes, resulting in considerable time savings compared to conventional methods. Within the framework of this thesis, the new methodology is developed, evaluated, and applied to quasi-static, fatigue, and fracture-related loading situations. Furthermore, it is extended to

wet fiber pre-aging in a water bath to additionally characterize the impact of fiber degradation.

Modeling and Prediction Approaches

Similarly to what was described and applied for the epoxy resin aging in Chapter 3, various composite property and lifetime prediction models have been developed over the past decades [74]. Considering environmental effects, many of them rely on Arrhenius-based approaches, correlating time and temperature as convertible parameters [67, 239, 240]. However, often, these are based on accelerated aging tests and only very few data points. For modeling the fatigue life of UD composites, recent publications demonstrated that the interphase properties are essential for long-term durability. In detail, micromechanical models recently evolved by Sörensen et al. [1, 189], Castro et al. [241], Swolfs et al. [242], and Fazlali et al. [243] all describe the damage growth process in UD composites under fatigue loading with a specific focus on the fiber/matrix interphase. Thus, the results presented below and the newly developed test methodology are aimed to provide an opportunity to verify the micromechanical models experimentally. Furthermore, by employing this methodology in the industry, fast and straightforward comparisons of sizing and fiber durability can be achieved to estimate maritime use capabilities.

4.2 Materials, Methods and Experimental Setup

This study used seven different fiber inputs (different non-crimp fabrics (NCFs)) to examine the effects of environmental aging on different fiber types. To reveal the fiber's durability, the fibers' long-term behavior in contact with high humidity or water was examined using fiber bundle tests and single fiber fragmentation (SFF) tests. For fatigue testing, the pre-aging approach provides a novel possibility to highlight the individual impacts of decreased interphase, fiber and interphase, or matrix properties on the lifetime behavior.

4.2.1 Design of Experiments and Theoretical Background

As introduced, the typical procedures to evaluate the composite's durability are based on storing the material in hot/wet conditions or when wholly immersed in water. Unfortunately, the results must always be considered in the context of

the actual, real operating environment. Because water acts simultaneously on all composite constituents, whether the respective degradation processes occur at the same rate and duration is often unclear. Consequently, it is difficult to attribute the changes in mechanical properties to the specific influence of fiber, matrix, and interphase. Therefore, to increase the understanding of the specific proportions of aging-related degradation, comprehensive studies with various kinds of aging conditions were performed in the framework of this thesis. In detail, these include mechanical tests (static, fatigue, fracture, and impact) after classical water bath or climate chamber aging at elevated temperatures of 50 °C, after aging at temperatures between 8 °C and 50 °C, and after pre-aging of the fibers using the newly developed methodology. Furthermore, one-sided aging without direct water contact at cutting surfaces was investigated in order to exclude additional effects due to direct fiber/interphase-water contact.

A pre-aging method was designed that allows the targeted aging of only the individual constituents of the composite by aging the NCFs before composite manufacturing to address some of the challenges described. This makes it possible to investigate the aging behavior of fabrics during transport and storage up to production and to measure the effects of selectively aged constituents on the composite properties. In particular, the aim here is to estimate the impacts of aged fiber sizings and fiber-matrix interphases on composites' mechanical properties and fatigue life. The studies of Peters [179], and more recently, of Cech et al. [234] suggest that the aging of sizings under conventional environmental conditions is a serious process, whose rate depends directly on the sizing formulation. For 11-year aging under production hall conditions, the sizing aging effects reduced the composites' interfacial strength during the first 40 months [234]. Afterward, no further reductions were found during the following seven years. Furthermore, considering the results of Peters [179] and Gibhardt [32], it seems likely that there is a lower limit of remaining fiber/matrix bonding capability for each sizing. Questions surrounding the rate of the aging progress and whether this is a linear process in time cannot be answered directly based on the results published to date.

For the development of a defined fiber and sizing pre-aging methodology, it is assumed that the accelerating effect of the temperature follows an Arrhenius relationship since most chemical reactions, diffusion and aging follow this principle [36, 54]. However, it is more difficult to estimate the accelerating effect of increased humidity since its presence in the natural aging process is an essential

requirement that is not always equally prevalent. Studies conducted by LeGuen Geffroy et al. [38] on the physical aging of epoxy resins show a dramatic acceleration (factor of ten) of aging processes by the presence of water in this context. Based on the previous assumptions and aiming not to generate physical or chemical effects that would not occur under normal conditions during natural aging of up to 40 months, the aging process was carried out at 50 °C and 80 % RH initially for one, five, and ten weeks. It was found that the aging process seemed to be mainly completed within five to ten weeks under these conditions. This corresponds to an accelerating factor of about 16–32 and seems reasonable regarding the Arrhenius principle for a temperature increase of about 30 °C under significantly increased humidity. Additionally, fabric pre-aging is implemented in two ways: allowing the fiber sizing to age only or the sizing and the fiber simultaneously. The developed aging methodology is schematically shown in Figure 4.2. Following the time-dependent pre-tests, the fabrics are stored either at 50 °C and 80 % RH for five weeks or in a water bath at 50 °C for the same period in the case of all main investigations. As both pre-aging processes are applied before resin infusion, they do not affect the composite matrix. Thus, the effects of matrix aging can be excluded from later test results.

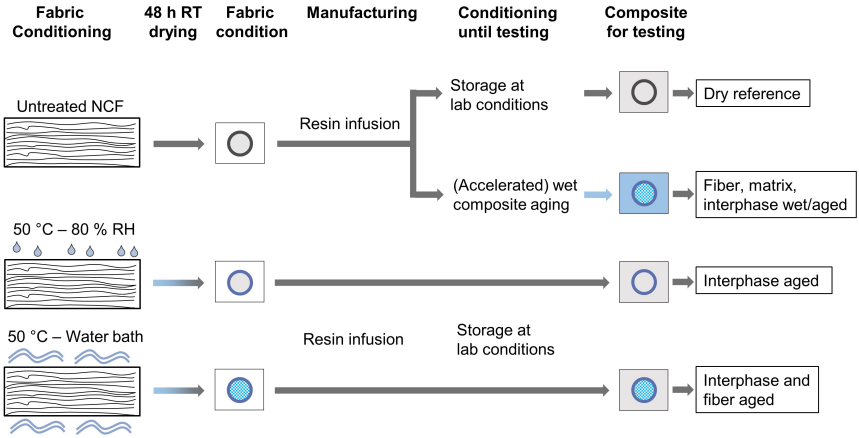

Figure 4.2: Schematic presentation of classical composite aging and the new pre-aging methodology.

Fiber bundle and longitudinal tensile tests on composites have been examined to clarify how both pre-agings affect fiber strength and fiber-dominated properties. There was no statistically meaningful effect on the bundle and, therefore, fiber strength after humid pre-aging for five weeks. The variations were $\leq 5\,\%$ com-

pared with the reference values for the five fiber types investigated during this pre-study. In contrast, previous water bath aging of the fibers substantially reduced the fiber strength (see Chapter 4.3.3) and, correspondingly, the composite tensile strength of up to 20 %. The development of the interphase strength was mainly investigated by means of transverse tensile tests. In addition, ILSS tests for shear loading and SFF tests were performed to investigate the effects of aging on a micromechanical scale. Impacts on the lifetime of the composite materials were analyzed using tension-tension fatigue tests. Finally, DCB and ENF tests were carried out to analyze the variation of the fracture behavior in terms of the composites ERRs in modes I and II. As an application-oriented case, the influence of ambient temperature and water bath aging on the impact behavior of multidirectional laminates was likewise investigated. For comparison, almost all composites were also conventionally aged in a water bath at 50 °C.

4.2.2 Fatigue Specimen Designs

As rectangular specimens, according to DIN EN ISO 527-5 standard, regularly fail inside the gripping region or by longitudinal splitting, a dogbone-shaped design was implemented for fatigue testing of UD composite specimens. The development of the exact sample geometry was initially based on dogbone variations from previous studies [244, 245]. In contrast to these studies, a limitation was established that a total sample length of 250 mm should not be exceeded.

Finite element analysis (FEA) was used to achieve a structured improvement of the specimen geometry. In detail, the width of the specimen in the free (parallel) length W_p and at the edges W_e, as well as the length of the parallel section L_p, were systematically varied. The scheme of the variations and the parameters of the final geometry are shown in Figure 4.3. The material model Composite Damage (CompDam) Progressive Damage Analysis Software of the NASA Langley Research Center Hampton, VA, USA, was used for analysis [246]. This code is a material model of fracture mechanics in the field of continuum damage mechanics (CDM) and is intended for use with the Abaqus FEA program from Dassault Systems. The software describes the damage mechanisms in the composite by means of an FE model in which each layer is represented. Matrix crack kinematics are represented according to the deformation gradient decomposition approach [247]. Conventional strain softening in the CDM describes the fiber damage due to tensile stress. Specimens are simulated in Abaqus FEA as a

quasi-static tensile test with an explicit solver. Here, the specimen is fixed on one side and loaded on a reference point on the other side. The mesh consists of 1 mm C3D8R elements starting from the clamping and oriented along the radius. The simulation is based on the models developed in the work of Körbelin et al. [146]. All parameters required for the GFRP material are selected based on the results of own tests or comparable studies [214, 244]. The failure index matrix (FIM) is analyzed to evaluate the FE analysis because splitting cracks initiate the final failure in the UD laminate. An FIM value of $\geq$1 displays a matrix crack that has fully formed. To evaluate geometries, all specimens were simulated at a nominal stress of 437.5 MPa (0.5 UTS) in the free (parallel) test length, and the FIM value was compared in the critical edge region. Based on the simulation results, three geometries were selected for fatigue testing based on UD composites with SE 1500 fibers. The best-performing shape in terms of lowest longitudinal splitting, no splitting from the edges, and the highest fatigue life was then chosen for the main investigations. At the selected comparative load level, the desired geometry endured an average of 230.000 load cycles, about 12.5 times more than the rectangular benchmark geometry. The corresponding fatigue results are shown in Figure 4.4.

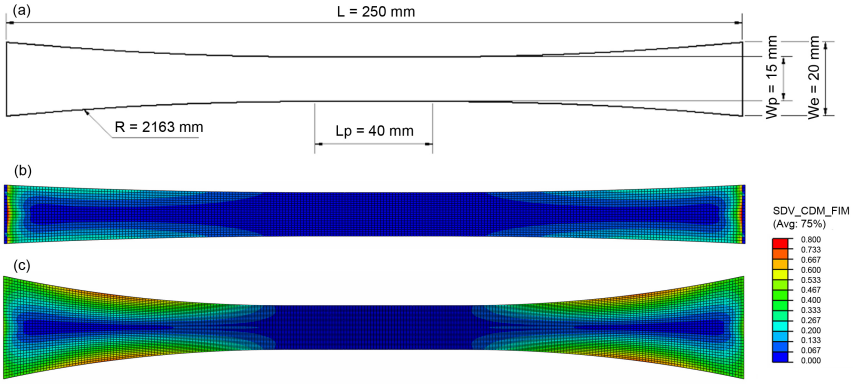

Figure 4.3: Schematic presentation of the final dogbone geometry (**a**). W_e, W_p and L_p were varied during the FEA investigation, as shown in (**b**,**c**).

4.3 Results and Discussion

In this section, the results of the introduced experimental GFRP aging campaigns are presented, discussed, and partly modeled following a reasonable order.

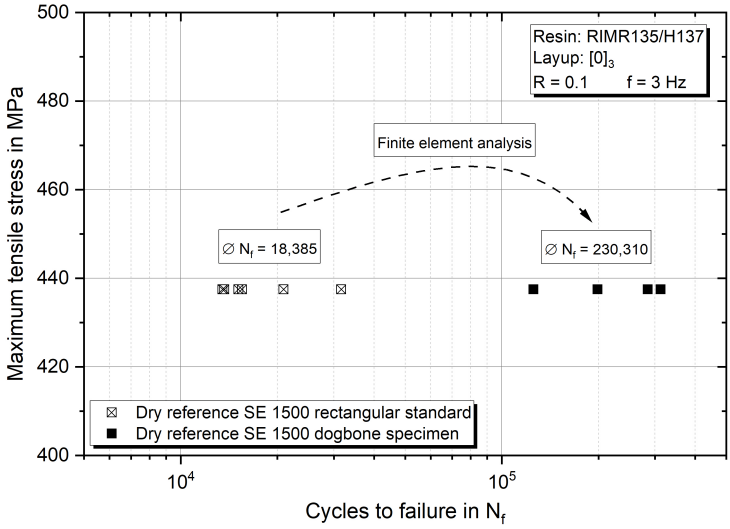

Figure 4.4: Results of the fatigue test of the geometry of the developed dogbone specimen compared to standard rectangular specimens at a maximum load level of 437.5 MPa.

First, initial GFRP properties and the consequences of fiber and matrix choice are presented for mainly unidirectional laminates. Subsequently, effects of wet-aging under initially typical accelerated aging conditions (immersion in 50 °C water baths) and later on also with divergent aging temperatures are analyzed for quasi-static, interlaminar, and fatigue properties. To better understand the phenomena occurring in the composite, specific analyses of the effects on the constituents, particularly the fibers and fiber sizings, are given next. For this purpose, the new fiber pre-aging method is applied. Finally, the results obtained are extended to multidirectional laminates and application-relevant cases, such as one-sided diffusion and the impact or damage behavior.

4.3.1 Initial GFRP Characterizations

Temperature, humidity, and water-related aging phenomena are highly dependent on the specific composition of fibers, sizings, matrix resins, and the resulting fiber-matrix interphases. Therefore, the investigations performed for this thesis include several different GFRP composites based on seven fiber types and four epoxy resins. However, similarly to the epoxy chapter, the central part of the

investigations is based on composites made from RIMR135/H137 resin. Furthermore, the fiber input includes standard E-glass (PPG and NEG 2002, R&G 600), corrosion-resistant E-CR glass (SE 1500, SE 2020, ER 469L), and high-strength R-glass (W2020). For laminate fabrication, NCFs were used. These usually contain a specific amount of backing fibers in the transverse direction to improve the shape stability and infusibility [248]. From a mechanical point of view, the transverse fibers are relatively detrimental as they might lead to fiber waviness of the 0°-plies, limit the 0°-fiber volume fraction, and act as crack initiators [184]. Consequently, the amount of backing fibers should always be considered for analysis. Representative tensile stress-strain curves of all RIMR135/H137-based UD-composites are shown for in-(left) and transverse (right) fiber direction in Figure 4.5. Here, the specific fiber volume fractions in fiber direction are explicitly given. In fiber direction, particularly noteworthy are the comparatively lower absolute strength deviations (850 to 940 MPa) and the clearly varying failure strains (2.0 to 3.0 %) and stiffnesses (33.7 to 47.2 GPa), which are a result of the different 0°-volume fractions, fiber moduli, and the NCF architectures.

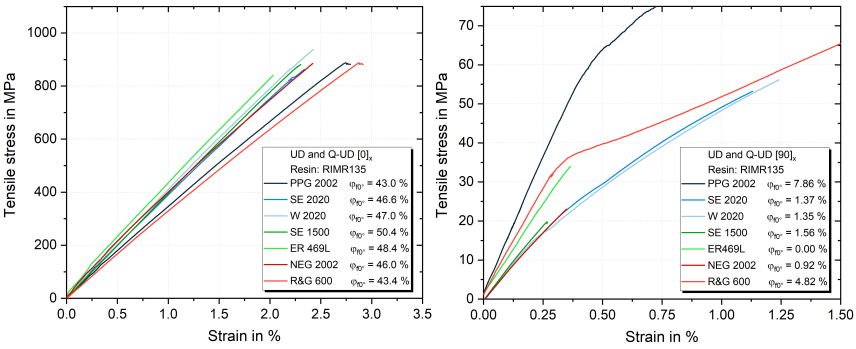

Figure 4.5: Representative tensile stress-strain diagrams of all UD and Q-UD composites based on RIMR135 resin. Absolute data in the fiber direction (left) and transverse direction (right) are shown with given 0° fiber volume fractions.

In the case of the transverse tensile tests, the effect of the backing fibers, which are in the loading direction, is clearly visible, as an increasing amount enhances the apparent strength and stiffness. However, for composites with low backing fiber content, the stress-strain curves are slightly non-linear until failure (which is most probably an effect of the mechanical wedge grips and the strain measurement via traverse movement). The first transverse crack always initiates the final failure. Here, the load carried by the backing fibers is negligible, and the

transverse strength is taken directly from the mechanical tests. This was verified by testing pure UD laminates of the SE 2020 composite without any backing fibers as a comparison. A clear knee is visible in the stress-strain response with high backing fiber content. Several transverse cracks evolve during this stage, but the specimens are still intact as the backing fibers carry a significant load. After a crack saturation is reached, the stress-strain response is linear until failure and reflects the loading of the backing fibers. For these cases, the transverse strength is micromechanically calculated based on the fiber proportions and the stress distribution between the different orientations. In this way, a reduction factor can be calculated for each backing fiber portion. Consequently, the apparent stress at the beginning of the knee is taken and reduced by the specific factor k_{tt} (0.76 for R&G 600 and 0.74 for PPG 2002). An overview of all longitudinal and transverse tensile strengths is given in Figure 4.6.

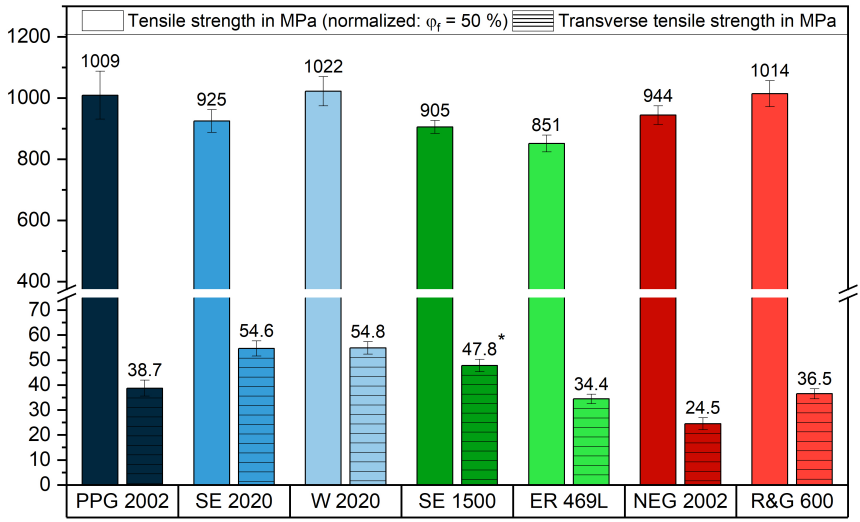

Figure 4.6: Quasi-static absolute longitudinal and transverse tensile strength of RIMR135/H137 UD GFRP composites with different NCF input (initial dry reference condition). *: Value according to [61].

The strengths of the laminates in the fiber direction range from 851 MPa to 1022 MPa, whereas the highest laminate strength was reached by the W 2020 composite containing high-quality R-glass fibers. The difference between the lowest and highest strength is about 17 % and thus relatively large. The reasons can be due to different fiber and interphase strengths and due to the NCF structures.

High strength in the direction of the fibers requires effective load transfer and the lowest possible influence of binder and backing fibers. Even more significant are the differences in the transverse tensile strengths. Here, the highest strength of the W 2020 composite (54.8 MPa) is about 2.2 times higher than the lowest strength of the NEG 2002 composite (24.5 MPa). Because the transverse tensile strength of UD composites is regularly taken as an indicator of the interphase quality, it is directly influenced by the fiber sizing and its interaction with the polymeric matrix. A low transverse tensile strength is critical for the initiation of damage and progress in composite structures, as it directly contributes to the lifetime. Therefore, a high transverse tensile strength is typically required as a quality characteristic and should be regularly verified as part of an incoming material inspection.

Since the transverse tensile strength depends on the fiber/matrix bonding and the matrix properties, this factor was investigated separately. Figure 4.7 presents the transverse tensile strengths of nine composites (three resins and three fiber types). The three epoxy resins are relatively similar (all based on amine hardeners, see Chapter 2.1) and used as matrix material in rotor blade manufacturing. While the differences caused by the matrix resins for systems SE 2020 and W 2020 are considerable, up to 13 %, the R&G composites are even more sensitive to the matrix choice. The resin-dependent strength variation was up to 15.8 MPa (38 %) in this case. The LY1568 matrix system generally resulted in the lowest strength throughout all the tests. Thus, the resin choice may significantly influence the fiber/matrix bonding and the resulting mechanical properties, even if the sizings and resin types are fundamentally matched.

As a consequence of the mechanical properties, the availability of high-quality NCFs, the wide application in rotor blade manufacturing, the promising corrosion resistance, and the easy manufacturing, the unidirectional SE 2020 composite based on the RIMR135/RIMH137 epoxy resin serves as the overall GFRP reference for this thesis. Therefore, the system has been fully characterized by static and fatigue tests. The resulting properties are summarized in the radar chart in Figure 4.8. However, due to the origin story of the investigations, the fiber type comparisons, and the high grammage of the fabrics, not all experiments could be performed with the SE 2020 composites. The effects of temperature and aging phenomena are investigated for most of the introduced composites to determine the impact of the specific GFRP composite choice.

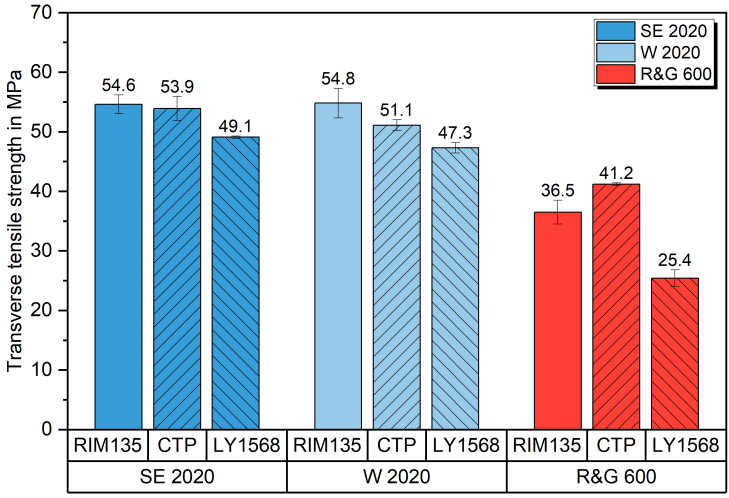

Figure 4.7: Effect of matrix resin on transverse tensile strength for UD composites with different fibers (initial dry reference condition).

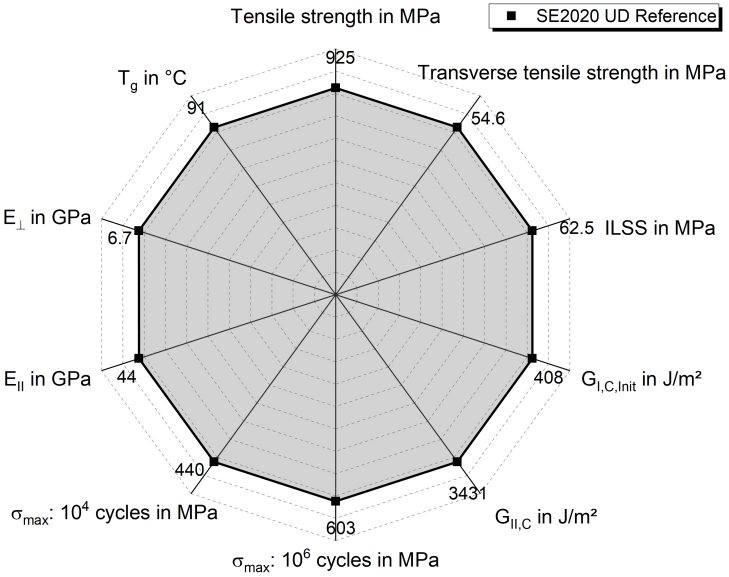

Figure 4.8: Overview of mechanical properties for reference GFRP system SE2020/RIM135 in initial dry conditions.

4.3.2 Accelerated Aging of UD-Composites

In the following section, the effects of long- and short-term wet aging, as well as of the aging and testing temperature, are investigated in detail.

Effects on Quasi-Static Properties

Following the most popular approaches for environmental or wet-aging of composites [54, 249], specimens were immersed in a regularly renewed distilled water bath at 50 °C for up to 3.25 years. The aging temperature is 40 °C lower than the dry T_g and about 15 °C lower than the wet T_g of the RIM epoxy matrix (see Chapter 3.3.9). Figure 4.9 presents the development of the tensile strength and water absorption (in terms of matrix fraction weight gain) over time for the PPG 2002, R&G 600, and SE 2020 composites. Additionally, the pure epoxy water saturation level is plotted for comparison. It is clearly visible that the tensile strength decreases at the same time as water is absorbed into the material until apparent and theoretical saturation is reached (about $25\sqrt{h}/mm$, which equals to ca. 1, 3, and 9 months for these specimens). At this point, the tensile strengths are already dramatically reduced by 49.2 %, 49.6 %, and 42.8 %, respectively. The slightly slower degradation of the SE 2020 composite can be explained by the fact that the ECR-glass is, on the one hand, more corrosion resistant than standard E-glass and, on the other hand, the aged laminate was remarkably thicker and thus had a lower surface to volume ratio, slowing down the aging effects. Remarkably, for the PPG 2002 composite, the tensile strength decreases by only another 4.0 % during the following 1.5 years, while the measured water absorption still increases by about 25 %.

This behavior indicates the following: (i) the further water absorption cannot be related to the matrix absorption. It takes place in the fiber/matrix interface and within evolving damages. Therefore, the weight increases step-wise in relation to the opening of interphase flaws, cracks, and delaminations. This is also in line with what was described in recent aging studies [69, 115]. And (ii) the most critical aging processes co-occur with the first water absorption until apparent saturation is reached. Therefore, it can be assumed that the interphase properties and the fiber strength will degrade significantly upon first contact with warm water. Contrary to what is assumed [250], the matrix thus hardly protects the fibers from moisture-induced damage in the present case of complete immersion. The long-term aging subsequently to saturation only has a marginal influence

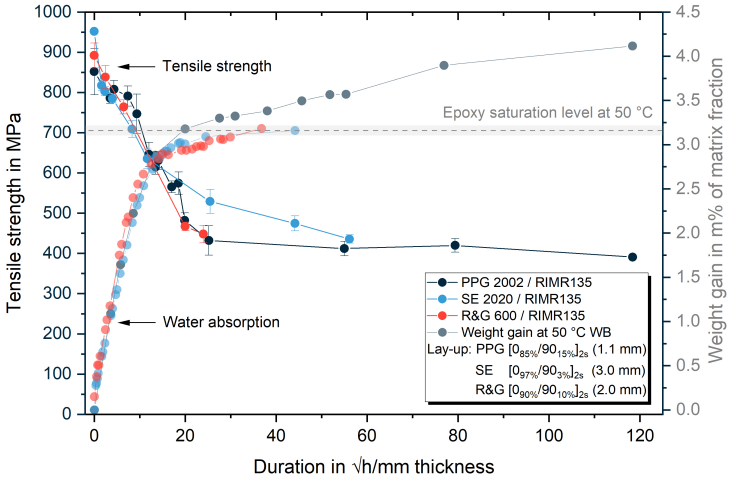

Figure 4.9: Development of tensile strength of several Q-UD composites during aging in a water bath at 50 °C (intense) and simultaneous water absorption related to the matrix fractions (pale).

on the strength because the fiber degradation is expected to undergo two stages of degradation: a fast non-steady and a slow and steady dissolution [76].

For high aging temperatures as 50 °C, the first dissolution stage takes place simultaneously with the absorption process and significantly decreases the fiber strength by the growth of flaws and surface cracks [76, 251]. Furthermore, a regular visual inspection uncovered the formation of small opaque regions within the specimens even before saturation was reached. These phenomena were found for almost all composites after immersed aging at 50 °C. However, the timing and extent of occurrence vary significantly. The standard E-glass composites are most affected (PPG 2002, NEG 2002, and R&G 600), followed by the ECR-glass composites (whereby the SE 2020 showed far less and later occurrence than the SE 1500) and the R-glass composite W 2020. Gagani et al. [54] and Rocha et al. [18] also described similar types of aging-related damages after immersion of GFRP samples in 60 °C water. Using optical microscopy, it was possible to correlate the opaqueness with the formation of fiber/matrix debondings around fiber bundles and cracks within these bundles. The amount of these defects increased further with time, whereby the distance between them decreased simultaneously. Microscopic images of a wet-aged and polished composite cross-section are representatively shown for the R&G 600 composite in Figure 4.10. Fiber/matrix

debondings, which evolve into large inter-fiber cracks, can be found in each layer all through the thickness. These cracks are typically either around or directly within a fiber bundle, as the swelling-related stresses are highest in the closely packed regions. Additionally, larger, partly opened delaminations can be found, which are the reasons for the opaqueness in places. Wherever this extensive damage occurs, the fibers appear to be affected, and fiber degradation and decomposition can be clearly seen. Nevertheless, it turned out that the strength decreased significantly even without or before the debonding formation.

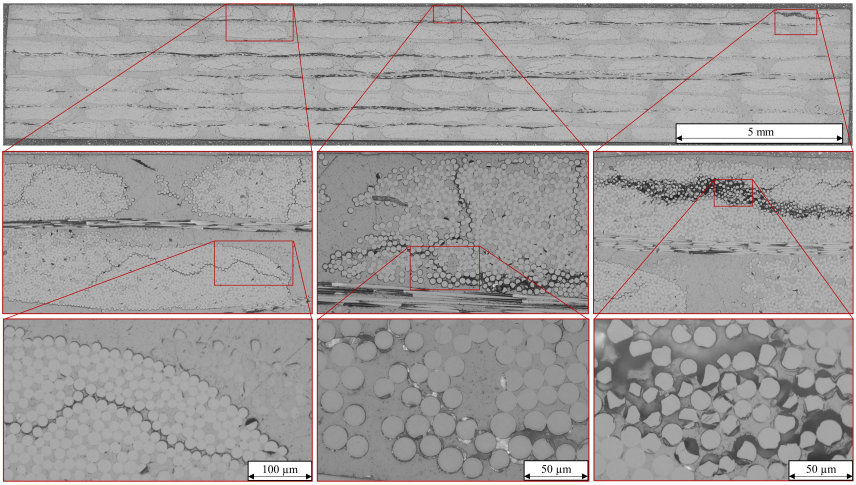

Figure 4.10: Microscopy images of damages (cracks and delaminations) evolving during aging at 50 °C by example of the R&G 600 composite. The images were made after 300 days of immersion without mechanical loading.

Similar to the longitudinal strengths, the transverse tensile strength evolutions were investigated for several composites. The results are presented in Figure 4.11. Even though accelerated aging at 50 °C results in severe transverse strength and, therefore, interphase strength reductions, huge differences arise between the different composites. In contrast to the NEG 2002 and ER 469L composites, which almost completely lose their integrity even before saturation, the SE 2020 and W 2020 composites have a continuously high residual interphase strength of about 46 MPa (−15.8 %) and 40 MPa (−27.0 %), respectively. The significant differences revealed are interpreted as a direct effect of the fiber sizings and resulting interphases, as the impact on the epoxy was always the same, and the fiber strength has a negligible effect on the transverse strength. Both

systems with the so-advertised marine suitable sizing 2020 from 3B show indeed a superior behavior.

Nevertheless, the interphase strength is expected to decrease further over time, as the aging-related damages described before were also found for the 2020 composites. As soon as fiber/matrix debonding and cracks occur, the transverse strength will decrease as well. This can already be seen partly in the extended tests of the W 2020 system. In summary, the complex combination of the matrix polymer and various sizing components appears to be significantly more susceptible to water-induced weakening than the neat epoxy itself (wet epoxy strength $\geq 46\,\mathrm{MPa}$ under all aging conditions). The main reason for this could be an increased water affinity of polar components in the interphase and possible hydrolysis reactions of the silanes at high temperatures, as highlighted by Thomason et al. [177].

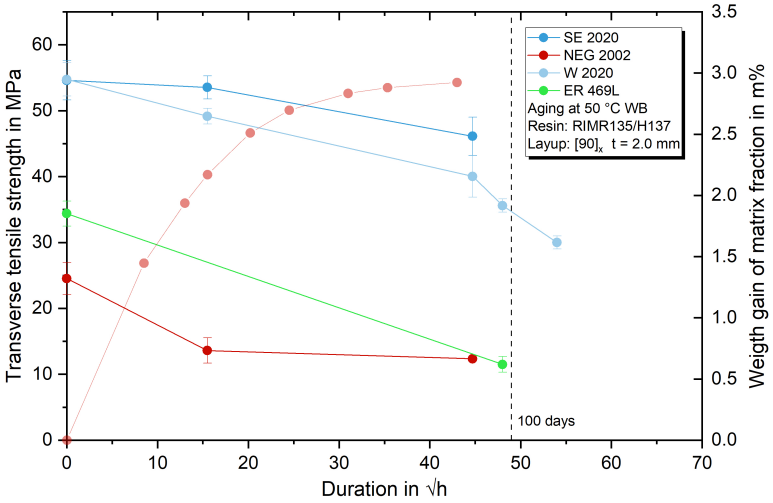

Figure 4.11: Transverse tensile strength of UD GFRP composites with different NCF input during accelerated aging in 50 °C water until saturation. Water absorption of the NEG 2002 system is exemplarily shown in a transparent shade for comparison.

The classic aging of UD GFRP composites in 50 °C water reveals substantial variations in the durability of the leading mechanical properties depending on the fiber input, as shown in Figure 4.12. The wet-aged composites are compared when apparent saturation is reached. Here, the reductions in 0°-composite

tensile strengths range from 22 % (W 2020) to 50 % (PPG 2002) and cover approximately the entire range previously reported in other studies of accelerated aging with GF/EP composites [28, 31, 202, 252]. In contrast to the literature comparison, the matrix resin system is always the same in the present case. Therefore, the differences in durability can be mainly attributed to the fibers and the fiber/matrix interphases. Given that the fibers largely determine the 0°-strength, it can be assumed that these have a correspondingly high contribution to the overall reduction. The fiber effect can also be proven, as the wet-strengths follow an explicit ordering. The R-glass composite is by far the most durable, followed by the ECR-glass composites, which are slightly more resistant than the standard E-glass composites. With residual strengths (normalized to 50 % 0°-fiber fraction) of around 500 MPa, hydrothermal aging enormously weakens the latter. As a decreased interphase strength is more associated with earlier and accelerated damage progression and reduced load transfer, the differences in the transverse strength can be attributed to the durability of the interphase and the sizings used. Here, most of the composites (except SE 2020 and W 2020) show severe degradation and insufficient residual strength. With reductions of up to almost 80 %, use in marine or offshore applications is not recommendable based on the accelerated aging tests.

Similar to the strength reductions, proportional reductions of the failure strains of the composites can be found, as the stress-strain behavior remains basically unchanged during aging. In this context, it can be stated that the Young's modulus is not or only barely affected by aging. The highest modulus reduction found during the aging of two years was about 4.0 % in the case of the PPG 2002 composite. However, this result is statistically insignificant due to comparatively large standard deviations for the modulus (COV: 5.3 %).

Effects on Fatigue Properties

In addition to the static results presented, fatigue testing was performed on specimens in dry conditions and after accelerated aging (here only 50 °C WB). All fatigue tests on UD composites were performed with dogbone-shaped specimens, according to Chapter 4.2.2. A comparison of the dry reference fatigue results for the SE 1500-based composite with important data from the literature is given in Figure 4.13. All data shown are based on composites made of RIMR135/H137 resin and different types of NCFs with comparably low backing fiber content. Analyzing the selected data allows to make some highly relevant findings: The

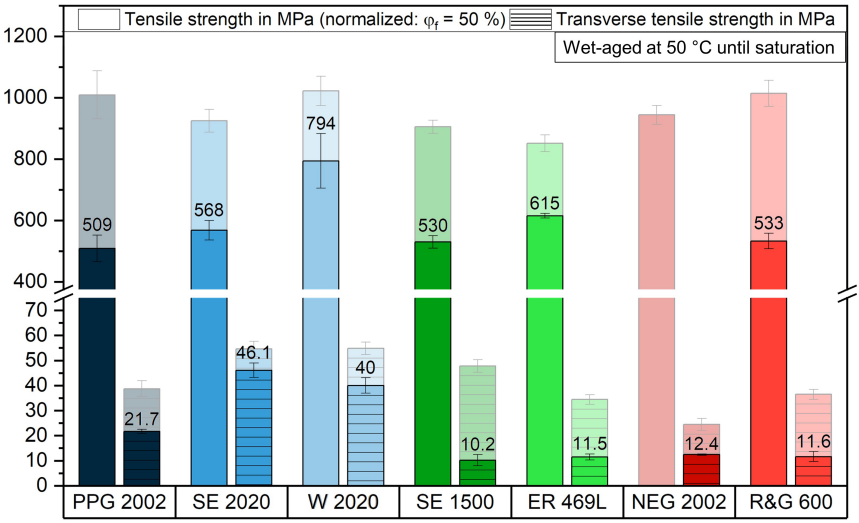

Figure 4.12: Quasi-static absolute longitudinal and transverse tensile strength of UD GFRP composites with different NCF input after accelerated aging of the composites in 50 °C water until saturation (ca. $25\sqrt{h}/mm$). Dry reference values are shown in a transparent shade for comparison.

comparison with the fatigue data given in [253] for the same combination of SE 1500 fibers and the RIM epoxy reveals a significantly better fatigue strength for the specimens tested within this work. While the slope of the Wöhler curves is about the same, the average lifetime is approximately 50 times higher for all load levels. This corresponds to a lifetime increase of about 1.5 decades or an acceptable load increase of about 170 MPa for the same lifetime. Regarding the results presented in Figure 4.4 for rectangular specimens, it becomes clear that the difference cannot only be related to the optimized geometry (impact of geometry ca. factor 12.5). Therefore, other effects, such as the lower fiber volume content (this work 49 % vs. 62 %) and the different NCF structure (stitching, backing fibers), also have a significant impact.

Overall, the results obtained can be classified in the upper range of the literature values, also exceeding the results for composites made of the same fibers with higher quality sizing (SE 2020) or high-strength fibers (W 2020) [204, 253–255]. Consequently, comparisons with fatigue data from literature or different testing situations should always be considered cautiously, as the damage mechanisms, progress, and geometry effects can severely change the results obtained. For

design purposes, especially the impact of the specimen geometry (damage and failure progress) and the fiber volume content have to be considered in order to neither overestimate nor clearly underestimate the allowable loads.

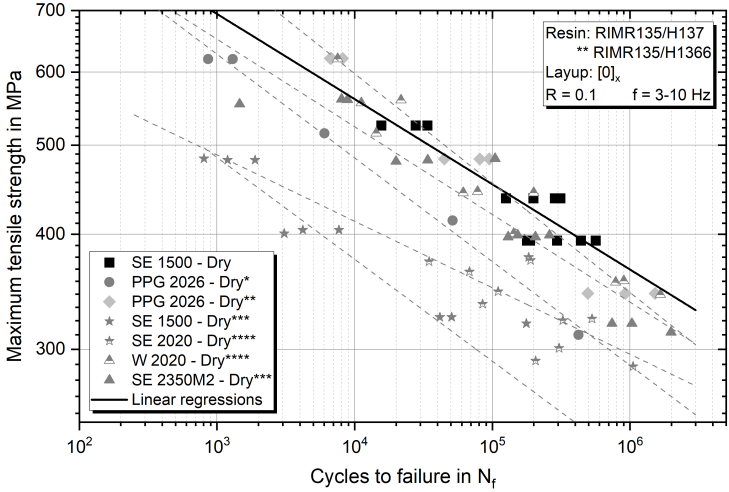

Figure 4.13: Tensile fatigue data for SE 1500 UD (dogbone specimens) in comparison with fatigue data for similar composites. Data from: *[204], **[254], ***[253], ****[255].

The impact of accelerated aging on the fatigue life of UD GFRP is presented for the SE 1500 composite and compared with results from two environmental aging studies on PPG 2026 (Hybon 2002 fibers with multi compatible sizing) composites by Hu et al. [204] and the SNL/MSU/DOE fatigue database [254]. Basically, all systems show similar behavior. On the one hand, the lifetime is considerably reduced at comparatively high loads (more than one decade at 50 % UTS), and, on the other hand, the differences become smaller the lower the loads and the higher the lifetime. These two aspects are more pronounced in the results obtained in this work and in the study by Hu et al. [204], which could either be an effect of the underlying damage mechanisms and growth (fibers and interphase) or by the aging temperature and duration (Hu: 60 °C for three months) or by the interphase and sizing performance, as no information are available about the age of the fabrics before manufacturing in case of the literature data. The fiber/matrix debondings due to wet aging, described for the static tests, have not been evolving during the five weeks of aging in the case of the fatigue specimens. Therefore, all tested specimens were visually undamaged be-

fore testing. However, it is remarkable that the lifetime decrease disappears in the high-cycle regime from about 10^6 cycles onward for all systems. The impact of accelerated wet aging is accordingly load level dependent. Considering the static test results of composites and the resin, it is most likely that the fiber strengths and damage growth primarily drive the fatigue life. In other words, the ability of the interphase to transfer loads and the fracture properties of the matrix resin are fundamental. In the high-cycle regime, when the fiber strength is still higher than the loads, the wet aging might also positively affect the resin, as it was shown that, e.g., the mode I ERR increases by about 60 % (see Chapter 3.3.3). Assuming that not all inter-fiber damage will occur and grow only in the fiber-matrix interphase, the enhanced fracture toughness can result in a decreased crack growth rate. A more detailed distinction of the aging damage proportions of fiber, matrix, and interphase on the fatigue life is not possible based on standard aging procedures with fully immersed specimens.

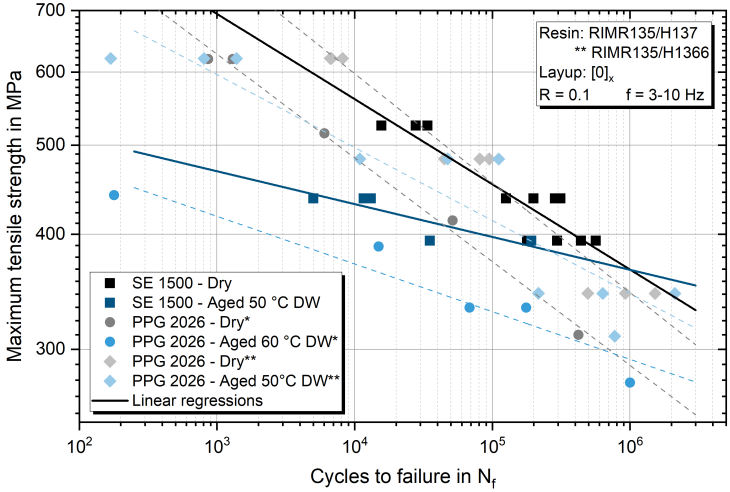

Figure 4.14: Tensile fatigue data for SE 1500 UD (dogbone specimens) after accelerated aging in 50 °C DW until saturation in comparison with fatigue data for similar composites with rectangulat geometry. Data from: *[204], **[254].

Nevertheless, an analysis of the damage progress by interrupted fatigue tests, the study of the dynamic modulus development, and the final damage pattern of the SE 1500 composite revealed that accelerated aging affects all constituents (F/M/I) simultaneously. Correspondingly, the damage initiation by weak fiber breaks and inter-fiber cracks, F/M debonding, and local delaminations, espe-

cially close to the backing fibers and stitching yarns, appeared earlier and more widely distributed. Additionally, the damage growth progressed faster, the fibers and fiber bundles were detached from resin over a longer distance, and the final failure of the fiber bundles appeared more local, indicating a higher defect density and poorer load transfer. Representative curves for the change of the dynamic modulus in relation to the normalized load level-dependent mean lifetime are given in Figure 4.15 for the high- and low-cycle regimes. These measurements show that the initial damage growth rate and extent are higher for the aged composites, even though the final mean lifetime is comparable. Thus, the cumulated stiffness loss within the first 20 % of the mean lifetime is, on average, between 3 % and 6 % larger in the aged case. This trend indicates primarily that the number of (initially) broken fibers is significantly higher and, therefore, coincides with the static strength results. It is noteworthy that, especially under low loads, the curves do not continue to converge throughout the fatigue life but remain at a relatively similar level until the final failure. From the steps, especially in the dry curves, it is also apparent that these specimens can survive some cluster or splitting damage.

In contrast, it can be hypothesized that the final failure of aged specimens is initiated as soon as one cluster of fiber breaks reaches a size, which allows a first large splitting crack to evolve. From this point on, the wet specimens fail quickly due to the rapid breaking of nearby clusters, while the dry specimens might survive one or two larger cluster breaks. Based on these findings and the descriptions of fatigue failure progress in UD composites by [189, 241, 256, 257], a schematic representation summarizing the primary damage types and failure evolution is developed, and shown in Figure 4.16.

For dry specimens, it is assumed that most of all weak fibers (e.g., statistically weak, undulated, poorly infused) break within the first load cycles. In the case of a high-quality composite, these first fiber failures are far from each other and homogeneously distributed all over the specimen [189, 257]. Simultaneously, local fiber/matrix debondings occur directly at the tip of broken fibers, and transverse matrix and interphase cracks evolve in or next to the backing fiber bundles [1, 241]. Under high loads, the debondings continue to grow along the F/M interphase, affecting the neighboring fibers by a stress concentration field [1, 241]. This might lead to further fiber breaks in a larger surrounding area of the first break. The process is repeated at each fiber break if the stress concentration field reaches another weak point of a neighboring fiber, leading

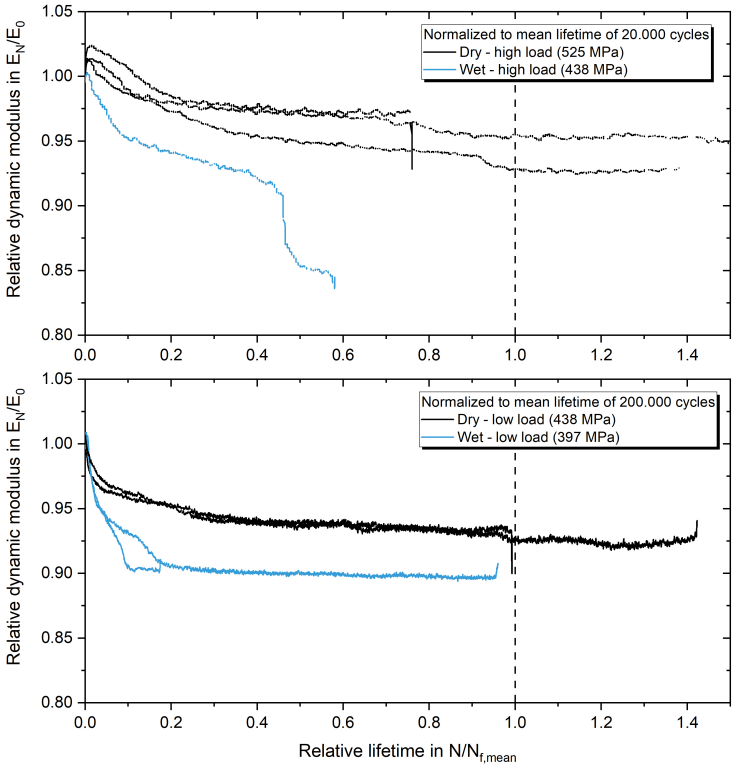

Figure 4.15: Representative developments of normalized dynamic modulus and lifetime for high (top) and low (bottom) stress fatigue tests of dry and wet specimens at comparable average lifetimes.

to clusters of broken fibers. If this is not the case, the damage accumulation stops. In UD composites, it is known that large longitudinal splitting cracks frequently accompany final failure. Sörensen et al. [189] have described this phenomenon with a micromechanical model concerning the impact of mechanical properties on the appearance of a critical damage size that favors longitudinal splitting. Assuming that linear elastic fracture mechanics can be applied and that a splitting crack is a mode II dominated crack, a critical cluster size can be defined in consideration of the macroscopic fracture energy G^c_{IIc}, the elastic modulus in the fiber direction E_0, and the geometric ratio between the cluster surface size S (in the plane normal to the fiber direction) and the total specimen

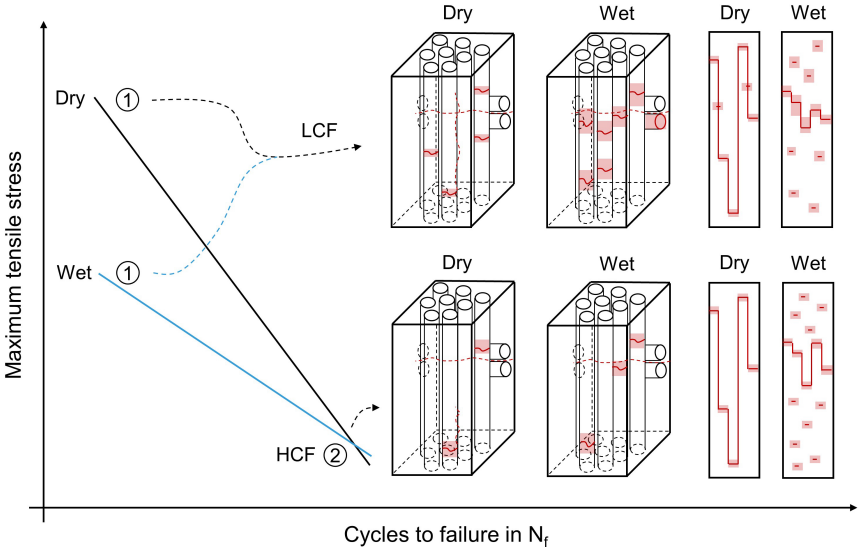

Figure 4.16: Schematic representation of the dry and wet aged Wöhler curves (left), the microscopic damage evolution in the surrounding of backing fibers (middle), and the macroscopic failure pattern (right).

cross-section A. Simplified, the load needed for a critical splitting growth σ_{sp} can be described as [189]:

$$\sigma_{sp} = \sqrt{\frac{2G^c_{IIc}E_0S}{A}}. \tag{4.1}$$

Rearranged as an expression taking into account the longitudinal strain instead of the stress and assuming a typical hexagonal cluster shape with the width of the splitting pattern being $2g$, a splitting criterion based on the cluster size can be formulated as [189]:

$$g_{sp} = \frac{4G^c_{IIc}}{E_0\epsilon_0^2}. \tag{4.2}$$

Consequently, most unidirectional composites fail when several critical cluster sizes are connected by longitudinal splitting. Under high loads, this process is driven by the faster F/M debonding growth, accelerating the growth of the cluster size (see Figure 4.16). The debondings are expected to arrest at lower loads when the F/M interphase strength is sufficiently high, and matrix yielding and mode I cracking are expected to be the main drivers of damage progress [241]. Especially in regions with high fiber volume content, kinking of cracks from the

interphase debonding into the matrix under mode I is favorable [257]. When these matrix cracks reach the neighboring fibers, they introduce a stress concentration larger than the stress concentrations due to a fiber break and the corresponding k-field at the tip of the debonding crack. Here, the stress concentration factors (SCF) depend on the fiber distance and can be taken as exponentially increasing from 1.02 to 1.13 for distances smaller than 50 μm [257]. However, even though the mechanisms are slower under lower loads, the final failure is also driven by the evolution of clusters of failed fibers and, subsequently, longitudinal splitting.

Important is now how accelerated aging affects the damage progress. As shown in Figure 4.16, water-induced aging has severe, load-level dependent, and complex impacts on fatigue life and damage progress. Based on the aging results presented for the matrix resin, the static properties, and the microscopic damage analysis, it is hypothesized that the reduced fiber strength and increased defect density play a major role under high loads. Due to the severely reduced fiber strength, many more fiber breaks already occur within the first load cycles. Furthermore, the weakened interphase strength leads to an extended growth of fiber/matrix debondings around broken fibers, magnifying the probability of breaking neighboring fibers due to stress concentrations. The combination of weak fibers and interphases expresses itself in a rapid local spread of damage, which is connected by small splitting cracks, as the distances between the clusters are clearly smaller than in the dry case. As a result, the specimens are characterized by very localized breakage throughout the entire specimen, with fiber breakage and detachment already evident at numerous other locations. Analyzing the modulus degradation over time, a very fast and unstable damage growth can be seen in the wet case (see Figure 4.15).

When the fatigue life of dry and wet specimens are similar at low loads, the damage progress is still somewhat different. Since the fiber and interphase strengths of the aged composite are likewise lower, more fiber breaks and larger interphase debondings occur during the first cycles. The modulus curves and the microscopy analysis can verify this theory. However, during the second stage of fatigue life, the damage growth does not seem to be faster in the wet case. A possible explanation could be based on the theory of Sörensen et al. [189], showing that the critical damage size is larger, the larger the fracture toughness of the composite and the matrix are (see Eq. 4.2). Equally, Castro et al. [241] propose that fatigue damage growth under low loads is dominated by matrix yielding and cracking,

which is reduced for tougher materials. Considering that the matrix's fracture toughness increases by about 60 % in the wet case, the matrix damage will be significantly slowed down. At loads so low that interphase debonding cracks will arrest or propagate very slowly, for wet specimens, the growth of critical fiber-breaking clusters is also slowed down, even though the fiber strength is lower. Consequently, the matrix toughening due to water absorption can positively affect the fatigue life in the high-cycle regime. Nevertheless, it should be taken into account that a coupon test is also dependent on the geometry of the specimen, the load introduction, and the overall test setup. Often, one critical defect is enough to lead to the final failure of a coupon. The widespread damage and severe fiber strength decrease of wet specimens for real and large structures could still be more critical, especially for low loads.

At this point, it can be concluded that accelerated aging of UD GFRP composites leads to a severe impact on fatigue performance, especially at high loads, which is important for design processes and the operation of structures that might be highly loaded in exceptional cases such as strong wind gusts. However, a clear distinction between the impacts of different damage mechanisms like fiber and interphase strength reductions can hardly be made. Several specific test campaigns were performed to overcome this limitation of immersed accelerated aging tests and will be analyzed in the following chapters. First, the effects of the aging temperature on composites will be investigated. Then, the impact of aging on the single constituents (fibers, interphases, and sizings) will be revealed with constituents and specific composite tests.

Effects of Aging Temperature

Two comprehensive tensile and transverse tensile test series were performed to investigate the effects of the aging temperature and duration on the mechanical properties of GFRP composites. Furthermore, the effects of fiber, sizing, and matrix choice were analyzed by changing individual constituents. In Figure 4.17, experimental results are shown as relative residual tensile strength for long-term aging of Q-UD PPG 2002/RIMR135 composites over more than two years. The strength degradation curves are fitted with a commonly used exponential decay function representing a simple Arrhenius degradation model as used, e.g., in recent studies [28, 258, 259]:

$$\sigma_{res} = \exp^{\left(\frac{-t}{\tau_{deg}}\right)}, \tag{4.3}$$

where σ_{res} is the residual strength after aging, t is the aging duration, and τ_{deg} is the Arrhenius fitting parameter. In contrast to the studies mentioned before, the simple degradation model cannot predict the correct residual strength in several places at once. This has several reasons: (i) the applied model presumes that only one physical degradation process accounts for the strength retention, (ii) the monotonically decreasing function used assumes to end with zero residual strength, (iii) the experimental data reveals particularly for higher aging temperatures an at least two-stage process of strength degradation, and (iv) the models presented in the literature are mainly based on fits between the dry reference strength and one single strength measurement after an arbitrary aging period (probably after saturation was reached), not including intermediate values. However, only accounting for the best fitting solutions for the Arrhenius parameter τ_{deg}, a degradation activation energy of about 72.2 $\frac{\text{kJ}}{\text{mole}}$ and a respective acceleration factor of 2.7 per temperature increase of 10 K can be calculated. Even though these values are basically in line with what was reported in the literature before [259, 260], the strength degradation rate and acceleration factors calculated are slightly higher in the current work, probably because the specimen dimensions (thickness of about 1 mm) are smaller. Saturation was reached early during aging, which was not the case with the aged and tested rods in the literature.

To overcome the limitation of the model to predict a final residual strength σ_∞ different than zero after infinite aging time, Eq. 4.3 can be extended to:

$$\sigma_{res} = (1 - \sigma_\infty) \exp^{\left(\frac{-t}{\tau_{deg}}\right)} + \sigma_\infty, \tag{4.4}$$

when the strength after infinite aging σ_∞ is known. A clearly better match can be achieved by fitting this model to the results obtained. However, it is remarkable that the calculated activation energy (74 $\frac{\text{kJ}}{\text{mole}}$) and acceleration factor are similar to what was found with the simpler model.

Due to the remaining strength difference after an aging duration, which should be long enough to lead to the same residual strength after aging at 50 °C and 30 °C, it is questionable if a simple master curve prediction model using the calculated time-shift or temperature-acceleration-factors (TSF or TAF) can forecast the strength in a meaningful way. Additional Arrhenius plots were first generated based on the pure test data for specific residual strength levels (instead of using the fitting parameter of the models proposed) to clarify the concerns for

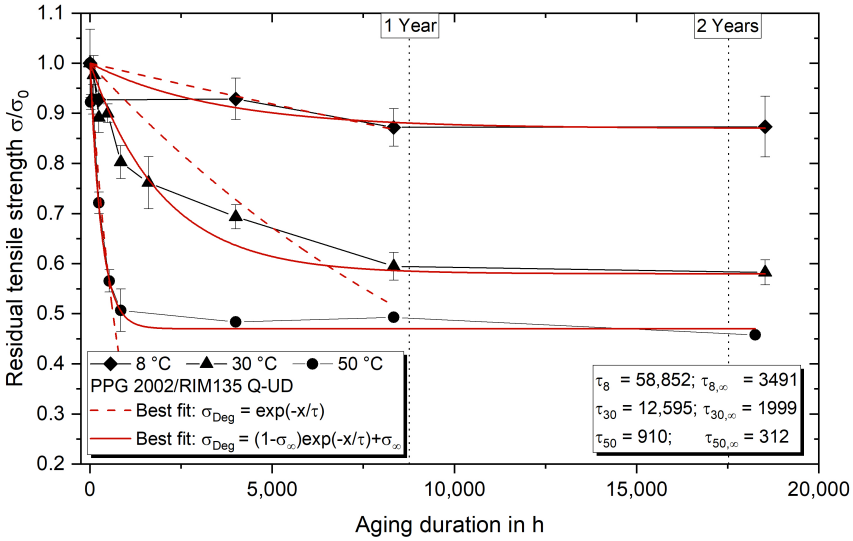

Figure 4.17: Development of tensile strength of PPG Q-UD composite during aging in water baths at 50, 30, and 8 °C. Experimental data and basic Arrhenius correlations best fit.

lifetime predictions. The results are presented in Figure 4.18 and again suggest a reasonable Arrhenius correlation of the degradation process. In detail, the calculated activation energies (based on the slopes) slightly depend on the residual strength region. Furthermore, the activation energies (between 92 $\frac{\text{kJ}}{\text{mole}}$ and 115 $\frac{\text{kJ}}{\text{mole}}$) are a bit higher than those obtained from the model fits, resulting in a higher temperature dependence of the degradation process. The experimental data were shifted on the time-axis by multiplication with the TSFs shown in Table 4.1 to build the master curves for the strength degradation during aging at specific environmental reference temperatures. These factors can be calculated regarding the aging temperature difference and the activation energy according to [259] as:

$$TSF(T_0, T_1) = \exp^{\frac{E_a}{R}\left(\frac{1}{T_0}-\frac{1}{T_1}\right)}. \tag{4.5}$$

The master curves for strength degradation at reference temperatures of 8 °C and 22 °C are presented in Figure 4.19. Even though the shifted data seem well aligned at first glance and the prediction curves based on Eq. 4.4 show a reasonable fit (R^2 = 0.888 to 0.916), the results must be analyzed in more detail. Generally, the effects on the degradation rate are as expected. The

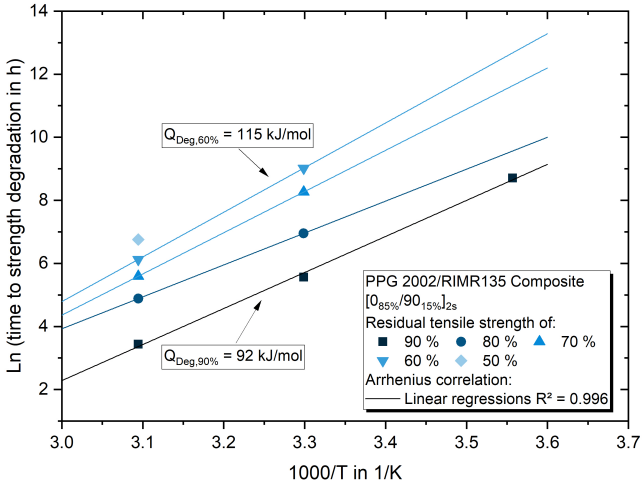

Figure 4.18: Arrhenius plots of the tensile strength degradation to specific residual strengths during aging in water baths at 8, 30, and 50 °C.

higher the aging temperature and the lower the necessary activation energy, the faster the degradation rate. However, regarding prediction accuracy, the effect of the measured activation energy is significant.

Table 4.1: Overview of the time-shift factors (TSF) used to shift the experimental results of the PPG 2002 composite on the time axis for two reference temperatures with different activation energies.

TSF 74 kJ/mole	Ref. 8 °C	Ref. 22 °C	TSF 92 kJ/mole	Ref. 8 °C	Ref. 22 °C
8 °C	1.00	0.22	8 °C	1.00	0.15
30 °C	10.47	2.25	30 °C	18.53	2.75
50 °C	67.07	14.68	50 °C	186.51	27.70

As an example, the predicted residual strength after three years of aging at 8 °C differs by about 107 MPa (ca. 12.5 % of UTS and 23.1 % of the maximum expected strength decrease) depending on the chosen E_a. Furthermore, the predictions show significant deviations from the test data, especially during short- and long-term aging durations. Here, both the temperature-independent strong degradation at the beginning and the different final residual strengths as a function of the aging temperature become apparent. The residual strength difference of about 106 MPa after aging of more than two years in 30 °C and 50 °C water propagates as a deviation for long-term predictions. Remarkably,

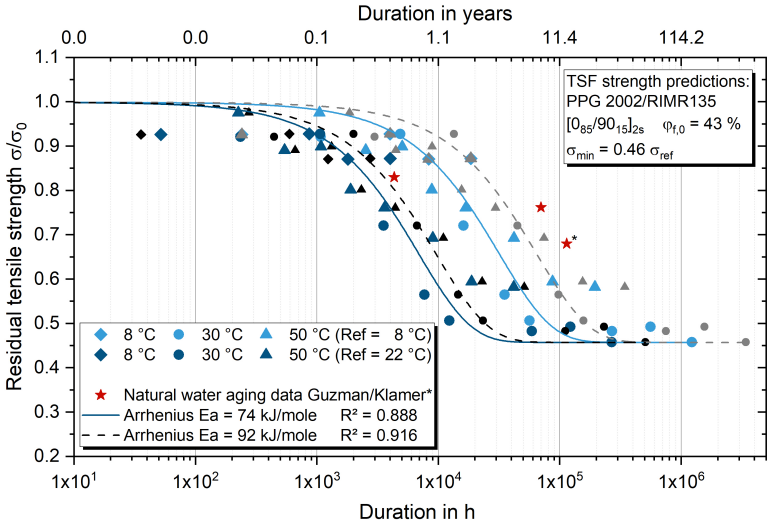

Figure 4.19: Degradation master curves based on Arrhenius time-shift functions for two different reference temperatures and activation energies (8 °C: 74 kJ/mole (blue) and 92 kJ/mole (gray) and 22 °C: 74 kJ/mole (dark blue) and 92 kJ/mole (black)). Additionally, the best fit with the Arrhenius degradation model based on Eq. 4.4 is shown. Natural aging data are taken from [193] and [197] for immersion at 22 °C and the North Sea, respectively.

the same residual strength difference (107 MPa) was found for long-term aging of the SE 2020/RIMR135 (ECR-glass) composite after two and three years of aging in 30 °C and 50 °C water. Long-term and natural-aging studies at moderate temperatures ($\leq$ 25 °C) to compare the predictions are rare. However, for the investigated composites based on the PPG 2002 fibers, there are two studies on multidirectional (MD) laminates available. The strength retentions after eight years in a water bath at RT [193] or 13 years submersed in the North Sea (mean ca. 12 °C) [197] are presented in Figure 4.19 as well. Assuming that the expected maximum relative strength degradation for MD laminates is in a comparable dimension to UD composites, as the load carrying 0°-fibers account for most of the tensile strength, it can be seen that the model predictions are too conservative. It is especially remarkable that the strength prediction for aging at 22 °C fits well for the short-term results obtained by Guzman et al. [193] (for six months of aging), while the eight-year results demonstrate a much higher strength than expected. Similar to what was hypothesized for this work's 30 °C aging results, the reasons could be either because the maximum strength loss

at lower temperatures will not fall to the low level that the accelerated aging suggests, or because the long-term degradation is much slower than expected.

The study was expanded with composites based on the LY1568 and the CeTePox 3329A/B epoxy systems to check the impact of the matrix resin choice and the interphase on the long-term strength degradation. Both resins absorb less water than the RIMR135/H137 epoxy (ca. 1.8 m% and 2.1 m% vs. 3.1 m% at elevated temperature of 50 °C, see Chapter 3.3.10). The tensile strength evolution is presented in Figure 4.20 in terms of absolute values. The values of the benchmark study with the RIMR135/H137 composite are also shown for comparison.

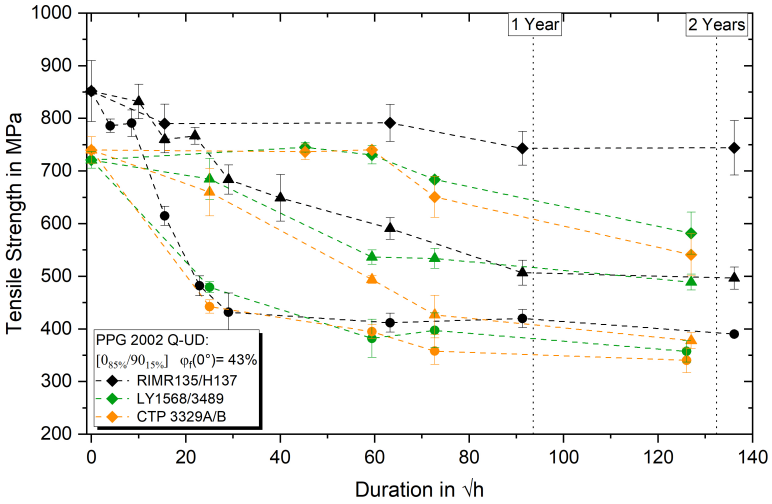

Figure 4.20: Development of tensile strength of several PPG Q-UD composites with different matrix resins during aging in water baths at 50, 30, and 8 °C.

First, it is conspicuous that the initial strength of the composites is about 15 % lower than the benchmark strength. This is most likely because the interphase properties are already significantly worse in the new reference condition than in the first part of the study. As the fabric was about one year older, the fiber sizing is expected to be significantly less reactive, resulting in a lower interphase strength. Consequently, earlier transverse cracks within the backing fiber bundles and larger debonding around broken fibers will occur under tensile loading in the main fiber direction. Thus, there is evidence that the interphase strength can severely impact the longitudinal composite strength, particularly

when a reasonable amount of transverse fibers acting as damage initiators are present.

Considering the aging temperature-dependent strength evolution, similarities and differences can be found compared to the benchmark study. During aging at high temperatures, no differences can be found at all. Both the degradation rate and its extent are the same. Thus the predominant damage mechanisms are independent of the water absorption capability of the matrix resin as soon as the aging temperature exceeds the capacity of the interphase to protect the fibers. Again, unimpeded fiber degradation is the main driving damage mechanism. The results for the medium and low-temperature aging are more remarkable, as deviations can be seen. Particularly important are the progressing degradation under aging at 8 °C. In contrast to the benchmark results, the composite strength further reduces from 3600 hours (ca. time of saturation) onward. These results give more evidence that an intact and valuable interphase can protect the fibers from degradation and that fibers also degrade under low temperatures, at least to some extent.

Consequently, the effects of the aging temperature were also investigated for UD transverse tensile specimens, as the fiber degradation is irrelevant to the strength under these loading conditions. Matrix and especially interphase-related aging will dominate this load case. The aging test results of up to two years are visualized in Figure 4.21. Besides the large variations of the initial transverse strength described before, the results reveal a strong dependence of the interphase degradation on the aging temperature. While all composites suffer from aging in 50 °C water, although not to the same degree, aging at 30 °C significantly reduces the degradation rate and extent for most of the systems. Only the NEG 2002 composite shows an equally low transverse strength of about 12 MPa after 90 days of aging. The composites made of the fibers SE 2020 and W 2020 containing the marine suitable sizing lose about 11 % during the first 90 days and a further 14 % during the following 620 days (nearly two years) by immersed aging at 30 °C. At low temperatures of 8 °C, the strength decrease is only 2.6 % (SE 2020) to 5.5 % (W 2020) for 90 days and about 7 % for 710 days. Thus, both systems show a residual strength of over 50 MPa after two years of immersion. Compared to the strength development of epoxy (see Figure 3.27) during cold water aging, it has to be considered that the strength of about 50 MPa is likewise the maximum strength predicted for the resin. The question of whether the loss of strength

is a direct consequence of minor interphase degradation or the residual epoxy strength cannot be answered beyond doubt.

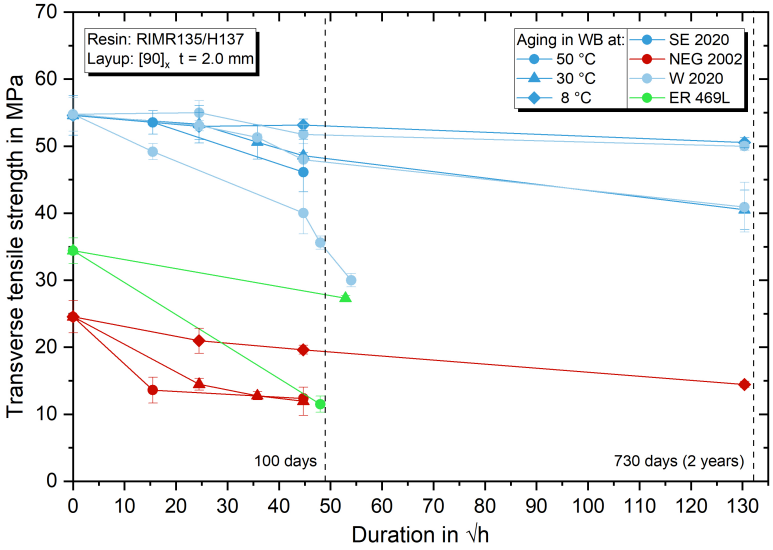

Figure 4.21: Development of transverse tensile strength of several 90° composites during aging in water baths at 50, 30, and 8 °C of up to two years.

However, the long-term results presented reveal that all composites have a different temperature-depending interphase degradation rate and extent. While some aging follows an Arrhenius-type correlation where increasing aging temperature leads to a predictable increase in the degradation rate, this cannot be confirmed continuously for all systems. If we assume a typical accelerated aging approach and apply the Arrhenius correlation described in Eq. 4.3 to the experimental results gained, the calculated activation energy for interphase degradation or transverse tensile strength reduction of the SE 2020 composite is about 50.5 $\frac{\text{kJ}}{\text{mole}}$. The only minimal deviations from the assumed Arrhenius correlation can also be seen by plotting the reduction parameter τ against the inverse temperature, as presented in Figure 4.22. In this case, the linear fits for the cold or warm aging environments indicate that the degradation process is simply accelerated by temperature, and no limiting temperatures are passed within the investigated temperature range. A temperature increase of 10 K leads to an acceleration by a factor of two. In contrast, the results obtained for the NEG 2002 composite reveal both the rapid total loss of interphase integrity due to aging at

temperatures $\geq 30\,°C$ (about one month to reach minimum strength) and the non-uniform acceleration by temperature changes. Therefore, it is apparent that the interphase cannot withstand elevated temperatures. Furthermore, hydrolysis reactions likely occur at these higher temperatures, passed during aging in the warm water baths. In this case, the Arrhenius plot (Figure 4.22) shows a distinct knee. From the absolute magnitude of τ, it becomes clear that the degradation process of the NEG 2002 interphase is at least one order of magnitude faster than that of the SE 2020 composite. Continuous tests in a narrow temperature range are required to determine these effects in a fiber system-dependent manner. For susceptible F/M interphases, temperature steps of about 10 K between 10 °C and 50 °C for at least 180 days of aging seem reasonable. During this duration, a minimum of five test events is recommended.

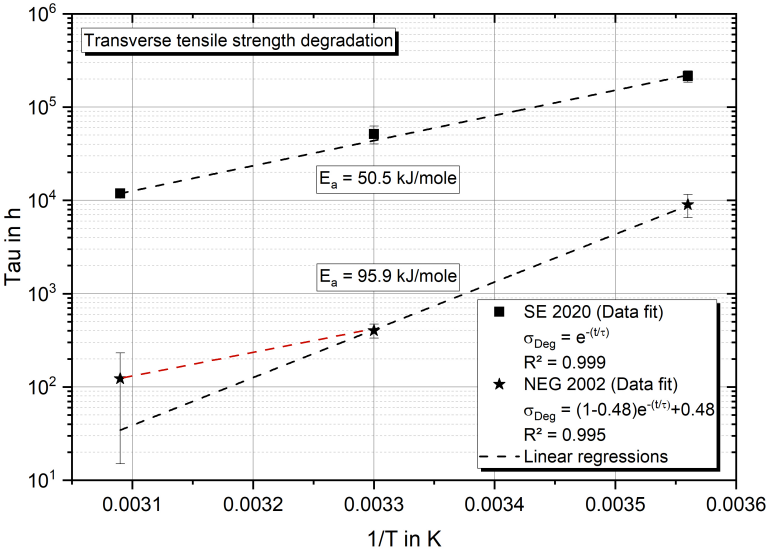

Figure 4.22: Arrhenius correlation of the temperature dependence for the transverse tensile strength reduction of the SE 2020 and NEG 2002 composites. τ is based on the best fit of the experimental data to the exponential reduction equation.

The differences in the fiber/matrix adhesion related to the aging condition and duration were visually inspected using SEM microscopy of post-mortem SE 2020 transverse tensile specimens. Representative images are shown in Figure 4.23. It is noticeable that the fracture surfaces of the dry reference and the long-term aged specimens at 8 °C show hardly any differences. Typically, a third or

sometimes half the fiber circumference is uncovered, and cohesive matrix failure is visible between single fibers. Generally, the fibers are still widely embedded in the matrix, and no signs of fiber/matrix debonding are visible. The matrix fracture surfaces themselves are a little different. While there are distinct hackles and an overall high roughness, the fracture of the wet matrix is smoother and shows some larger crumbles. The surfaces look entirely different after short-term aging in a water bath at 50 °C or when the sizing was pre-aged. In these cases, the fibers are largely separated from the matrix. Bare fibers and their imprint in the undamaged remaining matrix characterize the picture. Only very few regions of cohesive matrix failure are visible.

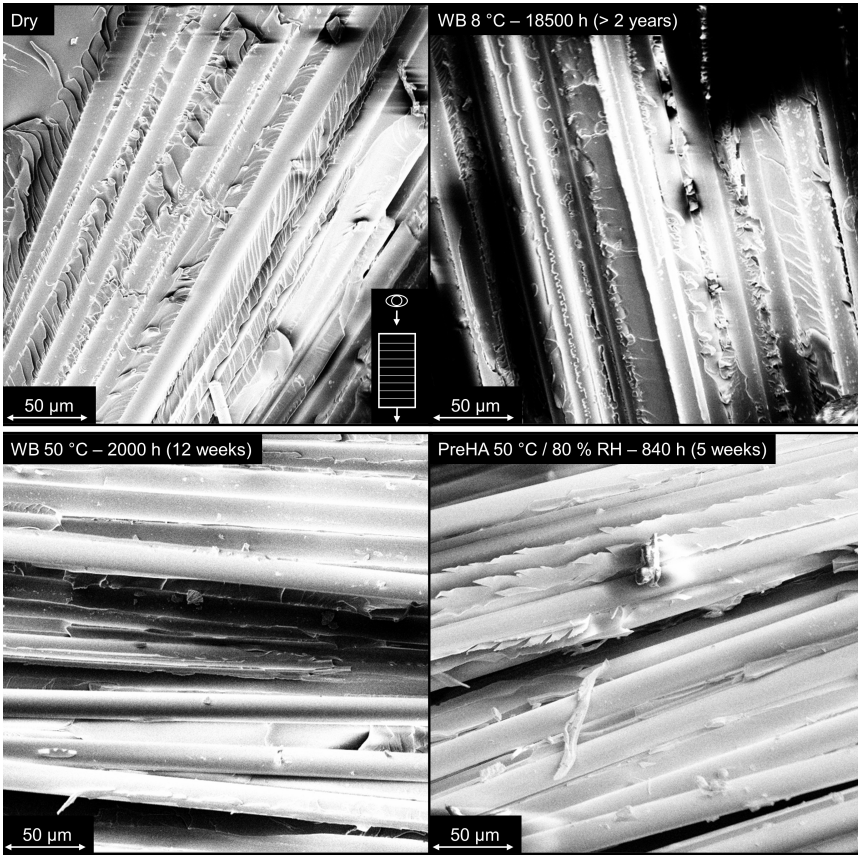

Figure 4.23: SEM images of broken transverse tensile specimens (view on top of the fracture plane) for different aging conditions showing the F/M interphase region in detail. All pictures show the SE 2020 composite.

As a short summary, a scheme showing the probably dominating processes concerning the aging temperature and duration is presented in Figure 4.24. In the first few hours or days of wet-aging (during water absorption), the composite tensile strength reduces instantly by a significant amount, independent of the aging temperature. It is hypothesized that this strength reduction is attributed to the growth of already present glass surface flaws, which are not sufficiently covered and protected by the sizing and formed interphase. Two processes play a role here: on the one hand, the significantly higher diffusion rate within the interphase [18, 115, 170] and, on the other hand, the already proven high fiber-water interaction and faster fiber dissolution at the beginning of the aging process [27, 76, 261].

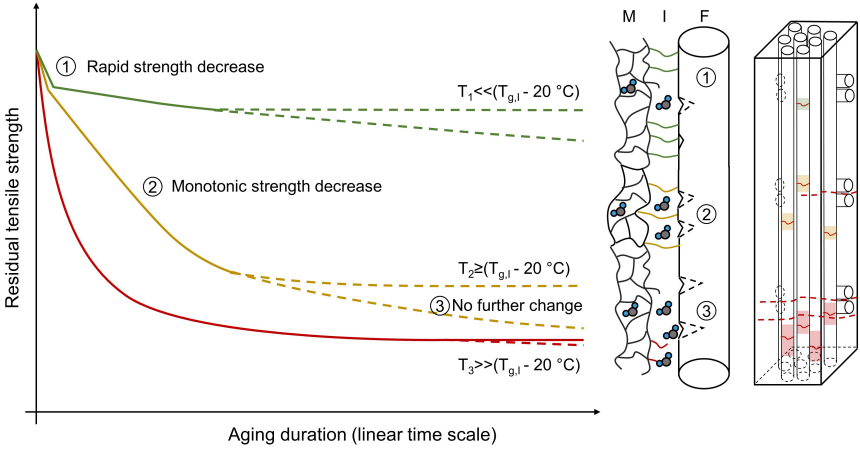

Figure 4.24: Schematic residual tensile strength evolution for (Q-)UD composites during wet aging at different temperatures concerning the T_g of the interphase and the related diffusion rate.

Next comes a phase of monotonic strength degradation. At high-temperature accelerated aging, the dominant degradation processes are at least as fast as the diffusion rate. As can be seen in Figure 4.17, the strength reached the absolute minimum already when the material was saturated (ca. one month). During the next two years, the strength does not decrease further. In this case, the water absorption goes along with severe damage to the interphase region. Under the presence of water and elevated temperature, decomposing reactions, such as the reversible condensation of silanes to the glass surface, can occur [179]. Furthermore, it is expected that the T_g of the interphase is lower than that of the

bulk matrix since the interphase consists of many short-chain, non-crosslinked molecules [178]. Aging at temperatures close to the wet T_g of the resin could consequently exceed the T_g of the interphase region and lead to additional degradation. As a result, fiber/matrix debonding occurs, and more water is absorbed in direct contact with the fibers. Thus, all inherent surface flaws are exposed to direct water contact and can grow to a critical size. However, both aging tests on single fibers [251] and fiber bundles [27, 76] (see also Chapter 4.3.3) reveal that the fiber strength seems to approach a lower limit, which is still about half of the original strength for high-temperature aging. Under tensile loading, the weakened fibers break at the largest flaws and debond considerably. Within this debonding distance, neighboring weak fibers break, and an unstable growth of fiber breaks initiates the final failure.

Aging at lower temperatures also causes a monotonic strength decrease. However, the rate and final extent are temperature-dependent and do not seem to follow a simple Arrhenius correlation. Unlike the previous case, the strength at lower temperatures continues to decrease even after saturation. Here, the interphase likely plays an important role. As long as the aging temperatures are so low that the interphase remains intact, the fibers are partially protected from hydrolytic attacks. Accordingly, the fiber strength seems not to decrease further over time, and the debonding length next to broken fibers is small. Additionally, matrix swelling-related tensile stresses of up to 60 MPa [262] can occur on the fibers. They might also explain a significant proportion of the strength loss after cold-temperature wet aging.

In addition to the long-term static tests, another study was performed under reversed fatigue loading ($R = -0.5$) with Q-UD composites based on R&G E-glass fibers. Details about the specimen geometry and the whole test series, including water absorption, static properties, and fatigue damage progress analysis, are given in the materials section (Section 2.1) and in Gibhardt et al. [31]. In the context of the present thesis, only three outstanding results will be emphasized.

First, a two-part behavior with enormous lifetime reductions under comparably high loads was revealed for saturated specimens after long-term aging at 50 °C salt water (SW). These results are significantly more concise than already determined for the tensile-tensile investigations and are likely the consequence of the dramatic loss of fiber strength in connection with a decreased buckling resistance

under compression loads. Second, short-term water absorption of up to 50 % of the maximum amount showed no negative effects on the lifetime, even during aging at 50 °C. This is probably due to the plasticizing effect of the matrix, and simultaneously only limited fiber degradation as little water reached the central specimen layers within 19 days of aging. Third, it could be demonstrated that aging at RT (22 °C) extended the fatigue lifetime and, therefore, might have positive effects compared to the initial dry condition.

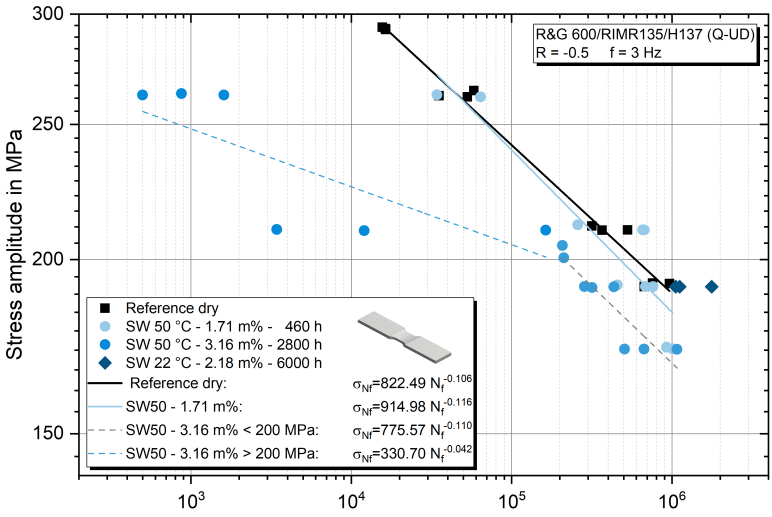

Figure 4.25: Tensile-compression fatigue results for R&G Q-UD composites after aging in salt water (SW) at different temperatures and periods.

In summary, the test results and modeling approaches reported in the literature and applied to the testing results from aging of UD composites within this work allow to draw some conclusions on the time-temperature accelerated aging processes and damage progress in UD composites regarding their residual strength. Thus, it can be assumed that the water-induced fiber degradation, e.g., leaching of ions and nano-crack and flaw growth, and the related fiber strength reduction are the main drivers for the long-term decrease of the composite longitudinal strength. However, even though the underlying processes are temperature-dependent and often approximated by an Arrhenius correlation, significant deviations have been found, particularly for long-term predictions based on accelerated (warm) aging. These deviations can have various reasons. For example, several temperature-dependent degradation mechanisms could be

present and, therefore, dominate the overall process to a greater or lesser extent, depending on the temperature. This may involve different constituents (F/M/I) and different reaction mechanisms within a constituent. For example, the activation energies required to dissolve various components (ions) from the fiber vary [263, 264]. So, it might be that some dissolution reactions are not taking place at low temperatures. In addition, the integrity of the F/M interphase likely has a vital role in protecting the fibers, even under submerged conditions. Here, significant differences could be revealed for the systems under investigation. While some demonstrated excellent durability at low and reasonable durability at moderate temperatures, maintaining more than 92 % or 75 %, respectively, of the transverse strength during two years of immersion, others broke down fast and entirely. Considering the strength-temperature-water correlations for the epoxy resins (see Chapter 3), it is suggested that aging and operation temperatures should be chosen about 20 °C lower than the T_g of the interphase to obtain a safe long-term use. To further deepen the understanding of the fiber and interphase degradation processes in a composite, the effects of aging on the single constitutes are investigated in more detail.

4.3.3 Glass Fiber Degradation

The degradation of the load-carrying glass fibers in GFRP is one of the most critical damage mechanisms that can occur during operation in severe environments. To better estimate their contribution to the overall degradation, investigations on aged fibers and fiber bundles and relevant results from the literature are discussed below. Following a fiber bundle testing approach successfully implemented by other research groups before [27, 265–268], tensile tests on loose fiber bundles of different fiber types and with different aging temperatures were performed. In this context, the important results of Krauklis and Echtermeyer [27, 76] were first supplemented by further experiments. While the authors completed various dissolution studies under different aging temperatures and pH environments, mechanical strength data of the fibers are only available for aging in 60 °C DW at a pH of 5.5. All model predictions are then based on the fit between these results and the dissolution rates using the newly developed DC-ZOK model. This model was adapted and slightly modified as described in the following.

Krauklis et al. [27, 115] described the dissolution rate of the glass fibers with two constants resulting from dissolution experiments. Their experiments likewise revealed a two-staged behavior resulting in two different dissolution rate constants, denoted as an unsteady phase with K_0^I and a steady phase with K_0^{II}. The applicability of the respective constant was defined by a fixed aging duration of 166 h, whereby for shorter periods, K_0^I and for longer, K_0^{II} has to be used. By combining the dissolution kinetics with a Griffith or fracture toughness approach, the environmental aging-dependent fiber strength $\sigma_f(t)$ was described as:

$$\sigma_f^I(t) = \frac{\sigma_{f0}}{\sqrt{1 + \frac{K_0^I \cdot (\vartheta - \xi_{sizing})}{a_0 \cdot \rho_{glass}} \cdot t}} \quad for \quad t \leq t_{st} \tag{4.6}$$

$$\sigma_f^{II}(t) = \frac{\sigma_f^I}{\sqrt{1 + \frac{K_0^{II} \cdot (\vartheta - \xi_{sizing})}{a_0 \cdot \rho_{glass}} \cdot t}} \quad for \quad t > t_{st} \tag{4.7}$$

and

$$\sigma_f^I = \frac{\sigma_{f0}}{\sqrt{1 + \frac{K_0^I \cdot (\vartheta - \xi_{sizing})}{a_0 \cdot \rho_{glass}} \cdot t_{st}}} \tag{4.8}$$

with time t, glass density ρ_{glass} ($2.54\,\frac{g}{cm^3}$), initial crack length a_0 ($0.2\,\mu m$), sizing factor ξ_{sizing} (0.165) and the crack sharpness amplification factor ϑ (993). For further details on the derivation, it is referred to the original literature at this point [115].

However, while working with the proposed model in the context of this thesis, an error in the original formulation was noticed and discussed with the original author. Using the model with the originally proposed crack sharpness amplification factor ϑ of 993 does not fit the experimental results. Due to a small mistake with the unit conversion, ϑ should be 16.55 instead to receive the published model.

As it was found that the data obtained during the present study can be described with higher accuracy using two constants for ϑ, the model is used with a split ϑ. From a physical point of view, the division of the crack sharpness amplification factor into two factors regarding the steady and unsteady phase seems legitimate, as it describes the processes inside the intrinsic cracks (flaws) of the fibers. These

are initially covered by sizing and have a different geometry than the fiber surface. Therefore, it is reasonable to argue that the crack sharpness changes significantly more within the first phase, as the cracks are uncovered from sizing during this period.

However, the basic short- and long-term prediction results are mostly the same. Figure 4.26 shows the normalized fiber bundle strength results for aging at 30 °C, 50 °C, and according to Echtermeyer and Krauklis et al. [27], for 60 °C DW. Additionally, the model strength predictions based on the temperature-dependent dissolution rates proposed by Krauklis et al. [76] were calculated and are presented as well. The used parameters are shown in Table 4.2.

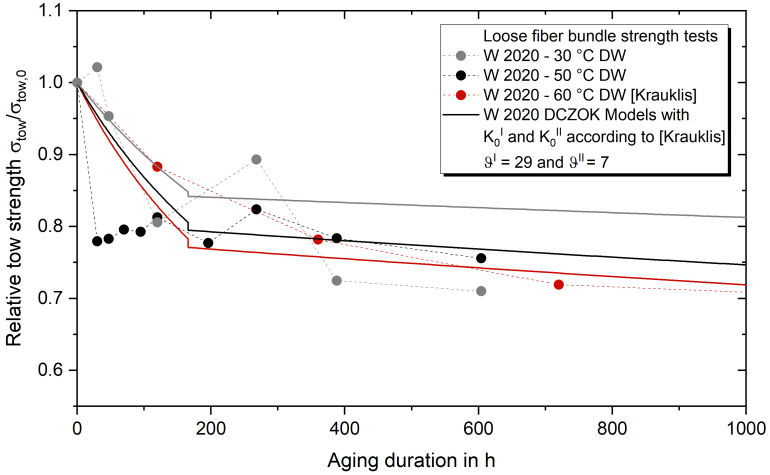

Figure 4.26: Development of loose fiber bundle (tow) strength during aging in water baths at 30, 50, and 60 °C. SDs are up to 10 %. Data for 60 °C taken from [27].

Table 4.2: Overview of the parameters used for the adjusted DCZOK fiber strength model.

Specification	K_0^I in g/m^2s	K_0^{II} in g/m^2s	ϑ^I	ϑ^{II}	t_{st} in h
W 2020 30 °C	$1.15 \cdot 10^{-8}$	$1.85 \cdot 10^{-9}$	29	7	166
W 2020 50 °C	$1.60 \cdot 10^{-8}$	$3.39 \cdot 10^{-9}$	29	7	166
W 2020 60 °C	$1.82 \cdot 10^{-8}$	$4.05 \cdot 10^{-9}$	29	7	166

Notably, the absolute strength obtained by the bundle tests for the W 2020 fibers in the context of this work was about 30 % higher than that reported by Krauklis [76]. Most likely, this is due to the different test setups (wheels vs. straight grips). However, analyzing the results makes it clear that the relative strength loss due to aging is in the same dimension. Looking more closely, some differences between the experimental and modeling results attract attention. First, it is evident that the strength decrease due to aging in warm water (50 °C) proceeds much faster ($\leq$ 30 h) than expected by the models and former studies, and second, the proposed significant difference in residual strength for aging at 30 °C and higher temperatures cannot be confirmed experimentally. Even though some of the differences may be due to experimental reasons, such as the typically high standard deviation of the bundle tests, the overall trend of the very frequent testing (every 24 h) indicates a faster strength reduction within the first few hours.

Analyzing the reported dissolution rates by Krauklis et al. [76], there is evidence that the dissolution during the first hours is also higher than proposed by the model, taking an aging duration of 166 h as a fixed value for the change of the dominating mechanism. Nevertheless, the rapid strength decrease found for aging at elevated temperatures is well in line with what was reported, e.g., by Ramirez et al. [251] and Scheffler et al. [267]. Therefore, it is hypothesized that the fiber strength degradation is not primarily and only dependent on the total dissolution rates but predominantly on the unprotected and effective flaw size and distribution of the fiber surface. At the same time, this is partially accounted for by linking Griffith's strength and determined corrosion rates in the model [268]. The effect of an intact fiber sizing on strength is foreseen by a reduction factor that artificially slows down the reaction rate by an order of magnitude. However, a temperature dependence of the sizing durability is not implemented.

Thus, it was demonstrated by Scheffler et al. [267] that applying high-quality sizings on unsized fibers can, on the one hand, raise the fiber strength by more than 25 % and, on the other hand, can significantly reduce the rate and final extent of the strength decrease during wet aging. In detail, under room temperature aging, the strength reduction was avoided entirely, while it was reduced by about 10 % at 40 °C. Considering the variety of possible dissolution reactions within the fibers [76] and the possible reactions at the (sized) fiber surface [179], an aging-time and temperature-dependent strength development somewhat de-

viating from the model presented so far [27, 76] seems reasonable. Consequently, at least a term accounting for the aging-temperature-dependent capability of the sizing to protect the already existing flaws from becoming critical by first uncovering and then exposing them to hydrolytic attacks is proposed. However, more specific tests under various temperatures are necessary in the future to implement this reasonably.

From a chemical point of view, the activation energies needed for the single corrosion reactions are of importance, as an absence of some of these might explain the higher residual strengths of fibers aged at lower temperatures even after several thousand hours of exposure [251]. Another process that has not been accounted for yet is the possible formation of a secondary phase along the fiber surface, such as a silica-rich gel phase, which can significantly slow down the dissolution rate for long-term aging [269]. This may equally be why the fiber strength remains largely unchanged once the processes at the surface have attained a steady state. Finally, water's extremely slow diffusion rate into the fibers themselves ($D_{GF} = 10^{-18}$ to 10^{-22} $\frac{\mathrm{m}^2}{\mathrm{s}}$) restricts the reaction depth to only a few nanometers [269].

In addition to the results obtained for the relative corrosion-resistant R-glass fiber W 2020, similar tests were also performed with SE 2020 ECR-glass and PPG 2002 E-glass fiber bundles. The results for the aging of up to 42 days at 50 °C DW are shown in Figure 4.27. Even though the standard deviations (not shown in the graph for clarity) were relatively high (up to 15 %), the mean values demonstrate clear trends. While the ECR-glass performed on a similar level as the R-glass, the E-glass showed both a rapid and more extensive strength decrease. After 25 days (600 h) of aging, the residual strength is only about 55 % of the pristine strength. Translated to the corrosion-based modeling approach, this implies a dissolution rate that is about a factor of 2.5 times higher than for the other glass fiber types. Nevertheless, the surface effects that occur directly at the beginning could be more decisive than the long-term decomposition.

The strengths evolutions for the PPG fiber bundles and the corresponding composites are presented in Figure 4.28 to estimate the overall proportion of fiber degradation on the composite strength reduction revealed before. The data show a clear correlation, where the rapid initial strength decrease of the composite can be related to the higher share of affected fibers when the specimens are immersed. Subsequently, the strength reduction proceeds slower than for the bare fibers,

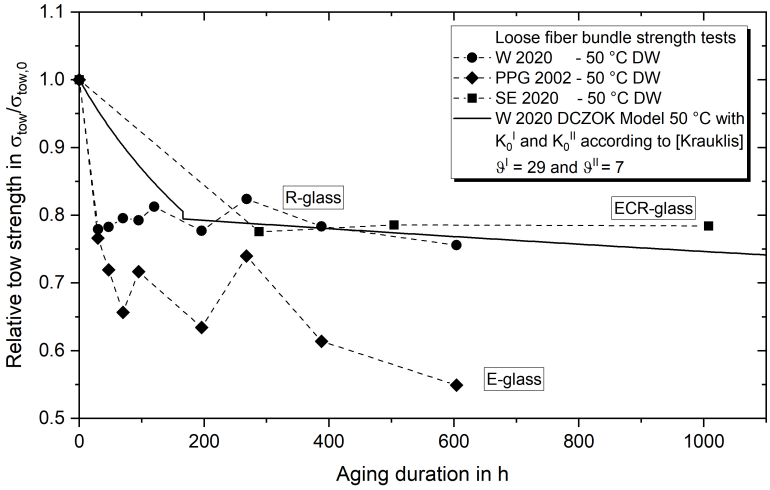

Figure 4.27: Development of loose fiber bundle (tow) strength during aging in water baths at 50 °C for three different types of fibers. SDs are up to 15 %.

but as soon as saturation is reached, the residual strength equals. Therefore, the data confirm the assumption that composite aging at 50 °C already removes any protective function of the sizing and the F/M interphase. Consequently, the accelerated aging tests are also only of limited value for considerably lower operating temperatures, as the fiber dissolution and sizing-related reactions are not only slowed down but most likely appear to a different extent.

In order to visually examine the effects of wet aging on glass fibers and sizings, SEM images were recorded for dry and unaged as well as for wet-aged (50 °C) E-glass fibers (R&G). Representative pictures are shown in Figure 4.29. While the initial fibers have a comparably smooth surface with (most likely) planar streaks of sizing, it is evident that underwater aging affects the sizing and surface significantly. Almost all the fibers examined show a drop-like and less areal (sizing) distribution on the surface (Figure 4.29 bottom right). Furthermore, fragment-like residues of between 0.5 μm and several micrometers can be identified. Whereas the droplets seem to be properly attached to the fiber surface, the fragments are partly detached and have many fractures. However, due to their expected tiny size of about 150 nm to 250 nm [265, 268], distinct fiber flaws cannot be seen in both conditions by SEM observations. For this purpose, techniques like AFM are more suitable. Thus, Scheffler et al. [267] have revealed that

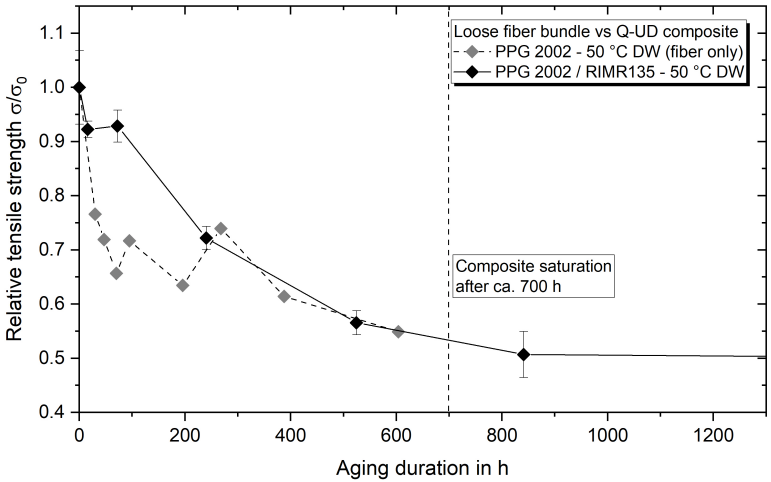

Figure 4.28: Loose fiber bundle (tow) and Q-UD composite strength for PPG 2002 E-glass during aging in water baths at 50 °C.

the fiber surface roughness and contact stiffness change during aging in (warm) water.

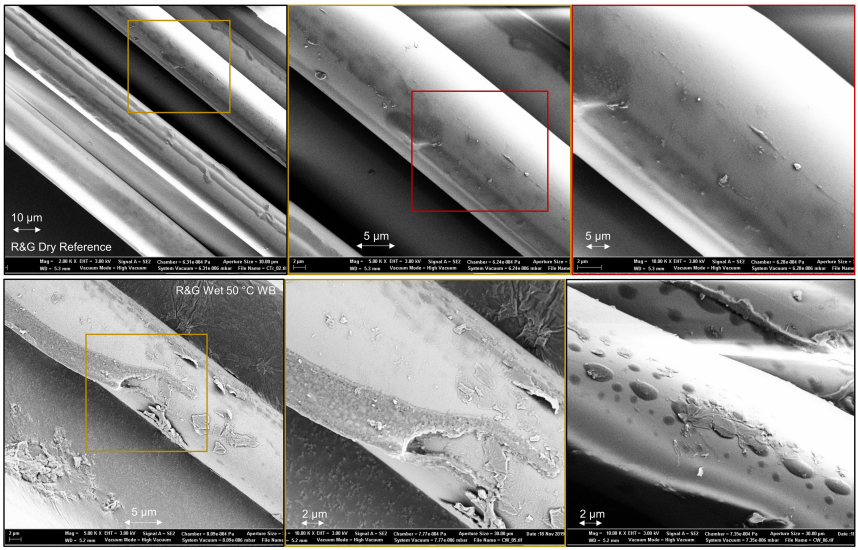

Figure 4.29: SEM images of R&G E-glass fibers in dry initial condition (top) and after aging in 50 °C DW for ca. 1000 h (bottom).

Figure 4.30 presents SEM images taken after short-term temperature treatment at 550 °C for dry reference and water-aged E-glass fibers (R&G). Compared with the untreated fibers, the surface after heating is smoother and free of the streaks described before. Considering additionally mass loss curves gained by thermogravimetric analysis during heating of up to 600 °C, which reveal a sizing-driven mass loss of between 0.25 % and 0.65 % for all fiber systems investigated, there is enough evidence that the streaks and fragments shown in Figure 4.29 are organic and must therefore be related to the fiber sizings. Furthermore, it is remarkable that the wet-aged fibers show lots of residues (≤ 0.4) microns, which cannot be found on the dry fiber surfaces to this extent. Even though the exact composition of the residues is unknown (e.g., dust or ash), it might indicate that the surface chemistry (polarity, charge, etc.) could be changed by wet aging. A more detailed analysis of the surface and its composition should be performed in the future, e.g., by combined AFM and EDX techniques as well as by molecular dynamics simulations.

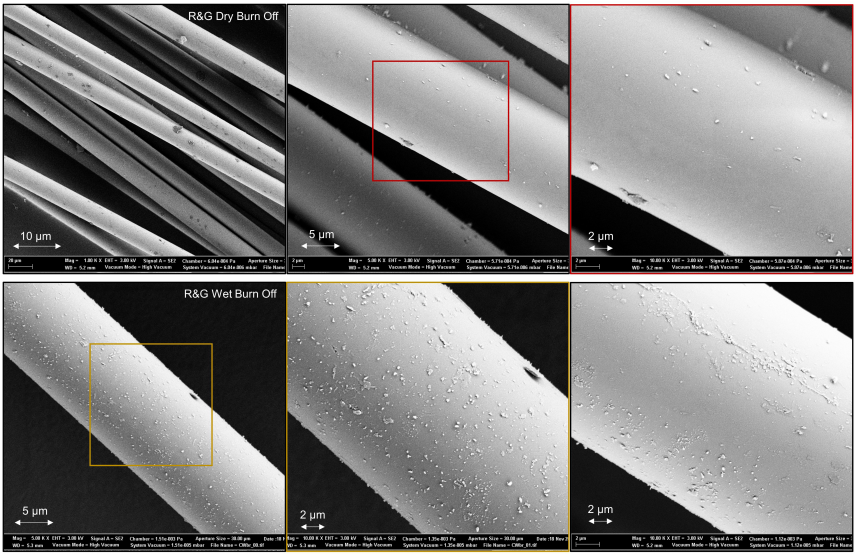

Figure 4.30: SEM images of R&G E-glass fibers after 0.5 h at 550 °C of dry reference fibers (top) and after aging in 50 °C DW for 1000 h (bottom).

4.3.4 Sizing and Interphase Degradation

As introduced in Chapter 4.2.1 and as emphasized by discussing the results presented before, one of the leading open questions regarding the aging behavior of composites is the detailed role of the F/M interphase. Here, two assigned functions and their impacts on static and fatigue properties are of large interest: (i) the capability to transfer loads between the fibers and the matrix and (ii) the protection of the fibers from hydrolytic degradation. Because it is experimentally impossible to specifically age the F/M interphase of a composite without affecting the matrix and/or fibers simultaneously, the fiber pre-aging method described in Chapter 4.2.1 was developed as an alternative approach in the framework of this study. A scheme demonstrating the differences and similarities between a composite's humid pre-aging and classical wet aging is shown in Figure 4.31 based on a gradual interphase model.

The pre-aging method is based on two main assumptions: (i) storage under high humidity at elevated temperatures enables and accelerates hydrolysis reactions of the reactive organofunctional sizings [179], which are usually foreseen to covalent bond to the matrix resin, and (ii) the condensation of silanes to the glass surface is a reversible reaction, which in turn can lead to a break of the covalent bonding between sizing and fiber [115, 179]. Although water molecules entering a thoroughly interconnected F/M interphase will affect the ambient structures (fiber surface atoms, sizing, and resin molecules) differently than the same molecules entering the sized fiber surface before the curing reaction with the epoxy matrix resin took place, it is hypothesized that the consequences in terms of integrity are very similar. Therefore, it is assumed, as a first approximation, that it makes little difference to the mechanical effects (interphase strength) whether the separation of fiber and matrix occurs directly at the fiber surface (silane hydrolysis) or at the bond to the matrix (polymer hydrolysis).

For the humid pre-aging, the preexisting hydrolysis of the functional groups will primarily inhibit the reaction between the coupling agent and the epoxy network. This type of reaction minimizes the reactivity of the sizing and is not reversible by subsequent cool down and drying. Contrary to this permanent impact, it is not excluded that the possible hydrolysis of the silane-surface bonding (Si-O-Si) during humid aging can (partly) be followed by re-condensation during cooling and drying. Here, water molecules adsorb to the surface, diffuse into the sizing, and incrementally resolve the fiber/sizing bonding [177, 234]. Besides the

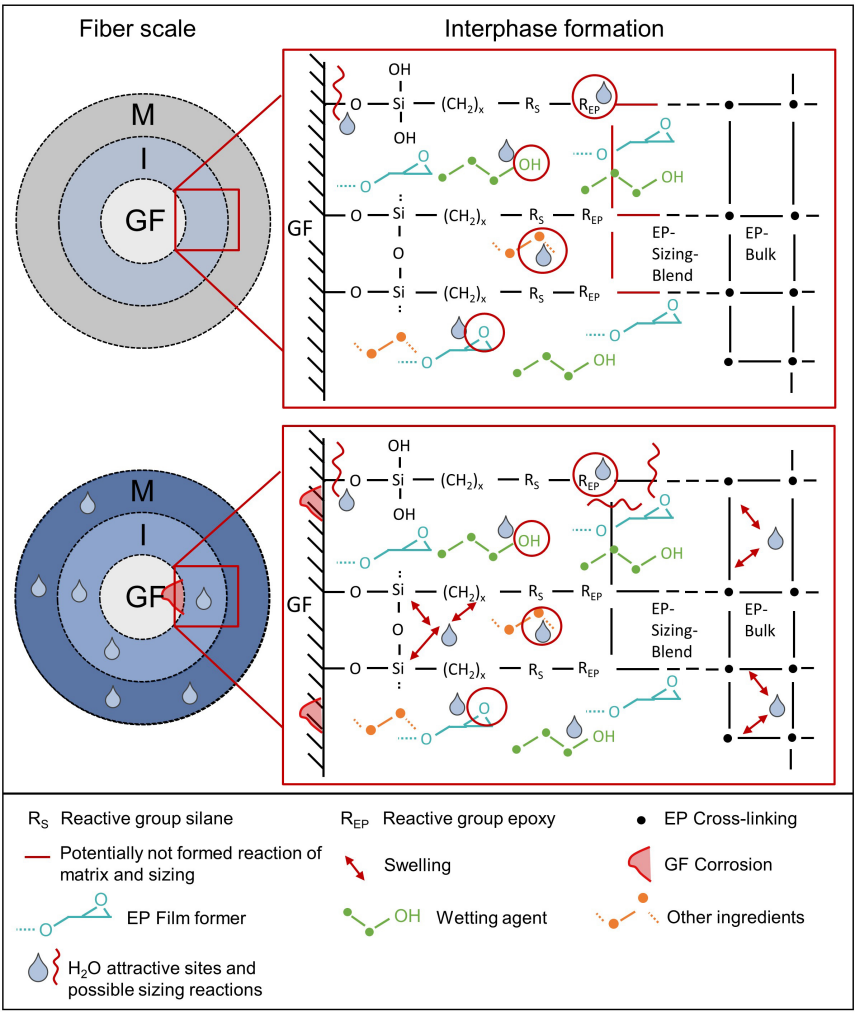

Figure 4.31: Schematic presentation of the differences and similarities between the humid aging of the fiber sizing before manufacturing (pre-aging) (top) and the classical aging of a composite (bottom).

coupling agents, which only make a proportion of about 10 % of the sizing, water molecules can react or attach to several polymeric ingredients such as (epoxy) film formers, lubricants, anti-static agents, emulsifiers, and others [115, 178, 237]. Although it is not clear to what extent the film formers will be integrated by chemical bonding into the matrix [178], it was found by FTIR investigations that

the reactivity of, e.g., epoxy functions decreases during storage and aging [179, 238]. The reduced reactivity of the sizing then also causes a significant reduction in F/M adhesion in the subsequently manufactured composites.

In the case of composite aging, the water molecules diffuse with preference into the interphase as they are attracted by the comparably higher polarity and the larger available space. Again, hydrolysis of the silanes and polymer bindings is possible, but the silane hydrolysis is probably favorable since the (used) epoxy is not hydrolyzable. In this context, Krauklis et al. [115] have proposed a model estimating the dissolution of the sizing-rich interphase by immersion in warm water. It has been shown that up to 50 % of the interphase components can be released in a short time if the interphase has direct and free contact with the surrounding water. However, diffusion of water into the interphase also introduces significant swelling stresses [115, 203] and significantly enlarges the affected interphase volume [170, 270]. Subsequently, either local molecular detachment or larger interphase debonding occurs, which likewise reduces the mechanical performance of the interphase.

Based on the theoretical background, multiple investigations were performed on specimens after the tailored pre-aging process and compared to classical water aging to evaluate the effects and processes during interphase (sizing) and composite aging. To verify that the accelerated sizing aging process reflects the aging process that naturally occurs during the storage of sized fibers, the resulting composite interphase strengths were analyzed by transverse tensile tests. Therefore, strength data after the natural aging of NCFs under laboratory conditions of up to 3.5 years were compared with accelerated humid-aged fabrics over ten weeks. The results are presented in Figure 4.32.

The transverse strength in dry conditions decreases during laboratory NCF storage time for both investigated fiber types. However, while the five-month reduction was relatively similar, the long-term performance dramatically differed. While the transverse strength of a laminate produced two years after NCF production in the case of the SE 2020 still shows a relatively high strength of about 44 MPa, the strength of the SE 1500 laminate was only about 18 MPa.

Compared to the standard (natural) aging process, the results gained from the accelerated NCF pre-aging tests of up to ten weeks are also shown. Here, two aspects become clear: on the one hand, aging can be dramatically accelerated (by a factor of four to eight), and on the other hand, it is shown that after five to ten

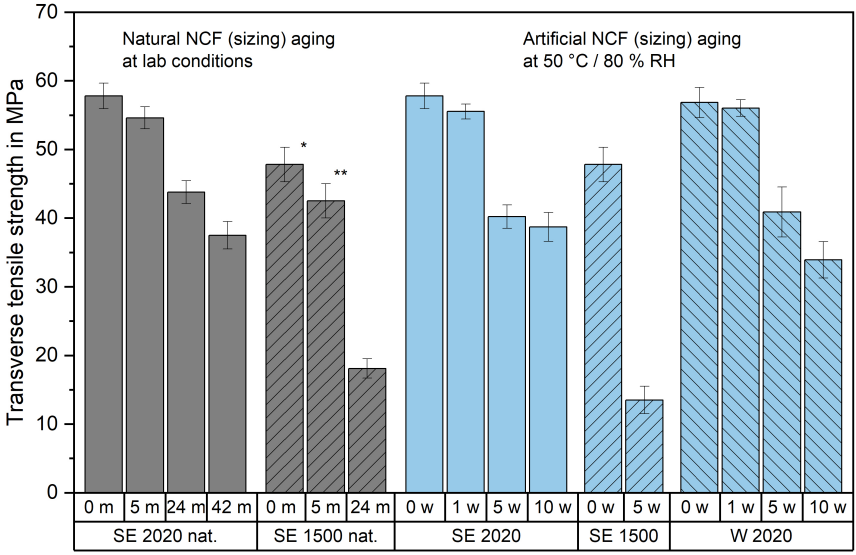

Figure 4.32: Development of transverse tensile strength due to standard NCF sizing aging under laboratory conditions (left) and tailored NCF aging at 50 °C and 80 % RH (right). Grey shades represent natural aging, blue shades accelerated aging. The duration of standard aging is given in months (m), and tailored aging is given in weeks (w). Natural aging data for the SE 1500 fibers are taken from Kraus et al. [61]* and Peters et al. [179]**.

weeks, almost the same residual strengths are achieved as after long-term natural aging. This implies that the tailored aging process does not promote other processes that would not occur under natural conditions. Furthermore, in this short time, a constant and individual level of the lowest transverse strength is reached for each fiber type, which is in good accordance with the results presented by Cech et al. [234]. Aging at elevated temperatures and moisture for extended periods does not further reduce the properties. Therefore, the process is also suitable for investigating and comparing the sizing stability of different systems qualitatively and quantitatively within a few weeks.

Apart from storage stability, the question naturally arises whether the new pre-aging approach can also be used to make any statements about the long-term performance of the resulting GFRP laminates. Therefore, the residual transverse strength after composite aging in a 50 °C water bath (see also Chapter 4.3.2) and the residual transverse strength after five-week NCF pre-aging in 50 °C humid air (Pre-HA) are compared in Figure 4.33. The results obtained with the six fiber

systems under investigation show a clear correlation between NCF pre-aging durability and composite water bath aging. The transverse tensile strength after NCF humid pre-aging was comparably low for the same four fiber systems that showed the largest reductions during composite aging. Even if the correlation found does not necessarily apply to all other glass fiber systems on the market, this result is remarkable.

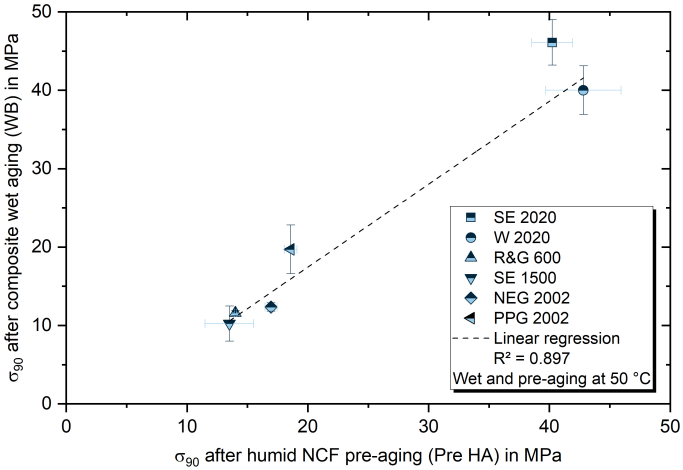

Figure 4.33: Correlation between transverse tensile strength after composite wet aging (WB) and NCF humid pre-aging (Pre-HA) for all investigated fiber types.

Therefore, the effects of moisture and temperature are clearly comparable, although a chemically bonded and fully formed fiber/matrix interphase should have a constitution different from pure sizing. One reason explaining the correlation could be that some of the weaker F/M interphases might undergo hydrolysis reactions during water bath aging, which results in a similar detachment of the interphase compared to the non-formation of bonds due to the aging of the sizing in advance. In other words, a protective function of the sizing also seems to act in the composite if the sizing itself has a high ability to withstand hygrothermal aging. This could also explain why the mechanical properties of the different composites vary considerably after classical accelerated aging in a water bath (Figure 4.21). Again, as all GFRP composites with a low transverse tensile strength after aging (and pre-aging) also show a significant reduction in 0°-tensile strength, a conclusive interpretation could be that the interphase remains protective for the fiber when the sizing has a high level of resistance to

degradation. However, based on the present study, it appears quite possible to distinguish more resistant systems from less resistant ones using the new NCF aging method.

To ensure that the humid pre-aging process does not affect the fiber strength by surface corrosion or dissolution reactions, fiber bundle tests were also performed on pre-aged fibers (SE 1500, SE 2020, W 2020, and PPG 2002) after five weeks of storage at 50 °C and 85 % RH. No significant effect was found. The residual fiber tow strength was between 97 % and 98 % of the pristine strength, while the standard deviations overlapped.

Micromechanical experiments in the sense of single fiber fragmentation (SFF) tests were performed to determine the aging effects on the interphase properties in more detail. Therefore, single fibers embedded in epoxy resin were tested in tension until fiber break saturation set in. Afterward, the specimens were analyzed under polarized light. On the one hand, this makes it possible to measure the number of fiber breaks and their distances, and on the other hand, it allows the determination of the extent of fiber/matrix debonding. Representative sections of fiber breaks of the dry, humid, and wet pre-aged fibers are shown in Figure 4.34. For the evaluation of the SFF tests, the interphase shear strength (τ_s) was calculated according to [271]:

$$\tau_s = \frac{\sigma_f \cdot d_f}{2l_c}, \tag{4.9}$$

with the fiber strength σ_f (2350 MPa), fiber diameter d_f (17 µm), and critical fiber length l_c, calculated as the average of the double fiber break distances of each of the five smallest fragment pieces:

$$l_c = 2 \cdot l_{min,5}. \tag{4.10}$$

While the mean break distance for the dry fibers is 550 ± 67 µm, and the respective mean of the minimal distances is 649 ± 78 µm, which corresponds to an interphase shear strength of 31.8 MPa using Equation (4.9), it is clear that the humid pre-aged fibers show a significantly larger distance. Here, the fiber average fracture distance of 1904 ± 479 µm equals an interphase shear strength of only about 7.7 MPa.

It is also noticeable that the F/M debonding in the humid pre-aged case is much greater than in the reference state. Consequently, the applied load cannot be

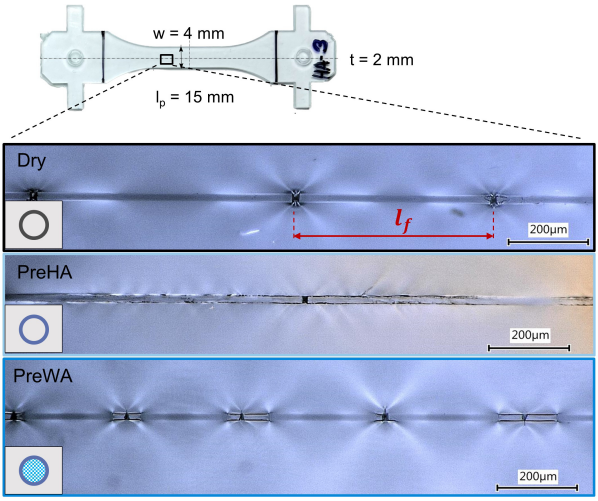

Figure 4.34: Single fiber fragmentation (SFF) test specimen (top) and representative microscopic pictures of fiber breaks for the different aging conditions.

introduced into the fiber, leading to strains and stresses in the matrix. This can also be seen in the cross-wise strain peaks in the stress-optical images. Additionally, the case of pre-aging the fibers in a water bath, similar to the tests presented in the fiber degradation chapter, was investigated. Contrary to intuitive expectations, the fiber break distance is reduced in this case, which would correspond to an increase in the interphase shear strength. However, two important factors must be remembered and considered here: Unlike aging in humid air, the fiber itself is weakened by direct contact with water.

Additionally, the fiber/matrix debonding is much more pronounced than the reference. Following this, both the interphase and the fiber strength are significantly reduced, which is also in line with the quasi-static test results for composites made after NCF pre-aging in a water bath. Here, strength reductions for longitudinal and transverse tensile tests are in a dimension of 12 % to 22 % for the SE 1500, SE 2020, and NEG 2002 systems.

To approximate the effect in numbers, it could be assumed, for example, that the interphase strength is reduced to a similar extent as in the humid case. Then, following Eq. (4.9), the residual fiber strength after water bath aging would be about 500 MPa, which is less than a quarter of the original strength. On the other hand, the interphase strength could also be somewhat higher than

in the humid aging case since the sizing in the initial application is also condensed from an aqueous solution onto the fiber surface. Nevertheless, based on the micromechanical tests, it can be said with certainty that, compared with the reference, both the fiber and the interphase strength decrease significantly. By using the new pre-aging approach, it is now possible to investigate the effects of a reduced interphase strength independently or in combination with a reduced fiber strength on the properties of a composite. In the future, additional micromechanical tests, such as droplet or single-fiber strength tests, can be used to validate the methodology further and reveal more exact fiber and interphase strength properties. However, it was proven that the method is suitable to investigate the effects exclusively arising from a weakened (aged) F/M interphase.

Impact of interphase and/or fiber aging on fatigue properties

Humid and wet pre-aged composites were tested with identical dogbone-shaped specimens under tensile fatigue loading as an extension of the fatigue tests presented in Chapter 4.3.2. Therefore, three types of NCFs (fiber systems SE 2020, SE 1500, and NEG 2002) and a pure UD winding of a laboratory modification of the SE 2020 fibers by 3B were humid aged for five weeks at 50 °C and 80 % RH prior to manufacturing. Wet pre-aging with immersion of the fabrics in distilled water at 50 °C was performed for two of the systems. It is worth noting that all NCF-based composites were made using similarly constructed fabrics marketed by Saertex as Ultra Fatigue UD. Therefore, the impacts of the NCF structure on the lifetime can be mostly excluded. The fatigue results for the ECR-glass fiber systems SE 1500 (older sizing variation) and SE 2020 (marine suitable sizing) are presented in Figure 4.35. The results for the NEG 2002 NCF-based composite and the pure unidirectional winding of the SE 2020 modification are shown in Figure 4.36.

By comparing the individual results and Wöhler-curves, several distinctions can be observed. So, the reduction in interphase strength due to humid pre-aging leads to a significant decrease in fatigue life without changing the slope of the Wöhler-curve for all systems except the NEG 2002, which is based on the fewest test results. This also suggests that there is no change in the fundamental damage procedure. The lifetime reduction due to only interphase aging can be up to a decade at the same load level or 100 MPa at the same lifetime. This is true independently of the total level of load/lifetime. In terms of absolute

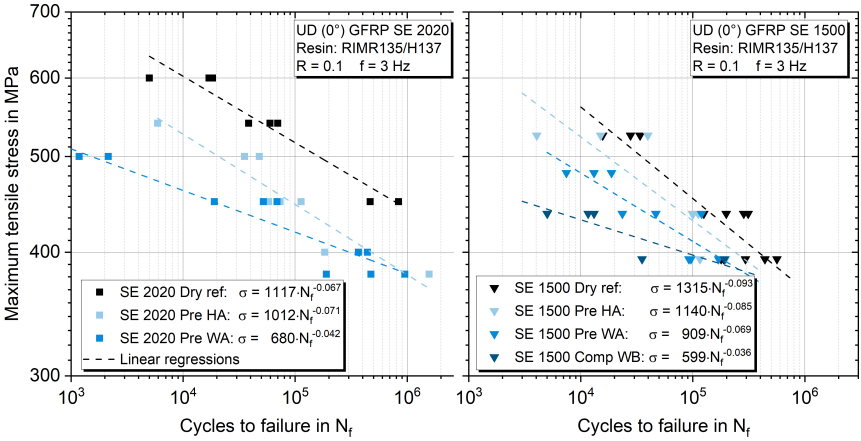

Figure 4.35: Tensile fatigue life diagram of SE 2020 (left) and SE 1500 (right) UD-composites (backing fiber share $\leq 5\,\%$) in dry, pre-HA, pre-WA, and immersed wet-aged conditions.

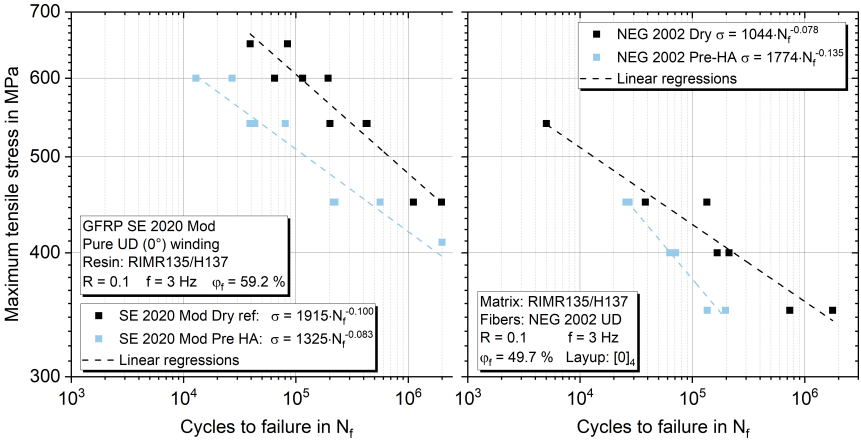

Figure 4.36: Tensile fatigue life diagram of SE 2020 Mod (left) and NEG 2002 (right) UD-composites (backing fiber share of NEG $\leq 5\,\%$, pure UD for SE 2020 Mod) in dry and pre-HA conditions.

load level, it corresponds to a reduction of tolerable fatigue loads by up to 20 %, which is particularly critical since the reduced strength is not observable in the quality of the composites after manufacturing. Furthermore, it was shown that sizing degradation can take place during storage by natural aging for most of the fiber systems.

The wet-aging of the NCFs and the associated reduction of interphase and fiber strength before composite fabrication further reduce fatigue performance for both ECR-glass systems. In addition to the reduction in lifetime, there is also a decline in the slope of the Wöhler-curve. The change in slope is due to reduced fiber strength (see Chapter 4.3.3). At high loads, disproportionately more fibers fail than at low loads, directly decreasing the load-bearing capacity and lifespan of the specimen. In contrast, the load transfer between the fibers is again highly important at lower loads. Due to the weakened interphase, this is inferior to the reference condition but comparable to the humid pre-aging case.

Figure 4.37 shows representative macroscopic images of failed fatigue specimens (top) and microscopic images of broken fiber bundles inside the specimens (bottom). Additionally, SEM images of different bundles from the same specimens are presented in Figure 4.38. Both visualizations are used to analyze the different damage mechanisms. Although it is impossible to distinguish between reference and pre-aged specimens based on their macroscopic appearance after testing, the microscopic views reveal major differences. In the un-aged condition, bundle failure is characterized by a relatively uniform fracture pattern of fibers totally embedded and bonded with matrix resin. Thus, there is no clear evidence of preceding fiber/matrix debonding. In contrast, the fibers in humid pre-aged specimens are completely free of the epoxy matrix over a distance of several hundred micrometers. Here, the damage and failure mechanism has changed significantly. However, large F/M debondings are expected to grow after a fiber failure occurs before the next weak fiber breaks in a larger distance than in the reference condition. The SEM images reveal a comprehensive debonding along the F/M interphase, where the matrix fractions visible have the negative form of the fibers without additional matrix damage. For the case of wet pre-aging, the picture is different again. The fiber ends are also entirely free of matrix residues, but the affected ends are significantly shorter. Considering the results of the SFF tests, this could be attributed to the drastically reduced fiber strength or the significantly increased defect density. As soon as a fiber break leads to a F/M debonding, the delamination stops early since another weak fiber is overloaded and breaks within a narrow radius. However, almost every fiber shows extensive F/M debondings along the interphase. Again, the matrix resin shows mirror-like, smooth fracture surfaces, while hackles and steps in the dry case characterize it. Importantly, the severe consequences of interfacial property

degradation on the lifetime of UD 0°-laminates could be revealed and characterized by the introduced stepwise aging methods in a new quality.

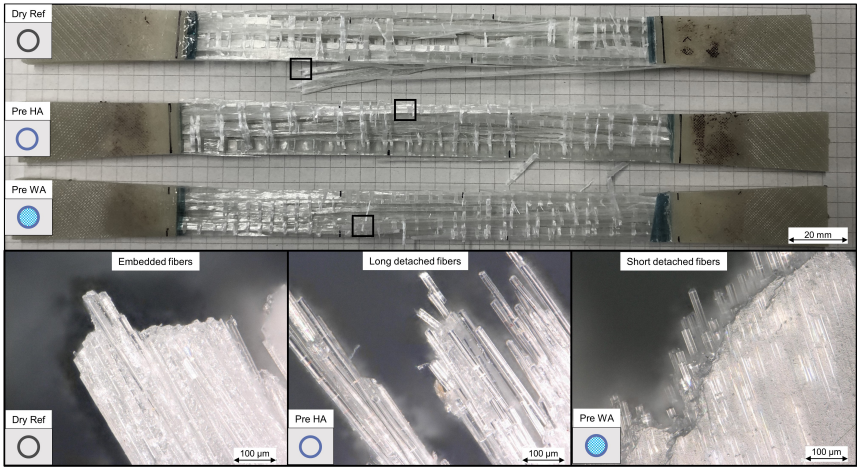

Figure 4.37: Macroscopic images of specimens after fatigue testing (top) and microscopic images of broken fiber bundles from specimens (black squares) in relation to different (pre)conditions (bottom) for the SE 2020 composite.

Modeling the Effects of Interphase Aging on Fatigue Properties

Sörensen et al. [1, 188, 189, 256] developed and introduced a comprehensive micromechanical model to predict the fatigue behavior of UD composites. The experimental results achieved and described previously are used to adjust the given model and further enhance the understanding of the importance of interphase properties on the fatigue life of UD composites. In short, the key ability of the model is to consider various interphase parameters for the prediction of the lifetime for unidirectional composites under tensile fatigue loading in the longitudinal fiber direction. This fundamental work provides a detailed description of the dominating damage mechanisms in UD composites. It highlights the importance of the F/M interphase, which usually attracts less attention than the fiber properties. The fatigue results achieved by using the novel pre-aging method to age the F/M interphase separately now provide a possibility to review the consistency between the model and experiments. Please refer to the original literature for a detailed derivation of the equations and correlations [1, 188, 189, 256]. However, the most important equations adopted for the modeling process will follow. Using the model, the strain ϵ_{max}, fiber debonding rate $\frac{\delta a}{\delta N}$, and

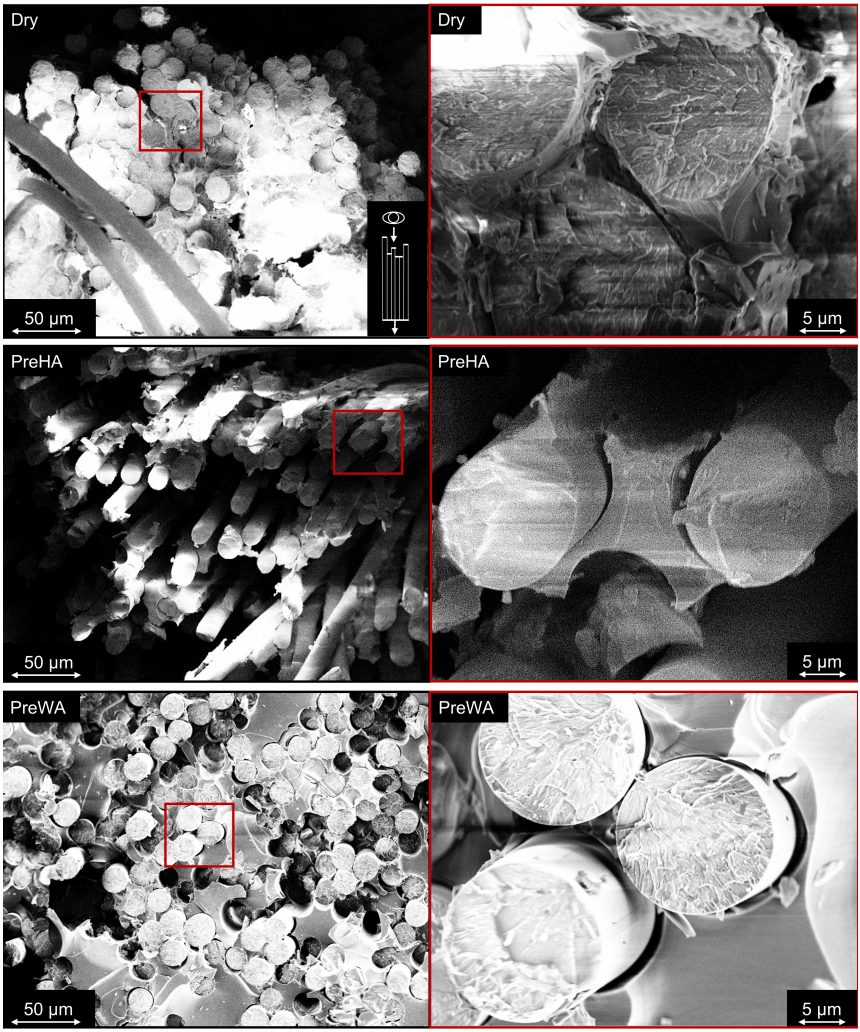

Figure 4.38: SEM images of broken specimens (view on top of single broken fiber bundles) after fatigue testing for different aging conditions (left) and zoom showing the F/M interphase region in more detail (right). All pictures show the SE 2020 composite.

mode II fracture toughness $G^c_{II,c}$ dependent fatigue cycles to failure N_f can be described as [1]:

$$N_f = \frac{4\,G^c_{II,c}}{E_c\,r\,\epsilon^2_{max}}\sqrt{\frac{2V_f}{\sqrt{3}\,\pi}}\,N^*, \tag{4.11}$$

with the composite modulus E_c, the fiber radius r, the fiber volume fraction V_f, and N^*, the number of cycles N where the next (neighboring) fiber breaks. Within the modeling approach $G^c_{II,c}$ is not directly taken from composite testing results, e.g., by ENF tests, but based on the micromechanical relation of the mode II fracture toughness of the matrix $G^m_{II,c}$ and the fracture toughness of the F/M interphase G^i_c. Therefore, $G^c_{II,c}$ is calculated as follows [1]:

$$G^c_{II,c} = \left(1 - \sqrt{\frac{2\sqrt{3}\,V_f}{\pi}}\right) G^m_{II,c} + \frac{\pi}{2}\sqrt{\frac{2\sqrt{3}, V_f}{\pi}}\,G^i_c. \tag{4.12}$$

Furthermore, the critical cycle number for the next fiber break N^* is defined as [1]:

$$N^* = N_c\left(\frac{\tau^0_s}{\tau^0_s - \tau^c_s}\left[1-(1-R)\left\langle\frac{2}{\epsilon_{max}}\left(2\frac{\tau^0_s\,l^*_d}{E_f\,r}+\frac{\overline{\sigma}_I}{E_c}\right)-(1+R)\right\rangle^{-1}\right]\right)^{\frac{1}{n}}, \tag{4.13}$$

with N_c, the number of cycles it takes to decrease the initial frictional sliding shear stress at the interphase τ^0_s to the final (low) value of τ^c_s (when no further debonding growth takes place), the R-ratio R, the fiber modulus E_f, the shape parameter n, the debonding initiation stress $\overline{\sigma}_I$, and the critical debonding length l^*_d, at which the next fiber break occurs with a probability of 50 %. Finally, the critical debonding length is defined as [1]:

$$l^*_d = r\left[\left(\frac{3\,ln(2)\,L_0}{2r}\right)\left\langle\left(\frac{\sigma^+_f + \hat{\sigma}^K_f}{\sigma_0}\right)^m + 2\left(\frac{\sigma^+_f}{\sigma_0}\right)^m\right\rangle^{-1}\right], \tag{4.14}$$

with the characteristic fiber strength σ_0 of a fiber length L_0, the fiber Weibull modulus m, and the fiber stresses far ahead of the debonding σ^+_f and at the debonding crack tip due to the K-field stress concentration $\hat{\sigma}^K_f$. According to [1, 188], these can be defined as:

$$\frac{\sigma^+_f\,\overline{\epsilon}_{max}}{E_f} = -\Delta\epsilon^T\frac{(1-V_f)\,E_m}{E_c} + \overline{\epsilon}_{max}, \text{ and} \tag{4.15}$$

$$\hat{\sigma}^K_f = 0.435\frac{E_f}{E_m}\sqrt{\frac{G^i_c\,E^*}{d^*}}, \tag{4.16}$$

with the thermal mismatch strain between fiber and matrix after curing $\Delta\epsilon^T$ due to the difference in longitudinal thermal expansion coefficients, the maximum applied strain on the specimen $\overline{\epsilon}_{max}$, the inter-fiber spacing distance d^* at perfect hexagonal fiber packing, and the plane stress modulus E^* given by [1]:

$$\frac{1}{E^*} = \frac{1}{2}\left(\frac{1}{E_f} + \frac{1}{E_m}\right), \text{ and} \tag{4.17}$$

$$d^* = r\left(\sqrt{\frac{2\,\pi}{\sqrt{3}\,V_f}} - 2\right). \tag{4.18}$$

Finally, the debond initiation stress $\overline{\sigma}_I$ can micromechanical (following the assumption for an SFF test situation) be defined as [1, 188]:

$$\frac{\overline{\sigma}_I}{E_c} = \frac{(1-V_f)\,E_m}{E_c}\Delta\epsilon^T + 2\sqrt{\frac{(1-V_f)\,E_m}{E_c}\left(\frac{G_c^i}{E_f\,r}\right)}. \tag{4.19}$$

Considering all these correlations, material parameters, and assumptions, the experimental fatigue test data presented in the previous chapter can be attempted to be described by the model. Therefore, the stress-related lifetime diagram was converted into a strain-related diagram. Furthermore, the model parameters presented and used by Sörensen et al. [1, 188] were adopted whenever reasonable and adjusted to the fiber, matrix, and interphase properties of the actual SE 2020 composite based on own test results. A list of all parameters used to describe the experimental results of the initially dry reference specimens with a reasonable good fit is given in Table 4.3. All parameters that might be changed due to humid or wet pre-aging of the fibers (fabrics) are given in Table 4.4 for the five fits presented in Figures 4.40 and 4.42. Interphase properties that can be (indirectly) determined by the SFF test are the interphase shear strength τ_s and the fracture toughness of the interphase G_c^i. In accordance with the fundamental description of the test on the micro-mechanical level, τ_s was not only determined by the classical approach using Eq. 4.9 (leading to τ_s =31.8 MPa), but also by evaluating the applied strain-dependent debond lengths. Therefore, the slope of the linear regression of the applied strain versus normalized debond length correlation can be used as [188]:

$$\tau_s = \frac{E_f}{2}\frac{d(\frac{\overline{\sigma}}{E_m})}{d(\frac{l_d}{r})}. \tag{4.20}$$

The evaluation of the debond length development during loading in an SFF test is presented in Figure 4.39. Here, it must be noted that the debonded length was evaluated in stress-free conditions after loading with the respective maximum load, as no in situ measurement was possible.

Table 4.3: Overview of the model parameters used to describe the fatigue results of the SE 2020 composite. These parameters are assumed to be unchanged for composites made after humid or wet pre-aging of the fibers. Index $^{a)}$ indicates values adopted from Sörenesen et al. [1, 189].

$\Delta\epsilon^T$ (–)	V_f (–)	E_f (GPa)	E_m (GPa)	E_c (GPa)	r (µm)	L_0 (m)	τ_s^c (MPa)	$G_{II,c}^m$ (J/m²)	R (–)	m (–)
$0.00346^{a)}$	0.495	81.0	2.8	39.0	8.5	$0.02^{a)}$	$3.1^{a)}$	$4500^{a)}$	0.1	$4.62^{a)}$

Table 4.4: Overview of the aging-dependent model parameters used and calculated (last three) to describe the fatigue results of the SE 2020 composite. These parameters are assumed to be affected for composites made after humid or wet pre-aging of the fibers. Index $^{a)}$ indicates values adopted from Sörenesen et al. [1].

Condition	G_c^i (J/m²)	τ_s^0 (MPa)	N_c (Cylces)	σ_0 (MPa)	n (–)	l_d^* (mm)	$G_{II,c}^c$ (J/m²)	$\overline{\sigma}_I$ (MPa)
Dry (reference)	72	31.0	$50000^{a)}$	2050	0.1	0.251	1259	156.8
PreHA (const. G_c^i)	72	22.0	10000	2050	0.1	0.251	1259	156.8
PreWA (const. G_c^i)	72	22.0	10000	1900	0.1	0.251	1259	156.8
PreHA (G_c^i, τ_s^0, N_c)	22	6.0	15	2050	0.1	0.999	1201	88.8
PreWA (G_c^i, τ_s^0, N_c, σ_0)	22	6.0	25	1800	0.1	0.543	1201	88.8

The interphase shear strength was calculated based on Eq. 4.20 and is 30.7 MPa. This value is very close to what was calculated by considering the fiber fragment length, even though the standard deviation is relatively high, as only a few fiber breaks could be evaluated subsequently. Based on both methods, the initial value for tau was defined as 31.0 MPa. As there are not enough own test results available to also precisely calculate the strain mismatch $\Delta\epsilon^T$ (0.0079 by own data) and G_c^i according to [188], the first value was adopted as $\Delta\epsilon^T = 0.00346$. G_c^i was taken from the graph given in [188] based on the applied stress and now known τ_s to $G_c^i = 72\,\mathrm{J/m^2}$.

Another parameter adopted from Sörensen et al. [189] is the mode II matrix fracture toughness ERR $G_{II,c}^m$ of $4500\,\mathrm{J/m^2}$, which seems to be a fairly high value that is by a factor of five to ten higher than results presented for toughened epoxy,

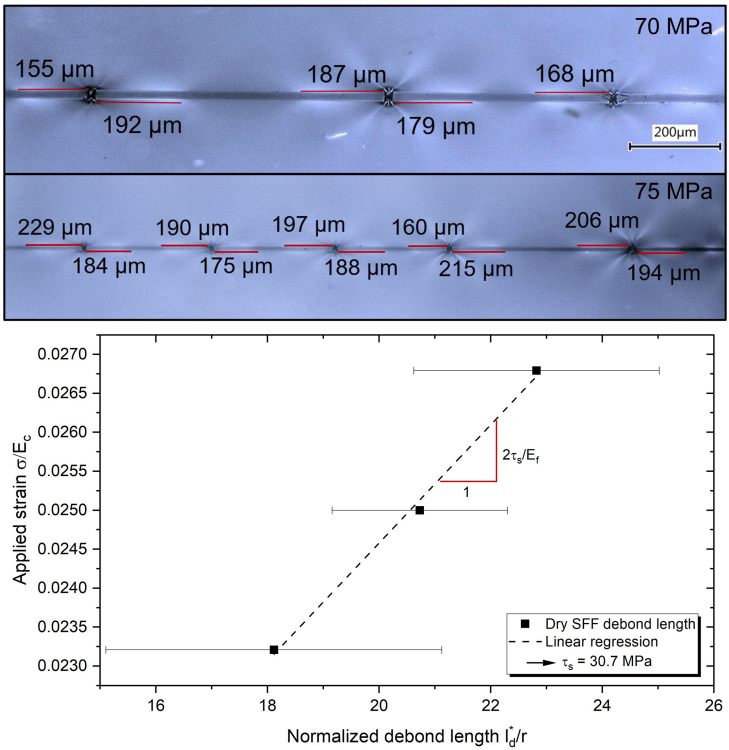

Figure 4.39: Image of SFF specimens and debonding length evaluation at 70 MPa and 75 MPa (top). Evaluation of the interphase shear strength τ_s by plotting the applied strain versus the average fiber debonding length (bottom).

e.g., by Körbelin [146], or Quan et al. [272]. However, it was demonstrated in 1988 by Chai [273] that the mode II matrix fracture toughness is very sensitive to the resin thickness, as the kinking of the crack in the direction of mode I is limited for very thin layers. Therefore, differences of more than a factor of five could be experimentally demonstrated for bulk specimens with a thickness of $\geq$ 200 µm and thin specimens with a thickness of 20 µm to 50 µm. Thus, a mode II fracture toughness of more than 3000 J/m^2 could be demonstrated for an epoxy adhesive. Assuming that the resin thickness between the fibers within a fiber bundle is only a few microns, the high fracture toughness seems meaningful. Furthermore, taking Eq. 4.12 into account, a value of $G^m_{II,c}$ 4500 J/m^2 leads to a $G^c_{II,c}$ value of about 1100 J/m^2, which is reasonable as well but lower than experimentally determined for the SE 2020 composite, see Chapter 4.3.5. The

modeling prediction for the strain-dependent fatigue lifetime of the SE 2020 composite is shown in Figure 4.40. All used parameters are given in Tables 4.3 and 4.4 based on the experimental results previously described and the respective literature survey.

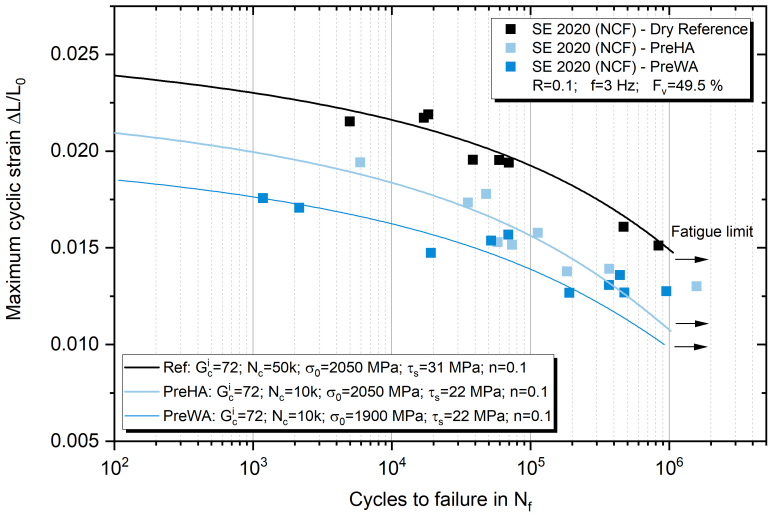

Figure 4.40: Initial tensile fatigue predictions according to Eq. 4.11 and test data (strain-based) for dry, humid, and wet pre-aged SE 2020 composites.

Even if one cannot assume that all selected parameters are based on physics and represent the true facts, the results obtained for the dry composite can be reproduced well with the chosen parameter set. Therefore, this set is taken as a reference to analyze further the effects of a weakened interphase (PreHA) or simultaneously weakened interphase and fibers (PreWA). The first fitting models for these two conditions are also shown in Figure 4.40. They are achieved by only varying the initial frictional sliding shear stress τ_s and the critical number of cycles needed to break a neighboring fiber N_c (PreHA) or, additionally, the fiber strength σ_0 (PreWA). However, even though these predictions align with the experimental data, it seems unreasonable that only two interphase-related parameters will change due to aging. This can also be comprehended by checking the calculated critical debond length, mode II composite fracture toughness, and debonding initialization stress given in Table 4.4. Without changing the interphase fracture toughness, none of these characteristic values changes by

aging, which is unlikely. Consequently, a parameter study of the potentially most affected parameters was conducted and is shown in Figure 4.41.

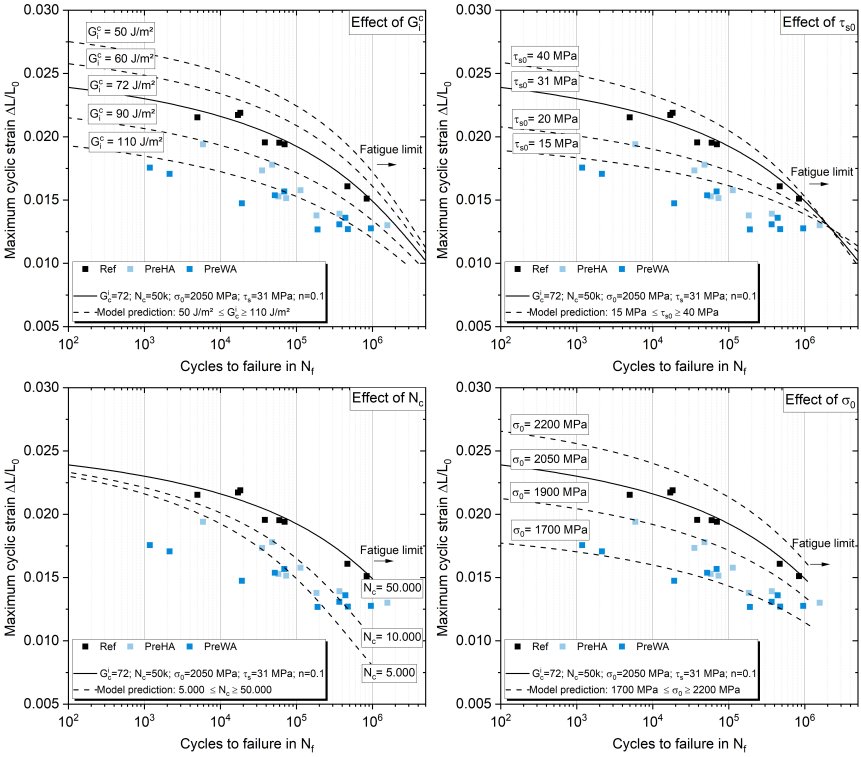

Figure 4.41: Modeling parameter study for the main interphase and aging dependent variables: G_c^i, $\tau_{s,0}$, N_c, and σ_0.

The graphs reveal the range and extent to which the predicted lifetimes change when only one parameter is modified separately. Thus, it becomes clear that changing the interphase fracture toughness strongly impacts the allowable strain at a fixed lifetime. In contrast, e.g., the critical number of cycles to trigger the next fiber break N_c affects primarily the high cycle fatigue regime. In particular, the counterintuitive correlation between the interphase fracture toughness G_c^i and the lifetime is noteworthy, as it implies that a higher interface strength will lead to lower fatigue life of unidirectional composites. This apparent contradiction can be explained by analyzing the equations 4.15 and 4.16. It becomes clear that the stress at the debonding crack tip $\hat{\sigma}_f^K$ is the higher, the higher G_c^i is. Similarly, the stress the neighboring fibers must endure in the crack tip area

also increases. As a result, it is more likely that a further fiber break will occur [1].

As shown with the SFF tests discussed in the previous chapter, the humid pre-aging of the fibers (fabrics) has dramatically reduced the interphase shear strength. With a four times increase of the average minimum fragment length, the experimentally found residual shear strength is only about 6 – 8 MPa. Assuming that the fiber strength is not changed by humid pre-aging (see Chapter 4.3.3), the fracture toughness has to decrease simultaneously, and the debonding rate (indicated by N_c) has to increase. The best-fitting solutions, taking the reduced τ_s of 6 MPa as a starting point, can be taken to evaluate the impact of aging on the interphase and damage parameters. This is presented in Figure 4.42. Therefore, it is likely and necessary to fit the experimental results that the interphase fracture toughness decreases by about 70 % due to humid pre-aging, which leads to a dramatic increase in the debonding growth rate. Here, the number of cycles to grow the debonding to the maximum length was found to be only 15.

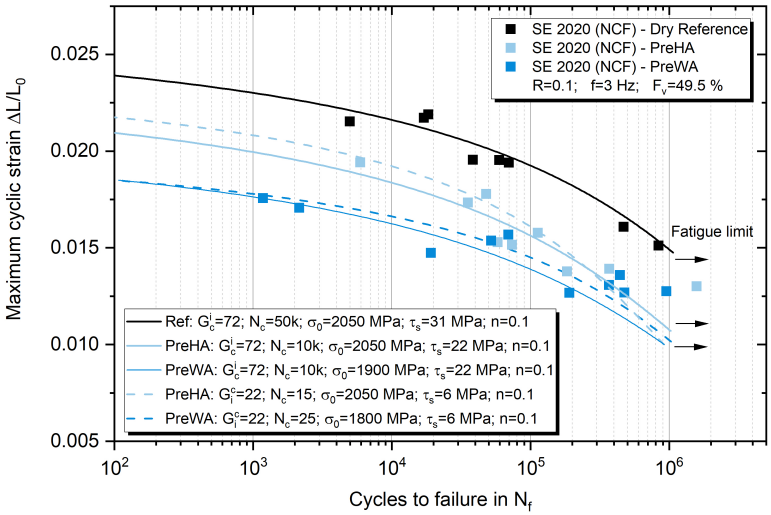

Figure 4.42: Initial and parameter-study-based tensile fatigue predictions according to Eq. 4.11 and test data (strain-based) for dry, humid, and wet pre-aged SE 2020 composites.

To finally describe the differences between the humid and wet pre-aging results, it is assumed that the main difference between both cases is the additionally

reduced fiber strength in the wet-aged case. Therefore, all other parameters than σ_0 were held constant to fit the experimental results. The best fit was obtained with a remaining fiber strength of 1800 MPa, which represents a reduction of about 13 %. This theoretical value also aligns well with the static tensile strength results obtained for the UD composites made of wet pre-aged fabrics. The static strength reductions found are between 11 % and 19 % for the different composites. Furthermore, the fiber bundle tests described in Chapter 4.3.3 revealed a fiber strength reduction of nearly 20 % for the SE 2020 fibers after five weeks of aging in a water bath at 50 °C.

In summary, revealing and describing lifetime reductions expected due to interphase and fiber strength reductions in a UD composite was experimentally and analytically possible. Experimentally, these isolated aging conditions were evoked by humid and wet pre-aging. Analytically, the models proposed by Sörensen et al. [1, 188] were adopted and adjusted based on the properties revealed by (micro)mechanical tests. Consequently, reasonable combinations of experimental results and analytical calculations were used to find model parameters that fit the test results well. In the case of the humid pre-aged specimens, the fracture toughness of the interphase, the interphase frictional sliding shear strength, and the critical number of cycles to drive the debonding to the maximum distance are dramatically reduced. For wet-aged specimens, the fiber strength is reduced as well. The experimental results, model curves, and chosen parameter sets are presented in Figure 4.42 with the dashed lines. Hence, it seems possible to predict the effects of classical aging and the contributions of fiber, matrix, and interphase degradation on UD composites with reasonable accuracy in the future.

4.3.5 Environmental Effects on Interlaminar Properties

The effects of different kinds of aging (interphase pre-aging, composite wet-aging, and their combination), as well as the effect of the environmental testing temperature on the composite's interlaminar properties, were determined by performing DCB and ENF tests. Test details are given in Chapter 2.1. The main fracture toughness results in terms of mode I and II initiation ERR are presented for the SE 2020 composite, with the highest sizing and interphase quality, and the NEG 2002 composite, with lower sizing and interphase quality, in Figures 4.43 and 4.47.

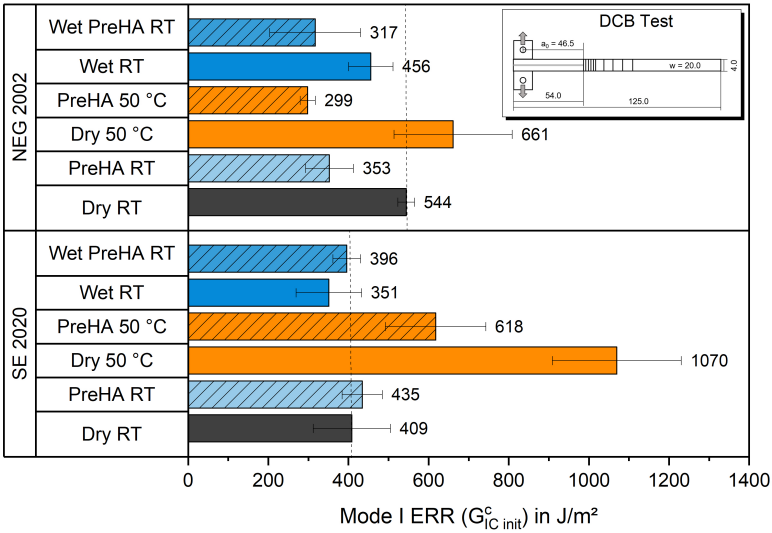

Figure 4.43: Mode I initial energy release rates of the SE 2020 and NEG 2002 composites for different aging conditions.

First, it becomes clear that the effects of the individual conditions under mode II loading exhibit a uniform trend for both composites, while under mode I, there are more pronounced differences for the NEG system. The mode I initiation ERRs in dry conditions at room temperature are with about 400 to 550 J/m² well in line with typical values reported for GF/EP composites at crack initiation [274, 275]. Wet-aging of the composite in distilled water at room temperature for nearly half a year (165 days) and humid pre-aging of the fibers reduce the mode I ERR of the NEG composite by about 16 % and 35 %, respectively. Consequently, the reduction by combining both pre-aging and additional wet-aging is with about 42 % even higher. This indicates that the mode I ERR depends on the matrix and the interphase properties. However, a weak interphase quality (strength) significantly decreases the mode I ERR of the NEG 2002 composite.

This observation can be confirmed by the SE 2020 composite tests only in the case of the tests at elevated temperatures (50 °C), where again, a reduction of about 42 % was found due to humid pre-aging. The tests at room temperature revealed only marginal differences in the mean values with overlapping standard deviations. Reasons for this could be both the significantly higher remaining interphase strength (≥40 MPa after pre-aging and ≥50 MPa after wet aging at

RT) of the SE 2020 system, a potentially lower glass transition temperature of the pre-aged interphase, and the relatively low number of three samples per configuration. The fact that the SE 2020 reference and the pre-aged composites have the same initiation ERR is remarkable, as the crack surfaces show mainly blank fibers after pre-aging (see Figure 4.46). Consequently, it could be hypothesized that the main proportion of the energy consumption in the DCB test can be associated with matrix fracture of the resin-rich regions and the geometry impact of, e.g., the stitching. In this case, the difference between a mode I crack growth in the brittle resin or the interphase with still acceptable quality is minor. In contrast, increasing the testing temperature to 50 °C significantly increased the mode I ERR of both composites, while it was more pronounced for the SE 2020. In this case, the composite's $G^c_{IC,init}$ follow explicitly the G^m_{IC} of the resin.

The differences described for the crack initiation phase, $G^c_{IC,init}$, diminish for most conditions with increasing crack length, as fiber bridging effects dominate the ERR at crack lengths of $\geq$ 20 mm. In the case of the SE 2020 specimens, $G^c_{IC,20mm}$ is around 1000 J/m², and for the NEG 2002, around 1500 J/m². The only marginal trend is an increase with rising temperature, which is less than 10 % for 50 °C and only becomes substantial at 70 °C (factor three higher).

The effect of the environmental temperature on the mode I ERR was tested in more detail for the SE 2020 composite. The results for a temperature range from −20 °C to 70 °C are presented in Figure 4.44. It is evident that the mode I ERR is relatively constant at lower temperatures and rises rapidly with elevation above room temperature, which corresponds to the results reported by Machado et al. [217] for epoxy-based CFRP. This is true for both non-aged and pre-aged composites with high and low interphase strengths. However, the increase is much lower when the interphase strengths are low, as in this case, the fracture paths are dominated by adhesively debonding of the F/M interphase, which means that the increased resin ductility is less prominent. Therefore, it is likely that the lower interphase strength of the NEG 2002 composite is also the reason for the comparably lower increase of the mode I ERR at elevated temperatures since the resin properties behave similarly in both composites.

Representative microscopic images of the fracture pattern at the crack tip and initiation region of the DCB specimens are shown in Figures 4.45 and 4.46. The differences caused by the aging conditions or the environmental temperature are visible. While the mode I crack runs through the matrix-rich region between

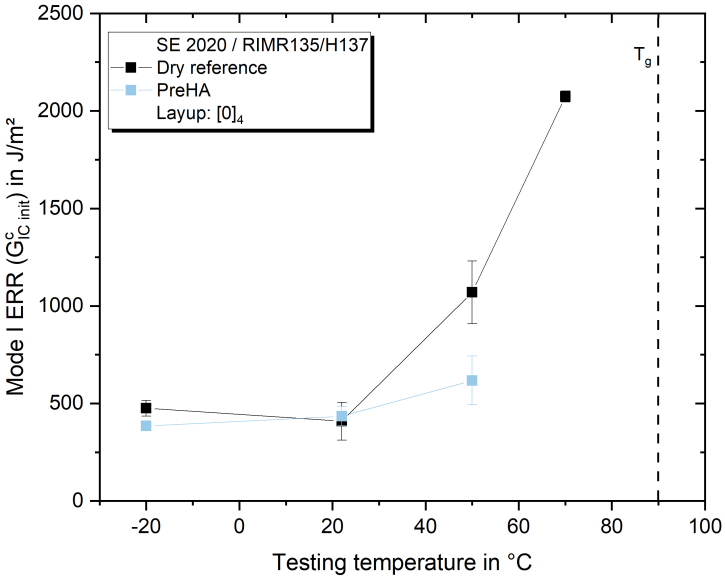

Figure 4.44: Mode I initial energy release rates of the SE 2020 composite for different testing temperatures.

both 0°-plies at reference conditions, the crack jumps over planes along the interphases (partly intralaminar) at 50 °C. This behavior could result from the significantly increased fracture toughness and simultaneously decreased yield strength of the resin and interphase, which both enlarge the (plastic) process zone. Therefore, energy-consuming crack jumps over plies become possible. In the water-aged condition, the crack still progresses in the matrix region but shows some ductile deformation at the crack surfaces. Concerning the top view on the fracture surfaces, the dry reference specimens at room temperature and 50 °C show fibers, mostly embedded in the matrix resin. The fibers appear much more released in all other cases.

Consequently, cohesive matrix failure is mainly seen in dry and un-aged conditions. Pre-aging of the fibers considerably changes the fracture paths from cohesive matrix failure to adhesive fiber/matrix debonding. The wet aging of the reference composite represents a mixed situation. Although more fibers appear to be separated from the matrix than in the dry state, cohesive matrix failure with pronounced small hackles of shear fractures occurs likewise. That is why the reduction in mode I ERR is comparatively small after wet aging.

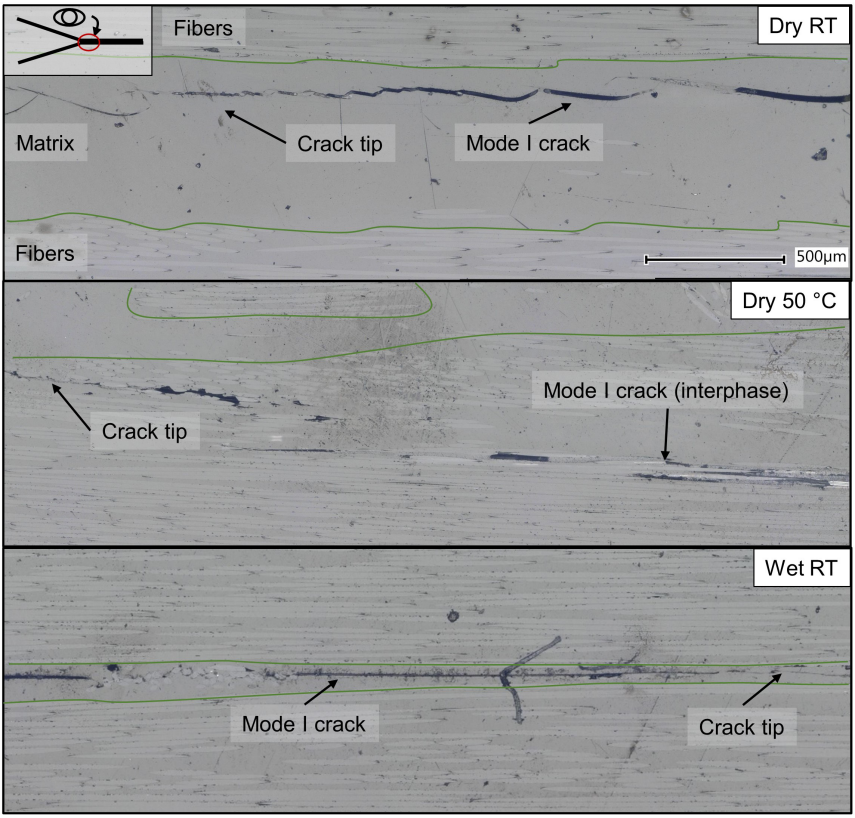

Figure 4.45: Microscopic images of the DCB mode I fracture of the SE 2020 composite at the crack tip region for different aging conditions and testing temperatures as a side view. Additionally, the F/M interphase is highlighted in green.

The results obtained by ENF tests demonstrate that the mode II ERR is more related to the F/M interphase properties than the mode I ERR. Humid pre-aging and the resulting lower interphase strength reduce the mode II ERR uniformly for both composites. The fracture toughness increase and yield strength decrease of the matrix due to water absorption and testing at elevated temperatures affect the mode II ERR in combination less within the tested range. These effects could partially neutralize each other. The composite mode II fracture toughness reduction due to the decreasing interphase strengths by humid pre-aging is between 12 % and 22 % for dry tests at room temperature. Elevating the testing temperature solely reduces the mode II ERR by about 16 %, while the

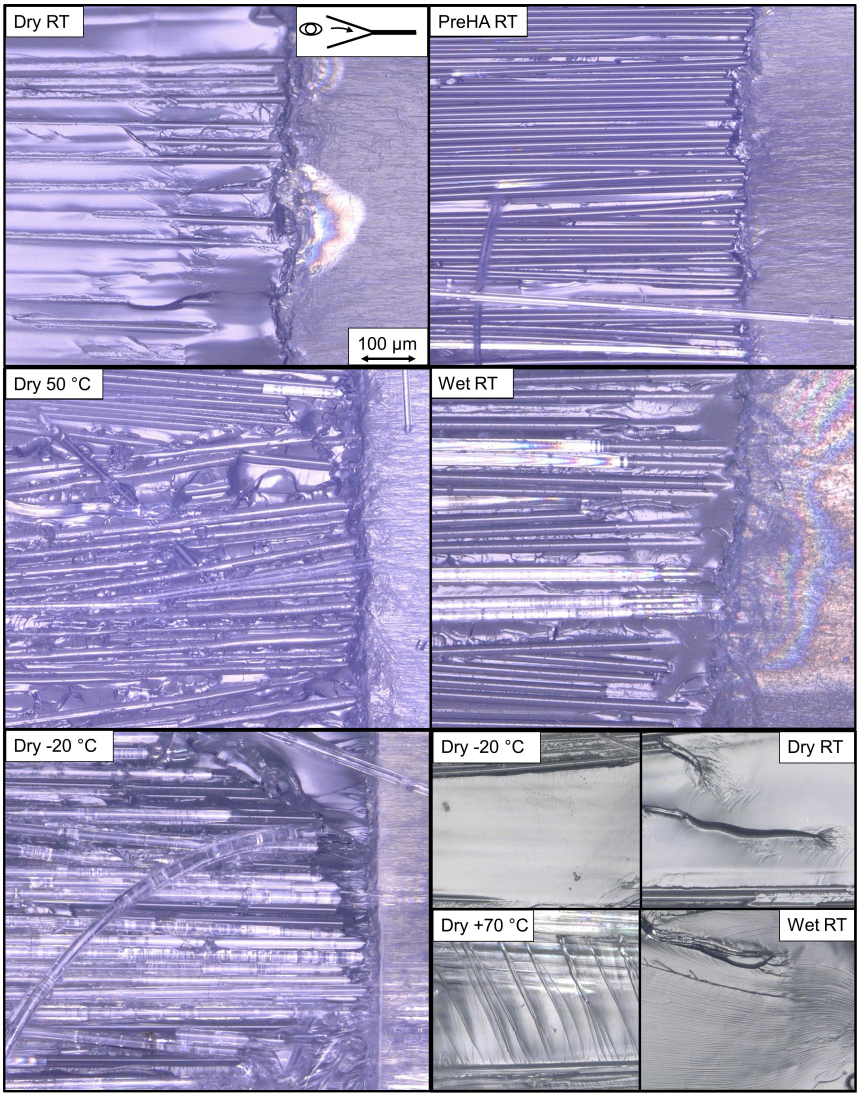

Figure 4.46: Microscopic images of the DCB mode I fracture surfaces of the SE 2020 composite at the crack initiation region for different aging conditions and testing temperatures. Additionally, fracture patterns of resin-rich regions are shown in the right lower edge.

combination with a weakened interphase leads to decreases between 30 % and 40 %. Wet aging of the composite, in contrast, slightly increases the mode II ERR

by about 5 %. Furthermore, the weakening effect of a debilitated interphase prevails for the combination of both aging procedures (reduction of between 22 % and 28 %). The pronounced differences between the wet-aged and pre-aged conditions and between the wet-aging of a standard and pre-aged composite also highlight the resilience of the F/M interphase to water aging at moderate temperatures of $\leq 22\,°C$.

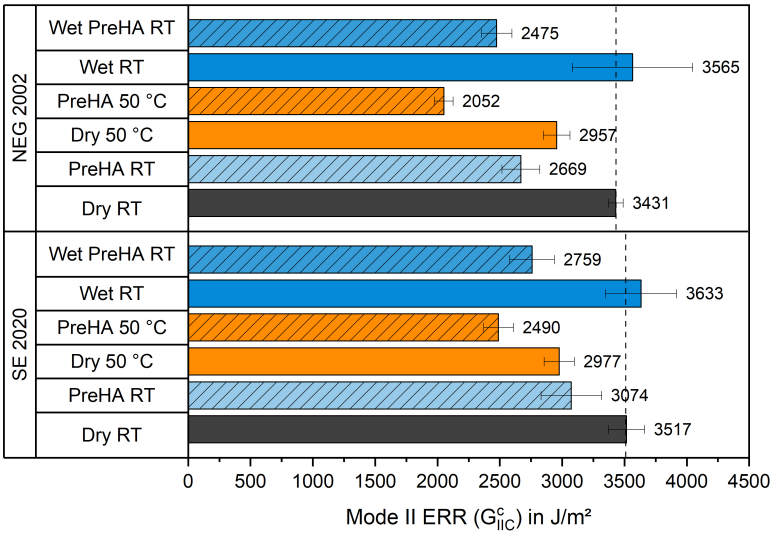

Figure 4.47: Mode II energy release rates of the SE 2020 and NEG 2002 composites for different aging conditions.

Considering the images of the mode II fracture paths shown in Figure 4.48, it becomes clear that the amount of mode II matrix fractures increases with temperature and water absorption. Different from what is intuitively expected, the appearance of this failure type reduces the mode II ERR. It thus consumes less energy than the pronounced interphase delaminations shown for the reference. Again, this behavior is associated with a significant decrease in shear yield strength, which apparently predominates the composite's global mode II ERR. Typically, for all failure paths, ply jumps and mode II cracks under 45° can be seen at the stitching yarns. Depending on the quality of their interfacial bonding with the resin, these areas can either be the origins of damage or partially stop the crack growth. Finally, it should be taken into account that the crack growth in an ENF test usually progresses unstablely after the maximum load is reached. The higher the non-linearity of the stress-strain curves, the more likely a stable

crack growth. For the GFRPs investigated, a non-linear flattening or plateau with a subsequent drop is the norm for all conditions.

In summary, the results obtained by the fracture toughness investigation confirm the trends assumed and hypothesized to explain at least a part of the fatigue behavior of unidirectional composites under different aging conditions. As demonstrated by the modeling in the last chapter, the reduction of the fatigue properties can be mainly attributed to a decrease of the $G^c_{II,C}$ (mode II ERR) due to the weakening of the F/M interphase strength. In contrast, water absorption without decomposition of the interphase can enhance the ERRs and, therefore, might also increase the fatigue life of UD composites, as shown in Gibhardt et al [31]. Furthermore, the study details reveal some major correlations of the complex damage behavior.

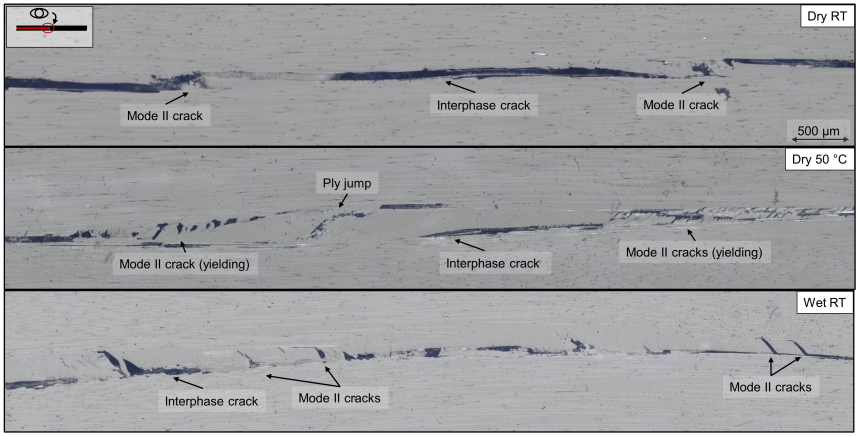

Figure 4.48: Microscopic images of the Mode II fracture paths.

First, a decreasing interphase strength significantly reduces $G^c_{II,C}$. The effects are even more severe than the changes in the matrix resin properties ($G^m_{I,C}$, σ_y, τ_y, E, G) caused by water absorption and temperature variation. As schematically shown in Figure 4.49, the matrix properties follow opposite directions. While strength and stiffness decrease, the fracture toughness increases. For the investigated composites, the declining strength seems to dominate the composite mode II ERR.

Furthermore, the fact that $G^c_{II,C}$, in contrast to $G^c_{I,C}$, reduces with an increase in temperature but increases slightly due to water absorption is also unintuitive at

first glance. These findings align with mode I and mode II (CFRP) temperature-dependence investigations by Machado et al. [216, 217], reporting an increase of $G^c_{I,C}$ by about 150 % at 80 °C. In comparison, $G^c_{II,C}$ simultaneously increases only by 10 %. Likewise, Beaumont et al. [223] found opposing trends for mode I and mode II ERR with increasing temperature for CFRP made from thermosetting cyanate esters. Here, $G^c_{I,C}$ increased by about 50 %, whereas $G^c_{II,C}$ decreased by about 50 % at 140 °C.

This behavior is hypothesized to be a result of the different contributions of the matrix and the interphase to mode I and mode II ERR [223]. According to Drzal [222] and Russel [276], mode I fracture is primarily dominated by the matrix and mode II by interphase properties. Under mode II at high temperatures, for example, the reduced energy required for debonding and pull-out might outweigh the increased ductility and thus reduce $G^c_{II,C}$. Following Irwin's approximation of the process zone size at the crack tip [277], it becomes clear that the zone severely increases with decreasing yield strength and increasing fracture toughness. The effective radius r_{eff} can be calculated as:

$$r_{eff} = \frac{1}{2\pi}\left(\frac{K_I}{\lambda\,\sigma_y}\right)^2, \tag{4.21}$$

where λ describes the boundary between elastic and plastic region and can be taken as $\sqrt{3}$ for plane strain situations. However, as shown in Figure 4.49 d) for the respective scales, the strength effect predominates progressively for lower yield strengths. Based on the strength and fracture toughness results presented in the epoxy chapter, approximations of the process zones have been calculated. These are shown in part d) of Figure 4.49 and are markedly different. Especially at elevated temperatures, the zone radius of about 80 µm is relatively large compared to the fiber radius of 17 µm. Therefore, interactions with the F/M interphase region are likely.

To estimate the residual interphase strength of the SE 2020 composite, transverse tensile tests have been performed at 50 °C. Compared to the room temperature, the strength decreases by almost 10 % to 49.5 MPa, which is exactly the epoxy strength at this temperature (see Figure 3.6). Therefore, it cannot be assumed that the interphase strength (under normal loading) is lower than the matrix strength at 50 °C. As a result, it should make almost no difference whether the crack grows in the interphase or through the matrix under mode I loading in this case. In the case of the mode II ERR, a strong dependence on both the resins

$G^m_{I,C}$ and the yield strength τ_y and shear modulus G is postulated by Lee [221]. Based on micromechanical relations in the forefront and at the mode II crack tip of thin resin layers between the fibers, applies according to Lee [221]:

$$G^c_{II,C} \propto (G^m_{I,C})^{(1-z)/2} \left(\frac{\tau_y^2}{G}\right)^{(1+z)/2}, \tag{4.22}$$

where z is a constant ($0 < z < 1$) of the numerical range related to the crack spacing, resin thickness, and resin shear modulus. The proportionality relation shows that either the matrix fracture toughness or the shear yield strength and stiffness-related strain energy density term (τ_y^2/G) dominate the composite mode II ERR under temperature variation or water-related aging. As these typically tend to follow contradictory trends, which, for example, may also not depend linearly on the ambient temperature, the predominance for different temperature ranges may also change or neutralize each other.

Considering the results obtained with the humid pre-aged fibers and respective lowered interphase strengths, it becomes apparent that neglecting the interphase properties is insufficient. For conditions where the interphase shear strength is sufficiently lower than the matrix shear strength, the fracture is not driven by matrix failure but by an interphase failure. However, the interphase-related reductions of mode I and II ERRs' are limited since, in a composite, matrix failure has to co-occur, at least in the delamination plane between the fibers. The separated interphase effects can reduce mode I and II ERRs by up to 30 % for all results presented. Furthermore, it was shown that the effects are more severe for composites with susceptible or weaker sizings and interphases. Even though the fracture behavior is complex, temperature and water-aging-dependent trends, as shown in part c) of Figure 4.49, apply to the fabric-based UD composites investigated. While mode I ERRs are dominated by mode I properties of the resin, mode II ERRs are determined by the matrix and interphase strength. A strong and durable interphase significantly enhances mode II properties.

Another essential result achieved by comparing the most important mechanical properties of the SE 2020 and NEG 2002 UD composites is that static properties alone are insufficient to fully explain the differences found for the tension-tension fatigue properties (see Figures 4.35 and 4.36). Even though the significant difference of 80 to 100 MPa allowable stresses to reach the same lifetime in dry reference conditions might be related to the superior interphase strengths of the SE 2020 composite (54.5 MPa vs. 24.5 MPa transverse tensile strength), at first

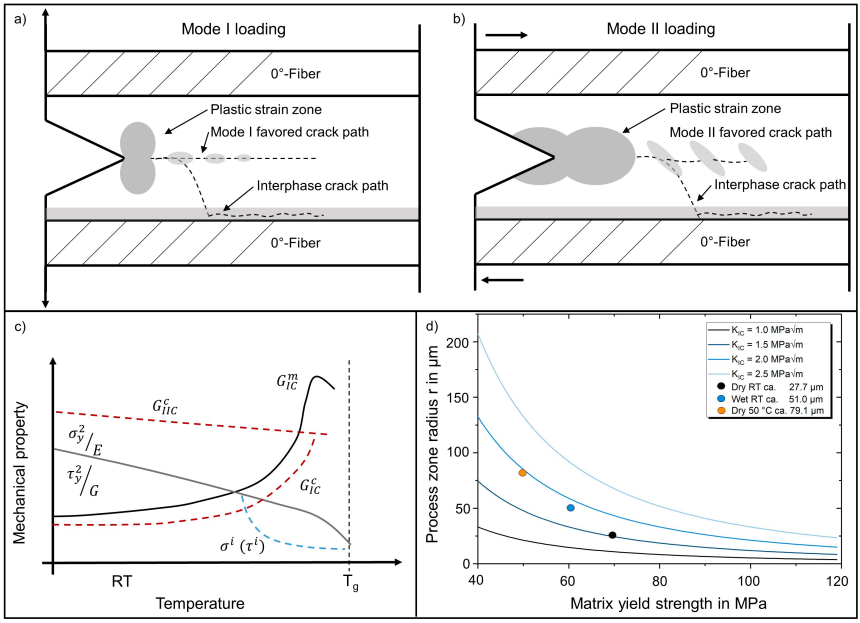

Figure 4.49: Schematic crack development options under a) mode I and b) mode II loading. Additionally, schematic relations of temperature and fracture properties are shown in c). In d) the relations between fracture toughness, yield strength, and process zone radius are shown for the RIMR135/H137 composites.

glance, the critical ERRs in mode I and II are similar or even higher for the NEG 2002 composite. Furthermore, all properties in the fiber direction (composite strength, fiber bundle strength, composite modulus, and fiber volume fraction) were almost identical. Therefore, it is suggested that the dynamic or cyclic damage behavior might be significantly different from the quasi-static. In this context, e.g., Sjögren and Asp [278] demonstrated that the fatigue growth thresholds of the mode I and II ERRs were only 25 % and 10 % of the critical initiation values defined by static tests.

Furthermore, was shown by Coronado et al. [279] with DCB fatigue tests under different temperatures that the crack growth rate, e.g., under mode I loading, can differ by several orders of magnitude for the crack initiation and about one magnitude during crack growth progress, even when the static critical ERRs differ not more than 15 % (between RT and −60 °C). Therefore, it cannot be ruled out that the crack growth rates vary for the two composites investigated

in the present study despite having similar static properties. Consequently, the crack growth rate of the NEG 2002 composite is expected to be higher due to the lower interphase strength and quality. Finally, it should be mentioned that the fatigue damage of UD composites is not primarily dominated by interlaminar delaminations but by fiber bundle failure due to fiber/matrix debonding and longitudinal splitting. A direct correlation with the mode I and II results is, for this reason, unlikely.

Figure 4.50 presents relevant mechanical properties of the RIMR135/H137 and SE 2020-based UD composites after aging at 50 °C water until saturation and after humid fiber pre-aging at 50 °C and 80 % RH compared to the dry reference values. The radar chart summarizes the results presented during the chapters of the thesis. It highlights the susceptibility of the longitudinal tensile strength and fatigue properties to environmental aging. Thanks to the pre-aging method, this can be related mainly to fiber degradation in the first case and to interphase degradation in the second case.

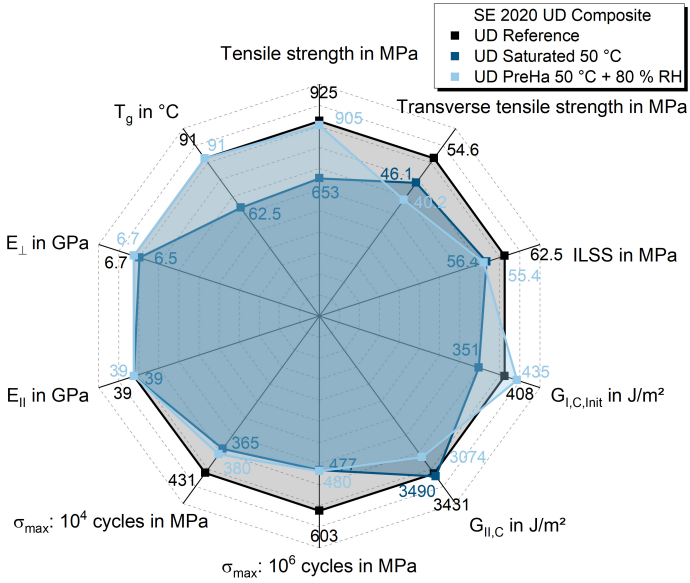

Figure 4.50: Effects of wet aging at 50 °C (dark blue) and fiber pre-aging at 50 °C and 80 % RH (pale blue) on relevant mechanical properties of SE 2020 and RIMR135/H137-based UD composites. Values compared with initial dry condition (black/gray).

4.3.6 Effects of Temperature and Aging on Impact Behavior

The results of a low-velocity impact (LVI) test series are presented and discussed below to obtain an initial insight into the effects of the typical, previously described operating conditions of temperature and moisture absorption on the damage resistance. Therefore, 4 mm thick, quasi-isotropic laminates $[\pm 45°/90°/0°]_{2s}$ are impacted with 18 J at temperatures between −30 °C and 70 °C or additionally at room temperature after aging in 40 °C distilled water for 69 days. The chosen impact energy was in accordance with the study of Perillo et al. [280] and defined after a pre-test series with impact energies of 11, 16, and 21 J, showing a linear increasing trend of the projected delamination area. The laminates consist of E-CR glass fibers (Jushi E6) and the standard RIMR135/H137 resin, which have a fiber volume fraction of 46.1 %. Following the impact event, the specimens are tested for residual compressive strength in compression after impact (CAI) tests. The damage is evaluated in terms of the projected delamination area of the front side and the projected crack propagation area on the backside based on high-resolution transmitted light scans. The results are shown in Figure 4.51.

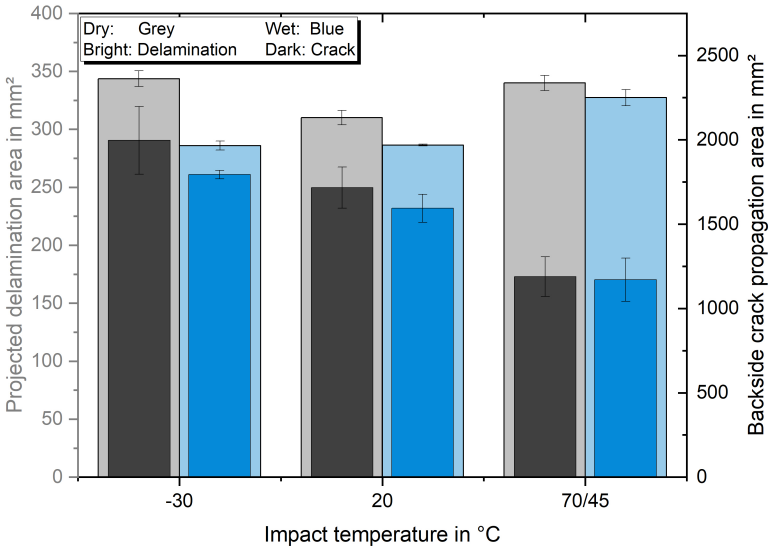

Figure 4.51: Projected delamination (bright) and backside crack propagation (dark) areas of dry (grey) and wet (blue) QI-composites after a low-velocity impact with 18 J.

Here, the impact of temperature and of water absorption are clearly visible for both damage types. Wet laminates always show slightly less delamination and crack propagation areas at the same impact temperature than dry laminates. The most substantial impact has the temperature on the matrix crack propagation at the backside, as the affected area decreases by about 40 % from −30 °C to 70 °C. These results can be explained by a combination of an enhancing resin mode I ERR $G^m_{I,C}$ and strain to failure in contrast to the simultaneously decreased resin strength and stiffness with increasing temperature and water content. As a result, the deformation at high temperatures is much more localized, leading to a higher indentation depth on the front and a larger dome height on the backside. The interlaminar stresses are not high enough to progress large delaminations in the upper half of the composite, which is in line with the findings of Körbelin [146] for high-performance CFRP composites. Pure resin fracture in resin-rich regions between the fiber bundles is fully suppressed at elevated temperatures as a result of the high fracture toughness and corresponding high allowable strain to failure. If intralaminar matrix fracture occurs, it is only within the dense bundles. The minor effect of temperature and water absorption on the delamination size at the lower half is attributed to the opposing effects of decreasing mode II ERR at the delamination surface and the simultaneously decreasing global stiffness of the laminate. The higher the temperatures, the lower the resulting stresses between the plies. Therefore, the delaminations at low temperatures, which imply higher mode II ERR and higher interlaminar stresses, grow to a similar extent as those at high temperatures with lower mode II ERR and lower interlaminar stresses. Figures 4.52, 4.53, and 4.54 give a detailed overview of the LVI damage by microscopic images of the cross-section through the central impact region.

The effects of the impact damages on the residual compressive strength and the typical failure by local buckling around the impacted area are presented in Figure 4.55. Similarly to the results given by Körbelin [146] for CFRP, the residual CAI strength of dry GFRP at room temperature is not significantly affected by the impact temperature. The standard deviations of all dry tests overlap. Similarly, no difference can be made between the wet laminates, but the residual strength is always slightly lower than for the dry laminates. These findings can be explained by the relatively similar size of the delaminations near the neutral plane, which is related to the global buckling resistance [281]. In the wet case, the reduced bending stiffness and reduced fiber and interphase strengths affect

Figure 4.52: Images of representative microscopic cross sections of the impacted area (central cut) for three impact temperatures in dry conditions.

Figure 4.53: Images of representative microscopic cross sections of the impacted area (central cut) for three impact temperatures in wet conditions.

the composite's compressive strength. However, the global impact is relatively small after short-term aging at 40 °C for 69 days.

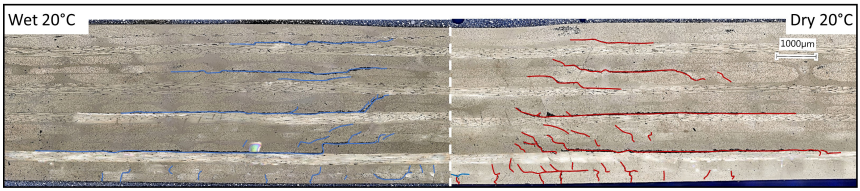

Figure 4.54: Comparison of representative microscopic cross sections of the impacted area (central cut) after impact at 20 °C for dry and wet conditions with highlighted delaminations and intralaminar cracks.

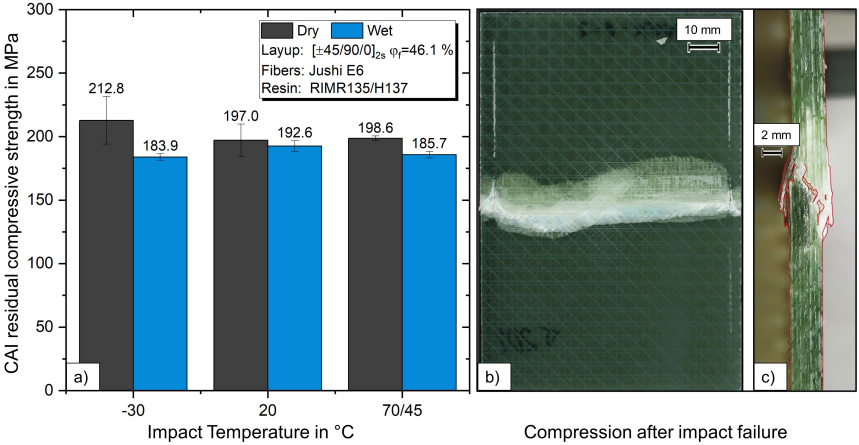

Figure 4.55: Residual compressive strength of the different GFRP/impact configurations after an 18 J low-velocity impact a) and representative pictures of the CAI test failure b, c).

4.3.7 One-Sided Aging of Thick Structures

One-sided aging and diffusion behavior was investigated with 9.0 mm thick quasi-isotropic laminates using four-point bending tests and FTIR measurements. Therefore, glass frames were first glued on top of several manufactured laminates, filled with distilled water, and stored inside a climate chamber at 50 °C and 70 % RH. These values were chosen as they accelerated the diffusion process and led to severe damage inside immersed specimens but not inside those aged in the climate chamber. A thick epoxy traveler specimen was also equipped with a water-filled glass frame on top to monitor the water or moisture distribution inside the specimens. After six months, the frame was removed, and a 0.3 mm thin stripe was cut from the central specimen region. This stripe was then

directly put into an FTIR microscope, and 100 single measurements were performed along a line from the top to the bottom of the sample. The whole process time was $\leq$ 10 minutes, sufficient to reduce drying to a minimum. The FTIR spectra were analyzed at the peak at 5250 cm^{-1}, as explained in Section 3.3.7. Additionally, a stripe cut of a specimen stored at room temperature and 50 % RH for the same time and prepared using the same method was analyzed. The peak areas were then transferred into absorbed mass-percent values according to Eq. 3.20. The results are presented in Figure 4.56.

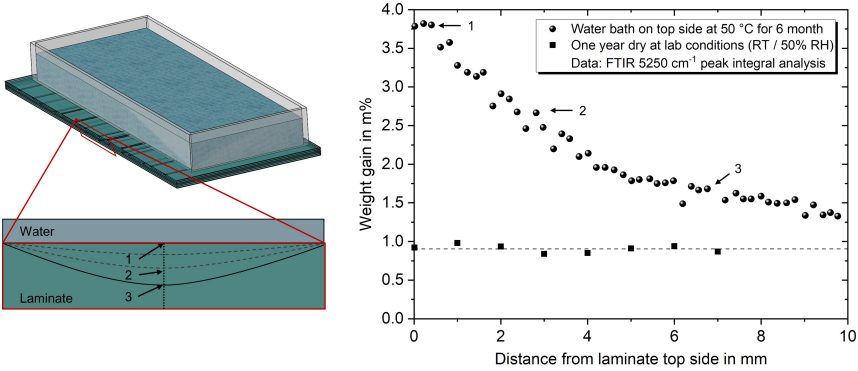

Figure 4.56: Schematic model of one-sided water absorption with a water bath on top of the laminate inside a climate chamber at 50 °C and 70 % RH (left). FTIR analysis of through the thickness water content after six months of one-sided diffusion on a 10 mm thick epoxy traveler plate (right).

In comparison with the expected water absorption amounts, see Figure 3.5, all edge regions confirm the validity of the measurement method. The water absorption of 0.95 m% at laboratory conditions and 1.45 m% at the surface exposed to the climate chamber correspond well to the predictions. However, the amount of about 3.75 m% at the water-exposed surface seems to be a bit too high. The measurements along a line through the thickness also reveal the water distribution, which follows a Fickian trend from the equilibrium of the water contact site to the equilibrium at the humid surface. The effect of the one-sided water absorption on the mechanical performance of the laminates was tested with four-point bending specimens cut from the exposed laminates. Additionally, specimens are distinguished between having the exposed site on the top and under compression or at the bottom and under tensile loading. The results of the bending tests and the aging-related damage at the water-exposed surface are shown in Figure 4.57.

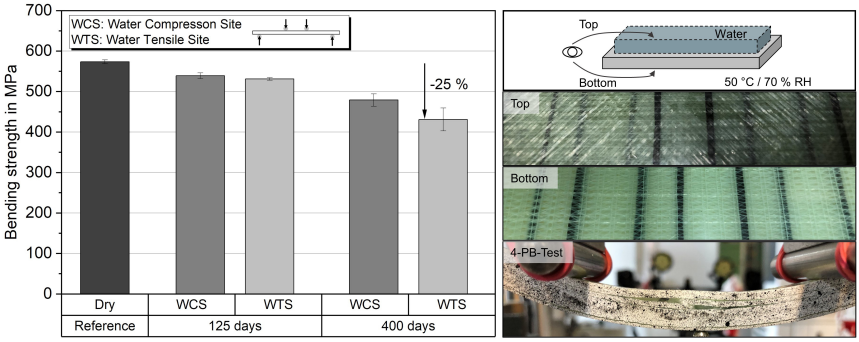

Figure 4.57: Four-point bending strength for one-sided aging of up to 400 days (left). Pictures of surfaces after 400 days of aging and of typical final fracture with delaminations in sub-laminates (right).

The results obtain a continuously decreasing bending strength of the laminates. After 400 days of exposure, the strength decrease was 25 % when the exposed site was under tensile loading. This is quite precisely in the range that can be predicted based on the short-term tensile tests after aging at 50 °C described in Figure 4.9, taking the thickness of the laminate into account. Furthermore, the typical damage and fracture pattern continuously changed. While dry and short-term aged specimens regularly failed by sub-laminate delamination through the 90°-layers and a final compression failure of the top ±45°-layers, the compression failure moved further into the composite. This aligns with what was previously reported for bending tests of aged GFRP, e.g., by Boisseau et al. [202]. Here, the authors found a continuous change from compression to tensile failure, as the glass fiber strength reduction has more impact on the tensile strength than on the compressive strength. As can be seen from the pictures in Figure 4.57, the same frequent F/M debonding occurred in the layers close to the water-exposed surface as were found for specimens after total immersion. Consequently, it can be assumed that even a closed surface cannot permanently protect the composite, and especially the fibers, from direct contact with water under these harsh conditions.

4.4 Conclusions

Concerning the presented results of both main chapters, the first formulated research hypothesis:

In contrast to the long-term behavior of the epoxy resin matrices, the corresponding performance of composites cannot be simply described by (aging-) temperature-dependent acceleration factors. This is because fiber and interphase degradation are neither independent of each other nor follow the same continuously accelerated mechanisms.

can be confirmed. Long-term aging of several composites and corresponding constituents at various temperatures between 8 °C and 50 °C revealed fundamental differences in the dominating aging mechanisms, which are not simply accelerated by temperature.

Accelerated aging at elevated temperatures severely affects all mechanical properties of GFRP composites. Differences between individual composites are reduced almost always after sufficient time. It is, therefore, often difficult to differentiate between the resistance qualities, although there are clear differences under operating conditions. Short-term accelerated aging can only reveal tendencies of durability. However, fibers are unprotected when the interphase degrades, and severe mechanical properties loss occurs. Consequently, accelerated aging tests at elevated temperatures should only be used to estimate the most conservative long-term behavior.

Throughout the thesis, it has been proved that the fatigue life of unidirectional GFRP composites is strongly dependent on the interphase condition and the fiber strength. The effects were distinguishable. Isolated interphase degradation or weakening homogenously reduces the fatigue lifetime at all investigated stress levels. Reduced fiber strength inclines the Wöhler curves and becomes increasingly important as loading rises. Lifetime analysis based on the typically used accelerated wet-aging procedures results in a superposition of both mechanisms, as fibers are unprotected when the F/M interphase fails during aging. At the same time, the impact of the time-temperature-dependent variation of the thermo-mechanical resin properties becomes minor when the interphase loses its integrity. On the contrary, as long as the interphase remains intact, water absorption can even positively affect damage tolerance and fatigue life. This

is demonstrated by fatigue life modeling and confirmed by initial experimental results.

Long-term aging at various temperatures revealed evident shortcomings of the usually applied Arrhenius-based prediction methods. Unlike assumed, the degradation at low temperatures is limited or much more decelerated than predicted by short-term tests if the interphase remains functional. This is because the water-induced strength loss of glass fibers appears to be a surface-driven process in the first place. Direct fiber-water contact immediately and significantly reduces the fiber strength. This is associated with the growth and exposition of fiber flaws, which are most likely already apparent but covered by the sizing or interphase. Thus, the environmental temperature mainly influences the long-term decomposition, while the strength is initially affected by the (uncovered) surface defects. As expected, significant differences between more susceptible E-glass and more resistant ECR- and R-glass fibers could be found. In a GFRP composite, the fiber degradation mechanisms are highly suppressed as long as the F/M interphase is undamaged. Furthermore, the tolerable aging temperature of a composite is likely still lower than the wet T_g of the matrix resin since, in the vast majority of cases, the (wet) interphase T_g is even lower. For epoxy and silane sizing-based composites, this implies that aging temperatures of 40 °C are usually already too high to compare similar degradation mechanisms.

The second research hypothesis of this chapter:

The resilience of the F/M interphase during aging is of utmost importance for the durability of GFRP composites. Both static and fatigue properties will break down when the integrity is disturbed.

can be confirmed based on developing and applying the novel fiber pre-aging method to several experimental investigations and modeling approaches, including micro-mechanical and fatigue testing. The humid fiber pre-aging can be used to exclusively investigate the effects of weakened F/M interphases, without or in combination with a fiber strength degradation. Consequently, the effects of matrix aging can be excluded from the results in both cases. The method allows, on the one hand, to compare the susceptibility of different sizings to degradation in the presence of moisture or water and, on the other hand, to assess the tendency for natural sizing aging during fiber (fabric) storage. The results obtained for

quasi-static and fatigue loads highlight the importance of the F/M interphase integrity for all damage-growth-related properties.

Based on the comprehensive testing campaign with the pre-aged composites, reasonable model representations of environmental aging and operational condition effects on the damage progress in GFRP composites could be established. The fiber, matrix, and interphase-related fatigue lifetime of unidirectional GFRP was successfully modeled with adequate accuracy by adjusting Sörensen's analytical descriptions to the present study. Here, single fiber fragmentation tests were used to analyze the F/M interphase properties and determine the micromechanical input parameters to model the macroscopic tension-tension fatigue behavior. Again, the importance of the F/M interphase was outstanding.

Investigations of the interlaminar fracture properties highlighted the opposing effects of environmental temperature and water-related aging on mode I and II ERRs. Water absorption and rising temperatures increase the fracture toughness of the resin and significantly delay the damage initiation, which dominates the mode I ERR of the composite. The mode II ERR, on the contrary, is controlled by the shear yield strength and stiffness of the resin and, in particular, of the interphase. Their decreasing trend prevails the increasing resin fracture toughness on the composite level. For fabric-based composites with highly inhomogeneous fiber (volume) distributions (dense bundles vs. interspace), the interphase effects are limited, as a substantial amount of matrix resin is always involved in the fracture process.

Considering additionally all investigations performed with thick, multidirectional composites, the last research hypothesis of this chapter:

The damage tolerance of GFRP composites is significantly affected by the operating conditions and environmental aging, whereas the damage processes are likewise controlled by resin and interphase properties.

can also be confirmed. The damage and fracture-related effects of temperature and water-based aging could be successfully transferred to explain the change of LVI damage appearance in GFRP. It became clear that the impact damage depends on the structural response of the laminate, which in turn is also related to the environmental temperature and aging condition. As the main driving factors of fracture toughness and strength are subject to a contradictory dependence, the residual compressive strength determining largest delaminations grow to a

similar extent. Consequently, no significant effect of the laminate condition during the impact event on the residual strength could be established, even though the micro and macroscopic damage substantially deviates.

Finally, it was demonstrated that the one-sided (accelerated) aging of thick structures likewise significantly decreased the mechanical performance. In detail, the same bending strength reduction of 25 % after 400 days of surface contact with 50 °C warm water was found that was predicted based on tests with thin tensile specimens fully immersed. Even though no open cutting edges were in contact with water, the same F/M debonding type damage appeared. Therefore, it is shown that the matrix's ability to protect the fibers is not considerably higher than in the immersed case. Environmental conditions, which are too excessive for interphase durability, always lead to severe degradation of the composite. Only the diffusion depth and speed are naturally reduced and depend on the conditions on the surface without water contact.

5 Summary and Conclusion

New insights were gained about the environmental impact on the durability and lifetime of GFRP. Therefore, novel methodologies were developed to separately investigate the influence of constituents aging on the mechanical performance of GFRP composites. Due to the comprehensive analysis of experimental and analytical studies, a more profound understanding of the interrelations was achieved. In addition, the importance of applying and defining meaningful aging procedures is emphasized. This will allow for more accurate prediction of effects under operating conditions. In conclusion, the results obtained allow to confirm the overarching research hypothesis:

Improving the long-term durability of GFRP structures under severe operating conditions requires an in-depth understanding of the effects of the various environmental conditions on the composite's constituents.

In summary, it was revealed within the two main chapters that all three constituents significantly influence the long-term mechanical properties and fatigue life in many ways. However, in particular, the F/M interphase has proven to be a decisive factor in this context. Even though the direct impact of weak or degraded interphases on the main mechanical and fracture-related properties is not always exceptionally high, the loss of protection and integrity functions is serious for long-term durability. In other words, most degradation processes in the composite can only occur if the interphase is damaged.

The impact of water- and moisture-related aging on GFRP can be described as a hierarchical structure or a defined cause-effect relationship. Here, a distinction must first be made as to whether the F/M interphase remains intact in the long term under the given conditions. If so, it can also be expected that most fibers will remain undamaged and functional. Then, all the aging-related structure-property relationships investigated and described in the third chapter

for the epoxy resin matrices have the most considerable effects and predominate the composite's long-term lifetime and fracture properties. In this case, it can also be assumed that the changes in properties can be accurately described and predicted with the temperature-dependent models applied. Damage initiation, growth, and the state of stress are directly related to the aging condition of the matrix. In detail, the correlation between water-induced plasticization and temperature-dependent physical aging determines the epoxy and, therefore, composite properties. Thus, as an example, even a fatigue life increase of composites can result from water absorption at low or moderate temperatures due to the increased fracture toughness and significantly higher ductility of the resin.

In contrast, the matrix-related aging effects are only secondary if the F/M interphase degrades and fails under the operating or chosen aging conditions. Depending on the loading, either the fiber or interphase degradation predominates the composite properties. Severe fiber degradation regarding flaw exposure, growth, and surface ion leaching occurs when the fibers come in direct contact with absorbed water. These processes are expected to increase the defect density and reduce the fiber strength. However, in terms of fiber strength, the degradation appears to be a surface-driven phenomenon, which is less aging temperature-dependent but more accessibility controlled. For longitudinal quasi-static loading, the remaining fiber strength is dominant. Under fatigue loading, the accelerated F/M interphase debonding rate additionally accelerates the damage progress. Under transverse loading or for inter- and translaminar fracture properties, the interphase degradation is crucial, as the composite transverse strength and fracture behavior are directly related to the interphase strengths. For example, the crack paths of interlaminar damage shift from predominantly matrix cracking to intralaminar cracking connecting fiber/matrix debondings.

The effects of water-related aging on the investigated low-viscosity infusion epoxies and corresponding GFRPs demonstrated a strong sensitivity to the exact aging and environmental conditions. By water absorption of about 3.0 m%, the epoxy tensile strength and the T_g can decrease by up to 33 %, while the failure strains can increase by more than 200 %. However, the epoxy properties are highly aging temperature-dependent and change over time. There needs to be more than the knowledge about the amount of absorbed moisture or water to predict the thermo-mechanical properties. Instead, the time-temperature history is of utmost importance. The composite properties are likewise highly dependent on the aging temperature and duration. In this context, long-term

aging immersed at low temperatures of 8 °C decreased the longitudinal tensile strength of UD-GFRP composites only by about 12.5 %, while aging at 50 °C reduced the strength by up to 50 % after just a few weeks. Notably, the low strength of about 50 % of the virgin strength appeared to be a long-term lower limit for the composites and the fibers themselves.

From a predictive modeling perspective, the results highlight the need to differentiate between the use of elevated temperatures for accelerated testing or accelerated aging. In the first case, modeling and prediction of long-term properties for a specific reference condition is feasible as long as it is ensured that the basic material state is unchanged during aging and testing. For the epoxies, this means that the superposition of temperature and water-plasticization effects can be used for long-term property prediction of any reference conditions as long as degradation or physical aging effects are insignificant and the same failure mechanisms predominate. Therefore, creep and constant strain-rate tests were combined and used to extend established time-temperature superposition approaches such as the Reiner-Weissenberg or Christensen criteria to model a time-temperature-moisture-loading dependent epoxy failure envelope. Otherwise, e.g., with accelerated aging at elevated temperatures, the opposing effects of plasticization and physical aging, or in the worst case, chemical degradation, must be considered. Therefore, extensions of the Arrhenius principle-based Kohlrausch-Williams-Watts correlations were developed and presented. Furthermore, it was demonstrated that the main findings regarding the time-temperature-aging relationships are transferable to other epoxies.

The long-term property prediction for the composites is even more complex, as it was again revealed that the predominating damage mechanisms are strongly aging and testing temperature-dependent. The typically used Arrhenius-based prediction models largely fail to predict the property evolution over time, as it turned out that damage mechanisms change in dependence of the F/M interphase durability. While accelerated aging at elevated temperatures close to the wet T_g of the matrix can be used to determine the lowest possible limit of mechanical properties, it is unlikely that the composite properties will degrade to the same extent at significantly lower operating temperatures. Here, the integrity of the interphase has to be considered in the models, which unfortunately always requires a series of additional tests due to the varying chemical composition depending on the fiber/sizing/matrix combination.

Finally, the need for meaningful and applicable standardization of aging procedures was emphasized. A novel fiber pre-aging methodology was developed, introduced, and applied to contribute to understanding the importance of the F/M interphase durability for various mechanical and fatigue properties. With its help, it is possible to isolate the impact of a weakened interphase on all important composite properties. In this context, it was demonstrated, e.g., to which degree the interphase or the fiber degradation plays a role in fatigue life reduction of wet-aged UD GFRP, which is impossible with classically immersed specimens. Furthermore, the micro- and macro-mechanical tests performed were used to model the fatigue life of the UD composites by adjusting Sörensen's fatigue life model [1] with experimental data. As a result, a pretty accurate fatigue life prediction was achieved based on considering the interphase properties.

In the future, the most urgent need is to develop reasonable aging standards, which give industry and academia advice for good practice in using any aging methodologies. Based on the comprehensive aging-temperature dependent tests, models, and the developed pre-aging method, this thesis can contribute to the goal. In particular, the correlation between natural degradation at operating conditions and the use of accelerated aging has to be improved. As a first suggestion, a fiber/matrix interphase durability criterion should be developed and considered. This criterion might define an aging temperature window, in which the use of accelerated aging is meaningful concerning long-term operating conditions of composites. Otherwise, the blind use of accelerated aging methods or the acquisition of published data will lead, in most cases, to a misinterpretation of the long-term properties. However, using accelerated aging methods leads at least to conservative predictions, which, in turn, result in safe designs.

Bibliography

[1] B. F. Sørensen, S. Goutianos, L. P. Mikkelsen, and S. Fæster. "Fatigue damage growth and fatigue life of unidirectional composites". In: *Composites Science and Technology* 211 (2021), p. 108656. DOI: 10.1016/j.compscitech.2021.108656.

[2] L. C. Hollaway. "Advanced fiber-reinforced polymer (FRP) composite materials for sustainable energy technologies". In: *Advanced Fiber-Reinforced Polymer(FRP) Composites for Structural Applications*. Vol. vol. 2. Elsevier, 2013, pp. 637–673. ISBN: 9780128203460. DOI: 10.1016/B978-0-12-820346-0.00018-6.

[3] S. Moy. "Advanced fiber-reinforced polymer (FRP) composites for civil engineering applications". In: *Developments in Fiber-Reinforced Polymer (FRP) Composites for Civil Engineering*. Vol. 2. Elsevier, 2013, pp. 177–204. ISBN: 9780857092342. DOI: 10.1533/9780857098955.2.177.

[4] P. Brøndsted, H. Lilholt, and A. Lystrup. "COMPOSITE MATERIALS FOR WIND POWER TURBINE BLADES". In: *Annual Review of Materials Research* 35.1 (2005), pp. 505–538. DOI: 10.1146/annurev.matsci.35.100303.110641.

[5] F. Rubino, A. Nisticò, F. Tucci, and P. Carlone. "Marine Application of Fiber Reinforced Composites: A Review". In: *Journal of Marine Science and Engineering* 8.1 (2020), p. 26. DOI: 10.3390/jmse8010026.

[6] A. G. Olabi, T. Wilberforce, K. Elsaid, E. T. Sayed, T. Salameh, M. A. Abdelkareem, and A. Baroutaji. "A Review on Failure Modes of Wind Turbine Components". In: *Energies* 14.17 (2021), p. 5241. DOI: 10.3390/en14175241.

[7] Y. Miyano, M. Nakada, and N. Sekine. "Accelerated testing for long-term durability of GFRP laminates for marine use". In: *Composites Part B: Engineering* 35.6-8 (2004), pp. 497–502. DOI: 10.1016/j.compositesb.2003.11.006.

[8] J. D. Garcia-Espinel, D. Castro-Fresno, P. Parbole Gayo, and F. Ballester-Muñoz. "Effects of sea water environment on glass fiber reinforced plastic materials used for marine civil engineering constructions". In: *Materials & Design* 66 (2015), pp. 46–50. DOI: 10.1016/j.matdes.2014.10.032.

[9] J. Y. Choi, J. H. Jeon, J. H. Lyu, J. Park, G. Y. Kim, S. Y. Chey, Y.-J. Quan, B. Bhandari, B. G. Prusty, and S.-H. Ahn. "Current Applications and Development of Composite Manufacturing Processes for Future Mobility". In: *International Journal of Precision Engineering and Manufacturing-Green Technology* 10.1 (2023), pp. 269–291. DOI: 10.1007/s40684-022-00483-3.

[10] S. Beura, D. N. Thatoi, A. P. Chakraverty, and U. K. Mohanty. "Impact of the ambiance on GFRP composites and role of some inherent factors: A review report". In: *Journal of Reinforced Plastics and Composites* 37.8 (2018), pp. 533–547. DOI: 10.1177/0731684418754359.

[11] A. T. Echtermeyer, A. Gagani, A. Krauklis, and T. Mazan. "Multiscale Modelling of Environmental Degradation—First Steps". In: *Durability of Composites in a Marine Environment 2*. Ed. by Peter Davies and Yapa D.S Rajapakse. Vol. 245. Solid Mechanics and Its Applications. Cham: Springer International Publishing, 2018, pp. 135–149. ISBN: 978-3-319-65144-6. DOI: 10.1007/978-3-319-65145-3_8.

[12] A. E. Krauklis. *Environmental Aging of Constituent Materials in Fiber-Reinforced Polymer Composites: Ph.D. Thesis*. Trondheim, 2019.

[13] A. E. Krauklis, C. W. Karl, I. B. C. M. Rocha, J. Burlakovs, R. Ozola-Davidane, A. I. Gagani, and O. Starkova. "Modelling of Environmental Ageing of Polymers and Polymer Composites-Modular and Multiscale Methods". In: *Polymers* 14.1 (2022). DOI: 10.3390/polym14010216.

[14] R. L. Sierakowski. *Damage Tolerance in Advanced Composites*. First edition. Boca Raton, FL: Routledge, 1995. ISBN: 9781351456715. URL: https://permalink.obvsg.at/.

[15] D. Hull and Y. B. Shi. "Damage mechanism characterization in composite damage tolerance investigations". In: *Composite Structures* 23.2 (1993), pp. 99–120. DOI: 10.1016/0263-8223(93)90015-I.

[16] H. Reddick and K. Harold. *Safe-life and damage-tolerant design approaches for helicopter structures*. 1983. URL: https://ntrs.nasa.gov/citations/19830025690.

[17] J. Krautkrämer and H. Krautkrämer. *Ultrasonic Testing of Materials*. 4th Fully Revised Edition. Berlin and Heidelberg: Springer, 1990. ISBN: 9783662106822. DOI: 10.1007/978-3-662-10680-8.

[18] I.B.C.M. Rocha, S. Raijmaekers, F. P. van der Meer, R. P. L. Nijssen, H. R. Fischer, and L. J. Sluys. "Combined experimental/numerical investigation of directional moisture diffusion in glass/epoxy composites". In: *Composites Science and Technology* 151 (2017), pp. 16–24. DOI: 10.1016/j.compscitech.2017.08.002.

[19] B. C. Ray and D. Rathore. "Environmental damage and degradation of FRP composites: A review report". In: *Polymer Composites* 36.3 (2015), pp. 410–423. DOI: 10.1002/pc.22967.

[20] E. Oterkus, C. Diyaroglu, D. de Meo, and G. Allegri. "Fracture modes, damage tolerance and failure mitigation in marine composites". In: *Marine Applications of Advanced Fibre-Reinforced Composites*. Vol. 64. Elsevier, 2016, pp. 79–102. ISBN: 9781782422501. DOI: 10.1016/B978-1-78242-250-1.00004-1.

[21] T. S. Gates. *On the Use of Accelerated Test Methods for Characterization of Advanced Composite Materials*. Ed. by NASA.

[22] ASTM D5229. *Test Method for Moisture Absorption Properties and Equilibrium Conditioning of Polymer Matrix Composite Materials*. West Conshohocken, PA, 2020. DOI: 10.1520/D5229_D5229M-20.

[23] ASTM C481-99. *Test Method for Laboratory Aging of Sandwich Constructions*. West Conshohocken, PA, 2016. DOI: 10.1520/C0481-99R16.

[24] ASTM C1560-03. *Test Method for Hot Water Accelerated Aging of Glass-Fiber Reinforced Cement-Based Composites*. West Conshohocken, PA, 2023. DOI: 10.1520/C1560-03R16.

[25] A. Kaluza, A. Genest, T. Steinert, A. Schiffleitner, and C. Herrmann. "Consideration of Environmental Impacts of Automotive Lightweight Body Parts During the Conceptual Design Stage". In: *Life Cycle Design & Engineering of Lightweight Multi-Material Automotive Body Parts*. Ed. by Thomas Vietor. Vol. 186. Zukunftstechnologien für den multifunktionalen Leichtbau. Berlin, Heidelberg: Springer Berlin Heidelberg, 2023, pp. 79–97. ISBN: 978-3-662-65272-5. DOI: 10.1007/978-3-662-65273-2_6.

[26] J. C. Kelly, J. L. Sullivan, A. Burnham, and A. Elgowainy. “Impacts of Vehicle Weight Reduction via Material Substitution on Life-Cycle Greenhouse Gas Emissions”. In: *Environmental science & technology* 49.20 (2015), pp. 12535–12542. DOI: 10.1021/acs.est.5b03192.

[27] A. T. Echtermeyer, A. E. Krauklis, A. I. Gagani, and E. Sæter. “Zero Stress Aging of Glass and Carbon Fibers in Water and Oil—Strength Reduction Explained by Dissolution Kinetics”. In: *Fibers* 7.12 (2019), p. 107. DOI: 10.3390/fib7120107.

[28] A. H. Idrisi and A.-H. I. Mourad. “Fiber reinforced polymer composites sustainability under prolonged exposure to hot seawater: Experimental and prediction study”. In: *Materials Letters* 304 (2021), p. 130689. DOI: 10.1016/j.matlet.2021.130689.

[29] A. Le Guen-Geffroy, P. Davies, P.-Y. Le Gac, and B. Habert. “Influence of Seawater Ageing on Fracture of Carbon Fiber Reinforced Epoxy Composites for Ocean Engineering”. In: *Oceans* 1.4 (2020), pp. 198–214. DOI: 10.3390/oceans1040015.

[30] J. D. Nunemaker, M. M. Voth, D. A. Miller, D. D. Samborsky, P. Murdy, and D. S. Cairns. “Effects of moisture absorption on damage progression and strength of unidirectional and cross-ply fiberglass–epoxy composites”. In: *Wind Energy Science* 3.1 (2018), pp. 427–438. DOI: 10.5194/wes-3-427-2018.

[31] D. Gibhardt, A. Doblies, L. Meyer, and B. Fiedler. “Effects of Hygrothermal Ageing on the Interphase, Fatigue, and Mechanical Properties of Glass Fibre Reinforced Epoxy”. In: *Fibers* 7.6 (2019), p. 55. DOI: 10.3390/fib7060055.

[32] D. Gibhardt, C. Fleschhut, and B. Fiedler. “The influence of different glass fiber/epoxy matrix combinations on the durability under severe moisture impact”. In: *IOP Conference Series: Materials Science and Engineering* 942 (2020), p. 012009. DOI: 10.1088/1757-899X/942/1/012009.

[33] D. Gibhardt, D. Meyer, L. Braun, C. Buggisch, and B. Fiedler. “Effects of the hygrothermal aging history on epoxy resins and GFRP composites”. In: *Proceedings of the 20th European Conference on Composite Materials - Composites Meet Sustainability (Vol 1-6)*. Ed. by A. Vassilopoulos and V. Michaud. Vol. F. EPFL Lausanne, Composite Construction Laboratory,

2022, pp. 347–354. ISBN: 978-2-9701614-0-0. DOI: 10.5075/epfl-298799_978-2-9701614-0-0.

[34] D. Gibhardt, C. Buggisch, D. Meyer, and B. Fiedler. "Hygrothermal Aging History of Amine-Epoxy Resins: Effects on Thermo-Mechanical Properties". In: *Frontiers in Materials* (2022). DOI: 10.3389/fmats.2022.826076.

[35] J. Drummer, D. Gibhardt, J. Körbelin, and B. Fiedler. "General influence of the environmental temperature on the matrix strength under tensile and compressive loading - A comprehensive study on high performance matrices". In: *Composites Science and Technology* 39.4 (2022), p. 109486. DOI: 10.1016/j.compscitech.2022.109486.

[36] D. Gibhardt, A. E. Krauklis, A. Doblies, A. Gagani, A. Sabalina, O. Starkova, and B. Fiedler. "Time, temperature and water aging failure envelope of thermoset polymers". In: *Polymer Testing* 118.14 (2023), p. 107901. DOI: 10.1016/j.polymertesting.2022.107901.

[37] D. Gibhardt, C. Buggisch, L. Blume-Werry, and B. Fiedler. "Influence of Sizing Aging on the Strength and Fatigue Life of Composites Using a New Test Method and Tailored Fiber Pre-Treatment: A Comprehensive Analysis". In: *Journal of Composites Science* 7.4 (2023), p. 139. DOI: 10.3390/jcs7040139.

[38] A. Le Guen-Geffroy, P.-Y. Le Gac, B. Habert, and P. Davies. "Physical ageing of epoxy in a wet environment: Coupling between plasticization and physical ageing". In: *Polymer Degradation and Stability* 168 (2019), p. 108947. DOI: 10.1016/j.polymdegradstab.2019.108947.

[39] E. S.-W. Kong. "Physical aging in epoxy matrices and composites". In: *Epoxy Resins and Composites IV*. Ed. by Henri Benoit, Hans-Joachim Cantow, Gino Dall'Asta, Karel Dušek, Hiroshi Fujita, Manfred Gordon, Gisela Henrici-Olivé, Günter Heublein, Hartwig Höocker, Hans-Henning Kausch, Joseph P. Kennedy, Anthony Ledwith, Seizo Okamura, Salvador Olivé, Charles G. Overberger, Helmuth Ringsdorf, Takeo Saegusa, John L. Schrag, Güunther Victor Schulz, William P. Slichter, John K. Stille, and K. Dušek. Vol. 80. Advances in Polymer Science. Berlin, Heidelberg: Springer Berlin Heidelberg, 1986, pp. 125–171. ISBN: 978-3-540-16423-4. DOI: 10.1007/3-540-16423-5_14.

[40] *DIN EN ISO 1172:1998-12, Textilglasverstärkte Kunststoffe_- Prepregs, Formmassen und Laminate_- Bestimmung des Textilglas- und Mineralfüllstoffgehalts; Kalzinierungsverfahren (ISO_1172:1996); Deutsche Fassung EN_ISO_1172:1998*. Berlin. DOI: 10.31030/8003549.

[41] ASTM D4065. *Practice for Plastics: Dynamic Mechanical Properties: Determination and Report of Procedures*. West Conshohocken, PA, 2020. DOI: 10.1520/D4065-12.

[42] ASTM D7028. *Test Method for Glass Transition Temperature (DMA Tg) of Polymer Matrix Composites by Dynamic Mechanical Analysis (DMA)*. West Conshohocken, PA, 2015. DOI: 10.1520/D7028-07R15.

[43] ASTM D5045. *Test Methods for Plane-Strain Fracture Toughness and Strain Energy Release Rate of Plastic Materials*. ASTM, 2014. DOI: 10.1520/D5045-14.

[44] ASTM D5528. *Test Method for Mode I Interlaminar Fracture Toughness of Unidirectional Fiber-Reinforced Polymer Matrix Composites*. West Conshohocken, PA, 2021. DOI: 10.1520/D5528_D5528M-21.

[45] ASTM D7905. *Test Method for Determination of the Mode II Interlaminar Fracture Toughness of Unidirectional Fiber-Reinforced Polymer Matrix Composites*. West Conshohocken, PA, 2019. DOI: 10.1520/D7905_D7905M-19E01.

[46] *DIN EN ISO 527-4:2020-08, Kunststoffe - Bestimmung der Zugeigenschaften - Teil 4: Prüfbedingungen für isotrop und anisotrop faserverstärkte Kunststoffverbundwerkstoffe (ISO/DIS 527-4:2020); Deutsche und Englische Fassung prEN ISO 527-4:2020*. Berlin. DOI: 10.31030/3171033.

[47] *DIN EN ISO 527-5:2020-08, Kunststoffe - Bestimmung der Zugeigenschaften - Teil 5: Prüfbedingungen für unidirektional faserverstärkte Kunststoffverbundwerkstoffe (ISO/DIS 527-5:2020); Deutsche und Englische Fassung prEN ISO 527-5:2020*. Berlin. DOI: 10.31030/3171035.

[48] *DIN EN 1007-5:2010-06, Hochleistungskeramik - Keramische Verbundwerkstoffe - Verfahren zur Prüfung der Faserverstärkungen - Teil 5: Bestimmung der Verteilung von Zugfestigkeit und Zugdehnung von Fasern im Faserbündel bei Raumtemperatur; Deutsche Fassung EN 1007-5:2010*. Berlin. DOI: 10.31030/1554604.

[49] *DIN EN ISO 527-2:2012-06, Kunststoffe - Bestimmung der Zugeigenschaften - Teil 2: Prüfbedingungen für Form- und Extrusionsmassen (ISO 527-2:2012); Deutsche Fassung EN ISO 527-2:2012*. Berlin. DOI: 10.31030/1860304.

[50] ASTM D2344. *Test Method for Short-Beam Strength of Polymer Matrix Composite Materials and Their Laminates*. West Conshohocken, PA, 2020. DOI: 10.1520/D2344_D2344M-16.

[51] *DIN EN ISO 14125:2011-05, Faserverstärkte Kunststoffe - Bestimmung der Biegeeigenschaften (ISO 14125:1998 + Cor.1:2001 + Amd.1:2011); Deutsche Fassung EN ISO 14125:1998 + AC:2002 + A1:2011*. Berlin. DOI: 10.31030/1753441.

[52] ASTM D7136. *Test Method for Measuring the Damage Resistance of a Fiber-Reinforced Polymer Matrix Composite to a Drop-Weight Impact Event*. ASTM, 2020. DOI: 10.1520/D7136_D7136M-15.

[53] ASTM D7137. *Standard Test Method for Compressive Residual Strength Properties of Damaged Polymer Matrix Composite Plates*. ASTM, 2017. DOI: 10.1520/D7137_D7137M-17.

[54] A. I. Gagani, A. B. Monsås, A. E. Krauklis, and A. T. Echtermeyer. "The effect of temperature and water immersion on the interlaminar shear fatigue of glass fiber epoxy composites using the I-beam method". In: *Composites Science and Technology* 181 (2019), p. 107703. DOI: 10.1016/j.compscitech.2019.107703.

[55] S. Budhe, M. D. Banea, and S. de Barros. "Bonded repair of composite structures in aerospace application: a review on environmental issues". In: *Applied Adhesion Science* 6.1 (2018), p. 1797. DOI: 10.1186/s40563-018-0104-5.

[56] R. S. Amano. "Review of Wind Turbine Research in 21st Century". In: *Journal of Energy Resources Technology* 139.5 (2017), p. 051201. DOI: 10.1115/1.4037757.

[57] C. Humeau, P. Davies, and F. Jacquemin. "An experimental study of water diffusion in carbon/epoxy composites under static tensile stress". In: *Composites Part A: Applied Science and Manufacturing* 107 (2018), pp. 94–104. DOI: 10.1016/j.compositesa.2017.12.016.

[58] O. Starkova, K. Aniskevich, and J. Sevcenko. “Long-term moisture absorption and durability of FRP pultruded rebars”. In: *Materials Today: Proceedings* (2020). DOI: 10.1016/j.matpr.2019.12.154.

[59] M. Bazli, H. Ashrafi, A. Jafari, X.-L. Zhao, R. K. S. Raman, and Y. Bai. “Effect of Fibers Configuration and Thickness on Tensile Behavior of GFRP Laminates Exposed to Harsh Environment”. In: *Polymers* 11.9 (2019). DOI: 10.3390/polym11091401.

[60] S. A. Grammatikos, B. Zafari, M. C. Evernden, J. T. Mottram, and J. M. Mitchels. “Moisture uptake characteristics of a pultruded fibre reinforced polymer flat sheet subjected to hot/wet aging”. In: *Polymer Degradation and Stability* 121.1 (2015), pp. 407–419. DOI: 10.1016/j.polymdegradstab.2015.10.001.

[61] D. Kraus and V. Trappe. “Transverse damage in glass fiber reinforced polymer under thermo-mechanical loading”. In: *Composites Part C: Open Access* 5 (2021), p. 100147. DOI: 10.1016/j.jcomc.2021.100147.

[62] A. Tcharkhtchi, F. Nony, S. Khelladi, J. Fitoussi, and S. Farzaneh. “Epoxy/amine reactive systems for composites materials and their thermomechanical properties”. In: *Advances in Composites Manufacturing and Process Design*. Vol. 43. Elsevier, 2015, pp. 269–296. ISBN: 9781782423072. DOI: 10.1016/B978-1-78242-307-2.00013-0.

[63] H. Mivehchi and A. Varvani-Farahani. “The effect of temperature on fatigue strength and cumulative fatigue damage of FRP composites”. In: *Procedia Engineering* 2.1 (2010), pp. 2011–2020. DOI: 10.1016/j.proeng.2010.03.216.

[64] Y. Ou, D. Zhu, H. Zhang, L. Huang, Y. Yao, G. Li, and B. Mobasher. “Mechanical Characterization of the Tensile Properties of Glass Fiber and Its Reinforced Polymer (GFRP) Composite under Varying Strain Rates and Temperatures”. In: *Polymers* 8.5 (2016). DOI: 10.3390/polym8050196.

[65] A. Ilioni, P.-Y. Le Gac, C. Badulescu, D. Thévenet, and P. Davies. “Prediction of Mechanical Behaviour of a Bulk Epoxy Adhesive in a Marine Environment”. In: *The Journal of Adhesion* 95.1 (2019), pp. 64–84. DOI: 10.1080/00218464.2017.1377616.

[66] M. Bordes, P. Davies, J.-Y. Cognard, L. Sohier, V. Sauvant-Moynot, and J. Galy. "Prediction of long term strength of adhesively bonded steel/epoxy joints in sea water". In: *International Journal of Adhesion and Adhesives* 29.6 (2009), pp. 595–608. DOI: 10.1016/j.ijadhadh.2009.02.013.

[67] V. Jaksic, C. R. Kennedy, D. M. Grogan, S. B. Leen, and C. M. Ó. Brádaigh. "Influence of Composite Fatigue Properties on Marine Tidal Turbine Blade Design". In: *Durability of Composites in a Marine Environment 2*. Ed. by Peter Davies and Yapa D.S Rajapakse. Vol. 245. Solid Mechanics and Its Applications. Cham: Springer International Publishing, 2018, pp. 195–223. ISBN: 978-3-319-65144-6. DOI: 10.1007/978-3-319-65145-3_11.

[68] M. Frigione and A. Rodríguez-Prieto. "Can Accelerated Aging Procedures Predict the Long Term Behavior of Polymers Exposed to Different Environments?" In: *Polymers* 13.16 (2021). DOI: 10.3390/polym13162688.

[69] A. E. Krauklis, O. Starkova, D. Gibhardt, G. Kalinka, H. A. Aouissi, J. Burlakovs, A. Sabalina, and B. Fiedler. "Reversible and irreversible effects on the epoxy GFRP fiber-matrix interphase due to hydrothermal aging". In: *Composites Part C: Open Access* 12.6 (2023), p. 100395. DOI: 10.1016/j.jcomc.2023.100395.

[70] Y. Zheng, R. D. Priestley, and G. B. McKenna. "Physical aging of an epoxy subsequent to relative humidity jumps through the glass concentration". In: *Journal of Polymer Science Part B: Polymer Physics* 42.11 (2004), pp. 2107–2121. DOI: 10.1002/polb.20084.

[71] D. McGeorge, A. T. Echtermeyer, K. H. Leong, B. Melve, M. Robinson, and K. P. Fischer. "Repair of floating offshore units using bonded fibre composite materials". In: *Composites Part A: Applied Science and Manufacturing* 40.9 (2009), pp. 1364–1380. DOI: 10.1016/j.compositesa.2009.01.015.

[72] I. Grabovac and D. Whittaker. "Application of bonded composites in the repair of ships structures – A 15-year service experience". In: *Composites Part A: Applied Science and Manufacturing* 40.9 (2009), pp. 1381–1398. DOI: 10.1016/j.compositesa.2008.11.006.

[73] V. O. Startsev, M. P. Lebedev, K. A. Khrulev, M. V. Molokov, A. S. Frolov, and T. A. Nizina. "Effect of outdoor exposure on the moisture diffusion and mechanical properties of epoxy polymers". In: *Polymer Testing* 65 (2018), pp. 281–296. DOI: 10.1016/j.polymertesting.2017.12.007.

[74] O. Starkova, A. I. Gagani, C. W. Karl, I. B. C. M. Rocha, J. Burlakovs, and A. E. Krauklis. "Modelling of Environmental Ageing of Polymers and Polymer Composites-Durability Prediction Methods". In: *Polymers* 14.5 (2022). DOI: 10.3390/polym14050907.

[75] M. Bruyneel, P. Jetteur, J. P. Delsemme, S. Siavoshani, and A. Cheruet. "Modeling and Simulating Progressive Failure in Composite Structures for Automotive Applications". In: *SAE Technical Paper Series*. SAE Technical Paper Series. SAE International400 Commonwealth Drive, Warrendale, PA, United States, 2014. DOI: 10.4271/2014-01-0962.

[76] A. E. Krauklis, A. Gagani, K. Vegere, I. Kalnina, M. Klavins, and A. T. Echtermeyer. "Dissolution Kinetics of R-Glass Fibres: Influence of Water Acidity, Temperature, and Stress Corrosion". In: *Fibers* 7.3 (2019), p. 22. DOI: 10.3390/fib7030022.

[77] G. Z. Xiao and M. E. R. Shanahan. "Swelling of DGEBA/DDA epoxy resin during hygrothermal ageing". In: *Polymer* 39.14 (1998), pp. 3253–3260. DOI: 10.1016/S0032-3861(97)10060-X.

[78] A. Toscano, G. Pitarresi, M. Scafidi, M. Di Filippo, G. Spadaro, and S. Alessi. "Water diffusion and swelling stresses in highly crosslinked epoxy matrices". In: *Polymer Degradation and Stability* 133.1 (2016), pp. 255–263. DOI: 10.1016/j.polymdegradstab.2016.09.004.

[79] N. Karak. *Sustainable Epoxy Thermosets and Nanocomposites*. Vol. 1385. Washington, DC: American Chemical Society, 2021. ISBN: 9780841298316. DOI: 10.1021/bk-2021-1385.

[80] A. E. Krauklis, A. I. Gagani, and A. T. Echtermeyer. "Near-Infrared Spectroscopic Method for Monitoring Water Content in Epoxy Resins and Fiber-Reinforced Composites". In: *Materials (Basel, Switzerland)* 11.4 (2018). DOI: 10.3390/ma11040586.

[81] M. Wang, X. Xu, J. Ji, Y. Yang, J. Shen, and M. Ye. "The hygrothermal aging process and mechanism of the novolac epoxy resin". In: *Composites Part B: Engineering* 107.5 (2016), pp. 1–8. DOI: 10.1016/j.compositesb.2016.09.067.

[82] T. C. Clancy, S. J. V. Frankland, J. A. Hinkley, and T. S. Gates. "Molecular modeling for calculation of mechanical properties of epoxies with moisture ingress". In: *Polymer* 50.12 (2009), pp. 2736–2742. DOI: 10.1016/j.polymer.2009.04.021.

[83] A. E. Krauklis, A. Gagani, and A. T. Echtermeyer. "Prediction of Orthotropic Hygroscopic Swelling of Fiber-Reinforced Composites from Isotropic Swelling of Matrix Polymer". In: *Journal of Composites Science* 3.1 (2019), p. 10. DOI: 10.3390/jcs3010010.

[84] O. Starkova, S. Gaidukovs, O. Platnieks, A. Barkane, K. Garkusina, E. Palitis, and L. Grase. "Water absorption and hydrothermal ageing of epoxy adhesives reinforced with amino-functionalized graphene oxide nanoparticles". In: *Polymer Degradation and Stability* 191.17 (2021), p. 109670. DOI: 10.1016/j.polymdegradstab.2021.109670.

[85] M. J. Marks and R. V. Snelgrove. "Effect of conversion on the structure-property relationships of amine-cured epoxy thermosets". In: *ACS applied materials & interfaces* 1.4 (2009), pp. 921–926. DOI: 10.1021/am900030u.

[86] A. J. Guenthner, K. R. Lamison, V. Vij, J. T. Reams, G. R. Yandek, and J. M. Mabry. "New Insights into Structure–Property Relationships in Thermosetting Polymers from Studies of Cocured Polycyanurate Networks". In: *Macromolecules* 45.1 (2012), pp. 211–220. DOI: 10.1021/ma202513h.

[87] A. Antoniou, M. Rosemeier, K. Tazefidan, A. Krimmer, and G. Wolken-Möhlmann. "Impact of Site-Specific Thermal Residual Stress on the Fatigue of Wind-Turbine Blades". In: *AIAA Journal* 58.11 (2020), pp. 4781–4793. DOI: 10.2514/1.J059388.

[88] H. Schürmann. *Konstruieren mit Faser-Kunststoff-Verbunden*. 2nd ed. Springer-Verlag Berlin Heidelberg, 2007. ISBN: 978-3-540-72189-5.

[89] B. Fiedler, T. Hobbiebrunken, M. Hojo, and K. Schulte. "Influence of stress state and temperature on the strength of epoxy resins". In: *11th International Conference on Fracture 2005, ICF11* 3 (2005).

[90] O. Starkova, S. Gaidukovs, O.Platnieks, A. Barkane, K. Garkusina, E. Palitis, and L. Grase. "Water absorption and hydrothermal ageing of epoxy adhesives reinforced with amino-functionalized graphene oxide nanoparticles". In: *Polymer Degradation and Stability* 191 (2021), p. 109670. DOI: 10.1016/j.polymdegradstab.2021.109670.

[91] H. Chai. “The effects of bond thickness, rate and temperature on the deformation and fracture of structural adhesives under shear loading”. In: *International Journal of Fracture* 130.1 (2004), pp. 497–515. DOI: 10.1023/B:FRAC.0000049504.51847.2a.

[92] M. D. Banea, F. S. M. de Sousa, L. F. M. da Silva, R. D. S. G. Campilho, and A. M. Bastos de Pereira. “Effects of Temperature and Loading Rate on the Mechanical Properties of a High Temperature Epoxy Adhesive”. In: *Journal of Adhesion Science and Technology* 25.18 (2011), pp. 2461–2474. DOI: 10.1163/016942411X580144.

[93] W Araki, T Adachi, M Gamou, and A Yamaji. “Time-temperature dependence of fracture toughness for bisphenol A epoxy resin”. In: *Proceedings of the Institution of Mechanical Engineers, Part L: Journal of Materials: Design and Applications* 216.2 (2002), pp. 79–84.

[94] S. Chandrasekaran, N. Sato, F. Tölle, R. Mülhaupt, B. Fiedler, and K. Schulte. “Fracture toughness and failure mechanism of graphene based epoxy composites”. In: *Composites Science and Technology* 97.16 (2014), pp. 90–99. DOI: 10.1016/j.compscitech.2014.03.014.

[95] S.-W. Koh, J.-K. Kim, and Y.-W. Mai. “Fracture toughness and failure mechanisms in silica-filled epoxy resin composites: effects of temperature and loading rate”. In: *Polymer* 34.16 (1993), pp. 3446–3455. DOI: 10.1016/0032-3861(93)90474-O.

[96] B. Fiedler, M. Hojo, S. Ochiai, K. Schulte, and M. Ando. “Failure behavior of an epoxy matrix under different kinds of static loading”. In: *Carbon Nanotube (CNT) - Polymer Composites* 61.11 (2001), pp. 1615–1624. DOI: 10.1016/S0266-3538(01)00057-4.

[97] J. Zhou and J. P. Lucas. “Hygrothermal effects of epoxy resin. Part I: the nature of water in epoxy”. In: *Polymer* 40.20 (1999), pp. 5505–5512. DOI: 10.1016/S0032-3861(98)00790-3.

[98] A. E. Krauklis, A. I. Gagani, and A. T. Echtermeyer. “Hygrothermal Aging of Amine Epoxy: Reversible Static and Fatigue Properties”. In: *Open Engineering* 8.1 (2018), pp. 447–454. DOI: 10.1515/eng-2018-0050.

[99] J. Zhou and J. P. Lucas. “Hygrothermal effects of epoxy resin. Part II: variations of glass transition temperature”. In: *Polymer* 40.20 (1999), pp. 5513–5522. DOI: 10.1016/S0032-3861(98)00791-5.

[100] G. Baschek, G. Hartwig, and F. Zahradnik. “Effect of water absorption in polymers at low and high temperatures”. In: *Polymer* 40.12 (1999), pp. 3433–3441. DOI: 10.1016/S0032-3861(98)00560-6.

[101] M. R. Vanlandingham, R. F. Eduljee, and J. W. Gillespie. “Moisture diffusion in epoxy systems”. In: *Journal of Applied Polymer Science* 71.5 (1999), pp. 787–798. DOI: 10.1002/(SICI)1097-4628(19990131)71:5{\%}3C787::AID-APP12{\%}3E3.0.CO;2-A.

[102] A. F. Abdelkader and J. R. White. “Water absorption in epoxy resins: The effects of the crosslinking agent and curing temperature”. In: *Journal of Applied Polymer Science* 98.6 (2005), pp. 2544–2549. DOI: 10.1002/app.22400.

[103] Y. Elkebir, S. Mallarino, D. Trinh, and S. Touzain. “Effect of physical ageing onto the water uptake in epoxy coatings”. In: *Electrochimica Acta* 337 (2020), p. 135766. DOI: 10.1016/j.electacta.2020.135766.

[104] I. Kada, D. Trinh, S. Mallarino, and S. Touzain. “Physical ageing effect on water uptake and adhesion of epoxy coatings by EIS and the blister test”. In: *Electrochimica Acta* 454 (2023), p. 142381. DOI: 10.1016/j.electacta.2023.142381.

[105] R. P Kambour. “Correlations of the dry crazing resistance of glassy polymers with other physical properties”. English. In: *Polymer communications* (1983).

[106] P.-Y. Le Gac, M. Arhant, M. Le Gall, and P. Davies. “Yield stress changes induced by water in polyamide 6: Characterization and modeling”. In: *Polymer Degradation and Stability* 137.12 (2017), pp. 272–280. DOI: 10.1016/j.polymdegradstab.2017.02.003.

[107] V. Bellenger, J. Verdu, and E. Morel. “Structure-properties relationships for densely cross-linked epoxide-amine systems based on epoxide or amine mixtures”. In: *Journal of Materials Science* 24.1 (1989), pp. 63–68. DOI: 10.1007/BF00660933.

[108] X. Colin. “Nonempirical Kinetic Modeling of Non-fickian Water Absorption Induced by a Chemical Reaction in Epoxy-Amine Networks”. In: *Durability of Composites in a Marine Environment 2*. Ed. by Peter Davies and Yapa D.S Rajapakse. Vol. 245. Solid Mechanics and Its Applications. Cham: Springer International Publishing, 2018, pp. 1–18. ISBN: 978-3-319-65144-6. DOI: 10.1007/978-3-319-65145-3_1.

[109] J. B. Enns and J. K. Gillham. "Effect of the extent of cure on the modulus, glass transition, water absorptio, and density of an amine-cured epoxy". In: *Journal of Applied Polymer Science* 28.9 (1983), pp. 2831–2846. DOI: 10.1002/app.1983.070280914.

[110] P. Musto, G. Ragosta, G. Scarinzi, and L. Mascia. "Probing the molecular interactions in the diffusion of water through epoxy and epoxy-bismaleimide networks". In: *Journal of Polymer Science Part B: Polymer Physics* 40.10 (2002), pp. 922–938. DOI: 10.1002/polb.10147.

[111] E. Gaudichet-Maurin, F. Thominette, and J. Verdu. "Water sorption characteristics in moderately hydrophilic polymers, Part 1: Effect of polar groups concentration and temperature in water sorption in aromatic polysulfones". In: *Journal of Applied Polymer Science* 109.5 (2008), pp. 3279–3285. DOI: 10.1002/app.24873.

[112] S. Muroga, Y. Hikima, and M. Ohshima. "Near-Infrared Spectroscopic Evaluation of the Water Content of Molded Polylactide under the Effect of Crystallization". In: *Applied spectroscopy* 71.6 (2017), pp. 1300–1309. DOI: 10.1177/0003702816681011.

[113] S. Cotugno, D. Larobina, G. Mensitieri, P. Musto, and G. Ragosta. "A novel spectroscopic approach to investigate transport processes in polymers: the case of water–epoxy system". In: *Polymer* 42.15 (2001), pp. 6431–6438. DOI: 10.1016/S0032-3861(01)00096-9.

[114] P. Musto, G. Ragosta, and L. Mascia. "Vibrational Spectroscopy Evidence for the Dual Nature of Water Sorbed into Epoxy Resins". In: *Chemistry of Materials* 12.5 (2000), pp. 1331–1341. DOI: 10.1021/cm9906809.

[115] A. E. Krauklis, A. Gagani, and A. T. Echtermeyer. "Long-Term Hydrolytic Degradation of the Sizing-Rich Composite Interphase". In: *Coatings* 9.4 (2019), p. 263. DOI: 10.3390/coatings9040263.

[116] M. K. Hagnell, S. Kumaraswamy, T. Nyman, and M. Åkermo. "From aviation to automotive - a study on material selection and its implication on cost and weight efficient structural composite and sandwich designs". In: *Heliyon* 6.3 (2020), e03716. DOI: 10.1016/j.heliyon.2020.e03716.

[117] A. Arteiro, G. Catalanotti, J. Reinoso, P. Linde, and P. P. Camanho. "Simulation of the Mechanical Response of Thin-Ply Composites: From Computational Micro-Mechanics to Structural Analysis". In: *Archives of*

Computational Methods in Engineering 26.5 (2019), pp. 1445–1487. DOI: 10.1007/s11831-018-9291-2.

[118] M. Nakada, Y. Miyano, H. Cai, and M. Kasamori. "Prediction of long-term viscoelastic behavior of amorphous resin based on the time-temperature superposition principle". In: *Mechanics of Time-Dependent Materials* 15.3 (2011), pp. 309–316. DOI: 10.1007/s11043-011-9139-8.

[119] I. Emri. "Rheology of solid polymers". In: *Rheology reviews* (2005).

[120] H. F. Brinson and L. C. Brinson. *Polymer Engineering Science and Viscoelasticity: An Introduction*. 2nd ed. 2015. New York, NY: Springer US, 2015. ISBN: 978-1-4899-7768-7.

[121] M. L. Williams, R. F. Landel, and J. D. Ferry. "The Temperature Dependence of Relaxation Mechanisms in Amorphous Polymers and Other Glass-forming Liquids". In: *Journal of the American Chemical Society* 77.14 (1955), pp. 3701–3707. DOI: 10.1021/ja01619a008.

[122] H. Cai, M. Nakada, and Y. Miyano. "Simplified determination of long-term viscoelastic behavior of amorphous resin". In: *Mechanics of Time-Dependent Materials* 17.1 (2013), pp. 137–146. DOI: 10.1007/s11043-012-9174-0.

[123] V. Fabre, G. Quandalle, N. Billon, and S. Cantournet. "Time-Temperature-Water content equivalence on dynamic mechanical response of polyamide 6,6". In: *Polymer* 137 (2018), pp. 22–29. DOI: 10.1016/j.polymer.2017.10.067.

[124] F. Huber, H. Etschmaier, H. Walter, G. Urstöger, and P. Hadley. "A time–temperature–moisture concentration superposition principle that describes the relaxation behavior of epoxide molding compounds for microelectronics packaging". In: *International Journal of Polymer Analysis and Characterization* 25.6 (2020), pp. 467–478. DOI: 10.1080/1023666X.2020.1807680.

[125] B. C. Hancock and G. Zografi. "The relationship between the glass transition temperature and the water content of amorphous pharmaceutical solids". In: *Pharmaceutical research* 11.4 (1994), pp. 471–477. DOI: 10.1023/A:1018941810744.

[126] P. P. Simon and H. J. Ploehn. “Modeling the effect of plasticizer on the viscoelastic response of crosslinked polymers using the tube-junction model”. In: *Journal of Rheology* 44.2 (2000), pp. 169–183. DOI: 10.1122/1.551082.

[127] A. Doblies, C. Feiler, T. Würger, E. Schill, R. H. Meißner, and B. Fiedler. “Mechanical degradation estimation of thermosets by peak shift assessment: General approach using infrared spectroscopy”. In: *Polymer* 221.9 (2021), p. 123585. DOI: 10.1016/j.polymer.2021.123585.

[128] Y. Miyano. *Durability of Fiber-Reinforced Polymers*. Weinheim, Germany: Wiley-VCH Verlag GmbH & Co. KGaA, 2017. ISBN: 9783527811984. DOI: 10.1002/9783527811984.

[129] A. Müller. “Schädigungscharakterisierung an Faser-Kunststoff-Verbunden im Schwingversuch mittels Röntgenrefraktionstopographie unter Berücksichtigung der Matrixeigenschaften”. PhD thesis. Bundesanstalt für Materialforschung und-prüfung (BAM), 2018.

[130] A.R Berens and H.B Hopfenberg. “Diffusion and relaxation in glassy polymer powders: 2. Separation of diffusion and relaxation parameters”. In: *Polymer* 19.5 (1978), pp. 489–496. ISSN: 00323861. DOI: 10.1016/0032-3861(78)90269-0.

[131] O. Starkova, S. Chandrasekaran, T. Schnoor, J. Sevcenko, and K. Schulte. “Anomalous water diffusion in epoxy/carbon nanoparticle composites”. In: *Polymer Degradation and Stability* 164 (2019), pp. 127–135. DOI: 10.1016/j.polymdegradstab.2019.04.010.

[132] Li-Rong Bao, Albert F. Yee, and Charles Y.-C Lee. “Moisture absorption and hygrothermal aging in a bismaleimide resin”. In: *Polymer* 42.17 (2001), pp. 7327–7333. ISSN: 00323861. DOI: 10.1016/S0032-3861(01)00238-5.

[133] G. Capiel, J. Uicich, D. Fasce, and P. E. Montemartini. “Diffusion and hydrolysis effects during water aging on an epoxy-anhydride system”. In: *Polymer Degradation and Stability* 153 (2018), pp. 165–171. DOI: 10.1016/j.polymdegradstab.2018.04.030.

[134] J. Crank. *The mathematics of diffusion*. 2. ed., reprinted. Oxford science publications. Oxford: Oxford Univ. Press, ca. 2009. ISBN: 0198534116.

[135] O. Starkova, S. T. Buschhorn, E. Mannov, K. Schulte, and A. Aniskevich. "Water transport in epoxy/MWCNT composites". In: *European Polymer Journal* 49.8 (2013), pp. 2138–2148. DOI: 10.1016/j.eurpolymj.2013.05.010.

[136] L. R. Grace. "Projecting long-term non-Fickian diffusion behavior in polymeric composites based on short-term data: a 5-year validation study". In: *Journal of Materials Science* 51.2 (2016), pp. 845–853. DOI: 10.1007/s10853-015-9407-0.

[137] F. X. Perrin, M. H. Nguyen, and J. L. Vernet. "Water transport in epoxy–aliphatic amine networks – Influence of curing cycles". In: *European Polymer Journal* 45.5 (2009), pp. 1524–1534. DOI: 10.1016/j.eurpolymj.2009.01.023.

[138] D. T. Hallinan, M. G. de Angelis, M. Giacinti Baschetti, G. C. Sarti, and Y. A. Elabd. "Non-Fickian Diffusion of Water in Nafion". In: *Macromolecules* 43.10 (2010), pp. 4667–4678. DOI: 10.1021/ma100047z.

[139] M. B. Satterfield, P. W. Majsztrik, H. Ota, J. B. Benziger, and A. B. Bocarsly. "Mechanical properties of Nafion and titania/Nafion composite membranes for polymer electrolyte membrane fuel cells". In: *Journal of Polymer Science Part B: Polymer Physics* 44.16 (2006), pp. 2327–2345. DOI: 10.1002/polb.20857.

[140] D. Kraus. "Ermüdungsverhalten von Glasfaser-Kunststoff-Verbunden unter thermomechanischer Beanspruchung". PhD thesis. 2021.

[141] B. Fiedler, T. Hobbiebrunken, M. Hojo, and K. Schulte. "Influence of stress state and temperature on the strength of epoxy resins". In: *11th International Conference on Fracture 2005, ICF11* Vol 3 (2005), pp. 2271–2275.

[142] M. Fernández-García and M. Y. M. Chiang. "Effect of hygrothermal aging history on sorption process, swelling, and glass transition temperature in a particle-filled epoxy-based adhesive". In: *Journal of Applied Polymer Science* 84.8 (2002), pp. 1581–1591. DOI: 10.1002/app.10447.

[143] G. C. Papanicolaou, Th.V. Kosmidou, A. S. Vatalis, and C. G. Delides. "Water absorption mechanism and some anomalous effects on the mechanical and viscoelastic behavior of an epoxy system". In: *Journal of Applied Polymer Science* 99.4 (2006), pp. 1328–1339. DOI: 10.1002/app.22095.

[144] S. Alessi, M. Di Filippo, G. Pitarresi, M. Scafidi, and A. Toscano. "Fracture Toughness of Hydrothermally Aged Epoxy Systems with Different Crosslink Density". In: *Procedia Engineering* 109.8 (2015), pp. 507–516. DOI: 10.1016/j.proeng.2015.06.257.

[145] J. T. Han and K. Cho. "Nanoparticle-induced enhancement in fracture toughness of highly loaded epoxy composites over a wide temperature range". In: *Journal of Materials Science* 41.13 (2006), pp. 4239–4245. DOI: 10.1007/s10853-006-6219-2.

[146] J. Körbelin. "Damage tolerance of high-performance composites". PhD thesis. TUHH Universitätsbibliothek, 2022. DOI: 10.15480/882.4276.

[147] H. Meeuw, J. Körbelin, V. K. Wisniewski, A. S. Nia, A. R. Vázquez, M. R. Lohe, X. Feng, and B. Fiedler. "Carbon Nanoparticles' Impact on Processability and Physical Properties of Epoxy Resins-A Comprehensive Study Covering Rheological, Electrical, Thermo-Mechanical, and Fracture Properties (Mode I and II)". In: *Polymers* 11.2 (2019). DOI: 10.3390/polym11020231..

[148] Y. Miyano and M. Nakada. "Accelerated testing methodology for durability of CFRP". In: *Composites Part B: Engineering* 191 (2020), p. 107977. DOI: 10.1016/j.compositesb.2020.107977.

[149] M. Nakada and Y. Miyano. "Accelerated testing for long-term fatigue strength of various FRP laminates for marine use". In: *Composites Science and Technology* 69.6 (2009), pp. 805–813. DOI: 10.1016/j.compscitech.2008.02.030.

[150] Y. Miyano, M. Nakada, and N. Sekine. "Accelerated Testing for Long-term Durability of FRP Laminates for Marine Use". In: *Journal of Composite Materials* 39.1 (2005), pp. 5–20. DOI: 10.1177/0021998305046430.

[151] R. M. Guedes. "Lifetime predictions of polymer matrix composites under constant or monotonic load". In: *Composites Part A: Applied Science and Manufacturing* 37.5 (2006), pp. 703–715. DOI: 10.1016/j.compositesa.2005.07.007.

[152] C. C. Hiel, H. F. Brinson, and A. H. Cardon. "The Nonlinear Viscoelastic Response of Resin Matrix Composites". In: *Composite Structures 2*. Ed. by I. H. Marshall. Vol. 4. Dordrecht: Springer Netherlands, 1983, pp. 271–281. ISBN: 978-94-009-6642-0. DOI: 10.1007/978-94-009-6640-6_20.

[153] O. Starkova and A. Aniskevich. "Application of time-temperature superposition to energy limit of linear viscoelastic behavior". In: *Journal of Applied Polymer Science* 114.1 (2009), pp. 341–347. DOI: 10.1002/app.30528.

[154] R. M. Guedes. "Review article: Time-dependent failure criteria for polymer matrix composites: a review". In: *Journal of Reinforced Plastics and Composites* 29.20 (2010), pp. 3041–3047. DOI: 10.1177/0731684410370067.

[155] R. M. Christensen and R. E. Glaser. "The Application of Kinetic Fracture Mechanics to Life Prediction for Polymeric Materials". In: *Journal of Applied Mechanics* 52.1 (1985), pp. 1–5. DOI: 10.1115/1.3168997.

[156] Y. Ding, M. Liu, S. Li, S. Zhang, W.-F. Zhou, and B. Wang. "Contributions of the Side Groups to the Characteristics of Water Absorption in Cured Epoxy Resins". In: *Macromolecular Chemistry and Physics* 202.13 (2001), pp. 2681–2685. DOI: 10.1002/1521-3935(20010901)202:13{\%}3C2681::AID-MACP2681{\%}3E3.0.CO;2-E.

[157] X. Monnier, S. Marina, X. Lopez de Pariza, H. Sardón, J. Martin, and D. Cangialosi. "Physical Aging Behavior of a Glassy Polyether". In: *Polymers* 13.6 (2021). DOI: 10.3390/polym13060954.

[158] K. Chen and K. S. Schweizer. "Molecular theory of physical aging in polymer glasses". In: *Physical review letters* 98.16 (2007), p. 167802. DOI: 10.1103/PhysRevLett.98.167802.

[159] J. M. Hutchinson. "Physical aging of polymers". In: *Progress in Polymer Science* 20.4 (1995), pp. 703–760. DOI: 10.1016/0079-6700(94)00001-I.

[160] G. B. McKenna. "Physical Aging in Glasses and Composites". In: *Long-Term Durability of Polymeric Matrix Composites*. Ed. by Kishore V. Pochiraju, Gyaneshwar P. Tandon, and Gregory A. Schoeppner. Vol. 3. Boston, MA: Springer US, 2012, pp. 237–309. ISBN: 978-1-4419-9307-6. DOI: 10.1007/978-1-4419-9308-3_7.

[161] G. M. Odegard and A. Bandyopadhyay. "Physical aging of epoxy polymers and their composites". In: *Journal of Polymer Science Part B: Polymer Physics* 49.24 (2011), pp. 1695–1716. DOI: 10.1002/polb.22384.

[162] A. J. Kovacs, J. J. Aklonis, J. M. Hutchinson, and A. R. Ramos. “Isobaric volume and enthalpy recovery of glasses. II. A transparent multiparameter theory”. In: *Journal of Polymer Science: Polymer Physics Edition* 17.7 (1979), pp. 1097–1162. DOI: 10.1002/pol.1979.180170701.

[163] C. T. Moynihan, A. J. Easteal, M. A. Bolt, and J. Tucker. “Dependence of the Fictive Temperature of Glass on Cooling Rate”. In: *Journal of the American Ceramic Society* 59.1-2 (1976), pp. 12–16. DOI: 10.1111/j.1151-2916.1976.tb09376.x.

[164] X. Li, X. Zhang, J. Chen, L. Huang, and Y. Lv. “The mechanical properties and creep behavior of epoxy polymer under the marine environment: A molecular dynamics investigation”. In: *Materials Today Communications* 28.2–5 (2021), p. 102737. DOI: 10.1016/j.mtcomm.2021.102737.

[165] L. Tam, D. Lau, and C. Wu. “Understanding interaction and dynamics of water molecules in the epoxy via molecular dynamics simulation”. In: *Molecular Simulation* 45.2 (2019), pp. 120–128. DOI: 10.1080/08927022.2018.1540869.

[166] S. G. Lee, S. S. Jang, J. Kim, and G. Kim. “Distribution and Diffusion of Water in Model Epoxy Molding Compound: Molecular Dynamics Simulation Approach”. In: *IEEE Transactions on Advanced Packaging* 33.2 (2010), pp. 333–339. DOI: 10.1109/TADVP.2009.2033570.

[167] A. Tcharkhtchi, J.-P. Trotignon, and J. Verdu. “Yielding and fracture in crosslinked epoxies”. In: *Macromolecular Symposia* 147.1 (1999), pp. 221–234. DOI: 10.1002/masy.19991470122.

[168] G. Xian and V. M. Karbhari. “DMTA based investigation of hygrothermal ageing of an epoxy system used in rehabilitation”. In: *Journal of Applied Polymer Science* 104.2 (2007), pp. 1084–1094. DOI: 10.1002/app.25576.

[169] G. Xian and V. M. Karbhari. “Segmental relaxation of water-aged ambient cured epoxy”. In: *Polymer Degradation and Stability* 92.9 (2007), pp. 1650–1659. DOI: 10.1016/j.polymdegradstab.2007.06.015.

[170] Y. Joliff, W. Rekik, L. Belec, and J. F. Chailan. “Study of the moisture/stress effects on glass fibre/epoxy composite and the impact of the interphase area”. In: *Composite Structures* 108 (2014), pp. 876–885. DOI: 10.1016/j.compstruct.2013.10.001.

[171] T. Morii, N. Ikuta, K. Kiyosumi, and H. Hamada. "Weight-change analysis of the interphase in hygrothermally aged FRP: Consideration of debonding". In: *Composites Science and Technology* 57.8 (1997), pp. 985–990. DOI: 10.1016/S0266-3538(97)00051-1.

[172] B. Abdel-Magid, S. Ziaee, K. Gass, and M. Schneider. "The combined effects of load, moisture and temperature on the properties of E-glass/epoxy composites". In: *Composite Structures* 71.3-4 (2005), pp. 320–326. DOI: 10.1016/j.compstruct.2005.09.022.

[173] H. Li, P. Gu, J. Watson, and J. Meng. "Acid corrosion resistance and mechanism of E-glass fibers: boron factor". In: *Journal of Materials Science* 48.8 (2013), pp. 3075–3087. DOI: 10.1007/s10853-012-7082-y.

[174] B. D. Caddock, K. E. Evans, and D. Hull. "Stress-corrosion failure envelopes for E-glass fibre bundles". In: *Journal of Materials Science* 25.5 (1990), pp. 2498–2502. DOI: 10.1007/BF00638049.

[175] H. Li and J. C. Watson. "Continuous Glass Fibers for Reinforcement". In: *Encyclopedia of Glass Science, Technology, History, and Culture*. Ed. by Pascal Richet, Reinhard Conradt, Akira Takada, and Joël Dyon. Vol. 55. Wiley, 2021, pp. 95–109. ISBN: 9781118799420. DOI: 10.1002/9781118801017.ch1.6.

[176] J. L. Thomason. *Glass fibre sizing : a review of size formulation patents*. Glasgow: James L. Thomason, 2015. ISBN: 9780957381438.

[177] J. L. Thomason. "Glass fibre sizing: A review". In: *Composites Part A: Applied Science and Manufacturing* 127 (2019), p. 105619. DOI: 10.1016/j.compositesa.2019.105619. URL: https://www.sciencedirect.com/science/article/pii/S1359835X19303689.

[178] J. L. Thomason. "Sizing Chemistry of Glass Fibers". In: *Fiberglass Science and Technology: Chemistry, Characterization, Processing, Modeling, Application, and Sustainability*. Ed. by Hong Li. Cham: Springer International Publishing, 2021, pp. 259–321. ISBN: 978-3-030-72200-5. DOI: 10.1007/978-3-030-72200-5_4. URL: https://doi.org/10.1007/978-3-030-72200-5_4.

[179] L. Peters. "Influence of Glass Fibre Sizing and Storage Conditions on Composite Properties". In: *Durability of Composites in a Marine Environment 2*. Ed. by Peter Davies and Yapa D.S Rajapakse. Vol. 245. Solid

Mechanics and Its Applications. Cham: Springer International Publishing, 2018, pp. 19–31. ISBN: 978-3-319-65144-6. DOI: 10.1007/978-3-319-65145-3_2.

[180] I.B.C.M. Rocha, F. P. van der Meer, S. Raijmaekers, F. Lahuerta, R.P.L. Nijssen, L. P. Mikkelsen, and L. J. Sluys. "A combined experimental/numerical investigation on hygrothermal aging of fiber-reinforced composites". In: *European Journal of Mechanics - A/Solids* 73 (2019), pp. 407–419. DOI: 10.1016/j.euromechsol.2018.10.003.

[181] S. T. Pinho, P. Robinson, and L. Iannucci. "Fracture toughness of the tensile and compressive fibre failure modes in laminated composites". In: *Composites Science and Technology* 66.13 (2006), pp. 2069–2079. DOI: 10.1016/j.compscitech.2005.12.023.

[182] X. Xu, S.-I. Takeda, and M. R. Wisnom. "Investigation of fracture process zone development in quasi-isotropic carbon/epoxy laminates using in situ and ex situ X-ray Computed Tomography". In: *Composites Part A: Applied Science and Manufacturing* 166.13 (2023), p. 107395. DOI: 10.1016/j.compositesa.2022.107395.

[183] Y. Geboes, A. Katalagarianakis, J. Soete, J. Ivens, and Y. Swolfs. "The translaminar fracture toughness of high-performance polymer fibre composites and their carbon fibre hybrids". In: *Composites Science and Technology* 221.2 (2022), p. 109307. DOI: 10.1016/j.compscitech.2022.109307.

[184] J. Zangenberg, P. Brøndsted, and J. W. Gillespie. "Fatigue damage propagation in unidirectional glass fibre reinforced composites made of a non-crimp fabric". In: *Journal of Composite Materials* 48.22 (2014), pp. 2711–2727. DOI: 10.1177/0021998313502062.

[185] K. M. Jespersen, J. Zangenberg, T. Lowe, P. J. Withers, and L. P. Mikkelsen. "Fatigue damage assessment of uni-directional non-crimp fabric reinforced polyester composite using X-ray computed tomography". In: *Composites Science and Technology* 136.2 (2016), pp. 94–103. DOI: 10.1016/j.compscitech.2016.10.006.

[186] S. Korkiakoski, E. Sarlin, R. Suihkonen, and O. Saarela. "Influence of reinforcement positioning on tension-tension fatigue performance of quasi-unidirectional GFRP laminates made of stitched fabrics". In: *Compo-*

sites Part B: Engineering 112.10 (2017), pp. 38–48. DOI: 10.1016/j.compositesb.2016.12.017.

[187] S. Sánchez-Carmona, E. Correa, A. Barroso, and F. París. "Experimental observations of fatigue damage in cross-ply laminates using carbon/epoxy ultra-thin plies". In: *Composite Structures* 306.1 (2023), p. 116564. DOI: 10.1016/j.compstruct.2022.116564.

[188] B. F. Sørensen. "Micromechanical model of the single fiber fragmentation test". In: *Mechanics of Materials* 104 (2017), pp. 38–48. DOI: 10.1016/j.mechmat.2016.10.002.

[189] B. F. Sørensen. "The critical damage state controlling the tension-tension fatigue life of unidirectional fibre composites". In: *Composites Science and Technology* 172 (2019), pp. 172–181. DOI: 10.1016/j.compscitech.2018.11.044.

[190] A. E. Krauklis, A. G. Akulichev, A. I. Gagani, and A. T. Echtermeyer. "Time-Temperature-Plasticization Superposition Principle: Predicting Creep of a Plasticized Epoxy". In: *Polymers* 11.11 (2019). DOI: 10.3390/polym11111848.

[191] D. Dew-Hughes and J. L. Way. "Fatigue of fibre — reinforced plastics: a review". In: *Composites* 4.4 (1973), pp. 167–173. ISSN: 00104361. DOI: 10.1016/0010-4361(73)90108-0.

[192] "The environmental fatigue behaviour of reinforced plastics". In: *Proceedings of the Royal Society of London. A. Mathematical and Physical Sciences* 396.1811 (1984), pp. 315–338. DOI: 10.1098/rspa.1984.0125.

[193] V. Alzamora Guzman and P. Brøndsted. "Effects of moisture on glass fiber-reinforced polymer composites". In: *Journal of Composite Materials* 49.8 (2015), pp. 911–920. DOI: 10.1177/0021998314527330.

[194] J. Thomason and G. Xypolias. "Hydrothermal Ageing of Glass Fibre Reinforced Vinyl Ester Composites: A Review". In: *Polymers* 15.4 (2023). DOI: 10.3390/polym15040835.

[195] P. Wang, L.-Y.-W. Ke, H.-L. Wu, and C. K. Y. Leung. "Hygrothermal aging effect on the water diffusion in glass fiber reinforced polymer (GFRP) composite: Experimental study and numerical simulation". In: *Composites Science and Technology* 230.3 (2022), p. 109762. DOI: 10.1016/j.compscitech.2022.109762.

[196] Peter Davies and Yapa D.S Rajapakse, eds. *Durability of Composites in a Marine Environment 2*. Solid Mechanics and Its Applications. Cham: Springer International Publishing, 2018. ISBN: 978-3-319-65144-6. DOI: 10.1007/978-3-319-65145-3.

[197] E. Klamer, L. Tromp, A. de Boer, and R. Nijssen. "Long-term effects of wet and outdoor conditions on GFRP". In: *IABSE Symposium Report* 105.14 (2015), pp. 1–8. DOI: 10.2749/222137815818358989.

[198] G. Carra and V. Carvelli. "Ageing of pultruded glass fibre reinforced polymer composites exposed to combined environmental agents". In: *Composite Structures* 108.2 (2014), pp. 1019–1026. DOI: 10.1016/j.compstruct.2013.10.042.

[199] F. Ellyin and C. Rohrbacher. "The Influence of Aqueous Environment, Temperature and Cyclic Loading on Glass-Fibre/Epoxy Composite Laminates". In: *Journal of Reinforced Plastics and Composites* 22.7 (2003), pp. 615–636. DOI: 10.1177/073168403027609.

[200] L. Gautier, B. Mortaigne, and V. Bellenger. "Interface damage study of hydrothermally aged glass-fibre-reinforced polyester composites". In: *Composites Science and Technology* 59.16 (1999), pp. 2329–2337. DOI: 10.1016/S0266-3538(99)00085-8.

[201] P. Davies and Y. D. S. Rajapakse. *Durability of Composites in a Marine Environment 2*. Vol. 245. Cham: Springer International Publishing, 2018. ISBN: 978-3-319-65144-6. DOI: 10.1007/978-3-319-65145-3.

[202] A. Boisseau, P. Davies, and F. Thiebaud. "Sea Water Ageing of Composites for Ocean Energy Conversion Systems: Influence of Glass Fibre Type on Static Behaviour". In: *Applied Composite Materials* 19.3-4 (2012), pp. 459–473. DOI: 10.1007/s10443-011-9219-6.

[203] A. I. Gagani, A. E. Krauklis, and A. T. Echtermeyer. "Orthotropic fluid diffusion in composite marine structures. Experimental procedure, analytical and numerical modelling of plates, rods and pipes". In: *Composites Part A: Applied Science and Manufacturing* 115 (2018), pp. 196–205. DOI: 10.1016/j.compositesa.2018.09.026.

[204] Y. Hu, A. W. Lang, X. Li, and S. R. Nutt. "Hygrothermal aging effects on fatigue of glass fiber/polydicyclopentadiene composites". In: *Polymer Degradation and Stability* 110 (2014), pp. 464–472. DOI: 10.1016/j.polymdegradstab.2014.10.018.

[205] L. Bian, J. Xiao, J. Zeng, and S. Xing. "Effects of seawater immersion on water absorption and mechanical properties of GFRP composites". In: *Journal of Composite Materials* 46.25 (2012), pp. 3151–3162. DOI: 10.1177/0021998312436992.

[206] A.-H. I. Mourad, B. M. Abdel-Magid, T. El-Maaddawy, and M. E. Grami. "Effect of Seawater and Warm Environment on Glass/Epoxy and Glass/Polyurethane Composites". In: *Applied Composite Materials* 17.5 (2010), pp. 557–573. DOI: 10.1007/s10443-010-9143-1.

[207] J. Zhu, Y. Deng, P. Chen, G. Wang, H. Min, and W. Fang. "Prediction of Long-Term Tensile Properties of Glass Fiber Reinforced Composites under Acid-Base and Salt Environments". In: *Polymers* 14.15 (2022). DOI: 10.3390/polym14153031.

[208] J. F. Mandell, D. D. Samborsky, D. A. Miller, P. Agastra, and A. T. Sears. "Analysis of SNL/MSU/DOE Fatigue Database Trends for Wind Turbine Blade Materials 2010-2015." In: (Feb. 2016). DOI: 10.2172/1431256.

[209] W. He, X. Li, P. Li, S. Fang, and A. Ding. "Experimental Investigation on Hygroscopic Aging of Glass Fiber Reinforced Vinylester Resin Composites". In: *Polymers* 14.18 (2022). DOI: 10.3390/polym14183828.

[210] Z. Zhai, C. Gröschel, and D. Drummer. "Tensile behavior of quasi-unidirectional glass fiber/polypropylene composites at room and elevated temperatures". In: *Polymer Testing* 54 (2016), pp. 126–133. DOI: 10.1016/j.polymertesting.2016.07.003.

[211] A. Jafari, M. Bazli, H. Ashrafi, A. Vatani Oskouei, S. Azhari, X.-L. Zhao, and H. Gholipour. "Effect of fibers configuration and thickness on tensile behavior of GFRP laminates subjected to elevated temperatures". In: *Construction and Building Materials* 202.4 (2019), pp. 189–207. DOI: 10.1016/j.conbuildmat.2019.01.003.

[212] I. C. Rosa, J. P. Firmo, and J. R. Correia. "Experimental study of the tensile behaviour of GFRP reinforcing bars at elevated temperatures". In: *Construction and Building Materials* 324 (2022). DOI: 10.1016/j.conbuildmat.2022.126676.

[213] J. Drummer, F. Tafesh, and B. Fiedler. "Effect of Fiber Misalignment and Environmental Temperature on the Compressive Behavior of Fiber Composites". In: *Polymers* 15.13 (2023). DOI: 10.3390/polym15132833.

[214] A. Manalo, G. Maranan, S. Sharma, W. Karunasena, and Y. Bai. "Temperature-sensitive mechanical properties of GFRP composites in longitudinal and transverse directions: A comparative study". In: *Composite Structures* 173 (2017), pp. 255–267. DOI: 10.1016/j.compstruct.2017.04.040.

[215] A. Robin, M. Arhant, P. Davies, S. Lejeune, E. Lolive, T. Bonnemains, and B. Habert. "Effect of aging on the in-plane and out-of-plane mechanical properties of composites for design of marine structures". In: *Composites Part C: Open Access* 11.1 (2023), p. 100354. DOI: 10.1016/j.jcomc.2023.100354.

[216] J. J. M. Machado, E. A. S. Marques, RDSG Campilho, and Lucas F. M. da Silva. "Mode I fracture toughness of CFRP as a function of temperature and strain rate". In: *Journal of Composite Materials* 51.23 (2017), pp. 3315–3326. DOI: 10.1177/0021998316682309.

[217] J.J.M. Machado, E.A.S. Marques, R.D.S.G. Campilho, and Lucas F.M. da Silva. "Mode II fracture toughness of CFRP as a function of temperature and strain rate". In: *Composites Part B: Engineering* 114.6 (2017), pp. 311–318. DOI: 10.1016/j.compositesb.2017.02.013.

[218] J. A. Rodríguez-González and C. Rubio-González. "Seawater effects on interlaminar fracture toughness of glass fiber/epoxy laminates modified with multiwall carbon nanotubes". In: *Journal of Composite Materials* 55.3 (2021), pp. 387–400. DOI: 10.1177/0021998320950788.

[219] T. S. Plagianakos, K. Muñoz, G. Guillamet, V. Prentzias, A. Quintanas-Corominas, M. Jimenez, and E. Karachalios. "Assessment of CNT-doping and hot-wet storage aging effects on Mode I, II and I/II interlaminar fracture toughness of a UD Graphite/Epoxy material system". In: *Engineering Fracture Mechanics* 224.4 (2020), p. 106761. DOI: 10.1016/j.engfracmech.2019.106761.

[220] Y. Gong, L. Jiang, L. Li, and J. Zhao. "An Experimental and Numerical Study of the Influence of Temperature on Mode II Fracture of a T800/Epoxy Unidirectional Laminate". In: *Materials (Basel, Switzerland)* 15.22 (2022). DOI: 10.3390/ma15228108.

[221] S. M. Lee. "Mode II Interlaminar Crack Growth Process in Polymer Matrix Composites". In: *Journal of Reinforced Plastics and Composites* 18.13 (1999), pp. 1254–1266. DOI: 10.1177/073168449901801308.

[222] M. S. Madhukar and L. T. Drzal. "Fiber-Matrix Adhesion and Its Effect on Composite Mechanical Properties: IV. Mode I and Mode II Fracture Toughness of Graphite/Epoxy Composites". In: *Journal of Composite Materials* 26.7 (1992), pp. 936–968. DOI: 10.1177/002199839202600701.

[223] K. D. Cowley and P. W. R. Beaumont. "The interlaminar and intralaminar fracture toughness of carbon-fibre/polymer composites: The effect of temperature". In: *Composites Science and Technology* 57.11 (1997), pp. 1433–1444. DOI: 10.1016/S0266-3538(97)00047-X.

[224] R. F. Teixeira, S. T. Pinho, and P. Robinson. "Thickness-dependence of the translaminar fracture toughness: Experimental study using thin-ply composites". In: *Composites Part A: Applied Science and Manufacturing* 90.4 (2016), pp. 33–44. DOI: 10.1016/j.compositesa.2016.05.031.

[225] I.B.C.M. Rocha, S. Raijmaekers, R.P.L. Nijssen, F. P. van der Meer, and L. J. Sluys. "Hygrothermal ageing behaviour of a glass/epoxy composite used in wind turbine blades". In: *Composite Structures* 174.9 (2017), pp. 110–122. DOI: 10.1016/j.compstruct.2017.04.028.

[226] T. D'Antino, M. A. Pisani, and C. Poggi. "Effect of the environment on the performance of GFRP reinforcing bars". In: *Composites Part B: Engineering* 141.2 (2018), pp. 123–136. DOI: 10.1016/j.compositesb.2017.12.037.

[227] A. Ferhat and A. Seymanur. "Investigation of The Durability Performance of FRP Bars in Different Environmental Conditions". In: *Advances in Concrete Construction* 12 (2021), pp. 295–302. DOI: 10.12989/acc.2021.12.4.295.

[228] M. Dawson, P. Davies, P. Harper, and S. Wilkinson. "Composite Materials in Tidal Energy Blades". In: *Durability of Composites in a Marine Environment 2*. Ed. by Peter Davies and Yapa D.S Rajapakse. Vol. 245. Solid Mechanics and Its Applications. Cham: Springer International Publishing, 2018, pp. 173–194. ISBN: 978-3-319-65144-6. DOI: 10.1007/978-3-319-65145-3_10.

[229] C. R. Kennedy, S. B. Leen, and C. M. Ó Brádaigh. "Immersed Fatigue Performance of Glass Fibre-Reinforced Composites for Tidal Turbine Blade Applications". In: *Journal of Bio- and Tribo-Corrosion* 2.2 (2016), p. 151. DOI: 10.1007/s40735-016-0038-z.

[230] E. Brown. “Effect of surface treatment on the hydrolytic stability of E-glass fiber bundle tensile strength”. In: *Composites Science and Technology* 65.1 (2005), pp. 129–136. DOI: 10.1016/j.compscitech.2004.07.001.

[231] A. Bledzki, R. Spaude, and G. W. Ehrenstein. “Corrosion phenomena in glass fibers and glass fiber reinforced thermosetting resins”. In: *Composites Science and Technology* 23.4 (1985), pp. 263–285. DOI: 10.1016/0266-3538(85)90040-5.

[232] J. Lamon and M. R’Mili. “Statistical-Probabilistic Approach to the Lifetime and Strength Degradation of E-Glass Filaments and Bundles under Constant Tensile Loading in Water”. In: *Journal of Composites Science* 3.3 (2019), p. 78. DOI: 10.3390/jcs3030078.

[233] L. Riaño, J.-F. Chailan, and Y. Joliff. “Evolution of effective mechanical and interphase properties during natural ageing of glass-fibre/epoxy composites using micromechanical approach”. In: *Composite Structures* 258 (2021), p. 113399. DOI: 10.1016/j.compstruct.2020.113399.

[234] M. Jurko, L. Souckova, J. Prokes, and V. Cech. “The Effect of Glass Fiber Storage Time on the Mechanical Response of Polymer Composite”. In: *Polymers* 14.21 (2022). DOI: 10.3390/polym14214633.

[235] C. G. Pantano, L. A. Carman, and S. Warner. “Glass fiber surface effects in silane coupling”. In: *Journal of Adhesion Science and Technology* 6.1 (1992), pp. 49–60. DOI: 10.1163/156856192X00043.

[236] H. F. Wu, D. W. Dwight, and N. T. Huff. “Effects of silane coupling agents on the interphase and performance of glass-fiber-reinforced polymer composites”. In: *Composites Science and Technology* 57.8 (1997), pp. 975–983. DOI: 10.1016/S0266-3538(97)00033-X.

[237] R. Plonka, E. Mäder, S. L. Gao, C. Bellmann, V. Dutschk, and S. Zhandarov. “Adhesion of epoxy/glass fibre composites influenced by aging effects on sizings”. In: *Composites Part A: Applied Science and Manufacturing* 35.10 (2004), pp. 1207–1216. DOI: 10.1016/j.compositesa.2004.03.005.

[238] H. N. Petersen. “Investigation of sizing - from glass fibre surface to composite interface”. English. PhD thesis. 2017.

[239] J. Kim, W. I. Lee, and S. W. Tsai. "Modeling of mechanical property degradation by short-term aging at high temperatures". In: *Composites Part B: Engineering* 33.7 (2002), pp. 531–543. DOI: 10.1016/S1359-8368(02)00036-7.

[240] P. Ghabezi and N. M. Harrison. "Multi-scale modelling and life prediction of aged composite materials in salt water". In: *Journal of Reinforced Plastics and Composites* (2023), p. 073168442311601. DOI: 10.1177/07316844231160189.

[241] O. Castro, P. A. Carraro, L. Maragoni, and M. Quaresimin. "Fatigue damage evolution in unidirectional glass/epoxy composites under a cyclic load". In: *Polymer Testing* 74 (2019), pp. 216–224. DOI: 10.1016/j.polymertesting.2018.12.027.

[242] S. Ahmadvash Aghbash, C. Breite, M. Mehdikhani, and Y. Swolfs. "Longitudinal debonding in unidirectional fibre-reinforced composites: Numerical analysis of the effect of interfacial properties". In: *Composites Science and Technology* 218 (2022), p. 109117. DOI: 10.1016/j.compscitech.2021.109117.

[243] B. Fazlali, S. V. Lomov, and Y. Swolfs. "Fiber break model for tension-tension fatigue of unidirectional composites". In: *Composites Part B: Engineering* 220 (2021), p. 108970. DOI: 10.1016/j.compositesb.2021.108970.

[244] S. Korkiakoski, P. Brøndsted, E. Sarlin, and O. Saarela. "Influence of specimen type and reinforcement on measured tension–tension fatigue life of unidirectional GFRP laminates". In: *International Journal of Fatigue* 85.03 (2016), pp. 114–129. DOI: 10.1016/j.ijfatigue.2015.12.008.

[245] I. de Baere, W. van Paepegem, M. Quaresimin, and J. Degrieck. "On the tension–tension fatigue behaviour of a carbon reinforced thermoplastic part I: Limitations of the ASTM D3039/D3479 standard". In: *Polymer Testing* 30.6 (2011), pp. 625–632. DOI: 10.1016/j.polymertesting.2011.05.004.

[246] F. A. Leone, A. C. Bergan, and C. G. Dávila. *CompDam - Deformation Gradient Decomposition (DGD), v2.5.0*. https://github.com/nasa/CompDam_DGD. 2019.

[247] F. A. Leone. “Deformation gradient tensor decomposition for representing matrix cracks in fiber-reinforced materials”. In: *Composites Part A: Applied Science and Manufacturing* 76.20 (2015), pp. 334–341. DOI: 10.1016/j.compositesa.2015.06.014.

[248] H. Krieger, T. Gries, and S. E. Stapleton. “Design of Tailored Non-Crimp Fabrics Based on Stitching Geometry”. In: *Applied Composite Materials* 25.1 (2018), pp. 113–127. DOI: 10.1007/s10443-017-9603-y.

[249] P. Davies. “Accelerated Aging Tests for Marine Energy Applications”. In: *Durability of Composites in a Marine Environment*. Ed. by Peter Davies and Yapa D.S Rajapakse. Vol. 208. Solid Mechanics and Its Applications. Dordrecht: Springer Netherlands, 2014, pp. 165–177. ISBN: 978-94-007-7416-2. DOI: 10.1007/978-94-007-7417-9_8.

[250] H. Schürmann. *Konstruieren mit Faser-Kunststoff-Verbunden*. 2., bearbeitete und erweiterte Auflage. VDI-Buch. Berlin, Heidelberg: Springer-Verlag Berlin Heidelberg, 2007. ISBN: 3540721894. URL: http://external.dandelon.com/download/attachments/dandelon/ids/DEAGI30F98F28C2C323E9C12572BC00708B0E.pdf.

[251] F. A. Ramirez, L. A. Carlsson, and B. A. Acha. “Evaluation of water degradation of vinylester and epoxy matrix composites by single fiber and composite tests”. In: *Journal of Materials Science* 43.15 (2008), pp. 5230–5242. DOI: 10.1007/s10853-008-2766-z.

[252] M. Assarar, D. Scida, A. El Mahi, C. Poilâne, and R. Ayad. “Influence of water ageing on mechanical properties and damage events of two reinforced composite materials: Flax–fibres and glass–fibres”. In: *Materials & Design* 32.2 (2011), pp. 788–795. DOI: 10.1016/j.matdes.2010.07.024.

[253] L. Peters, G. Adolphs, J.I. Bech, and P. Brøndsted. “HiPer-tex WindStrand: A new generation of high performance reinforcement”. English. In: *Polymer composite materials for wind power turbines. Proceedings*. Ed. by H. Lilholt, B. Madsen, T.L. Andersen, L.P. Mikkelsen, and A. Thygesen. 27th Risoe International Symposium on Materials Science ; Conference date: 04-09-2006 Through 07-09-2006. Risø National Laboratory, 2006, pp. 297–305. ISBN: 87-550-3528-0.

[254] B. A. Hernandez-Sanchez, D. Miller, and D. Samborsky. “2018 SNL/MSU/DOE COMPOSITE MATERIAL FATIGUE DATABASE -

Environmental Version 28E". In: (Oct. 2018). DOI: 10.2172/1481599. URL: https://www.osti.gov/biblio/1481599.

[255] 3B Fibreglass. *High Performance Glass - HiPer-tex*. 2023. URL: https://www.3b-fibreglass.com/HiPer-tex.

[256] B. F. Sørensen and S. Goutianos. "Micromechanical model for prediction of the fatigue limit for unidirectional fibre composites". In: *Mechanics of Materials* 131 (2019), pp. 169–187. DOI: 10.1016/j.mechmat.2019.01.023.

[257] L. Zhuang, R. Talreja, and J. Varna. "Tensile failure of unidirectional composites from a local fracture plane". In: *Composites Science and Technology* 133.11 (2016), pp. 119–127. DOI: 10.1016/j.compscitech.2016.07.023.

[258] P. Ghabezi and N. Harrison. "Mechanical behavior and long-term life prediction of carbon/epoxy and glass/epoxy composite laminates under artificial seawater environment". In: *Materials Letters* 261.15 (2020), p. 127091. DOI: 10.1016/j.matlet.2019.127091.

[259] H. M. Lal, A. Uthaman, C. Li, G. Xian, and S. Thomas. "Combined effects of cyclic/sustained bending loading and water immersion on the interface shear strength of carbon/glass fiber reinforced polymer hybrid rods for bridge cable". In: *Construction and Building Materials* 314.3 (2022), p. 125587. DOI: 10.1016/j.conbuildmat.2021.125587.

[260] J. Tu, H. Xie, and K. Gao. "Prediction of the Long-Term Performance and Durability of GFRP Bars under the Combined Effect of a Sustained Load and Severe Environments". In: *Materials (Basel, Switzerland)* 13.10 (2020). DOI: 10.3390/ma13102341.

[261] P. J. Lezzi, E. E. Evke, E. M. Aaldenberg, and M. Tomozawa. "Surface Crystallization and Water Diffusion of Silica Glass Fibers: Causes of Mechanical Strength Degradation". In: *Journal of the American Ceramic Society* 98.8 (2015), pp. 2411–2421. DOI: 10.1111/jace.13597.

[262] K. Liao and Y.-M. Tan. "Influence of moisture-induced stress on in situ fiber strength degradation of unidirectional polymer composite". In: *Composites Part B: Engineering* 32.4 (2001), pp. 365–370. DOI: 10.1016/S1359-8368(01)00011-7.

[263] T. J. Lehtonen, J. U. Tuominen, and E. Hiekkanen. “Dissolution behavior of high strength bioresorbable glass fibers manufactured by continuous fiber drawing”. In: *Journal of the mechanical behavior of biomedical materials* 20 (2013), pp. 376–386. DOI: 10.1016/j.jmbbm.2013.01.032.

[264] W. Eastes, R. M. Potter, and J. G. Hadley. “Estimating in vitro glass fiber dissolution rate from composition”. In: *Inhalation toxicology* 12.4 (2000), pp. 269–280. DOI: 10.1080/089583700196149.

[265] G. Foray, A. Descamps-Mandine, M. R’Mili, and J. Lamon. “Statistical flaw strength distributions for glass fibres: Correlation between bundle test and AFM-derived flaw size density functions”. In: *Acta Materialia* 60.9 (2012), pp. 3711–3718. DOI: 10.1016/j.actamat.2012.03.019.

[266] Y. Zhou and P. K. Mallick. “Fatigue Strength Characterization of E-glass Fibers Using Fiber Bundle Test”. In: *Journal of Composite Materials* 38.22 (2004), pp. 2025–2035. DOI: 10.1177/0021998304044774.

[267] C. Scheffler, S. L. Gao, R. Plonka, E. Mäder, S. Hempel, M. Butler, and V. Mechtcherine. “Interphase modification of alkali-resistant glass fibres and carbon fibres for textile reinforced concrete I: Fibre properties and durability”. In: *Composites Science and Technology* 69.3-4 (2009), pp. 531–538. DOI: 10.1016/j.compscitech.2008.11.027.

[268] A. E. Krauklis and A. T. Echtermeyer. “Long-Term Dissolution of Glass Fibers in Water Described by Dissolving Cylinder Zero-Order Kinetic Model: Mass Loss and Radius Reduction”. In: *Open Chemistry* 16.1 (2018), pp. 1189–1199. DOI: 10.1515/chem-2018-0133.

[269] B. Grambow and R. Müller. “First-order dissolution rate law and the role of surface layers in glass performance assessment”. In: *Journal of Nuclear Materials* 298.1-2 (2001), pp. 112–124. DOI: 10.1016/S0022-3115(01)00619-5.

[270] S. A. Otogo Be, L. Belec, A. Fahs, I. Martin, G. Louarn, and J.-F. Chailan. “Impact of the sizing reactivity of glass fibers on composites hydrothermal aging”. In: *Polymer Degradation and Stability* 215 (2023), p. 110426. DOI: 10.1016/j.polymdegradstab.2023.110426.

[271] D. Tripathi and F. R. Jones. “Single fibre fragmentation test for assessing adhesion in fibre reinforced composites”. In: *Journal of Materials Science* 33.1 (1998), pp. 1–16. DOI: 10.1023/A:1004351606897.

[272] D. Quan, J. L. Urdániz, and A. Ivanković. "Enhancing mode-I and mode-II fracture toughness of epoxy and carbon fibre reinforced epoxy composites using multi-walled carbon nanotubes". In: *Materials & Design* 143.4 (2018), pp. 81–92. DOI: 10.1016/j.matdes.2018.01.051.

[273] H. Chai. "Shear fracture". In: *International Journal of Fracture* 37.2 (1988), pp. 137–159. DOI: 10.1007/BF00041716.

[274] R. Khan. "Experimental investigation of mixed mode fracture toughness of glass fiber/epoxy laminates with sea water absorption". In: *Polymer Composites* 42.6 (2021), pp. 2808–2816. DOI: 10.1002/pc.26015.

[275] S. Samborski, A. Gliszczynski, J. Rzeczkowski, and N. Wiacek. "Mode I Interlaminar Fracture of Glass/Epoxy Unidirectional Laminates. Part I: Experimental Studies". In: *Materials (Basel, Switzerland)* 12.10 (2019). DOI: 10.3390/ma12101607.

[276] A. J. Russell. "Micromechanisms of interlaminar fracture and fatigue". In: *Polymer Composites* 8.5 (1987), pp. 342–351. DOI: 10.1002/pc.750080509.

[277] N. Perez. *Fracture Mechanics*. Cham: Springer International Publishing, 2017. ISBN: 978-3-319-24997-1. DOI: 10.1007/978-3-319-24999-5.

[278] A. Sjogren. "Effects of temperature on delamination growth in a carbon/epoxy composite under fatigue loading". In: *International Journal of Fatigue* 24.2-4 (2002), pp. 179–184. DOI: 10.1016/S0142-1123(01)00071-8.

[279] P. Coronado, A. Argüelles, J. Viña, and I. Viña. "Influence of low temperatures on the phenomenon of delamination of mode I fracture in carbon-fibre/epoxy composites under fatigue loading". In: *Composite Structures* 112.11 (2014), pp. 188–193. DOI: 10.1016/j.compstruct.2014.02.007.

[280] G. Perillo, N. P. Vedivik, and A. T. Echtermeyer. "Damage development in stitch bonded GFRP composite plates under low velocity impact: Experimental and numerical results". In: *Journal of Composite Materials* 49.5 (2015), pp. 601–615. DOI: 10.1177/0021998314521474.

[281] J. Körbelin, C. Dreiner, and B. Fiedler. "Impact of temperature on LVI-damage and tensile and compressive residual strength of CFRP". In: *Composites Part C: Open Access* 3.12 (2020), p. 100074. DOI: 10.1016/j.jcomc.2020.100074.